THE WATER INGRESS CHARACTERISTICS OF STRESSED MASONRY

C J TAIT

A thesis submitted in partial fulfilment of the
requirements of Napier University
for the degree of Doctor of Philosophy

May 1999

DECLARATION

This thesis is submitted to Napier University, Edinburgh for the Degree of Doctor of Philosophy. The work described in this thesis was carried out under the supervision of Dr. Fouad Khalaf and Dr. Abdy Kermani. The work was undertaken in the School of the Built Environment, Napier University.

In accordance with Napier University regulations governing the Degree of Doctor of Philosophy, the candidate submits this thesis as original unless otherwise referenced.

During the period of this research one paper has been published. Details are presented below:

1. Tait, C.J., Kermani, A. and Khalaf, F.M., 'Permeability of Concrete: A Practical Approach,' Concrete in the Service of Mankind, International Congress, University of Dundee, Dundee, Scotland, June 1996, pp. 435-441.

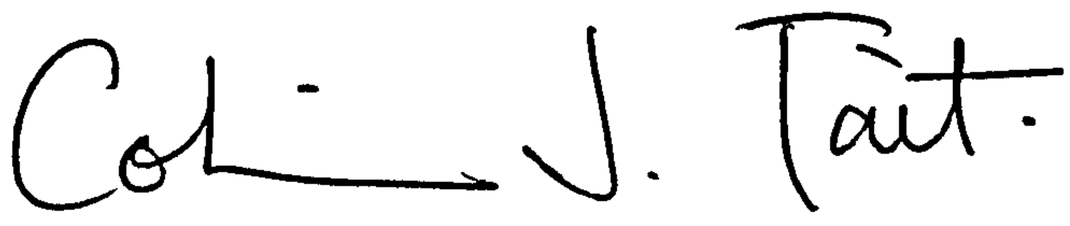

Colin J. Tait MEng

ACKNOWLEDGEMENTS

I would like to express my gratitude to my supervisors, Dr. A. Kermani and Dr. F. Khalaf for their advice and encouragement throughout the duration of this research project. I would also like to thank the technical support staff at Napier University, in particular Mr. J. Callaghan and Mr. W. Laing for their work within the laboratory and Mr. R. Hunter and Mr. P. McNeill. I would also like to thank my colleagues within the School of the Built Environment for their encouragement, especially Dr. M. Bensalem for his advice and Mr. J. Watson for both his interest in this research and the long, long discussions on football.

A special thank you to Dr. C. Stove for his advice, help, interest and enthusiasm during experimental work involving radar.

Most special thanks goes to my parents for their encouragement and help throughout all the years of study and to my Gran, brother and his family who have helped in many ways that they could not imagine.

Finally, this is for my wife, Sheila, without whom this could not be possible. I do not think I can thank you enough for all your encouragement, your advice and your shoulder and for the many countless ways that you have helped. I love you deeply.

This thesis, Sheila, is dedicated to you.

for Sheila,

SYNOPSIS

Water ingress, usually by wind-driven rain, is the main cause of premature deterioration in masonry structures. Water acts as a transport mechanism for aggressive chemicals and can also undergo freeze/thaw cycles leading to bursting of the masonry microstructure.

Factors such as the absorption rates of brick, water/cement ratio of the mortar, workmanship of the mason and poor design detail have all been identified as influencing the amount of water likely to penetrate a structure. It is also recognized that the majority of water ingress occurs at the brick unit/mortar joint interface, where interstices are present that allow access to the masonry interior.

The size, extent and influence that the brick/mortar interface has in governing water ingress is likely to be controlled by both the applied stress level and bed orientation of the main mortar beds relative to the direction of loading. Very little research has investigated these parameters in detail.

By using a new ingress measurement technique, the effect of the applied stress level and bed orientation was quantified. The main mortar beds of concentrically loaded masonry panels were found to deteriorate in their resistance to water ingress as they were orientated from perpendicular to parallel relative to the direction of loading. Poisson's ratio effects, which generated differential expansion between brick and mortar were believed to control water ingress at mortar joints orthogonal to the main beds. Water ingress at these mortar joints was also found greatly influenced by both applied stress level and bed orientation.

Factors such as the applied pressure head of water impinging onto the panel, the variability of the brick type used, eccentricity of applied loads and the pre-wetting of panels were also found to have some controlling influence on the water ingress characteristics of masonry.

Empirical modelling of water ingress dependent upon time, stress level, bed orientation and pressure head of water, was also undertaken. This enabled the volume of water ingress to be mathematically generated, with these models exhibiting good agreement with experimental data.

Suggestions for future work include assessing the effect of higher applied stress levels on water ingress, verification of the laboratory work with on-site tests and the introduction of freeze/thaw testing on loaded panels to simulate an abrasive external environment. Numerical analysis using finite element modelling was also identified.

LIST OF CONTENTS

TITLE PAGE		**i**
DECLARATION		**ii**
ACKNOWLEDGMENTS		**iii**
SYNOPSIS		**v**
LIST OF CONTENTS		**vii**
LIST OF FIGURES		**xii**
LIST OF TABLES		**xvi**
NOMENCLATURE		**xviii**
1	INTRODUCTION	1
1.1	Introduction	1
1.2	The Structure of the Thesis	4
2	LITERATURE REVIEW	6
2.1	Mortar	6
2.1.1	Mortar matrix	7
2.1.2	Pore size distribution	8
2.1.3	Simple permeability models	10
2.1.4	Factors controlling the permeability of mortar	12
2.1.5	Permeability test techniques	20
2.2	Permeability Characteristics of Brick	28
2.2.1	Brick parameters	29
2.2.2	Testing for absorption of brick	32
2.2.3	Permeability of brick	35
2.2.4	Pore structure of brick	37
2.2.5	Durability factor for brick	38
2.3	Permeability Characteristics of Masonry	40
2.3.1	Introduction	40
2.3.2	Rain penetration into a masonry structure	40
2.3.3	Evidence of rain penetration	46
2.3.4	Driving rain index (DRI)	50
2.3.5	Wall type	52
2.3.6	Workmanship	53
2.3.7	Brick/mortar bond	55
2.3.8	Morphology	55
2.3.9	Influence of the brick/mortar bond on the failure mode of masonry panels	56
2.3.10	Measurement of masonry permeability	66
2.4	Summary	68

3 MATERIAL TESTING 70

3.1 Introduction 70
3.2 Sieve Analysis of Sand 70
3.3 Mortar Preparation and Testing 71
3.3.1 Test Preparation 71
3.3.2 Fresh mortar tests 72
3.3.3 Mortar cube testing 75
3.4 Brick Testing 77
3.5 Conclusions 79

4 PERMEAMETER DEVELOPMENT 81

4.1 Introduction 81
4.2 Permeameter Development 81
4.3 Permeameter Attachment 84
4.4 Procedure for Testing Using Permeameters 85
4.5 Testing of Bricks and Mortars Using Permeameters 89
4.5.1 Permeameter assessment - bricks 89
4.5.2 Permeameter assessment - mortar 91
4.6 Conclusions 93

5 INSTRUMENTATION AND PRELIMINARY TESTING FOR THE ULTIMATE STRENGTH OF MASONRY PANELS 95

5.1 Introduction 95
5.2 Details of Test Panels 95
5.3 Specimen Preparation 96
5.4 Experimental Testing of Masonry Panels 97
5.5 Strain Measurement and Permeameter Positions on Test Panels 100
5.6 Conclusions 103

6 WATER INGRESS CHARACTERISTICS FOR CONCENTRICALLY LOADED MASONRY PANELS 104

6.1 Introduction 104
6.2 General Remarks on Tests and Measurements 105
6.3 Water Ingress Characteristics when Bed Orientation $\theta=0°$ 107
6.3.1 Panel testing 108
6.3.2 Modelling of water ingress rate results 113
6.3.3 Effect of varying applied stress level on strain for $\theta=0°$ panels 114

6.3.4 Effect of varying initial water head and applied stress level on water ingress through θ=0° panels 115
6.3.5 Relationship between water ingress and strain for θ=0° panels 118
6.3.6 Effect of joint type on water ingress for θ=0° panels 125
6.4 Water Ingress Characteristics when Bed Orientation θ=90° 126
6.4.1 Panel testing 126
6.4.2 Modelling of water ingress rate results 131
6.4.3 Effect of varying applied stress level on strain for θ=0° panels 131
6.4.4 Effect of varying initial water head and applied stress level on water ingress through θ=90° panels 134
6.4.5 Relationship between water ingress and strain for θ=90° panels 134
6.4.6 Effect of joint type on water ingress for θ=90° panels 138
6.5 Water Ingress Characteristics when Bed Orientation θ=90° 138
6.5.1 Panel testing 139
6.5.2 Modelling of water ingress rate results 144
6.5.3 Effect of varying applied stress level on strain for θ=30° panels 145
6.5.4 Effect of varying initial water head and applied stress level on water ingress through θ=30° panels 146
6.5.5 Relationship between water ingress and strain for θ=30° panels 148
6.5.6 Effect of joint type on water ingress for θ=30° panels 154
6.6 Water Ingress Characteristics when Bed Orientation θ=45° 155
6.6.1 Panel testing 155
6.6.2 Modelling of water ingress rate results 160
6.6.3 Effect of varying applied stress level on strain for θ=45° panels 161
6.6.4 Effect of varying initial water head and applied stress level on water ingress through θ=45° panels 162
6.6.5 Relationship between water ingress and strain for θ=45° panels 163
6.6.6 Effect of joint type on water ingress for θ=45° panels 168
6.7 Water Ingress Characteristics when Bed Orientation θ=90° 168
6.7.1 Panel testing 169
6.7.2 Modelling of water ingress rate results 173
6.7.3 Effect of varying applied stress level on strain for θ=60° panels 174
6.7.4 Effect of varying initial water head and applied stress level on water ingress through θ=60° panels 175
6.7.5 Relationship between water ingress and strain for θ=60° panels 175

6.7.6 Effect of joint type on water ingress for θ=60° panels 179
6.8 Effect of Bed Orientation on Water Ingress Characteristics 179
6.8.1 Effect of bed orientation at Joint 1 180
6.8.2 Effect of bed orientation at Joint 2 184
6.8.3 Effect of bed orientation at Joint 3 188
6.9 Comparative Study of Water Ingress into Calcium Silicate and Clay Brick Panels 192
6.9.1 Calcium silicate test panels 192
6.9.2 Water ingress through calcium silicate (Type 1) and clay (Types 2, 3 and 4) brick panels 193
6.10 Conclusions 196

7 WATER INGRESS BEHAVIOUR FOR ECCENTRICALLY LOADED AND CONCENTRICALLY LOADED PRE-SATURATED PANELS 199

7.1 Introduction 199
7.2 Eccentric Loading on Masonry Panels 200
7.3 Water Ingress Characteristics for Eccentrically Loaded Masonry Panels 202
7.3.1 Panel testing 203
7.3.2 The load-strain relationship for eccentrically loaded masonry panels 204
7.3.3 The influence of eccentric loading on water ingress 206
7.4 The Influence of Pre-Saturation on the Water Ingress Characteristics of Concentrically Loaded Masonry Panels 209
7.4.1 Panel testing and pre-saturation procedure 209
7.4.2 Assessment of pre-saturated panels in resisting water ingress 210
7.5 Conclusions 211

8 EMPIRICAL MODELLING OF WATER INGRESS FOR CONCENTRICALLY LOADED MASONRY PANELS 213

8.1 Introduction 213
8.2 Empirical Modelling of Masonry Panels 213
8.2.1 Typical example of empirically modelled water ingress 215
8.2.2 Empirical modelling incorporating bed orientation 224
8.3 Conclusions 229

9 CONCLUSIONS AND RECOMMENDATIONS FOR FUTURE WORK 230

9.1 Conclusions 230
9.2 Recommendations for Future Work 233
9.2.1 Experimental research 234
9.2.2 Numerical modelling 235

REFERENCES 236

LIST OF FIGURES

Fig. 2.1	Relationship between permeability and water/cement ratio [21]
Fig. 2.2	Effects of test duration on the permeability of moist cured concrete [1]
Fig. 2.3(a-c)	Permeability behaviour of stressed concrete [31,32]
Fig. 2.4(a-c)	Typical early test methods for the assessment of permeability [34]
Fig. 2.5	Figg test apparatus for determining air permeability of concrete [35]
Fig. 2.6	Apparatus suggested by Hansen et al to measure permeability of in-situ concrete [39]
Fig. 2.7	Vacuum permeability tester used by Schonlin and Hilsdorf [41]
Fig. 2.8	Clam method for determination of water permeability [42]
Fig. 2.9	Apparatus used in ISAT [44]
Fig. 2.10	Section through typical permeameter [31]
Fig. 2.11	Maximum and minimum expansion curves for bricks standing in air [56]
Fig. 2.12	Moisture expansion curves based on kiln temperature for typical clay brick units [56]
Fig. 2.13	Water uptake within a brick unit against square root of time [73]
Fig. 2.14	Correlation between frost resistance F_m and intruded pore volume P_v for constant P_3 values [76,77]
Fig. 2.15	Pitot tube estimation of static pressure due to wind velocity [78]
Fig. 2.16	Forces acting upon a molecule in close proximity to the tube wall [78]
Fig. 2.17	Crack development for masonry walls [90]
Fig. 2.18	Driving rain index isolines (DRI) for the USA [91]
Fig. 2.19	Typical effect of mortar/brick thickness ratio on brickwork compressive strength [101]
Fig. 2.20(a-e)	Failure modes for masonry panels with variable bed orientation [111]
Fig. 2.21	Stresses in brick-mortar composite [95]
Fig. 2.22	Hilsdorf's failure theory [113]
Fig. 2.23	Failure envelope for brick compression and tension [114]
Fig. 3.1	Specimen arrangement for measuring elastic modulus, E_m
Fig. 3.2	Sketches of cored brick types used in testing
Fig. 3.3	Typical relationship between average absorption and compressive strength [134]
Fig. 4.1	Development of permeameters during testing
Fig. 4.2	Typical permeameters attached to Type 4 test panels
Fig. 4.3	Typical permeameter positions on masonry test panel
Fig. 4.4	Typical falling head test for measuring water ingress rates using a permeameter
Fig. 4.5	Summary of test technique for measuring water ingress into a masonry panel
Fig. 4.6(i-iv)	Water ingress rates for Type 1-4 bricks at all initial test heads
Fig. 4.7(i-iv)	Water ingress rates for all mortar types

Fig. 5.1 Typical wall cut angles: 0°, 30°, 45°, 60° and 90° to original bed angle
Fig. 5.2 Effect of principal stress angle on the compressive capacity of a masonry panel
Fig. 5.3 Failure modes for test panels with variable bed orientations
Fig. 5.4 Permeameter details for Type 1 (calcium silicate) panels
Fig. 5.5 Demec button locations and permeameter details for Type 2 panels
Fig. 5.6 Demec button locations and permeameter details for Type 3 panels
Fig. 5.7 Demec button locations and permeameter details for Type 4 panels

Fig. 6.1 Typical permeameter positions on masonry test panels
Fig. 6.2 Idealisation of 'settling' effects encountered in permeameter attachment
Fig. 6.3 Permeameter and demec positions for panels with bed orientation θ=0°
Fig. 6.4 Average water ingress rates at Joint 1, bed orientation θ=0°
Fig. 6.5 Average water ingress rates at Joint 2, bed orientation θ=0°
Fig. 6.6 Average water ingress rates at Joint 3, bed orientation θ=0°
Fig. 6.7 Average stress-strain relationship for masonry joints, bed orientation θ=0°
Fig. 6.8 Volume intake within initial 10mins at Joint 1 under four levels of stress when bed orientation θ=0°
Fig. 6.9 Volume intake within initial 10mins at Joint 2 under four levels of stress when bed orientation θ=0°
Fig. 6.10 Threshold strains for minimum water ingress as influenced by initial water at Joint 2
Fig. 6.11 Volume intake within initial 10mins at Joint 3 under four levels of stress when bed orientation θ=0°
Fig. 6.12 Permeameter and demec positions for panels with bed orientation, θ=90°
Fig. 6.13 Average water ingress rates at Joint 1, bed orientation θ=90°
Fig. 6.14 Average water ingress rates at Joint 2, bed orientation θ=90°
Fig. 6.15 Average water ingress rates at Joint 3, bed orientation θ=90°
Fig. 6.16 Average stress-strain relationship for masonry joints, bed orientation θ=90°
Fig. 6.17 Volume intake within initial 10mins at Joint 1 under four levels of stress when bed orientation θ=90°
Fig. 6.18 Volume intake within initial 10mins at Joint 3 under four levels of stress when bed orientation θ=90°
Fig. 6.19 Volume intake within initial 10mins at Joint 2 under four levels of stress when bed orientation θ=90°
Fig. 6.20 Permeameter and demec positions for panel with bed orientation θ=30°
Fig. 6.21 Movement of demec buttons across Joint 1 leading to measurement of both compressive and tensile strains
Fig. 6.22 Water ingress rates at Joint 1, bed orientation θ=30°
Fig. 6.23 Water ingress rates at Joint 2, bed orientation θ=30°
Fig. 6.24 Water ingress rates at Joint 3, bed orientation θ=30°

Fig. 6.25 Average stress-strain relationship for masonry joints, bed orientation θ=30°
Fig. 6.26 Volume intake within initial 10mins at Joint 1 under four levels of stress when bed orientation θ=30°
Fig. 6.27 Threshold strains for minimum water ingress dependent upon initial head of water at Joint 1
Fig. 6.28 Volume intake within initial 10mins at Joint 2 under four levels of stress when bed orientation θ=30°
Fig. 6.29 Threshold strains for minimum water ingress as influenced by initial water head at Joint 2
Fig. 6.30 Volume intake within initial 10mins at Joint 3 under four levels of stress when bed orientation θ=30°
Fig. 6.31 Permeameter and demec positions for panels with bed orientation θ=45°
Fig. 6.32 Average water ingress rates at Joint 1, bed orientation θ=45°
Fig. 6.33 Average water ingress rates at Joint 1, bed orientation θ=45°
Fig. 6.34 Average water ingress rates at Joint 3, bed orientation θ=45°
Fig. 6.35 Average stress-strain relationship for masonry joints, bed orientation θ=45°
Fig. 6.36 Volume intake within initial 10mins at Joint 1 under four levels of stress when bed orientation θ=45°
Fig. 6.37 Volume intake within initial 10mins at Joint 2 under four levels of stress when bed orientation θ=45°
Fig. 6.38 Threshold strain across Joint 2 to induce minimum water ingress dependent upon initial water head
Fig. 6.39 Volume intake within initial 10mins at Joint 3 under four levels of stress when bed orientation θ=45°
Fig. 6.40 Permeameter and demec positions for θ=60° panels
Fig. 6.41 Average water ingress rates at Joint 1, bed orientation θ=60°
Fig. 6.42 Average water ingress rates at Joint 2, bed orientation θ=60°
Fig. 6.43 Average water ingress rates at Joint 3, bed orientation θ=60°
Fig. 6.44 Average stress-strain relationship for masonry joints, bed orientation θ=60°
Fig. 6.45 Volume intake within initial 10mins at Joint 1 under four levels of stress when bed orientation θ=60°
Fig. 6.46 Volume intake within initial 10mins at Joint 2 under four levels of stress when bed orientation θ=60°
Fig. 6.47 Volume intake within initial 10mins at Joint 1 under four levels of stress when bed orientation θ=60°
Fig. 6.48(a) Panel integrity relationship as orientation increased, applied stress = $0.3f_{ult}$ (Joint 1)
Fig. 6.48(b) Panel integrity relationship as orientation increased, applied stress = $0.45f_{ult}$
Fig. 6.48(c) Panel integrity relationship as orientation increased, applied stress = $0.6f_{ult}$
Fig. 6.49(a) Panel integrity relationship as orientation increased, applied stress = $0.3f_{ult}$ (Joint 2)

Fig. 6.49(b) Panel integrity relationship as orientation increased, applied stress = $0.45f_{ult}$
Fig. 6.49(c) Panel integrity relationship as orientation increased, applied stress = $0.6f_{ult}$
Fig. 6.50(a) Panel integrity relationship as orientation increased, applied stress = $0.3f_{ult}$ (Joint 3)
Fig. 6.50(b) Panel integrity relationship as orientation increased, applied stress = $0.3f_{ult}$
Fig. 6.50(c) Panel integrity relationship as orientation increased, applied stress = $0.3f_{ult}$
Fig. 6.51 Permeameter positions for calcium silicate (Type 1) test panels
Fig. 6.52 Comparison of average water ingress rates for unstressed calcium silicate panels (Type 1) and clay brick (Type 2, 3 and 4) panels

Fig. 7.1 Eccentrically loaded pinned-end column of brittle material [113]
Fig. 7.2 Standard eccentric loading positions [138]
Fig. 7.3 Design eccentricity [139]
Fig. 7.4 Demec and permeameter position for eccentrically loaded panels: (4Ai, 4Aii)
Fig. 7.5 Average stress-strain relationship for masonry joints
Fig. 7.6 Stress distribution across panel caused by eccentric loading
Fig. 7.7 Volume ingress under load at Joint 1 dependent upon eccentricity
Fig. 7.8 Volume ingress under load at Joint 2 dependent upon eccentricity
Fig. 7.9 Volume ingress under load at Joint 3 dependent upon eccentricity
Fig. 7.10 Demec and permeameter positions for pre-saturated panels

Fig. 8.1 Typical permeameter positions on masonry test panels
Fig. 8.2(i-iv) Experimental and modelled water ingress rates for Joint 1, bed orientation $\theta=0°$
Fig. 8.3(i-iv) Experimental and modelled water ingress rates for Joint 2, bed orientation $\theta=0°$
Fig. 8.4(i-iv) Experimental and modelled water ingress rates for Joint 3, bed orientation $\theta=0°$
Fig. 8.5(i-iv) Comparison of experimental and modelled water ingress rates for Joint 1 when bed orientation $\theta=0°$, (using Eqns. 8.6 and 8.7)
Fig. 8.6(i-iv) Comparison of experimental and modelled water ingress rates for Joint 2 when bed orientation $\theta=0°$, (using Eqns. 8.6 and 8.7)
Fig. 8.7(i-iv) Comparison of experimental and modelled water ingress rates for Joint 3 when bed orientation $\theta=0°$, (using Eqns. 8.6 and 8.7)

LIST OF TABLES

Table 2.1 Summary of available test techniques

Table 3.1 Building sands for mortar used in masonry panels [126]
Table 3.2 Moisture contents for fresh mortar
Table 3.3 Average penetration depths using the dropping ball technique [129]
Table 3.4 Average water retentivity for mortar mixes
Table 3.5 Average consistence retentivity for mortar mixes after suction
Table 3.6 Summary of mortar cube test results
Table 3.7 Average results of water absorption test
Table 3.8 Average brick properties

Table 4.1 Water ingress curves for test bricks
Table 4.2 Water ingress curves for mortar cubes

Table 5.1 Actual and predicted failure loads for masonry under uniaxial compression

Table 6.1 Average decay curves and coefficient of correlation values for panels with bed orientation $\theta = 0°$
Table 6.2 Typical results of water head drop within 45mins of test commencing for Joint 1 and within 10mins for Joint 3 for $\theta=0°$ panels as influenced by applied stress and initial water head
Table 6.3 Standard decay equations for water ingress at Joint 1
Table 6.4 Standard second order polynomial equations for water ingress at Joint 2
Table 6.5 Standard decay equations for water ingress at Joint 3
Table 6.6 Average decay curves and coefficient of correlation values for panels with bed orientation $\theta=90°$
Table 6.7 Decay curves and coefficient of correlation values for panel with bed orientation $\theta=30°$
Table 6.8 Head drop in test reservoir within initial 10mins of testing dependent upon initial head, h
Table 6.9 Standard second order polynomial equations for water ingress at Joint 1
Table 6.10 Standard second order polynomial equations for water ingress at Joint 2
Table 6.11 Average decay curves and coefficient of correlation values for panels with bed orientation $\theta=45°$
Table 6.12 Standard second order polynomial equations for water ingress at Joint 2
Table 6.13 Average decay curves and coefficient of correlation for panels with bed orientation $\theta = 60°$
Table 6.14 Standard second order polynomial equations for water ingress at Joint 2
Table 6.15 Average volume of water ingress within initial 10mins of testing into unstressed calcium silicate and clay brick panels

Table 7.1 Average water ingress volumes within initial 10mins of testing for pre-saturated and dry panels when stressed to $0.6f_{ult}$

Table 8.1 Average decay curves and coefficients of correlation values for panels with bed orientation $\theta=0°$

Table 8.2 Decay coefficients b_0 as a function of applied stress level for $\theta=0°$ panels

Table 8.3 Coefficients a, b and c as a function of initial head

Table 8.4 Empirical modelling coefficients for Joint 1, (Eqn. 8.5)

Table 8.4 Empirical modelling coefficients for Joint 2, (Eqn. 8.5)

Table 8.6 Empirical modelling coefficients for Joint 3, (Eqn. 8.5)

Table 8.8 'A' coefficient for all joints, (Eqn. 8.6)

Table 8.8 'b_θ' coefficient for Joint 1, (Eqn. 8.6)

Table 8.9 'b_θ' coefficient for Joint 2, (Eqn. 8.6)

Table 8.10 'b_θ' coefficient for Joint 3, (Eqn. 8.6)

NOMENCLATURE

The following is a list of symbols used throughout the test. Additionally most symbols are identified where they are first used, or used if different from that given below.

A_{DRI} - annual rainfall precipitation as measured by the driving rain index
A_f - face area of the specimen
A_x - cross-sectional area of a specimen
B_{DRI} - annual precipitation of slow, sleet, hail etc. as measured by the driving rain index
b_k - constant for a given gas and porous media
C - constant dependant upon material type
C_m - correction factor dependant upon end moment conditions
c_e - effective cohesion
c_p - volume of concentration of particles
c_0 - uniaxial compressive strength of brick
DF - durability factor for bricks
DRI - driving rain index
D_{wi} - increase in water ingress volume
d - width of panel or specimen thickness
E_b - elastic modulus of brick
E_m - elastic modulus of mortar
e - eccentricity
e_a - additional eccentricity caused by lateral deflection
e_t - maximum eccentricity
e_x - resultant eccentricity
e_1, e_2 - end eccentricities
F_g - force due to gravity
F_m - frost resistance rating
f' - uniaxial compressive strength in the mortar
f_b - uniaxial compressive strength of brick
f'_{bt} - biaxial tensile strength of brick
$f_{cu(m)}$ - cube crushing strength of mortar
f_{ult} - panel failure stress
g - gravity
H - head difference in manometer
h_{ef} - effective wall height
i - cumulative volume of absorbed water per unit face area
i_l - head loss per unit length of capillary
I_{wi} - decrease in water ingress volume
k - permeability coefficient
k_g - gas permeability coefficient
k_l - liquid permeability coefficient
k_p - cement paste permeability coefficient
MTP - modified total pore volume
m_0 - magnetic permeability of free space
n - tortuosity factor
P - applied load or pressure
P_V - total induced pore volume of brick
p_c - capillary porosity of pores
P_m - mean pressure at which gas is flowing
P_1, P_2 - hydrostatic pressure at points 1 and 2
P_3 - percentage of the pore volume with pore diameter >3με
p_{ext} - exterior pressure
p_{int} - interior pressure
Q - steady state volumetric flow
Q_k - design vertical load
r - pore radius
$\bar{r}$ - mean radius of capillary tubes
r_n - reflection coefficient
S - sorptivity
S_r - slenderness ratio
T - temperature
TD - threshold diameter
t - elapsed time
t_d - panel thickness
t_n - transmission coefficient

t_0 - uniaxial tensile strength of the brick
U_u - factor of non-conformity
V - porosity
$\overline{V}$ - mean wind speed
V_A - pore volumes in the range of >1320Å
V_B - pore volume in the range of 290Å to 1320Å
V_1, V_2 -air velocity at points 1 and 2
v - wave propagation velocity
v_i - mean velocity in the tube
V_i - volume of water to ingress into a panel
x - depth of fluid penetration
y - water height in reservoir
Z - constant dependant upon the rapid filling of the open pores on the side faces of the brick
z - height above datum
z_r - impedance

α - ratio of height of brick to thickness of mortar bed
Δm - rate of change of momentum
Δp - pressure differential
ε - dielectric permittivity of a material
ε_r - dielectric constant
ε_0 dielectric permittivity of air
ϕ_A - shear angle
η - viscosity
θ - bed orientation
ρ - density of a fluid
ρ_a - air density
ρ_w - water density
σ - coefficient of surface tension
σ_b - basic stress
σ_c - applied stress
σ'_t - longitudinal tensile stress
σ_{ult} - longitudinal compressive stress
σ'_{ult} - ultimate longitudinal compressive stress
σ_x - lateral compressive strength in mortar joint
σ_{xb} - lateral stress in x-direction in brick
σ_{xm} - lateral stress in x-direction on mortar
σ_y - stress normal to bed joints
σ_{ym} - mean external compressive stress
τ_{xy} - shear stress
τ_p - shear strength
υ_b - Poisson's ratio of brick
υ_m - Poisson's ratio of mortar

CHAPTER 1

INTRODUCTION

1.1 Introduction

Masonry is an extremely versatile building material which has been used for millennia due to its high durability, low cost and excellent aesthetic properties. For the majority of cases, this material behaves adequately for both its design lifetime and beyond. Unfortunately in a small proportion of cases masonry shows signs of accelerated deterioration due to water ingress.

The deterioration of masonry is not a new problem. Research has for a number of years attempted to identify the various parameters that influence the deterioration mechanism.

Virtually every form of deterioration requires water penetration, usually through rain precipitation. Water acts as a transport or reactant mechanism bringing salts, acids or other harmful chemicals into the masonry interior. Water can also concentrate at the brick/mortar interface where there tends to be fissures providing a path to the interior. Freeze-thaw action then becomes influential leading to bursting, spalling and dusting of the masonry. Therefore, producing less permeable masonry is seen as an effective way in prolonging the lifetime of masonry structures.

The assessment of unstressed masonry panels for their water penetration characteristics has been studied for a large number of years. Parameters such as the water/cement ratio of mortar, absorption rate of brick and workmanship have all been found influential.

However, the behaviour of masonry in relation to water ingress is governed by its stress history. Although masonry is designed to accommodate a variety of loading conditions throughout its lifetime, it is felt that even at low load levels the resistance to water penetration may be compromised due to crack initiation and expansion.

Any crack initiation would likely be developed at the brick/mortar interface which are the inherent layers of weakness in masonry. Therefore, a good bond between brick and mortar is required to resist both structural loading and water ingress and is obtained by the ability of the mortar to flow into the interstices and surface irregularities of the brick. However, as mortar joints are relatively weak compared to the brick units, the bed and head joints are seen as the critical planes where failure is likely to be initiated and developed during loading.

When a masonry panel is loaded, the common stress condition is tension or compression in the plane of the panel. This can result from gravity loading, lateral wind loading and racking shear. However, orientating the main mortar bed causes a combined effect of these loading regimes on the panel producing distinct failure mechanisms highly dependent upon the brick/mortar bond, magnitude of orientation and level of applied load.

A compression mode of failure occurs in masonry panels when the applied load is perpendicular to the main mortar bed and is exhibited by vertical splitting of the masonry. For panels with mortar beds orientated parallel to the applied load then a tensile mode of failure occurs indicated by large vertical cracking at the main bed brick/mortar interface. Panels with bed orientation between these two extremes will exhibit a combination of both compression and tension failure usually exhibited by some degree of shear slip at the main mortar bed as the brick/mortar bond is compromised together with debonding at the perpend joint. The behaviour at the brick/mortar interface under load and at variable bed orientations would fundamentally control any water ingress.

Therefore to gain a full understanding of water ingress characteristics for masonry fundamental factors such as applied load level and the influence of bed orientation must be considered. Only limited studies have acknowledged the effect of these parameters, with this generally only being found via concrete research.

The main points of study for this research programme are therefore:

- The development of a practical, easy to use and repeatable test technique that can allow the assessment of water ingress into stressed and orientated masonry panels;
- The influence of the various failure modes associated with the bed orientation of masonry that controls the formation of cracks and hence water ingress;
- The effect of the applied water head on influencing water ingress;
- The effect of variable brick types and mortar mixes in controlling water ingress;
- Which brick/mortar interfaces are prone to water ingress when masonry panels are stressed;
- The effect of differing loading regimes (i.e. concentric or eccentric loads) in controlling water ingress;
- The development of empirical models based on experimental data that can be used to indicate levels of water ingress into stressed masonry panels.

Using experimental and analytical examination of water ingress influenced by a number of the above variable factors, considered both singly and in combination, a full understanding of the water ingress mechanism can be found.

1.2 The Structure of the Thesis

The structure of the thesis can be summarised as follows:

Chapter 1: Gives the introduction, scope and objectives of the present investigation.

Chapter 2: A general overview of research relating to water ingress of masonry is described. As masonry is an amalgam of brick and mortar, their influence on water ingress were considered independently. At later stages however, these were brought together to consider water ingress through masonry as a whole and the effect that the brick/mortar interface has on permeability. A review of current permeability and absorption testing techniques for mortar, brick and masonry is also shown.

Chapter 3: Indications of the basic tests required and undertaken on both brick and mortar that produced values of compressive strength, absorption rates, elastic modulii and levels of workability.

Chapter 4: Discusses the development of the new test permeameters and the required test technique. Tests on brick and mortar using these permeameters are considered alongside comparisons with related tests undertaken within Chapter 3.

Chapter 5: Gives details of the masonry test panels used, indicating how they were built, cured, stored and prepared prior to test. Details of failure load levels dependent upon bed orientation together with an outline of the water ingress rates into unstressed masonry samples are also shown.

Chapter 6: Discussion and interpretation of results for concentrically loaded masonry panels. This includes details of the effects of the variation in bed orientation and corresponding failure mechanism, applied stress level, mortar joint and brick type and the applied water heads on water ingress. A comparison of water ingress behaviour between clay brick and calcium silicate brick panels is also shown.

Chapter 7: Discussion and interpretation of water ingress results into masonry panels under eccentric loading or when panels are pre-saturated with water is given.

Chapter 8: The development of empirical relationships to simulate water ingress based on concentrically loaded specimens are described.

Chapter 9: Conclusions and recommendations for future work are given.

CHAPTER 2

LITERATURE REVIEW

This chapter provides a review of previous work covering the water ingress of masonry structures. As masonry is basically an amalgam of brick and mortar this review discusses these very different materials before considering them acting compositely. In the following sections the important aspects that influence the permeability of both the individual materials and then as a whole are detailed. These sections also examine the previous and current experimental procedures used to measure water ingress.

2.1 Mortar

Mortar is a mixture of sand, cement and water. For this to be impermeable three basic requirements must be satisfied. Firstly, that aggregates should be totally impermeable. Secondly, the cement paste should be sufficiently workable to fill any voids surrounding the aggregate. Finally, the cement paste should be impermeable once hardened. This final factor is dependent upon the water/cement ratio, extent of hydration and the cement characteristics [1].

Most cementitious mixes tend to satisfy the above criteria and combine this with high compressive strengths.

Lime mortar mixes have lower strength and are more vapour permeable than cementitious mixes which has lead to a decline in their use over the last 50 years. Recently lime mortars have regained some popularity due to their ability to concentrate moisture within the joint and not within the adjacent stone or brick. This is particularly pertinent for masonry conservation where stone replacement is more costly than joint repointing. Repointing with modern cement mixes resulted in the deterioration of the stone or brick and left the joint standing proud [2].

2.1.1 Mortar matrix

After the placement of fresh mortar or concrete, water, cement and fine sand particles are forced upwards due to their low specific gravity compared to that of aggregate. Large aggregate particles stabilise, maintained in position by point contact, and form a loose skeleton within which further settlement takes place. This settlement in turn forces water upwards and can result in both this water and latterly air voids being formed beneath any settled aggregates. Between sand grains, the cement particles settle to form a porous matrix.

Hydration (water chemically combining with cement) then takes place in which cement gel is formed. The hydration products have a characteristic porosity called gel pores. Chemically, cement gel primarily consists of fibrous calcium silicate hydrates (CSH) of various compositions and has a relatively high porosity.

Powers et al [3] suggested that the cement gel volume grows to 23 times greater than the original cement particles though this may vary dependant upon cement fineness and chemical composition. The cement gel is often not sufficient to fill all available pores. Capillary pores are then formed that allow air or moisture permeation through the gel. Pores are generally sub-microscopic with the gel pores being much smaller than the capillary pores [4].

These capillary pores can form up to 40% of the total paste volume. The capillary pores also directly contribute to the cement paste being 20-100 times more permeable than the cement gel [5,6]. Nyame [7] stated that for total elimination of capillary pores a water/cement ratio of 0.37 or less is required.

There is however no unique relationship between the total porosity (capillary and gel pores) and the permeability of mortar [8]. Instead permeability is closely linked to the continuity and size distribution of the pores.

2.1.2 Pore size distribution

Pore size distribution can relate pore volume with characteristic pore sizes within a cement paste. These distributions can be measured in a variety of ways, usually dictated by the maximum pore radius.

A common method of evaluating pore radii is by high pressure mercury intrusion porosimetery (MIP). This method works on the principle that a non-wetting fluid penetrates pores only if the resistance to wetting due to the surface tension can be overcome by an applied pressure. Large pores (>7500nm) caused by entrained air or microcracks are mostly not interconnected and therefore only reached by smaller capillary pores. This indicates that MIP is less reliable for measuring these larger pores [9]. Investigations of much smaller pore radii would use sorption methods with helium or methanol pycnometers [7].

It has however been observed that porosity values for cement pastes as determined by MIP were greater than those obtained by pycnometers. These results were attributed to damage caused to the pore structure by high differential pressures of the mercury during intrusion. The method of moisture removal prior to testing of paste samples (pre-treatment) has also proved influential [10].

Day and Marsh [11] stated that due to the complex nature of the pore structure in hardened cement pastes, it is desirable to use more than one experimental method to measure porosity.

Powers et al [12] found a semi-empirical relationship between the pore structure and permeability using viscous drag theory. This drag may be developed by particles falling through a fluid or by flow through a granular bed where the particles are in fixed positions.

By applying this theorem to hardened cement paste, permeability (k) was expressed as:

$$k = \frac{1.36 \times 10^{-10}}{\eta} \frac{(1 - c_p^{\,2})}{c_p} \exp -[(\frac{1242}{T} + 0.7) \frac{c_p}{1 - c_p}] \qquad \text{Eqn. 2.1}$$

where η - viscosity of fluid

c_p - volume of concentration of particles

T - absolute temperature

The link to porosity being $c_p = 1 - p_c$ where p_c is the capillary porosity of the paste.

Further work by Mehta and Manmohan [13] attempted to identify the effect of pore size distribution on permeability (k):

$$k = \exp[3.84V_A + 0.20V_B + 0.56 \times 10^{-6} TD + 8.09\,MTP - 2.53] \qquad \text{Eqn. 2.2}$$

where V_A - pore volumes in the range of > 1320 Å

V_B - pore volumes in the range 290 - 1320 Å

TD - threshold diameter

MTP - modified total pore volume = total pore volume/degree of hydration

This study concluded that larger pores were found to have a greater influence on the permeability than smaller pores. Pore size distribution rather than porosity therefore provided a better opportunity for developing an accurate correlation with permeability.

Luping and Nilsson [14] stated that fluid flow within mortar does not occur in every pore but is dependent upon the size of these pores and the pressure gradient applied. Under certain ranges of pressure gradient, the total flow does not linearly increase with a corresponding increment of pressure gradient until this pressure gradient reached a point at which flow occurred in all pore bodies.

2.1.3 Simple permeability models

Permeability can be assessed using alternative methods avoiding any need to include pore size distribution.

The coefficient of permeability (k) can be calculated using Darcy's law. This law relates hydraulic gradient to the steady-state flow of fluids in a saturated porous media:

$$Q = kA_x \frac{dh}{dx} \qquad \text{Eqn. 2.3}$$

where Q - steady state volumetric flow

A_x - cross sectional area of specimen

$\frac{dh}{dx}$ - hydraulic gradient across a sample in the direction of the flow

Darcy's law however is not uniquely defined and there is some ambiguity between the law postulated and actual experimental results [15]. Scheidegger [16] showed in broad terms that Darcy's law is not appropriate when flow velocities with large Reynold's numbers were present. However this is unlikely to occur for flow in hardened cement paste or at a mortar joint.

Molecular effects due to very high forces of attraction between the fluid and the surface of the solids in small flow channels were also found to effect Darcy's law. This is particularly relevant for hardened cement pastes although its internal structure, due to continued hydration, changes rapidly for steady state permeability tests making this phenomena difficult to quantify. However Darcy's law indicated that the resistance to flow is dependent upon both the structure of the material and the fluid properties.

An indication of the dependent factors that influence permeability can be obtained from flow in capillary tubes (Poiseuille's law):

$$v_i = \frac{\rho g i_l r_m^2}{8\eta} \qquad \text{Eqn. 2.4}$$

where v_i - mean velocity in the tube

ρ - density of the fluid at temperature under consideration

g - acceleration due to gravity

i_l - head loss per unit length of capillary

r_m - mean radius of capillary tube

η - viscosity of fluid at temperature under consideration

Hughes [17] showed that by using Poiseuille's law and a model of pores arranged in a random 3-D array, the total flow rate (Q) can be calculated. This showed that the flow rate was a function of pore radius rather than total porosity:

$$Q = \frac{r^2 \Delta p V}{32 n^2 \eta d} \qquad \text{Eqn. 2.5}$$

where r - pore radius

Δp- pressure difference

V - porosity

n - tortuosity factor

η - viscosity

d - specimen thickness

The permeability of mortar to water and air showed marked differences. Air permeability results can be as much as 100 times greater than those for water permeability [18].

Differences can be explained by gas flow slippage theory as shown by Klinkenberg [19,20]. Gas that flowed close to a capillary wall has a finite velocity and consequently allows a greater gas flow than can be predicted by Poiseuille. This is particularly noticeable for material with an inherently low permeability.

Klinkenberg [20] also derived an equation that related liquid and gas permeability coefficients (k_l, k_g):

$$k_l = \frac{k_g}{\left(1 + \frac{b_k}{P_m}\right)} \qquad \text{Eqn. 2.6}$$

P_m - mean pressure at which gas is flowing

b_k - constant for a given gas and porous media

Using this equation, Bamforth [20] showed that for typical structural concrete, the gas permeability coefficient may be about one order of magnitude higher than the water permeability value.

Gas slippage is dependent upon a number of factors which influence the 'free' path of the molecules through the microstructure. These can include pressure, temperature and the nature of the gas. Generally, the lower the density of the fluid, the more easily flow occurred. Thus large discrepancies between air and water permeability occur [14].

2.1.4 Factors controlling the permeability of mortar

A number of parameters influence the permeability of mortar. Some parameters exhibited a huge influence whilst with others, the effect was more subtle. Some of the main parameters are shown below:

(a) Water/cement ratio (w/c):

Water/cement ratio (w/c), which controls porosity, has been shown to be the most influential factor in governing permeability of mortar.

Generally increasing w/c caused a corresponding increase in permeability [7,21] (Fig. 2.1).

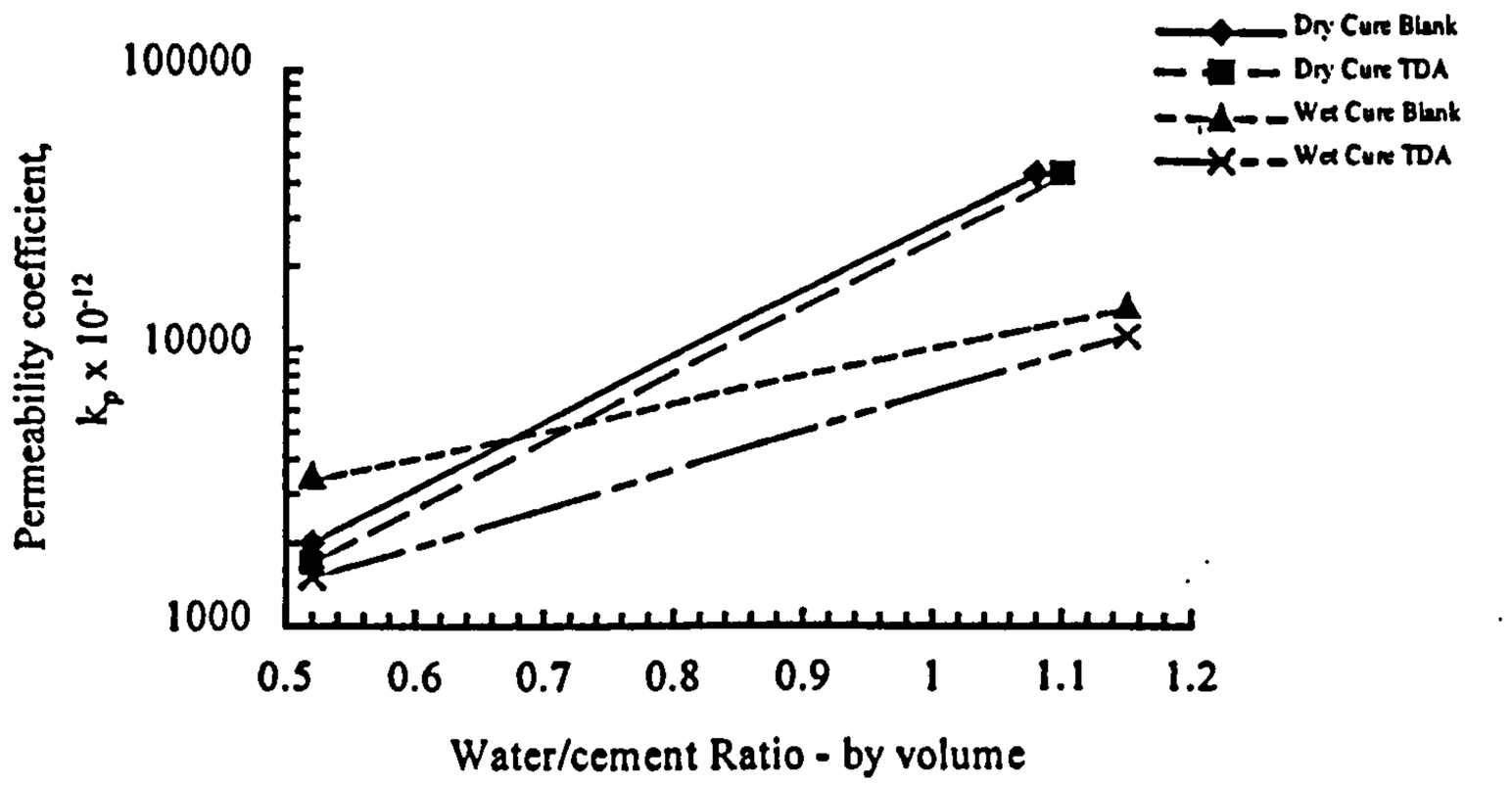

Fig. 2.1 Relationship between permeability and water/cement ratio [21]

Note:

k_p - permeability coefficient with respect to paste.

$$k_p = \frac{K_T}{V_P} \qquad \text{Eqn. 2.7}$$

where K_T - total permeability of the specimen

V_P - volume of paste per unit volume of concrete

Dry cure - specimens cured in a moist closet for 24hrs then stripped and allowed to stand in the laboratory at 21-26°C until time of test.

Wet cure - specimens cured in a moist closet for 24hrs then stripped and allowed to be cured in water at 21°C.

TDA - indicates use with a dispersing agent within mortar (admixture).

Blank - no dispersing agent added.

Bamforth [18] stated that low permeability was the result of low free w/c ratios and high cement content together with additional water absorption by the aggregate and continued hydration within the interior of the cement.

When w/c was found to be low, then the permeability of air-entrained concrete was greater than that of plain concrete but increased when w/c was larger than 0.6 [18,22].

The w/c was also linked to both the characteristics of the cement and the extent of hydration. Evidence from tests [23] had also indicated that the type of mix also had an influence of comparable importance, such as its aggregate size and the addition of natural pozzolans.

(b) Curing:

Steam (autoclaving) and moist curing have been found to reduce the permeability of mortar.

Tests [1] showed that water leakage through a moist cured specimen of only 3 days was several times greater than those tested after 7 days. Further analysis after 28 days showed an even greater improvement in water tightness (Fig. 2.2).

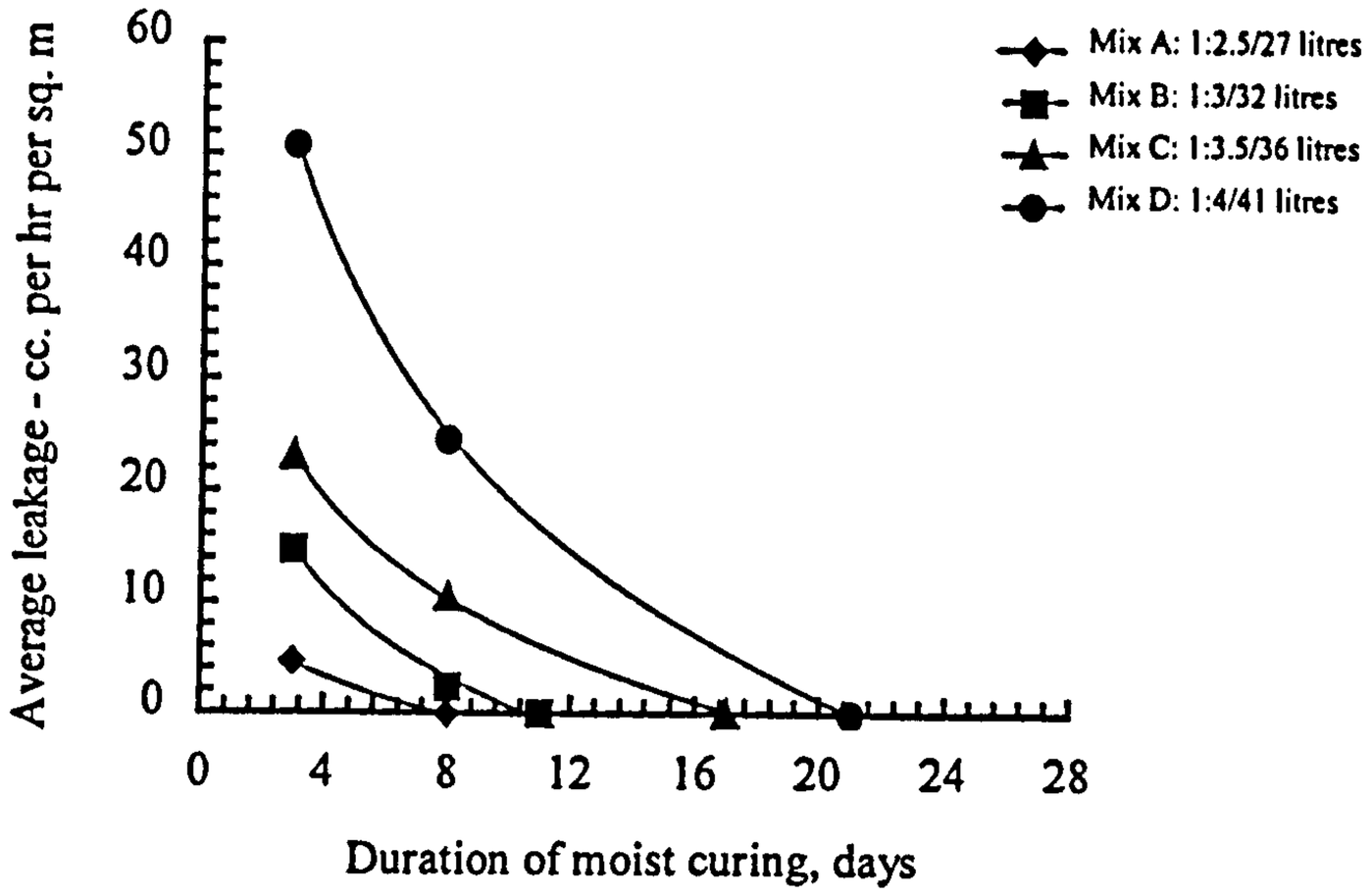

Fig. 2.2 Effects of test duration on the permeability of moist cured concrete [1]

Good similarity is exhibited between these relationships irrespective of the different quantities of mixing water. This implied that increased watertightness can be obtained either by additional curing or for any given curing condition, by reducing the quantity of mixing water.

Dhir et al [24] concluded that specifying concrete durability by means of a minimum cement content has serious shortcomings, as curing is one of the two main criteria in governing the quality or permeation characteristics of a concrete surface. The other criteria being w/c.

(c) Compressive strength:

Research has shown that there is a somewhat limited relationship between compressive strength and water permeability [18].

Bamforth [18] concluded that for concrete which was water cured for one day or less exhibited a semi-logarithmic relationship between water permeability and compressive strength and that generally the coefficient of permeability decreased as both compressive strength and duration of curing increased.

For a given compressive strength, substantially lower values of water permeability can be achieved using lightweight concrete. Strength is generally determined by total porosity, while permeability has already been established as being related to pore continuity. For small periods of curing it is expected that porosity of the sample changes, affecting strength more than permeability. However for longer curing periods, the continuity of the pore system is believed to become increasingly broken, this having a great effect on permeability. This was believed to be caused by low w/c being further reduced by absorption due to the aggregate which improved aggregate-cement paste bond and lowered the level of microcracking due to the shape and stiffness of the lightweight aggregate particles. Due to the continued polymerisation of concrete, microcracks caused by shrinkage would also influence permeability.

Permeability of concrete cannot then be derived from strength unless curing conditions are known.

(d) Cement fineness:

An increase in cement fineness has been found to have some beneficial effect in reducing permeability due to increased degrees and rates of hydration. Research [21] showed that fineness greatly influenced an air cured specimens' watertightness.

A larger surface area of cement allowed more hydration to take place and early strength to be reached, these factors having a marked influence on pore continuity. Further study [3] however showed that well cured pastes with coarse ground cements are no more permeable than those pastes using finer cement.

Generally, the ultimate porosities and pore continuity of coarse and fine ground cements were expected to differ but it was found to have a relatively minor effect on permeability.

(e) Admixtures:

The use of air-entraining agents and pozzolans such as pulverised fuel ash (PFA) and ground granulated blast furnace slag (GGBS) have been studied for their effects on permeability [25].

A natural pozzolan as a part cement replacement in mortar normally resulted in a reduction in the rate of strength development when comparisons were made at a constant w/c with mixes made without an admixture.

Mortars containing fly slag substitutes normally showed considerable strength gains due to the hydraulic activity of the slag. Correspondingly, mortars containing fly ash normally gained less strength as pozzolanic reactions were generally slower than those resulting from latent hydrualicity. The use of PFA and GGBS has no significant influence on permeability at 28 days when designed to achieve equal strength with OPC concrete.

Early findings [1] suggested differences in permeability were dependant upon whether an addition of an admixture would require extra water to be added to monitor plasticity.

However this parameter must not be given too much emphasis as the main advantage of an admixture lies in producing a desirable consistency or workability for placing of concrete on site and not for immediate watertightness.

(f) Aggregate size:

Sand grading has been studied by Harrison [26,27] for its durability aspects on mortar. This study showed that the strength of mortars reduced as the porosity and shrinkage increased with more finely graded sands.

Nyame [28] stated that increasing aggregate volume concentrations leads to interfacial effects causing an increased permeability. Absorption of paste water by some aggregates leads to a reduction in mortar permeability.

(g) Specimen surface characteristics:

The physical make-up of the specimen surface layer is not representative of the whole mortar specimen as the surface skin has higher cement contents and different aggregate grading. These factors can prove influential in governing permeability with the surface layer of the concrete or mortar being found to be half as permeable as the interior [23,29].

Dhir et al [24,30] showed that permeability of the concrete cover using commercially available permeability/absorption techniques is very sensitive to small changes in the w/c and the degree of moist curing.

(h) Loading history:

A loading regime acting on a mortar or concrete specimen is highly influential in governing the strain distribution and hence crack development. This has been proven to have a controlling effect on permeability. Stressed specimens were therefore more realistic for practical considerations as all concrete structures and mortar beds are loaded in some way.

Recent research [31,32] has shown that the applied stress level had a pronounced effect on permeability. At low and intermediate stress levels there was an unpredictably small change in permeability. At higher stress levels, greater than 40% of the ultimate failure load, permeability increased rapidly depending on the size, number and state of the propagated cracks. Normally mixed ordinary Portland cement concrete, at low stress levels, resisted moisture ingress most effectively compared to PFA and air entrained concrete (Fig 2.3 (a)-(c)).

Ludirja et al [33] noted that significant changes in permeability could be detected after loading above 75% of the ultimate failure level. Ultrasonic pulse velocity readings were used to indicate the extent of cracking.

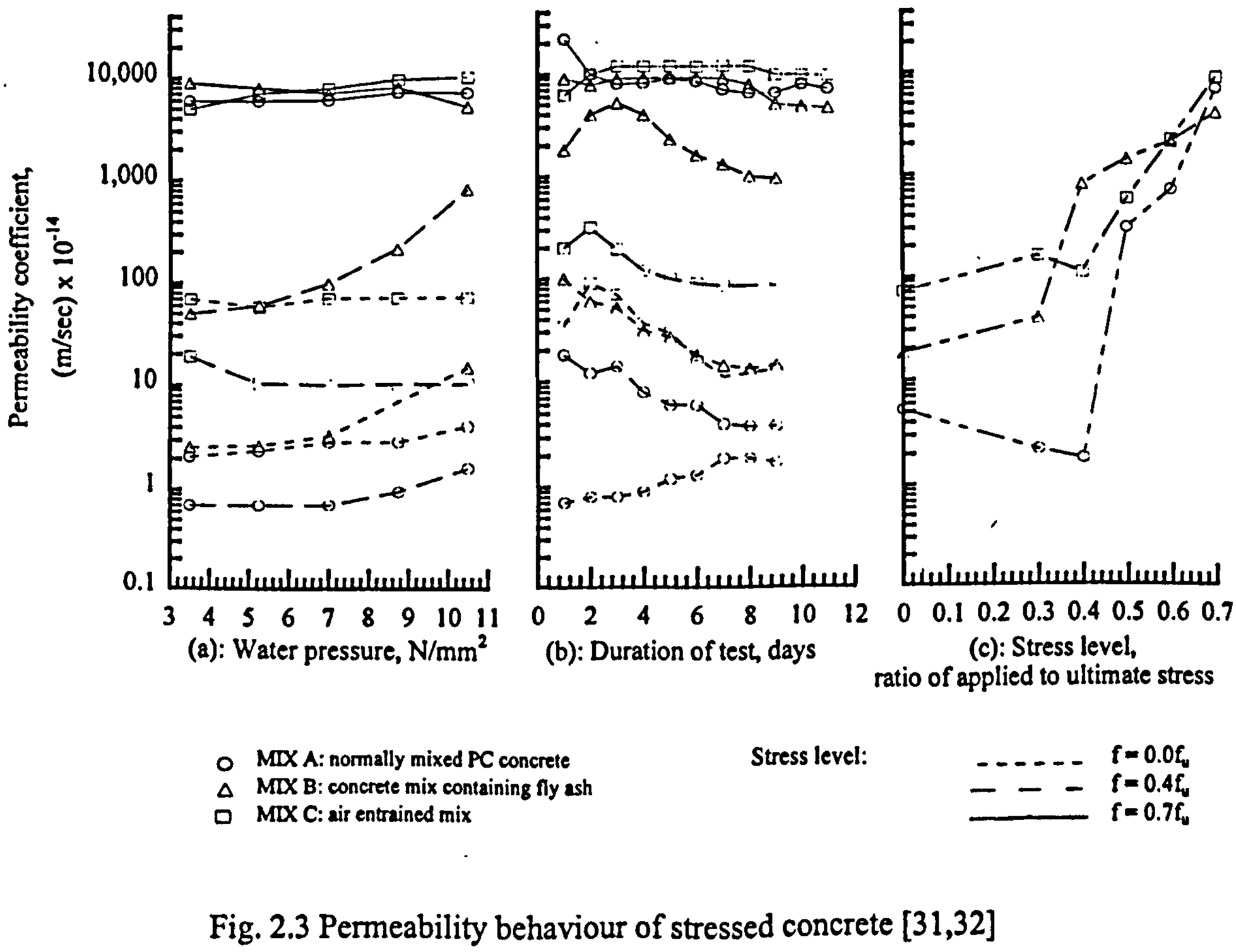

Fig. 2.3 Permeability behaviour of stressed concrete [31,32]

2.1.5 Permeability test techniques

There are basically only two different techniques by which permeability or water ingress through concrete or mortar can be measured. Direct methods allow tests to reach steady-state conditions of fluid inflow matching outflow. This is very difficult to achieve and may require long periods of testing. Some investigators [1,18] reported that steady states will never be achieved until there is complete hydration in the specimen.

Indirect testing concentrates on the amount of water that can be absorbed or forced into a specimen in a given time. Hence in-direct methods do not give a true measure of permeability but more an indication.

A number of methods that have been used in the measurement of permeability are described below:

(a) Early methods:

Simple 'Low Head' tests were used in the early stages of measuring indirect permeability. This test has a practical application due to the low applied head of water (200mm). This head is similar to driving rain striking a specimen surface at 50mph. However as surface characteristics of concrete differ to that of the interior, results should be treated with caution.

Basic test methods of this type include the 'Bomb' method, 'Porous Pot' method and the 'Output' method [34] (Fig 2.4 (a-c)).

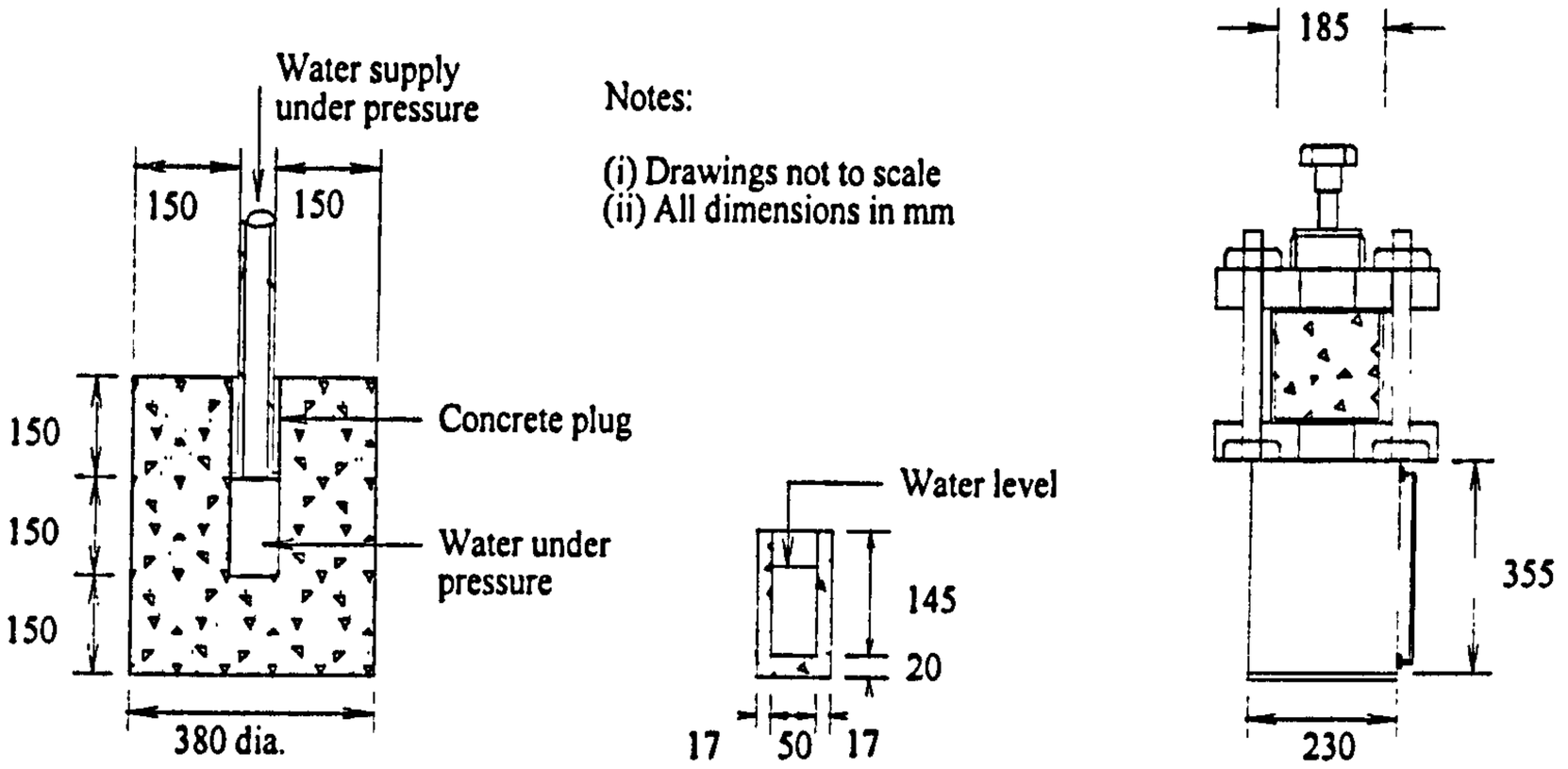

(a) Typical test apparatus for the 'Bomb Method'

(b) 'Porous Pot' test specimen used in low head tests

(c) 'Output Method' equipment, (U.S. Bureau of Standards)

Fig 2.4 (a-c) Typical early test methods for the assessment of permeability [34]

(b) Figg test and similar methods:

Figg [35,36] and Kasai et al [37] developed a semi-destructive test for the measurement of air and water permeability.

For the Figg test [35,36], a small hole is drilled into a concrete specimen which is then plugged with catalysed liquid silicone. This sets to give a resilient seal to the small cavity in the concrete. A hypodermic needle is connected to a manometer and vacuum pump then inserted through the rubber plug into the cavity (Fig. 2.5).

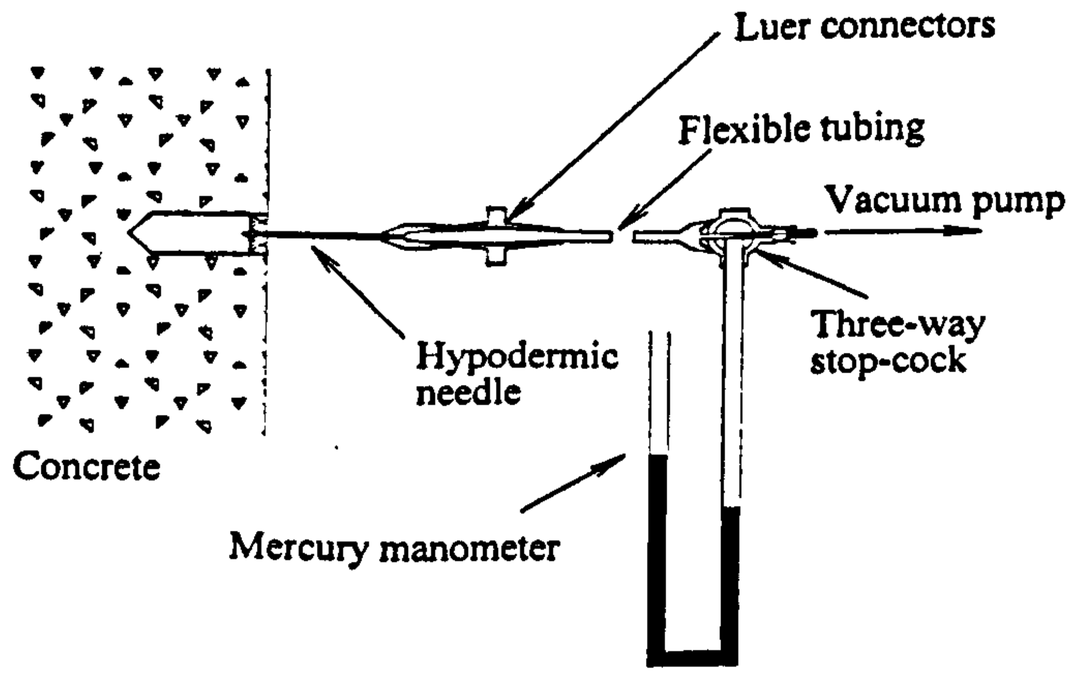

Fig. 2.5 Figg test apparatus for determining the air permeability of concrete [35]

Figg showed that air and water permeability results gave a correlation with w/c, compressive strength and ultrasonic pulse velocity. These results were shown to be affected by microcracking, aggregate type and moisture content [38].

Hansen et al [39] described a similar method of estimating the gas permeability for in-situ concrete.

A hole is drilled at 6° to the surface and a pressure sensor then inserted. A pressure head is attached to the concrete surface above the drilled hole. The sensor detects small changes of pressure in the concrete and records them at a connected manometer or pressure gauge (Fig. 2.6).

This test determined the ratio of gas permeability to total porosity. This ratio can be used to find the degree by which gas permeates through the concrete. Moisture content of a sample was found to be influential though only for specimens with low permeability.

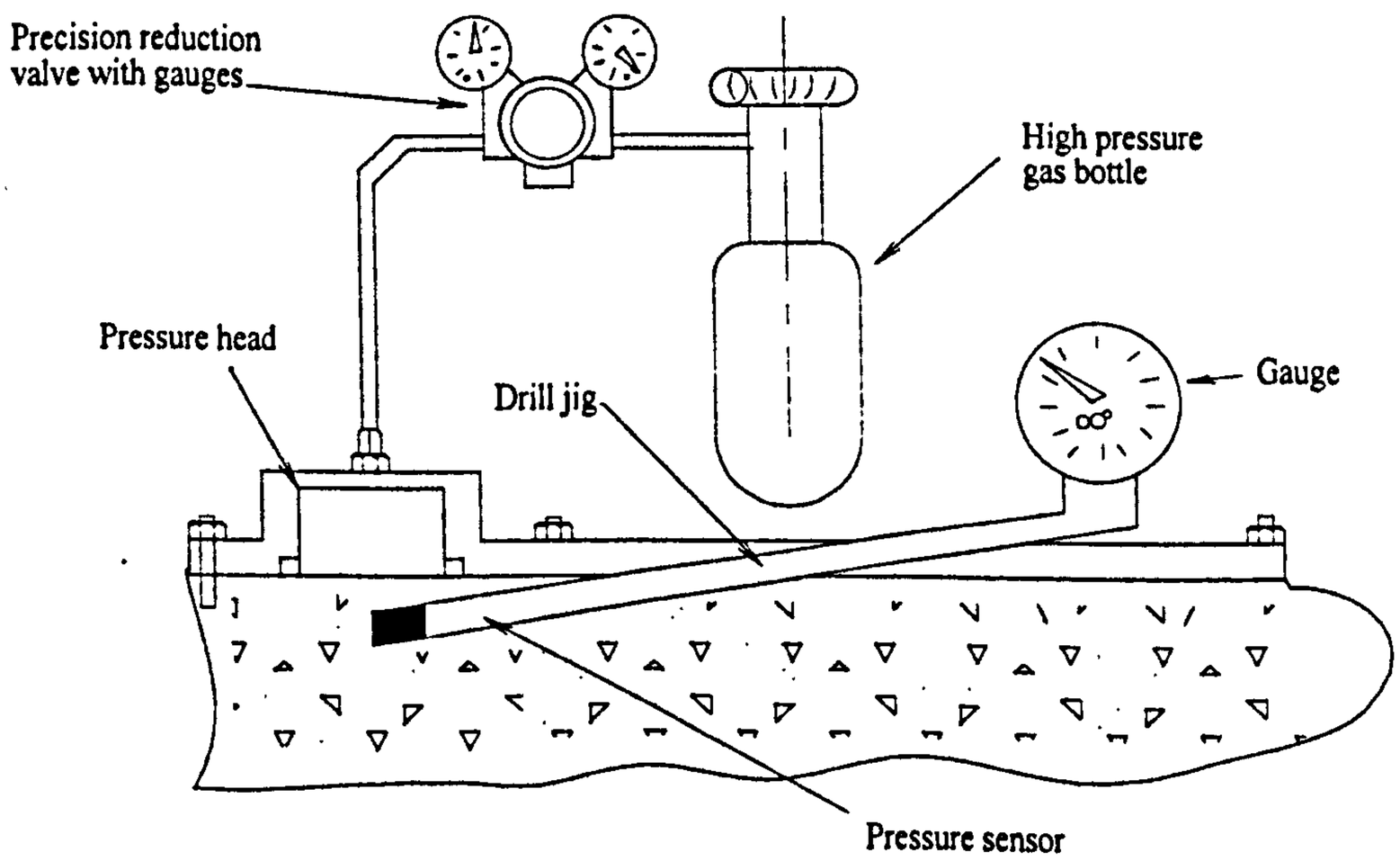

Fig. 2.6 Apparatus suggested by Hansen et al to measure permeability of in-situ concrete [39]

Hudd [40] developed a non-destructive version of the Figg air test, named the 'Egg' test. This test measures the near surface characteristics of concrete. This test used a 100mm dia silicone rubber dome sealed to a specimen surface. Through this rubber dome, a hypodermic needle was inserted. The procedure then followed that of Figg [35].

It was felt that results using Hudd's test [40] were more realistic as pre-drilling of holes used in alternative tests produced microcracking. Results showed that permeability generally increased as w/c ratio increased and that there is a wide range in permeability for a specimen when tested at variable inherent moisture contents.

Schonlin and Hilsdorf [41] used a non-destructive air test, based on vacuum pumping, as a measure of the effectiveness of curing on a concrete structure (Fig. 2.7).

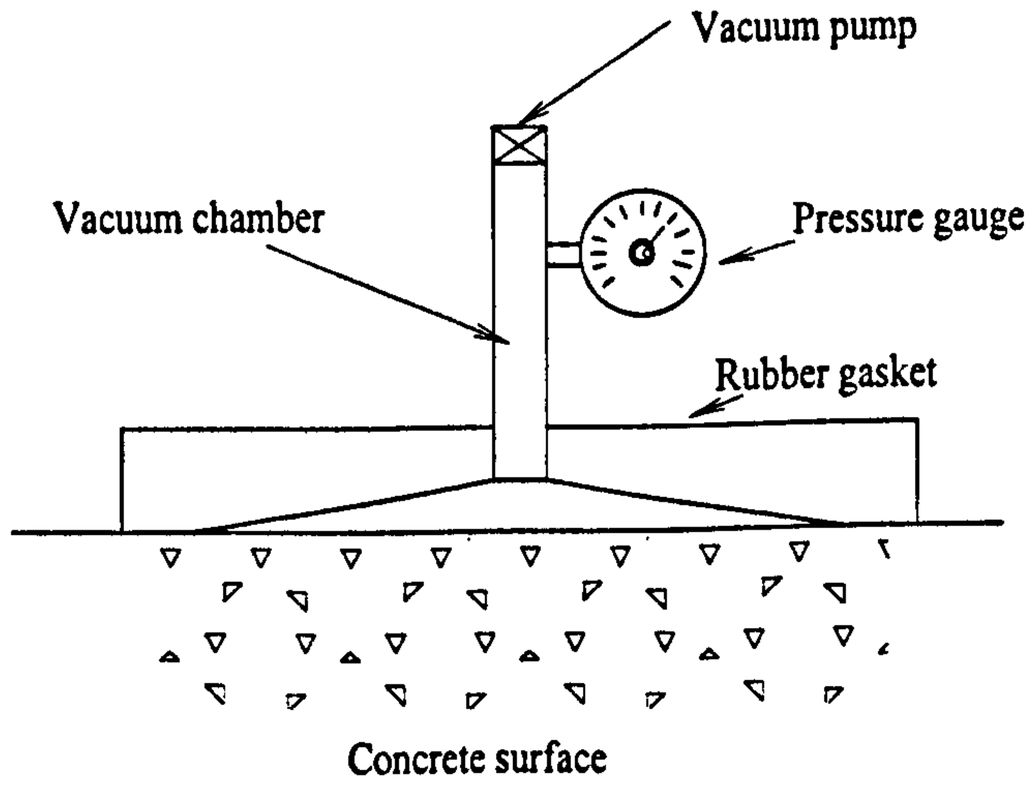

Fig. 2.7 Vacuum permeability tester used by Schonlin and Hilsdorf [41]

Once air in the vacuum chamber had been evacuated, exterior air permeates through the concrete and back into the vacuum causing an increase in pressure. The quickness of the pressure increase is dependant upon the near surface permeability characteristics of the concrete.

This method confirmed the influence of w/c and curing in governing permeability. The test also showed that permeability may vary considerably depending on the properties of the surface layers and can distinguish concrete to be 'good' or 'bad' respectively.

(c) Clam method:

Long et al [42,43] developed the 'Clam' method of testing concrete durability as it was felt that there are many problems inherent within the commercially available tests.

This method was designed to measure both air and water permeability on a large totally undisturbed section of concrete (Fig. 2.8).

To assess water permeability, a piston is pushed down in a hydraulic cylinder, exerting a pressure on the sample. For this applied pressure to be kept constant, the piston is allowed to travel freely. The amount of piston travel is a measure of the near surface permeability characteristics.

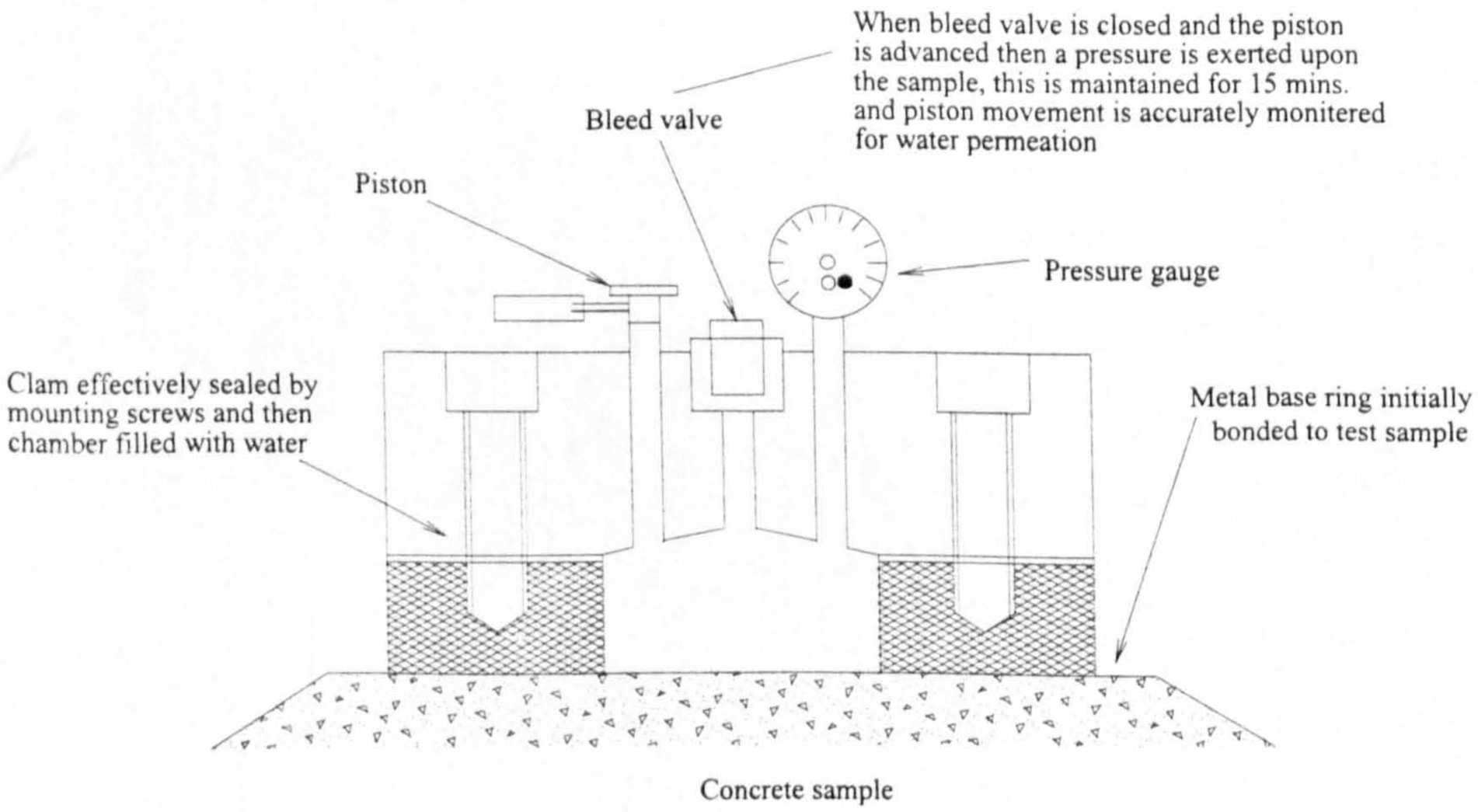

Fig. 2.8 Clam method for determination of water permeability [42]

The Clam test gives more representative results for permeability due to the relatively large test area measured. This avoids any discrepancies caused by poorly distributed aggregate particles.

Using this method it was found that by doubling the w/c ratio, the strength decreased by half and the permeability increased one hundred fold. Results also showed that prolonged curing of poor concrete could give rise to better durability characteristics than good quality concrete inadequately cured.

(d) Initial surface absorption test (ISAT):

BS 1881 [44] details a test to measure the water ingress characteristics of concrete on site.

The ISAT measures the rate at which water is absorbed into the surface and therefore gives an indirect measurement of permeability [38,40,45].

This test uses a water filled cap sealed to the concrete surface providing both a reservoir and pressure head of 200±20mm. This is roughly equivalent to heavy wind blown rain. Flow into the concrete is measured at 10mins, 30mins, 1hr and 2hrs from the start of test (Fig 2.9).

The code also provides a caveat against the influential and omnipresent moisture content by insisting there must be a minimum of 48hrs of dry weather before in-situ testing occurs.

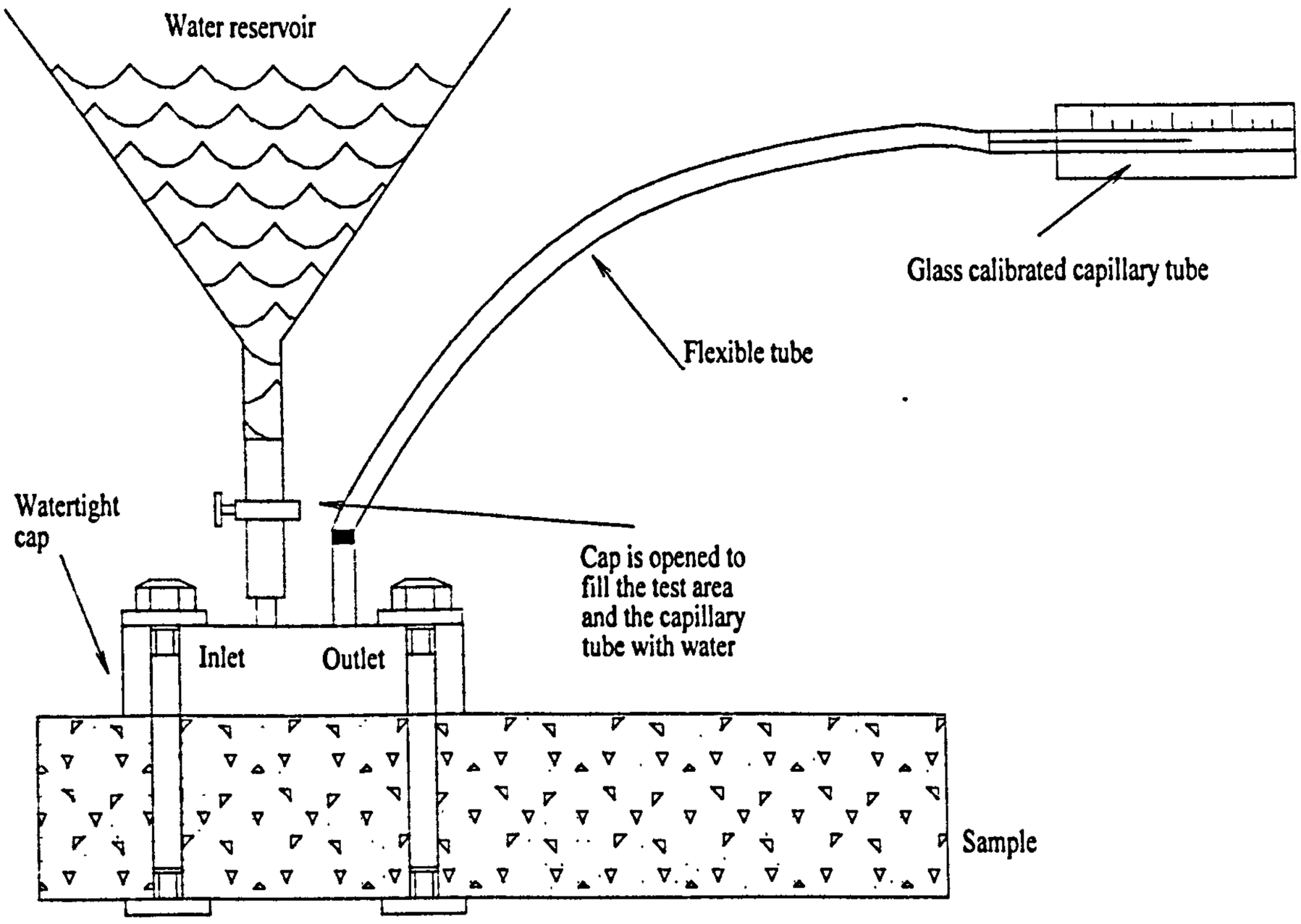

Fig 2.9 Apparatus used for the ISAT [44]

Problems can occur with sealing the apparatus to the specimen and the one dimensional aspect of absorption. This has produced a modified ISAT being available that generated pure uniaxial flow patterns.

Generally ISAT results show agreement with other test techniques regarding the importance of w/c and curing condition in governing water ingress for concrete or mortar.

Table 2.1 summarises all the in-situ permeation techniques discussed within this section [45].

Table 2.1 Summary of available test techniques

Test type	Reliability	Accuracy	Ease of use	Cost per test	Destructive effects	Testing usage	In use
ISAT [44]	good	fair	moderately easy	low	none	extensive	available to buy
Figg [35] (water)	poor	poor	moderately easy	low	some drilling	limited	available to buy
Figg [35] (air)	fair	fair	moderately easy	low	some drilling	limited	available to buy
Hilsdorf et al [41]	good	good	easy	modest	none	limited	can be assembled
Hansen et al [39]	fair	fair	moderately difficult	high	hole in concrete	fairly limited	available to buy
Clam test [40]	good	good	moderately easy	relatively low	marks left on surface	limited	available to buy
Figg test [40]	good	good	moderately easy	relatively low	none	very limited	can be assembled

(e) Sealed permeability tests:

These test techniques allowed a more controlled assessment of permeability characteristics and also tended to avoid problems associated with sealing the test apparatus to the specimen.

Kermani [31] and Tait et al [32] sealed a concrete specimen within a steel cylinder. The gap between the specimen and the cylinder surface is filled with water resistant epoxy resin. A watertight seal was made between this cylinder and the end plates using neoprene 'O' rings.

Lindsay [46] and other investigators [47] used a watertight pressure vessel into which the specimen was placed. The cylinder again is sealed to the end plates using neoprene 'O' rings. A hand pump was used to apply a hydraulic head.

Figure 2.10 shows a typical section of a sealed permeameter. This arrangement is broadly similar for all investigators using this technique [31,46-49].

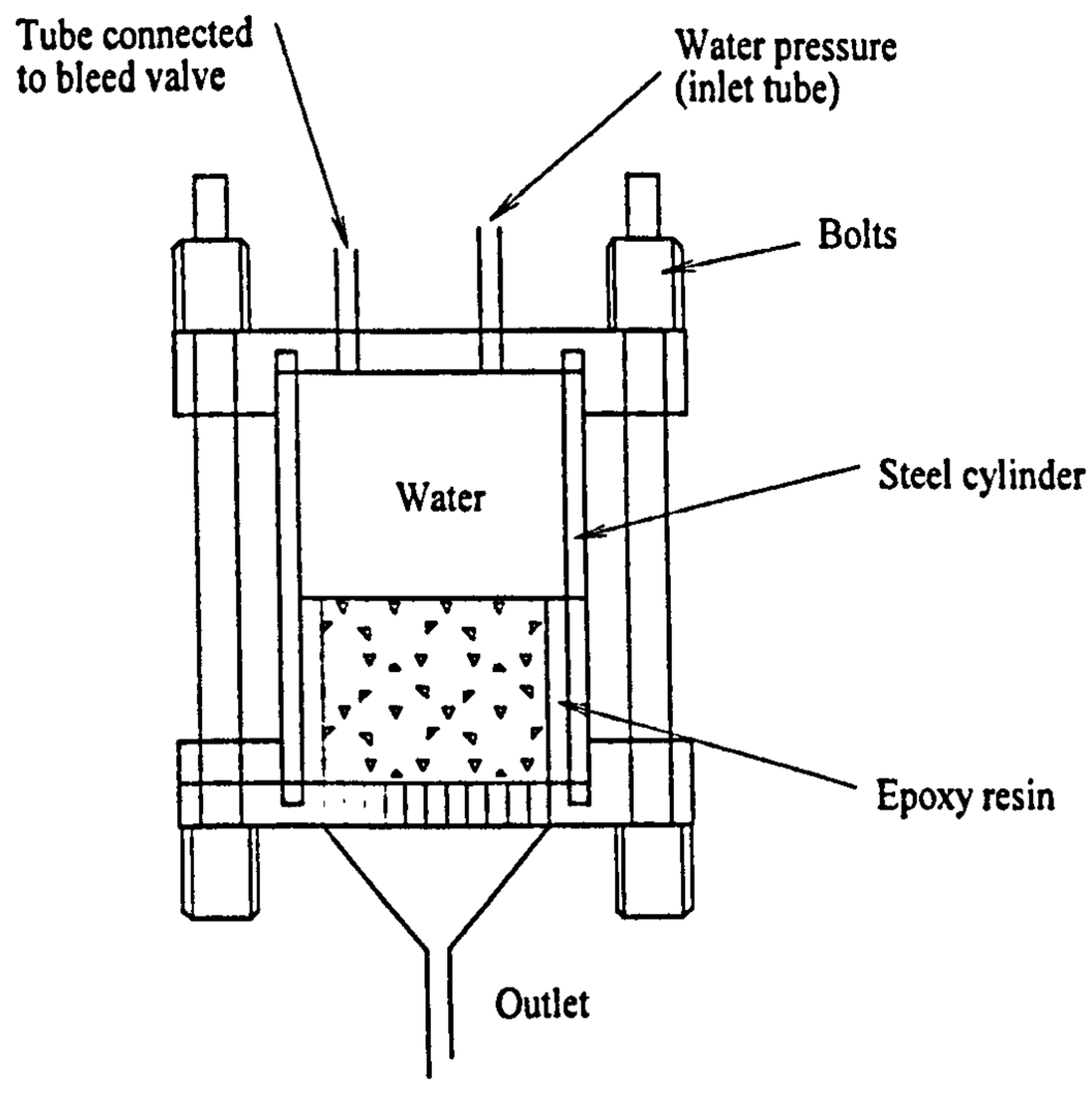

Fig 2.10 Section through typical permeameter [31]

These methods were found to be reliable, allowed repeatable testing and the influence of w/c and curing conditions was also found to hold using this test technique.

2.2 Permeability Characteristics of Brick

Bricks tend to be chosen more for their aesthetic appeal rather than their physical properties. However, a number of brick parameters are highly influential in creating a good and durable structure.

This section provides a brief review of these important brick parameters that influence the durability of masonry.

2.2.1 Brick parameters

(a) Absorption:

Water absorption into bricks can be considered as a two stage process [50,51].

Initially water travels from all sides towards the centre of the brick. Assuming an equal rate of water ingress, the interior of the brick would show a dry ellipsoid gradually shrinking to a point. The brick can then be considered as wetted throughout.

Further absorption proceeds at a much slower rate with water now searching out and filling the pores that had been initially bypassed.

The absorption rate of bricks showed considerable influence in governing the bond strength with mortar [52]. Connor [53] stated that bricks with high rates of absorption have a detrimental effect in terms of bond and produced excessive cracking in the mortar bed. Palmer [54] noted that for a good brick/mortar bond, moderate to slow rates of absorption (<40g/min) should be chosen.

For bricks with high rates of absorption, it is recommended that pre-wetting should be undertaken. This lowers the initial rate of absorption of a brick when placed upon a mortar bed. Pre-wetting has however proved unpopular with masons as they feel it is time wasting, uncomfortable and makes the bricks both heavy and difficult to lay [55].

(b) Penetrability:

Water penetrability into bricks can be estimated by measuring the height of water that has been drawn up the exterior of a brick in a given time.

Results using this test procedure should be treated with caution as a measured wetted height is not directly related to an increase in weight due to a gradient of saturation. Errors can also occur due to evaporation.

Penetrability is also highly sensitive to surface conditions of the brick and results should only be considered qualitatively [50].

However there is no doubt that size, shape, number and direction of capillaries within the brick control this relationship.

(c) Brick texture:

Impervious bricks with smooth, glassy bonding surfaces have generally lower bond strengths than those obtained with other makes of brick. Rough surfaced bricks or pre-wetted smooth porous bricks with low absorption rates also exhibit good bond characteristics [54].

(d) Brick expansion with time:

Further deterioration of masonry may occur due to the expansion of bricks with time.

The rate and amount of expansion depends upon the bricks' chemical-mineralogical composition, firing conditions, the temperature of exposure, the size of the specimen and the environment to which they are exposed.

Although heavily influenced by the above factors, it is known that clay bricks tend to expand with time. This can be considerable after only short periods and may continue for many years [56].

Expansion and contraction of brick units is mainly moisture driven and is caused by the absorption of water, usually from rain precipitation into the bricks, followed by evaporation during drier periods.

Figure 2.11 shows maximum and minimum expansion rates for a variety of brick types. This shows that bricks expand rapidly within the first year. Thereafter the rate slows and in some cases contraction can occur.

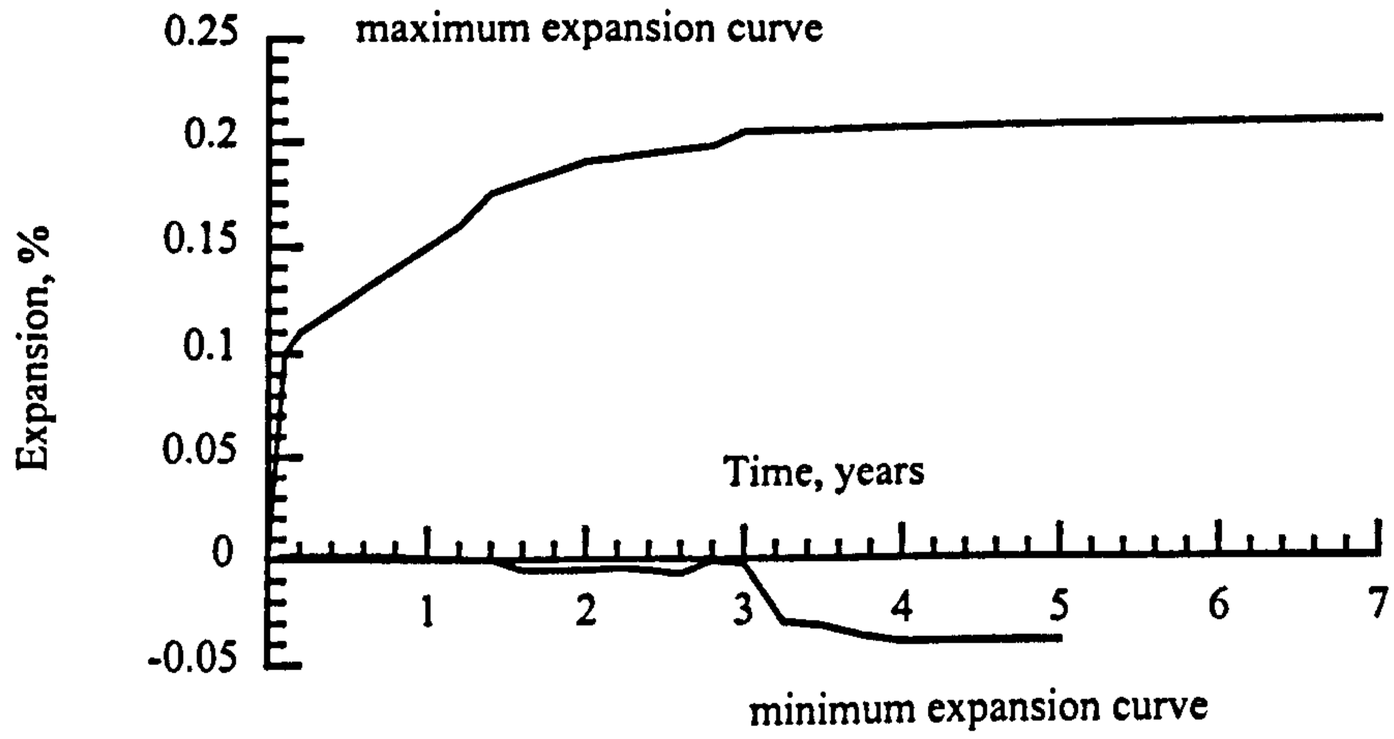

Fig 2.11 Maximum and minimum expansion curves for bricks standing in air [56]

Jessop [57] has identified eight basic factors that have an influence over moisture expansion:

(a) Time of exposure: - Size of expansion increases with increased length of time.

(b) Time of laying: - Walls built using bricks recently removed from a kiln show more expansion than those that have been allowed to stand for a period of time.

(c) Moisture temperature: - Increasing the temperature of the moisture to which the brick is exposed increases the rate of permanent moisture expansion. Whether or not an increase in the temperature of the moisture increases the total expansion of a brick is however uncertain.

(d) Kiln temperature: - When expansions are plotted against time (Fig. 2.12) then curves for each firing temperature are roughly parallel. Maximum expansions occur for clay bricks with a firing temperature of 850°C.

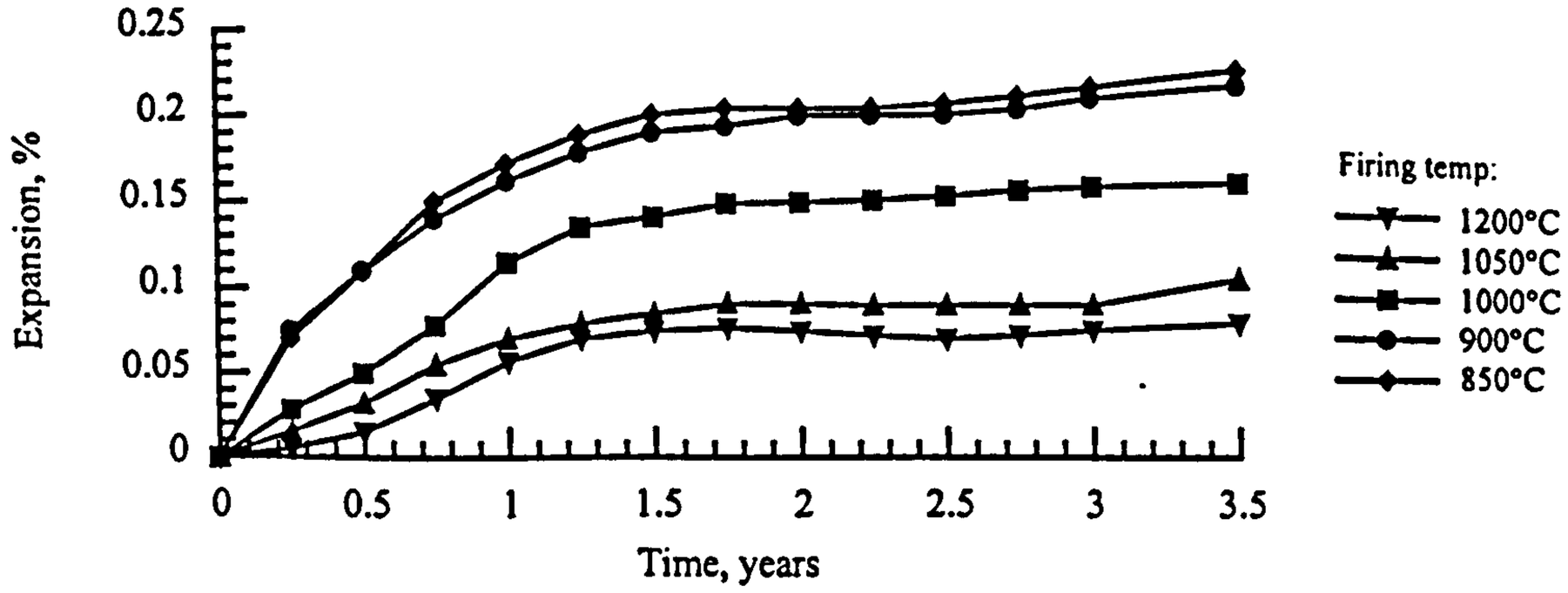

Fig. 2.12 Moisture expansion curves based on kiln temperature for typical clay brick units [56]

(e) Humidity: - Increasing the relative humidity or steam curing produces an increased rate of expansion [58].

(f) Cycles of wet and dry: - The cyclic wetting of bricks at 21°C and drying at 100°C results in far greater expansions than if the bricks are continuously soaked at 21°C. However, research indicates that the cyclic wetting and drying process itself does not affect the expansions of bricks unless drying is carried out at elevated temperatures.

(g) Mortar joints: - Provides restraint to brick expansion within a wall.

(h) Manufacturing process: - This has some minor effect over the total expansion of brick.

2.2.2 Testing for absorption of brick

A number of tests, both on site and within a laboratory, have been devised that allow the assessment of brick absorption and penetrability.

In practical cases, a calibrated tube is cemented to a clean or scabbled brick and the amount of water absorbed in 2mins is a measure of the absorption [53]. It was noted that absorption rates may vary as much as 50% within the same brick unit dependent upon which brick face is tested.

For the estimation of true absorption, total immersion techniques should be used. There has been varied test times chosen for total immersion from 1hr, 5hrs, 24hrs to 48hrs in cold water. Investigations showed that for some bricks, the weight at 48hrs and again at 200 days showed only an increase of 4% [50].

The current British Standard for clay bricks [59] indicates one method for measuring water absorption. Clay bricks are boiled in water for 5hrs and then allowed to cool to room temperature in 16-19hrs. The difference in weight is an indication of absorption.

Another method used to assess absorption involved evacuating a brick to a pressure less than 200mm of mercury followed by immersion in water for 10mins.

Peake and Ford [60] showed that the above two test methods do not give equivalent results, particularly with brick absorption rates less than 5%. Here the vacuum method gave significantly lower values. This was likely caused by the relatively short immersion time of the vacuum method and the influence of the rate at which bricks absorb water.

When water is absorbed through an end face of a brick, the rate of absorption varies inversely as the square root of the elapsed time, ($t^{1/2}$). The cumulative volume of absorbed water per unit face area (i) is [61-63]:

$$i = Z + St^{\frac{1}{2}} \qquad \text{Eqn. 2.7}$$

where S - sorptivity

Z - constant, based upon the rapid filling of surface pores on wetted faces of the brick

For sorptivity to occur, assumptions must be made that the material is homogenous, capillary absorption is normal to the specimens' surface, water is freely available at the inflow area and gravitational effects are neglected. Sorptivity values measured on initial contact with water will not be indicative of the longer term performance of the brick. Repeated wet and dry cycles to simulate practical situations should be used for this purpose [64].

The measure of water absorption is in some way related to the tendency for brick disintegration. Research has therefore lent to classification of brick durability in terms of their water absorption capacity.

Connor [53] suggested a classification for bricks dependent upon their rates of absorption. This is shown below:

Low < 0.26mg/min per mm^2

Moderate: 0.26-1.55mg/min per mm^2

High > 1.55mg/min per mm^2

Moderate rates were thought to be the most desirable for creating an adequate bond with mortar. Further work also showed that bond strength increased to a maximum for absorption rates between 0.5-1mg/min per mm^2 and decreased sharply for bricks with high absorption rates [65].

Dennis [66] stated that bricks with high initial rate of absorption (IRA) and low longer term absorption rates are the most advantageous. The advantages of a high IRA was that there is little risk of water penetrability through the cracks at the brick/mortar interface as any water entering here diffuses and evaporates within the matrix. Current recommendations in the USA advise that the IRA should be no more than 1.55mg/min per mm^2 of the specimen surface [67].

A more theoretical basis is proposed by the 'Krueger ratio' [50]. This stated that water expands as much as 10% on freezing and that there must be 10% of unfilled pore space so that bricks do not burst. Hence by comparing the apparent porosity (which is equivalent to 24hr partial immersion and 72hr total immersion expressed as a percentage of the bulk volume) to the true porosity (the sum of the closed and open pores expressed as a percentage of the bulk volume and calculated from the true specific gravity), a coefficient of water saturation can be found. This coefficient should not exceed 0.9.

Kralj, Middleton and Pande [68,69] also used the principal idea that the main cause of frost damage in any porous media is the tendency for water to increase by approximately 9% in volume when frozen. This allowed numerical modelling, using finite elements, to successfully simulate frost damage in masonry. In their study the authors assumed that the volume change in a frozen sample was similar to that of thermal loading. Modelling showed high stress levels in brick in an orthogonal direction to the freezing point can occur which in practical circumstances leads to flaking of the brick units.

2.2.3 Permeability of brick

The resistance to flow is proportional to the depth of penetration (x) and the average rate of flow dx/dt. The total pressure assisting the flow can be considered as p. The resultant force on the water contained within a unit cross section is given by [70]:

$$p - Cx\frac{dx}{dt} = \Delta m \qquad \text{Eqn. 2.9}$$

where Δm - rate of change of momentum

C - constant dependent upon material

Generally the rate of change of momentum is so small that it can be considered negligible ($\Delta m=0$).

$$p = Cx\frac{dx}{dt} \qquad \text{Eqn. 2.10}$$

and also known that:

$$Q = A_f V_{unit}\frac{dx}{dt} \qquad \text{Eqn. 2.11}$$

where Q - rate at which water enters the brick

A_f - face area of the material

V_{unit} - volume of water contained in a unit volume of wet material

Hence by incorporating the above two equations:

$$Q = \frac{A_f V_{unit} p}{Cx} = \frac{A_f kp}{x} \qquad \text{Eqn. 2.12}$$

where $k = V_{unit}/C$ which is known as the permeability.

Stull and Johnson [71] showed that water permeability both increased and decreased with respect to time. Permeability can decrease due to pores becoming clogged by mechanically broken off particles of brick, or by air within the water becoming entrapped in pores. It was found that capillary pores influence the changes in permeability. Capillaries <2μm generally produced increased values of permeability with respect to time. Mills [72] showed that the brick with the lowest permeability tended to have the lowest porosity though his comprehensive testing failed to derive a direct link between these two parameters.

2.2.4 Pore structure of brick

The filling of brick by water due to capillary action is directly related to the permeability. This in turn is controlled by the total pore volume of interconnected pores and the threshold diameter or the maximum diameter of the continuous pores.

Hansen and Kung [73] stated that a smaller threshold diameter and porosity indicated a lower permeability and therefore a longer time to saturate the brick.

Figure 2.13 shows the water uptake for a typical clay brick. The slope of the initial stage is indicative of the permeability of the specimen, i.e. steeper slope implies larger permeability. Those pores being filled during the initial stage are likely to combine to form a network. The flatter line represents the filling of larger discontinuous pores.

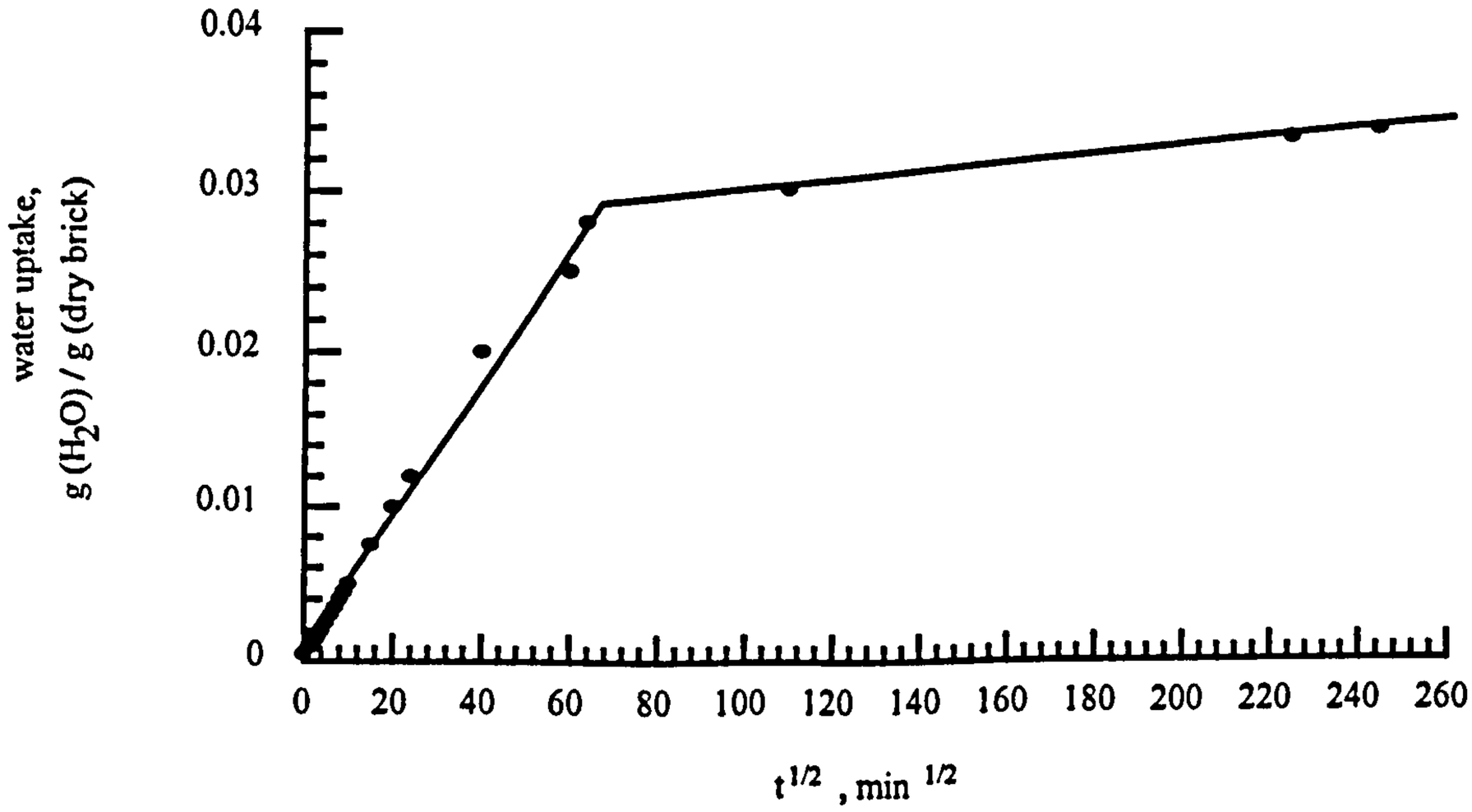

Fig. 2.13 Water uptake within a brick unit against square root of time [73]

Research by Davidson [74] showed that there are three distinct groups of pores and their related pore size distribution.

Very fine pores (<0.1μm), fine pores (0.1-1.0μm) and large pores (>5μm) have all been identified as each having their unique influence on the behaviour of bricks to moisture ingress. In freeze-thaw cycle tests, the vast majority of failed bricks had 81-94% of their total pore number within the fine pores category.

Bricks with good pore size distribution but with over 40% of total porosity being made up of pores >5μm showed the best durability characteristics.

Robinson [75] stated that bricks with the majority of pores >3μm and very few pores <1μm in size indicated a good durable brick. Those bricks with pores concentrated in the range of 0.1μm-1μm had very poor durability characteristics.

Durability is therefore influenced by both pore size distribution and porosity, which in turn is influenced by the firing temperature of the kiln, laminar structure of the brick, type of raw material used and the method of manufacture [75].

2.2.5 Durability factor for brick

Maage [76] realised that a greater pore volume would lead to a less durable brick and that large pores, although contributing to total pore volume, drain easily. Therefore, the durability of a brick should be dependent upon the proportion of large pores available.

A linear relationship between a frost resistance rating (F_m) and both the inverse value of intruded pore volume and the percentage of pores with diameters greater than 3μm was found. F_m is a classification based on numerous and differing freeze-thaw tests. An F_m rating of 100 would imply a brick unit with the highest frost resistance [76].

This allowed a durability factor (DF) to be calculated, and shows that increasing the intruded pore volume resulted in a lower frost resistance (Eqn. 2.13, Fig. 2.14).

$$DF = \frac{3.2}{P_V} + 2.4P_3 \qquad \text{Eqn. 2.13}$$

P_V - total intruded pore volume of the brick

P_3 - percentage of the pore volume with diameter greater than 3μm

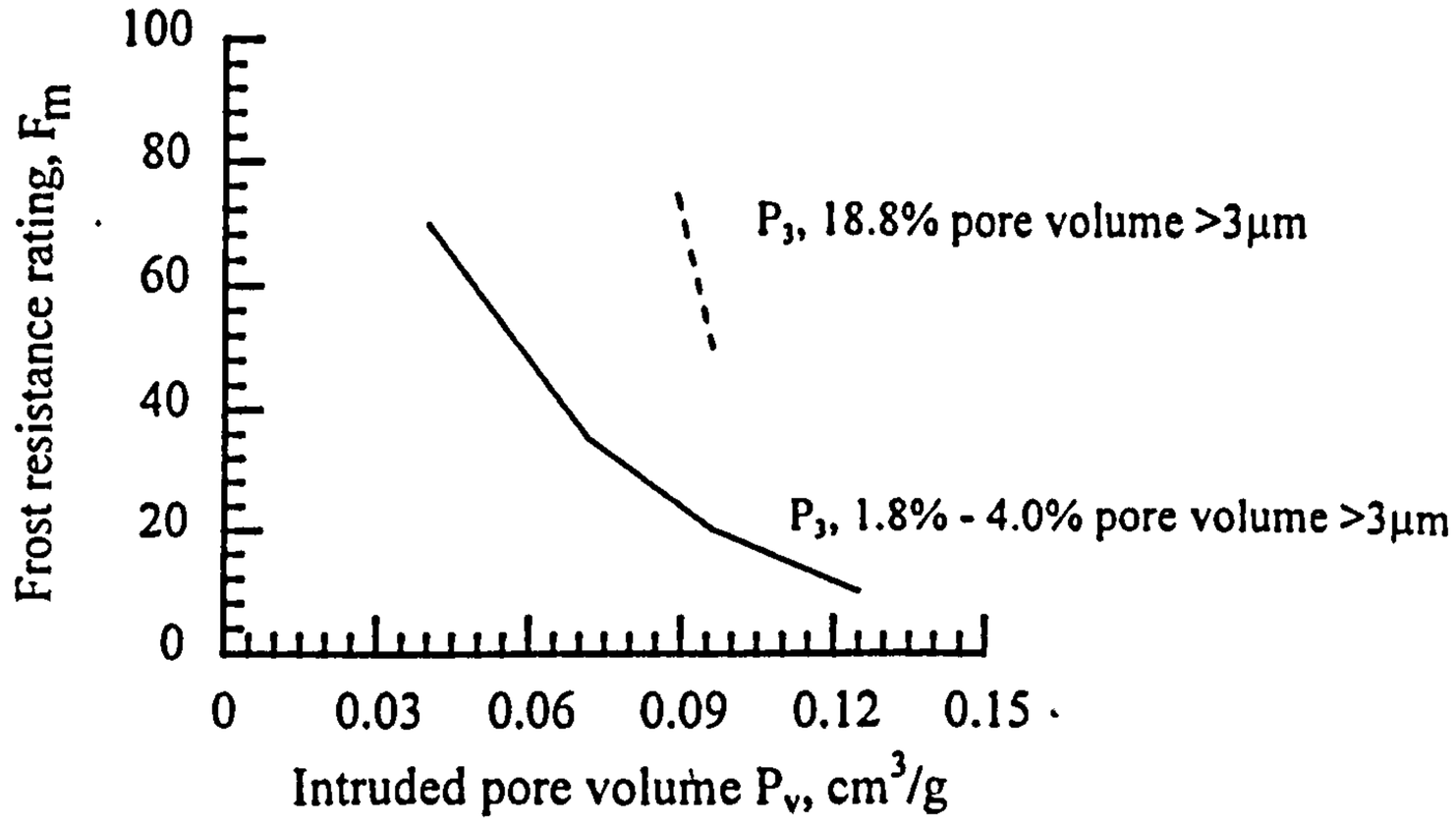

Fig. 2.14 Correlation between frost resistance F_m and intruded pore volume P_V for constant P_3 values [76,77]

Generally bricks with high porosity can be durable if the amount of pores with diameters >3μm is large. If typical pore diameters are unknown for the brick units, then bricks must have a low porosity.

From experimental studies a DF >70 would indicate a good durable brick [77].

Pore structure differs from the interior to the exterior of the brick leading to problems of deterioration. The surface represents a low porosity skin that impedes the flow of water. The centre is more porous and can store water. Under periods of long term soaking, the centre can become saturated and lead to problems of freeze-thaw deterioration.

2.3 Permeability Characteristics of Masonry

2.3.1 Introduction

Masonry is a durable and versatile building material. It combines low cost, aesthetic appeal with good physical properties that produce a popular design choice.

Essentially, masonry is layers of brick and mortar each having their unique contribution to overall durability characteristics.

This section presents a general review of relevant research that has considered the water ingress characteristics of masonry. Also included are details of the bond characteristics of masonry, the influence of bed orientation on the overall ultimate masonry strength and details of test apparatus for estimating water ingress into test panels.

2.3.2 Rain penetration into a masonry structure

Rain water is initially sucked or absorbed into masonry either at the brick or mortar surface or by exploiting any cracks or cavities.

If rain continues faster than the suction rate of the masonry then the mechanism is swamped. This causes the rain water to flow down the face of the structure creating a moisture film. This film is thicker at the base than at the top.

Wind as it blows over this film creates a pressure difference allowing the film to be forced into the structure.

It has been found that masonry exposed to the environment will be subjected to four differing forces that act singly or in combination to force water in and through an assemblage [78-80]. These are as follows:

(a) Wind and rain velocity (kinetic forces):

The wind and rain hammering onto a structure forces water into the interior. The force of this impact is directly related to the velocity of the wind. The kinetic energy generated will quadruple as the velocity doubles.

This force is particularly difficult to quantify as wind varies around a structure both temporally and spatially, particularly during storms.

The mass of rain droplets are also important as kinetic forces depend upon the concentration of droplets and the variable angles of impact. Assuming that the mass of the raindrops is negligible and that rain velocity is constant, a corresponding applied static pressure can be measured.

The static head exerted upon a structure is dependent upon wind velocity and can be calculated using Bernoulli's equation of steady state, non-viscous and incompressible flow.

$$\frac{P_1}{\rho_a g} + \frac{V_1}{2g} + z_1 = \frac{P_2}{\rho_a g} + \frac{V_2}{2g} + z_2 \qquad \text{Eqn. 2.14}$$

where P_1, P_2 - hydrostatic pressure at points 1 and 2 (Fig. 2.15)

V_1, V_2 - air velocity at points 1 and 2 (Fig. 2.15)

ρ_a - air density

z - height above datum

g - gravity

hence:

$$\frac{V_1}{2g} = \frac{1}{\rho_a g}(P_2 - P_1) \qquad \text{Eqn. 2.15}$$

Using the manometer equation:

$$P_2 = P_1 + H\rho_w g - H\rho_a g \qquad \text{Eqn. 2.16}$$

where H - head difference in manometer

ρ_w - density of water

Equations 2.15 and 2.16 can be used to describe the wind generated pressure head applied to a masonry structure.

This static head can also be measured and monitored by placing a manometer in the wind stream, forcing fluid to rise at one end (Fig. 2.15).

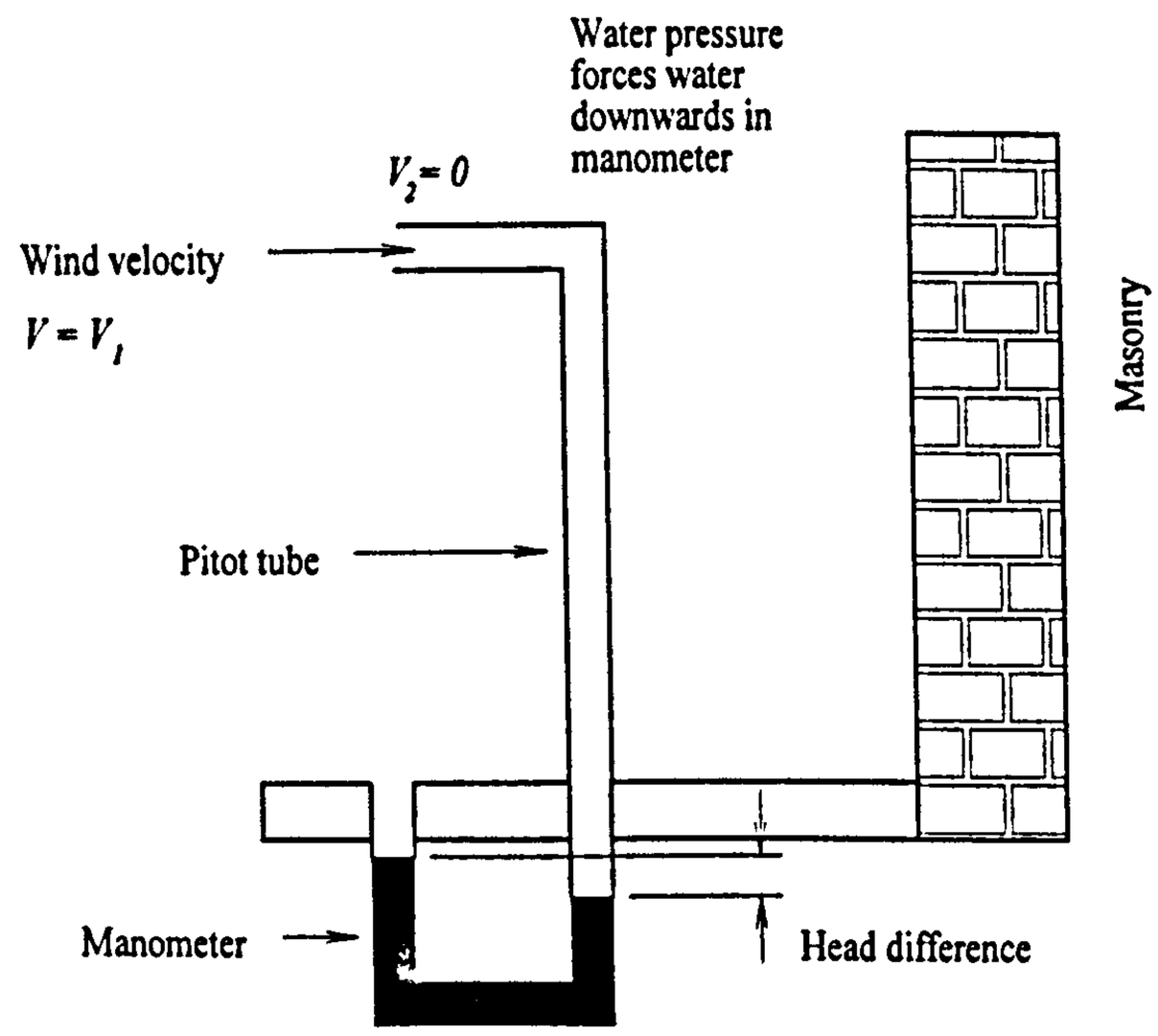

Fig. 2.15 Pitot tube estimation of static pressure due to wind velocity [78]

(b) Capillary pressure:

Capillarity occurs in masonry when water at the surface or within an assemblage is absorbed further into the interior. This phenomena is however closely related to surface tension. Surface tension results from molecular forces acting at an interface between two differing materials.

At the interface between water and air, a molecule is slightly raised. This stretches the cohesive bond between this molecule and its neighbour thereby creating a resistive force. The water will attempt then to conserve its resistive forces or surface tension forces by trying to form a sphere.

This has the effect of reducing the contact area and so releases forces to permit continuation of creep of the water along a surface. The force required to overcome these cohesive forces and break the surface tension is quantified by the coefficient of surface tension, σ.

If a thin tube of varying radius is placed into water, then the water may spontaneously rise to some equilibrium height. The upward force due to the surface tension supports the weight of the liquid column in the tube.

The vertical component of surface tension $\sigma\cos[\theta+\phi]$ if multiplied by the length of the contact surface $2\pi R$ gives the total vertical force $\sigma(2\pi R)\cos[\theta + \phi]$. The volume of the liquid can be described as $\pi R^2 h$ neglecting any meniscus effects. The weight of the liquid becomes $\rho(\pi R^2 h)g$.

Note that θ is the contact angle between the liquid and the glass tube, ϕ is the angle between the centre line of the capillary tube and its side, h is the supported height in the tube, R is the radius of the tube and ρ is the density of the fluid.

Using Fig. 2.16 and by equilibrium.

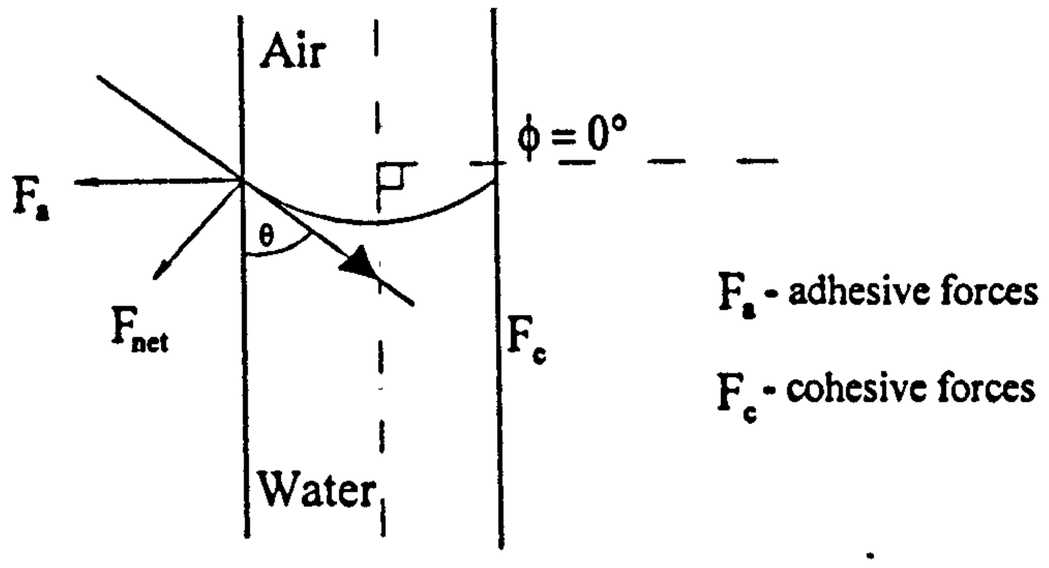

Fig. 2.16 Forces acting upon a molecule in close proximity to the tube wall [78]

Vertical upward force = Gravity

$$\sigma(2\pi R)\cos[\theta + \phi] = \rho(\pi R^2 h)g \qquad \text{Eqn. 2.17}$$

$$\text{and } h = [2\sigma\cos(\theta+\phi)] / \rho Rg$$

The tendency then for liquids to rise in these tubes can be thought of as a pressure exerted by the water within the tube. Hence a capillary pressure (P_c) may be measured as:

$$P_c = \rho gh = [2\sigma / R]\cos(\theta+\phi) \qquad \text{Eqn. 2.18}$$

Capillary pressures vary dependent upon pore diameter or whether the fluid is at rest or in motion. This is further dependent upon factors such as temperature and fluid viscosity.

Capillarity can augment other avenues of water migration, carrying water further into the masonry interior. In areas of a high piezometric surface, capillary action can draw the ground water up into the structure resulting in damage to the masonry courses near ground level.

(c) Differential pressure across the medium:

Pressure differentials across a structure can be caused by heating, ventilation and air conditioning systems which causes the interior air pressure in a portion of a building to be lower than the exterior atmospheric pressure. This contributes to water migration into the building by drawing surface water through cracks.

Air pressure differentials can be expressed as:

$$\Delta p = p_{ext} - p_{int} \qquad \text{Eqn. 2.19}$$

where p_{ext} - exterior pressure

p_{int} - interior pressure

The +ve or -ve sign of Δp indicates that it is either a driving or resisting force to water penetration.

Newman and Whiteside [81] showed that there is a clear relationship between air permeance (which is a good indicator of potential water leakage) and pressure differentials.

(d) Gravity:

Gravity can cause water to drip in through imperfections in the roof or flashing forcing water downwards into the specimen. Gravity and capillarity combine to form a 'siphon effect' which draws threads of water into the interior.

The force due to gravity (F_g) can be expressed as:

$$F_g = \rho g z \qquad \text{Eqn. 2.20}$$

where ρ - fluid density

g - acceleration due to gravity

z - height above some specified datum

Generally water penetrates some depth into the interior due to a sufficient wind velocity. Capillary pressure and a pressure differential then combine to draw penetrated water or additional surface water into the interior. Finally the force of gravity will attempt to draw water downward.

2.3.3 Evidence of rain penetration

Evidence of moisture penetration and remedial works has been documented since the late 1800's [82]. Factors such as spalling and dusting of bricks, efflorescence and the disintegration of mortar joints are examples of poor durability [83].

The evidence of rain penetration can be summarised as follows:

(a) Efflorescence:

Efflorescence is a common indication of moisture penetration. High humidity within a structure caused by the external environment allows moisture to penetrate the interior and in some cases egress to the exterior which then causes staining of the masonry.

The British Clayworker [84] notes that two main stain types occur on the mortar or brick caused by clay used in the manufacture of bricks. The yellowish-brown staining on bricks and the deep-brown stains on mortar were shown to be caused by an efflorescence of ferrous sulphate. The ferrous sulphate first forms an almost white efflorescence which later oxidises to yield brown ferric hydroxide.

Evidence of efflorescence is generally found around windows where sealing is often compromised.

Spalling and dusting of a brick usually follows efflorescence. As individual bricks often have a unique surface texture, this influences heavily the rate of decay. An even disintegration or weathering over a structure is unlikely and so requires remedial patchwork maintenance.

Efflorescence may however cause a reduction in the permeability as deposits in turn close or constrict surface pores. This minimises the risk of rain water ingress.

(b) Spalling and freeze/thaw action:

As the face of the brick tends to be relatively impervious, moisture enters at the brick/mortar interface. This allows moisture to penetrate through the relatively porous top area of brick units. The brick face then acts as an impervious barrier and allows little evaporation to take place.

Freezing then occurs causing disintegration and bursting through the internal structure of the masonry. Spalling therefore tends to occur due to this freezing action which can destroy the brick/mortar bond.

Marusin [85] concluded that differing physical and mechanical properties of brick and mortar microstructures combined to allow splitting during weather exposure. Hansen and Kung [73] also suggested that the performance of a masonry structure in resisting deterioration was a function of both the brick and mortar.

Fishburn [86,87] showed that alternative wetting and drying (or heating and cooling), though not freeze/thaw action, had little effect on the permeability of a masonry test panel and correspondingly did not influence the deterioration characteristics.

(c) Crack width:

The flow of water down a masonry structure is directly influenced by wind movements surface texture and gravity. Water infiltration can occur at open construction or expansion joints, roof flashings and cracks at the structures' surface.

Cracks can occur for a number of reasons such as thermal strains, differential absorption rates of brick, poor workmanship, settlement and applied loading.

Normally, a downward flowing water film tends to concentrate at the vertical joints exploiting any cracks that allow access to the masonry interior. Garden [88] suggested a number of crack widths that are required for various driving forces:

Kinetic energy:	crack width > 4.8mm
Capillary:	crack width < 0.5mm
Gravity:	crack width > 0.5mm
Air currents:	crack width > 4.8mm

It is noted that fine capillaries of less than 0.01mm width hold water with such high suction forces that this water cannot contribute to further rain penetration [88].

It is recognised that the main areas of moisture ingress are at the brick/mortar interface and are not due to the properties of the brick and mortar alone. Previous results [81] showed that only 17% of total panel leakage was due to brick and mortar implying that 83% were due to cracks at the interface.

It is unlikely that water ingress paths extend from one course of bricks to another. Mortar beds act as impermeable barriers restricting the maximum vertical moisture fall to one brick course only.

Little research is available in assessing micro-crack creation and further development due to loading. When a masonry panel is loaded a number of cracks may form or in some cases close. This is dependent upon factors such as bond strength and bed orientation of the main mortar bed within a masonry panel. However, the formation and extension of cracking will effect the water ingress characteristics of a masonry panel.

The strain required to cause brick masonry to crack in compression occurs at about half the ultimate strength. Frequent application and withdrawal of load may cause fatigue and strength reduction and therefore increased cracking probability. As few as 40 cycles of compressive load is said to cause a 30% reduction in strength [89].

Grimm [89] found that the average cracking in brick masonry walls of 44 buildings which had no wall leaks was 14.7% (4.48m of crack per 30.5m of mortar joint), compared with 36.3% (11.1m of crack per 30.5m of mortar joint) in 34 buildings which did leak.

Cracking can be considered to occur in four stages during loading [90] (Fig. 2.17). Microcracks initially close under compression load then gradually grow, exhibiting elastic behaviour, where axial, lateral and volumetric strain are both linear and recoverable. An increased stress level causes tensile stresses in the cracks to exceed a materials tensile strength and stable crack propagation occurs. Dilatancy (the volumetric expansion under load) also occurs at this stage.

Further loading encourages cracking to be more extensive and pronounced until a point is reached where the energy released in the cracking process is greater than that required by the loading process. At this final stage, cracks grow rapidly and coalesce forming visible cracks in the test specimen.

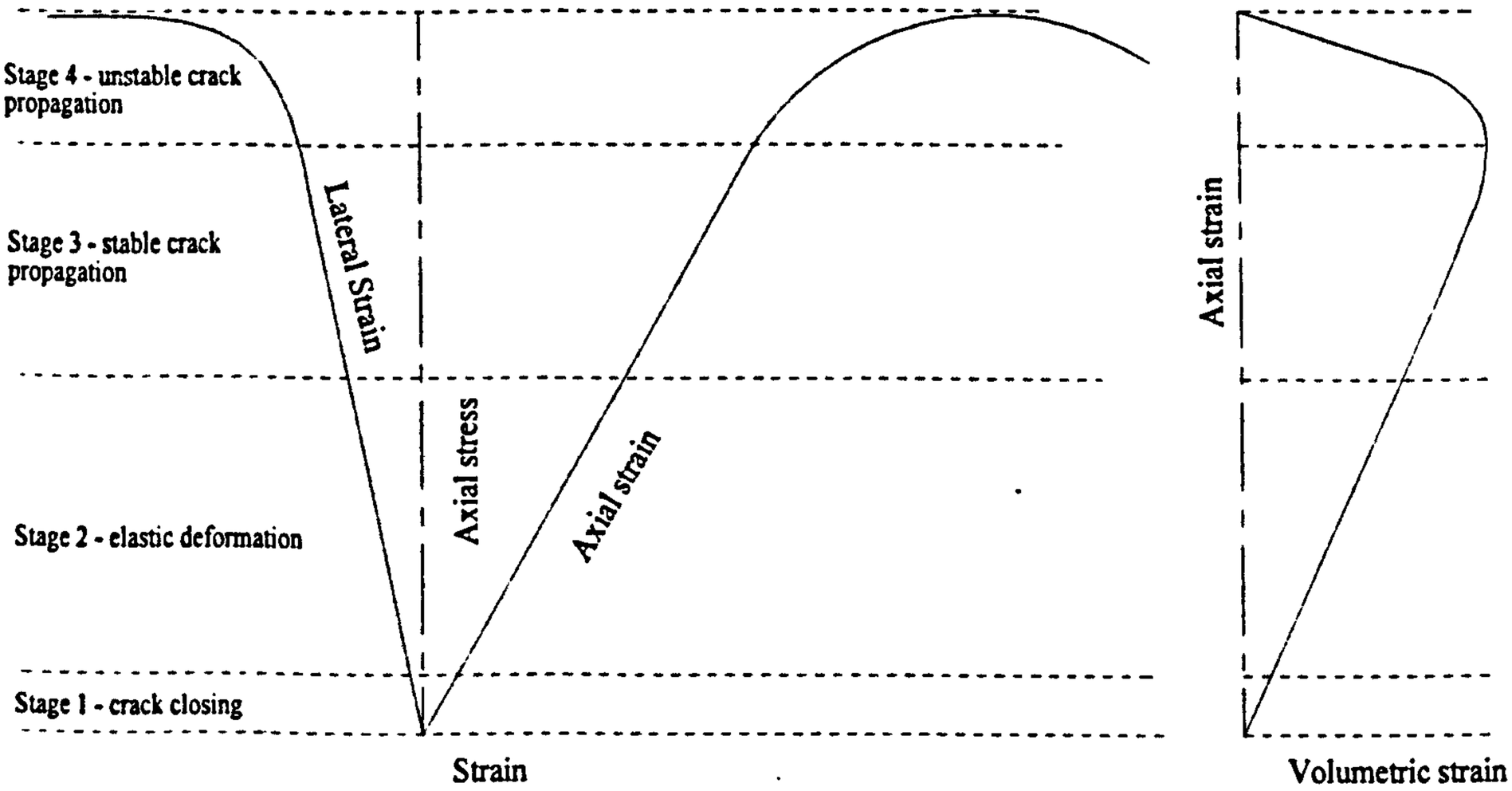

Fig 2.17 Crack development for masonry walls [90]

2.3.4 Driving rain index (DRI)

In a real environment any water ingress is almost wholly driven by rain penetration. This is influenced by a combination of forces, such as wind, that act as controlling factors. Eventually this resulted in a driving rain index (DRI) being formulated.

Generally rainfall in the UK increases with height and distance from the east coast. It is the associated wind speed with rainfall that gives many critical exposure conditions that are only rarely exceeded in North West Europe and America. Britain therefore developed a Driving Rain Index (DRI). Maps of the average wind speeds indicate that the highest velocities in the UK occur in western coastal areas. Thus the intensity of driving rain must be related to this pattern.

Problems with rain penetration have increased over the previous decade. This may have occurred due to problems such as defective cavity wall insulation and increasingly poor workmanship which can provide a path for rain water to enter the masonry interior.

The USA followed suit in mapping the country with isolines [91]. These are proportional to the amount of rain that would be driven onto a vertical surface facing the wind in an average year and is representative of the DRI (Fig. 2.18).

The DRI (USA version) is calculated as follows :

$$DRI = \frac{(A_{DRI} - \frac{B_{DRI}}{10})V_{mean}}{1000} \qquad \text{Eqn. 2.21}$$

where, A_{DRI} - annual rainfall precipitation

B_{DRI} - annual precipitation, (snow, sleet, hail)

V_{mean} - mean wind speed

Note: DRI isolines values in m^2/s

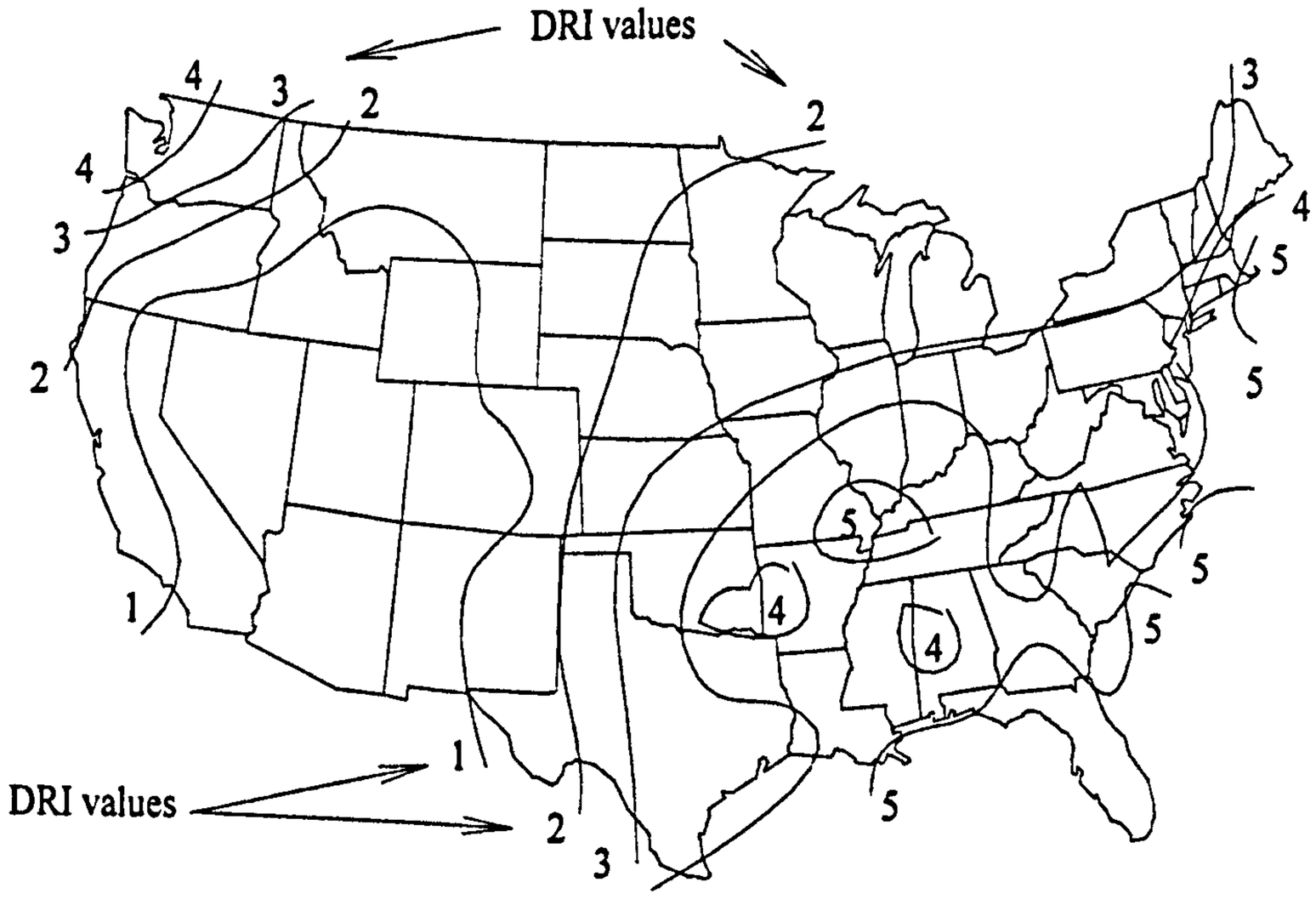

Fig. 2.18 Driving rain index isolines (DRI) for the USA [91]

From the DRI estimates have been made as to the exposure to water permeance, i.e. sheltered, moderate or severe [91,92]. These categories are rather wide in their scope but they do give some indication as to the rain penetration that may be expected.

Generally:

Sheltered - up to $3m^2/s$

Moderate - $3 - 7m^2/s$

Severe - $7 - 20m^2/s$

2.3.5 Wall type

In order to provide a rain proof load bearing masonry structure the design is of paramount importance [93]. The engineer normally resorts to a concrete load-bearing wall with a clay brick veneer. This screen can thus produce a cavity and is also aesthetically pleasing. A single skin concrete block has a poor record as a rain screen [94]. Four basic clay brick wall types have been identified in an attempt to achieve water-tight walls [95]:

(a) **Barrier wall:** These are walls which contain a barrier in a plane within the system parallel to and behind the exterior surface. This may be a sacrificial single skin clay brick masonry veneer.

Problems may arise due to the differing quality of workmanship between the sacrificial (external) skin and the internal. If water does break through into the interior, there is a risk that it may burst the wall due to freezing or the lack of an opportunity to evaporate.

(b) **Mass wall:** These contain several skins of masonry but no cavity between. This type of wall may to a certain extent be porous and have sufficient 'sponge-like' capacity to retain even the heaviest rain showers and allows moisture to evaporate later. However capillarity may create an even greater problem by drawing water further into the interior.

(c) **Skin walls:** These have an impervious dam, such as an effective water repellent on the exterior of the surface.

(d) **Cavity (drainage) walls:** These walls have proved excellent in their resistance to rain penetration. Cavity walls however often contain defects such as mortar drips and poorly laid ties which divert water across to the inner leaf

The introduction of cavity fill material has lead to an increase in the incidence of rain penetration [96]. Fill material bridges any cavity leaving a route for water to cross to the next skin. The fill materials are often themselves waterproof and rarely become sodden.

2.3.6 Workmanship

Cracks and depressions are an unavoidable part of the construction of masonry walls. These may be caused by incomplete covering of the brick by mortar or poor laying procedure. These and other similar factors combine to make workmanship the most influential parameter governing water ingress [97].

Most durable structures are built with competent masons using easily worked mortar and pre-wetted bricks that ensure well filled joints [98].

Poor workmanship is exhibited by [99,100]:

(i) Incorrect proportioning and mixing of water;
(ii) Incorrect adjustment of suction rate of masonry units;
(iii) Incorrect jointing procedures;
(iv) Disturbance of units after laying leading to 'pillowing';
(v) Failure to build walls level;
(vi) Failure to protect new work from weather.

These factors have the effect of reducing the aesthetic appeal of a structure and influencing its overall stability. Masonry built outwith adequate site procedures and with unsupervised masons can lead to a reduction in strength of between 50% and 60% compared with masonry built under supervision.

Incorrect jointing procedures would reduce non-structural performance in terms of sound insulation and resistance to rain penetration. Incomplete filling of bed joints may lead to a reduction in strength of approximately 33% [101].

Bed joints of excessive thickness (16-20mm) have the effect of reducing masonry compression and bond strength as it generates higher horizontal stresses than joints of only 10-14mm. This can reduce strength by as much as 30% [65,101]. Maurenbrecher [102] showed that incomplete filling of the central part of the mortar of a joint can reduce the strength of a panel by 33%.

Figure 2.19 shows the effect of excessive thickness of mortar bed in terms of strength reduction.

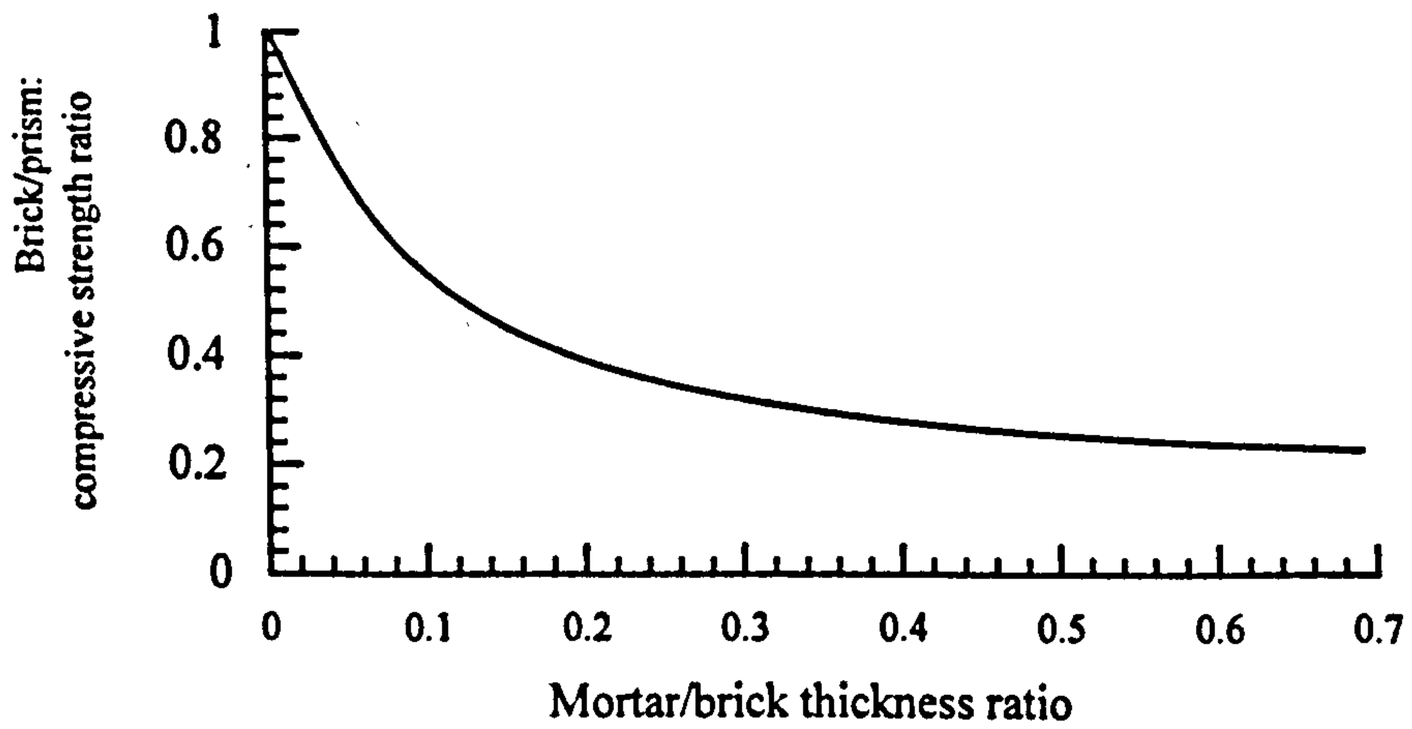

Fig 2.19 Typical effect of mortar/brick thickness ratio on brickwork compressive strength [101]

Walls which have not been built plumb encourage eccentric loading which can cause severe cracking and debonding in the main mortar bed as a masonry panel laterally buckles, leading to an increased likelihood of water penetration and a reduction in its load carrying capacity. The influence of eccentric loading is discussed in Chapter 7.

2.3.7 Brick/mortar bond

The properties of both brick and mortar are important in promoting the bond strength between them. These properties are the water retaining capacity of the mortar and the absorption rates of the brick. The bond can also be influenced by moisture content and surface characteristics of the brick, mortar consistency and sand grading within the mortar mix.

A good bond is obtained by the ability of the mortar to flow into the interstices and surface irregularities of the brick and can be measured by the force necessary to separate the mortar and the masonry unit.

2.3.8 Morphology

Scanning electron microscopy (SEM) of cut sections of brick/mortar bond show large variations in bond characteristics even within small areas. Some areas have a rather smooth surface with isolated pores. Other areas have surfaces with interconnected pores.

The morphology developed at a brick/mortar interface for both plain and lime-cement mixes can be characterised by a dual layered system. The first layer is a calcium rich film which is deposited on the brick surface shortly after coming into contact with the cement paste. This is more predominant for lime rich mortars. Calcium silicate hydrate particles and $Ca(OH)_2$ crystals grow to form a second layer [103].

The bond properties of the interface appear then to derive from the interlocking of hydration products formed in pores on the brick surface.

Better bond strengths can be expected if the network of hydration products is continuous. An increase in the depth of penetration of the paste into the brick would also improve the bond strength. This also provides a better load transport mechanism.

2.3.9 Influence of the brick/mortar bond on the failure mode of masonry panels

The common combined stress condition in masonry is tensile shear and compression in the plane of the wall. This can result from lateral wind loading and gravity loading. However, bed orientation of the main mortar bed causes a combination of these loading regimes on a wall producing differing failure mechanisms. The in-plane deformation and failure of masonry is influenced by the brick/mortar bond.

(a) Typical failure modes of masonry panels:

Mortar joints essentially create 'planes of weakness' and ultimately both the failure loads and failure surfaces are directly influenced. As mortar joints in masonry are relatively weak compared to the brick unit, the bed and head joint direction are the critical planes where failure is likely to be initiated and developed.

The compressive strength of mortar and brick is unlikely to be influential in governing the bond strength and more likely factors such as the initial rate of absorption and workmanship are important [104].

Hamid and Drysdale [105] have noted in their studies that mortar type does not have any significant effect on the capacity of masonry when a shear-slip mode of failure controls. However, the magnitude of the ratios of strength in three directions will depend on brick type.

Masonry built using solid bricks will have strength in three orthogonal directions very roughly equivalent whereas masonry built of highly perforated brick will be 2 to 3 times stronger perpendicular to the bed joint direction than in the other two directions [106].

Specimens under axial compression normal to the bed joints (bed orientation $\theta=0°$) exhibited progressive splitting behaviour initiated at the brick/mortar interface. The bricks constrain the mortar until they reach their unconfined compressive limits thereafter cracking develops. These stresses in combination with the vertical compression cause splitting failure of the units under a compression-tension state of stress. The splitting first develops in a vertical joint some distance below the load in line with the loading plate where the horizontal stresses are high. These stresses are then propagated vertically for the full height of the wall causing further crack growth [107].

Specimens under axial compression parallel to the bed joint (bed orientation $\theta=90°$) usually fail by debonding at the now vertical bed joints caused by lateral stresses developing at the brick/mortar interface. The resulting columns of masonry would be capable of sustaining further load. The final collapse of the panel occurs at much higher load levels. However from both a structural integrity and permeability viewpoint, the panel would be considered to have failed when full debonding occurred.

The transition between these two wholly distinct failure modes is hugely influenced by the bed orientation. This parameter indicates whether failure occurs by cracking, debonding or sliding within the panel or a combination of them all.

Page [108] showed that biaxial compression failure is greatly influenced by the applied principal stresses. When one principle stress dominated, failure occurred by cracking and sliding in the joints and/or bricks. The authors show that the strength of the panel was greatly reduced when failure occurred by sliding down an orientated bed joint. This indicated that joint properties as well as orientation are important parameters.

A mixed shear-tension failure occurs when the orientation of principal tension stresses are in directions other than parallel and normal to the bed joints. This includes debonding at the interface and splitting of both the brick units and mortar joints. This was caused by a failure crack not always following the most direct or obvious path for propagation [104].

At a bed orientation of θ=45° to the applied load, where both shear and normal stresses occur in the bed and head joints, the failure was essentially an equal contribution of shear and tension. Rivero and Phan [109] stated that the compressive strength of masonry is a function of bed orientation, with θ=45° being used as a position of symmetry.

The failure mode at θ=45° is distinguished by a stepped crack occurring mostly along the mortar bed and head joints and will tend to occur in units of higher tensile strength and mortars of lower bond strength.

Bernadini et al [111] observed that brittle splitting passes through both brick and joints along a straight line for θ=0°. Irregular patterns were observed when θ=30° and 45°.

Figure 2.20 shows the typical failure modes associated with panels of variable bed orientation.

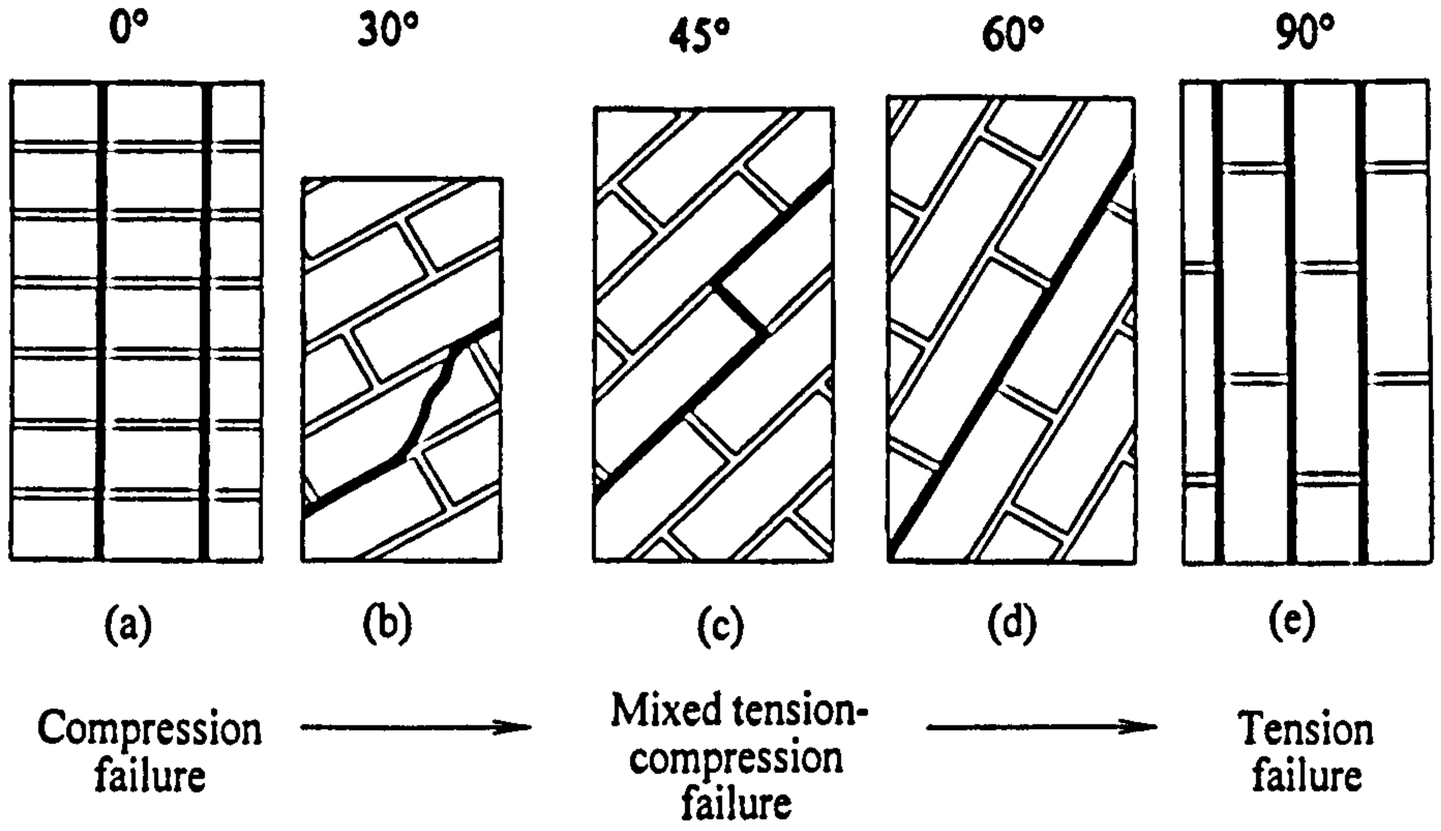

Fig. 2.20 Failure modes for masonry panels with variable bed orientation [111]

The authors conclude that there are two distinct modes of failure for brick masonry under combined shear and compressive loading conditions. A shear mode of failure along the bed joint is distinguished by slip at the interface under a shear-compression state of stress whereas a tension mode of failure is distinguished by vertical splitting of the masonry under a compression-tension state of stress. A mixed shear-tension mode of failure is dependant upon the relative magnitude of the shear and the normal compressive stresses along the bed joints and is the major controlling factor in governing the mode of failure [111].

(b) Theoretical failure envelopes for bed orientated panels:

Hamid and Drysdale [110,112] noted that where a load is applied uniformly to a panel, the resulting stress distribution is globally homogenous. This allows principal material directions (parallel (x) and normal (y) to the bed joint), a particular bed orientation φ and applied stress, σ_c to be expressed as follows:

$$\sigma_x = \sigma_c \cos^2\varphi \qquad \text{Eqn. 2.22}$$

$$\sigma_y = \sigma_c \sin^2\varphi \qquad \text{Eqn. 2.23}$$

$$\tau_{xy} = \sigma_c \sin\varphi\cos\varphi \qquad \text{Eqn. 2.24}$$

Brick and mortar have different lateral expansion characteristics. Under compression load mortar tends to expand more than the brick which creates lateral tension. However under low applied loads and within the elastic region the lateral forces in each distinct material are in equilibrium.

Figure 2.21 shows the typical stresses in a masonry panel. Equations 2.25 and 2.26 show these lateral stresses in equilibrium.

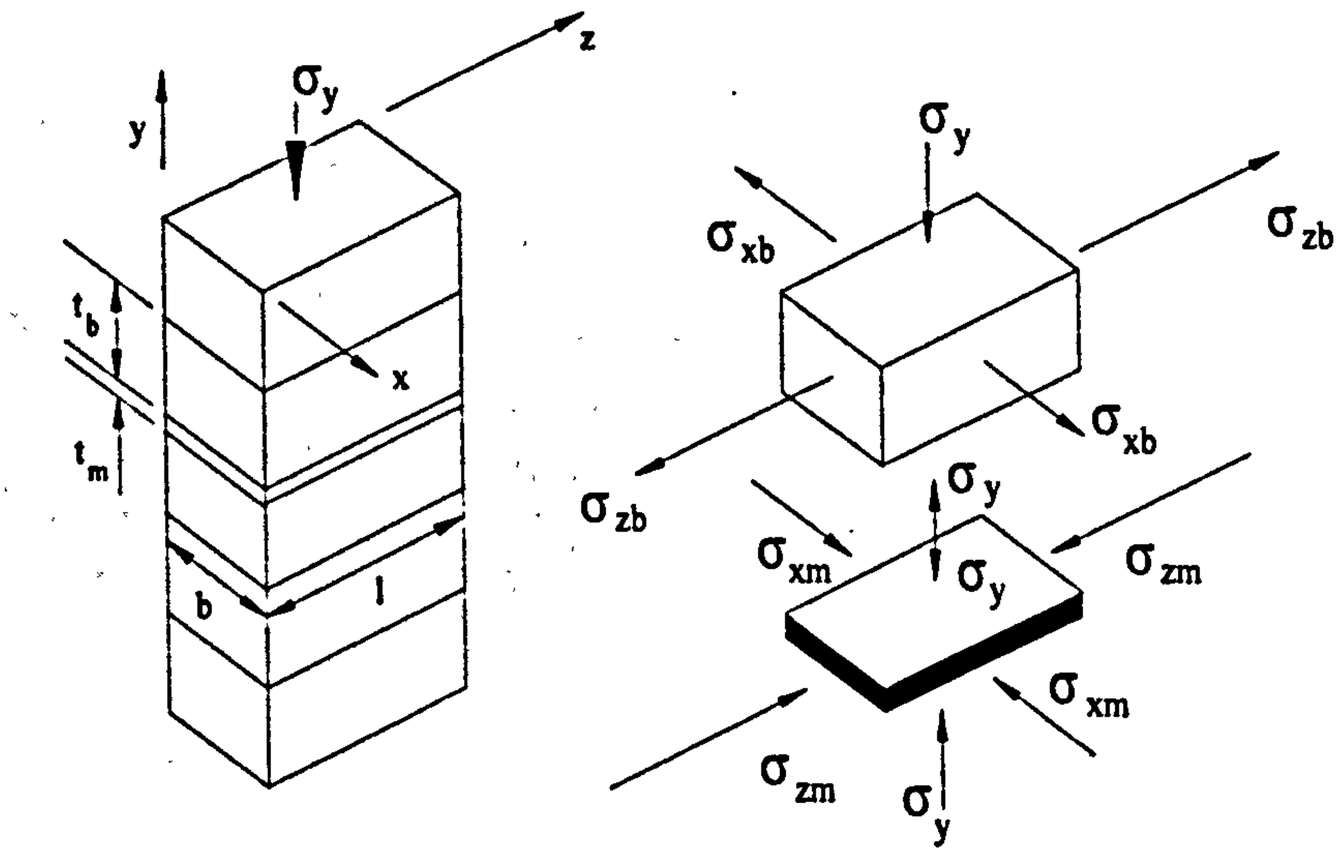

Fig. 2.21 Stresses in brick-mortar composite [95]

$$\sigma_{xm} = \alpha\sigma_{xb} \qquad \text{Eqn. 2.25}$$

$$\sigma_{zm} = \alpha\sigma_{zb} \qquad \text{Eqn. 2.26}$$

σ_{xm} - lateral stress in x - direction in mortar

σ_{xb} - lateral stress in x - direction in brick

σ_{zm} - lateral stress in z - direction in mortar

σ_{zb} - lateral stress in z - direction in brick

α - ratio of the height of brick (t_b) to the thickness of mortar bed (t_m)

As lateral strains are also the same in brick and mortar then:

$$\sigma_{zb} = \sigma_{xb} = \frac{\sigma_y(\beta\upsilon_m - \upsilon_b)}{1 + \alpha\beta - \upsilon_b - \alpha\beta\upsilon_m} \qquad \text{Eqn. 2.27}$$

σ_y - applied axial stress

υ_b, υ_m - Poisson's ratio for brick and mortar respectively

β - ratio of elastic modulus for brick (E_b) to that of mortar (E_m)

Assuming a linear relationship to exist between ultimate compressive stress and lateral tensile stress, then:

$$\sigma_{xb} = \frac{1}{\phi}\left(\sigma'_{ult} - \sigma_{ult}\right) \qquad \text{Eqn. 2.28}$$

where:

$$\phi = \frac{\sigma'_{ult}}{\sigma'_t}$$

σ'_{ult} - ultimate longitudinal compressive stress

σ_{ult} - longitudinal compressive stress

σ'_t - longitudinal tensile stress

Figure 2.22 shows a failure envelope for brickwork strength using Hilsdorf's approach [110]. This is based on an assumed linear relationship between the lateral biaxial tensile strength and the local compressive stress equal to the mean external compressive stress multiplied by a factor of non-conformity, U_u. This value of non-conformity varied according to brickwork strength [113].

This failure envelope shows that cracking will occur within the masonry panel when the internal tensile stresses caused by some external compressive stress intersect with the failure envelope (i.e. line B_1 or B_2 intersects with line A). Further cracking will appear for combined loading, though failure will not occur until the brick can no longer provide the restraint required to prevent failure in the mortar. This is shown in Fig. 2.22 when the triaxial strength of the mortar intersects with the failure line for the brick (i.e. line C intersects with line A).

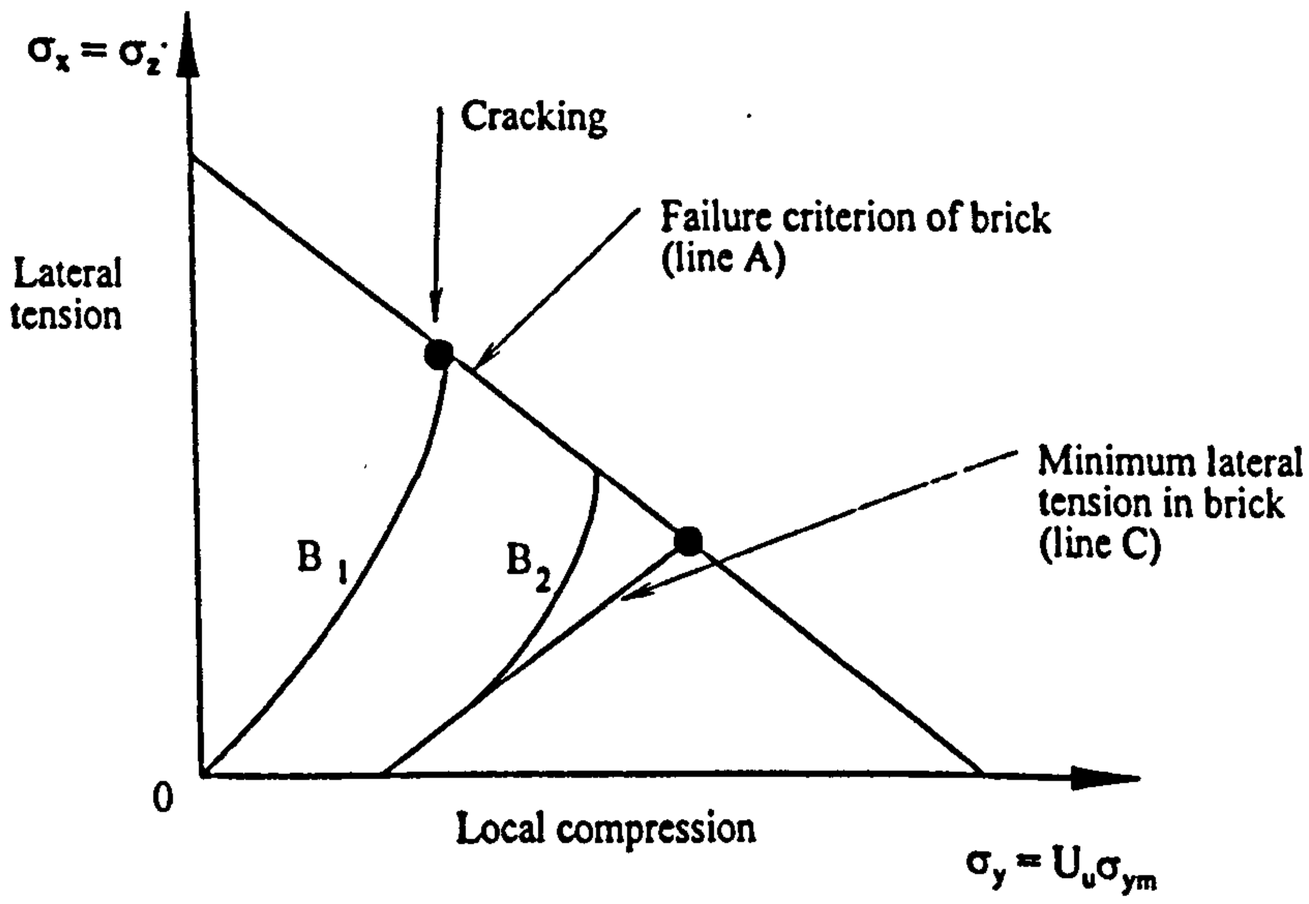

Fig. 2.22 Hilsdorf's failure theory [113]

Hilsdorf used the triaxial strength of mortar to establish the minimum lateral confinement of the joint, σ_{xy} which is given by:

$$\sigma_{xy} = \frac{1}{4.1}\left(\sigma_y - f'\right) \qquad \text{Eqn. 2.29}$$

σ_y - local compressive stress

f' - uniaxial compressive strength of mortar

By taking account of the equilibrium of lateral forces within brick and mortar to describe the minimum lateral tension in brick (line C) and the biaxial tensile strength and uniaxial compressive strength of brick to describe the brick failure criteria (line A), then the magnitude of the local stress at failure (σ_y) can be represented as the intersection of these lines:

$$\sigma_y = f'_b \left(\frac{f'_{bt} + \alpha f'}{f'_{bt} + \alpha f'_b} \right) \qquad \text{Eqn. 2.30}$$

f'_b - uniaxial compressive strength of brick

f'_{bt} - biaxial tensile strength of brick

α - $\frac{t_m}{4.1 t_b}$: where t_m and t_b have been defined earlier

The average masonry compressive stress (σ_{ym}) is then:

$$\sigma_{ym} = \frac{\sigma_y}{U_u} \qquad \text{Eqn. 2.31}$$

where U_u and σ_y have been defined earlier.

Investigations have shown that comparisons between predicted failure criteria and actual results were very poor [113]. This implied that elastic analysis may not be appropriate. These discrepancies were thought to be attributed to the very low values of the shear strength along the bed joints. The elastic failure theories also do not consider the possible shear failure along either the critical bed and head joints exhibiting brittle behaviour [90,115].

Developing from Hilsdorf failure envelope, Khoo and Hendry [113,114] showed that the biaxial compression-tension strength envelope for brick could be represented:

$$\left(\frac{\sigma_y}{c_0}\right) = 1 - \left(\frac{\sigma_t}{t_0}\right)^{0.546} \qquad \text{Eqn. 2.32}$$

c_0 - uniaxial compressive strength of brick

t_0 - uniaxial tensile strength of brick

σ_y - compressive stress

σ_t - tensile stress

Khoo and Hendry [113,114] also developed a failure theory for brickwork which assumed a failure envelope for brick in biaxial compression-tension within a brickwork prism (Fig. 2.23). Looking to Fig. 2.23, as the vertical compression load increased when acting upon the prism, the stress path followed OA. Failure occurs within the brick element when the line OA intersects the failure envelope at A, the compressive strength of the prism being given at this point. The stress path taken is highly dependent upon the properties of the mortar joint under triaxial compression. For example, weaker mortar joints where higher lateral strains are greater under load would result in a lower line (OB) which in effect reduces the brickwork compressive strength.

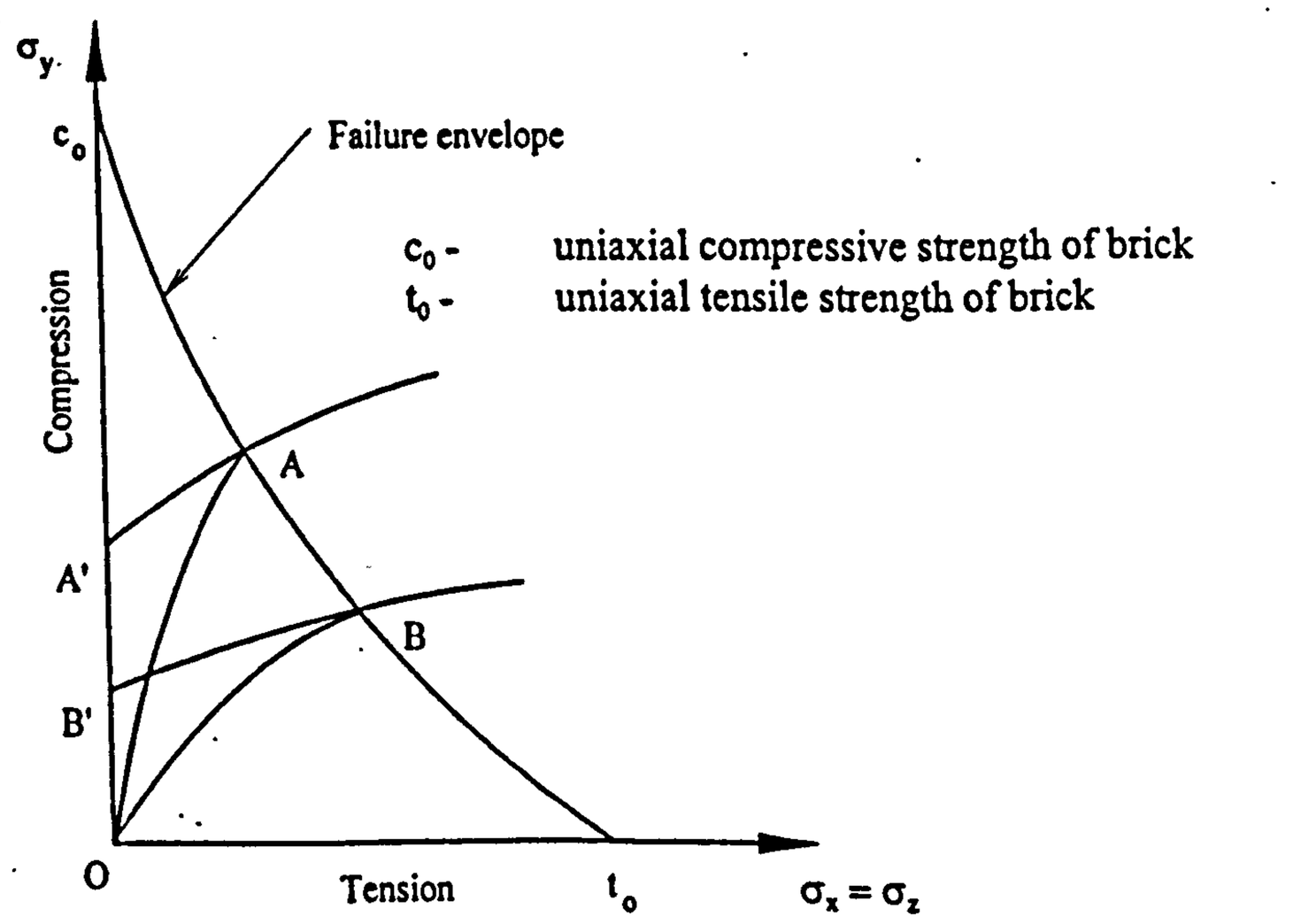

Fig. 2.23 Failure envelope for brick compression and tension [114]

(c) Shear strength of masonry:

Generally at pre-compression levels acting on a masonry panel of less than $2N/mm^2$, the relationship between shear strength (τ_p) and pre-compression (σ_n) can be adequately expressed using Mohr-Coulomb theory:

$$\tau_p = 0.3 + 0.5\sigma_n \qquad \text{Eqn. 2.33}$$

Ghazali and Riddington [115] showed that shear strength could also be empirically expressed as:

$$\tau_p = 0.83 + 0.78\sigma_y: \qquad \text{(solid bricks)} \qquad \text{Eqn. 2.34}$$

and

$$\tau_p = 0.17 + 0.81\sigma_y: \qquad \text{(frogged bricks)} \qquad \text{Eqn. 2.35}$$

σ_y - local compressive stress

Andreaus [116] proposed a modified Mohr-Coulomb shear failure indicating that slipping of the mortar joints is assumed to have occurred only when shear strength (τ_p) was attained:

$$\phi_A = \tau_p^2 - (c_e - \mu\sigma_n) \qquad \text{Eqn. 2.36}$$

ϕ_A - shear angle

τ_p - shear stress

c_e - effective cohesion

μ - frictional coefficient for slipping in the direction parallel to the bed joints

σ_n - stress normal to the bed joints

This was found to have good agreement within the specific experimental test walls but was likely to vary considerably, like all shear strengths for all failure criteria, upon the combination of brick and mortar.

2.3.10 Measurement of masonry permeability

The testing of masonry for permeability and resistance to rain penetration has been innovative and often used ingenious testing techniques.

Experimental work in Norway [117,118], where the climate is particularly harsh, provided both interesting and novel procedures. Using a combination of water spray accompanied by an air pressure differential supplied by a centrifugal fan, an indication of actual exposure conditions on masonry walls has been made.

Birkeland and Svendsen [118] using the above testing procedure concluded that pressure differentials would be the most influential factor in governing rain penetration, specifically through mortar joints.

Comparisons with field tests proved problematic. Although variations between laboratory built and site built test panels may be put down to differences in workmanship and building materials The main discrepancies are caused by curing and storage conditions for masonry panels within the laboratory. These differ markedly from the condition of those test panels built and cured outside.

Butterworth and Skeen [119] used a similar rain device though introduced intermittent spraying to mimic more realistic weather conditions and time lapse photography to provide a continuous record of the condition at the back of the test wall.

In Britain, laboratory tests have been developed to assess walls for their integrity. BS 4315: Part 1 [120] was used mostly in the glazing industry and Part 2 [121,122] describing the test for permeable walling.

The BS 4315 test used a test box placed into an airtight chamber with one face left open to receive the specimen. Inside the box it is possible to produce an air differential of at least 150mm. Water is then sprayed onto the 'weather side' of the specimen in a horizontal band of 250mm thick at the top of the test specimen. The spray is made up of roughly equal sized droplets.

This British Standard [121] then shows that there are three different methods to evaluate the water penetration of the wall.

Method A involves the recording of wetting by time lapse photography, Method B suggests weighing the specimen before and then after 30 minutes of wetting and Method C states that the measurement of the quantity of water that leaks through the walling should be an indication of the walls effectiveness, i.e. permeability.

Experimental studies [117,118,121] tended to show that the pressure difference over the exterior of the wall is the most critical climatic factor in controlling rain penetration. The differentials can occur by a combination of water on the wall, openings to permit passage and forces to drive moisture towards the masonry interior.

Krogstad and Weber [95] listed six different methods for evaluating the performance of masonry specimens, the most relevant to this experimental research programme being the RILEM tube test.

This test involves sealing a 25.4mm diameter clear plastic tube to a wall. The attached vertical tube is open, and filled with water to a desired height where it can then simulate an exposure to both rain and pressure differentials. During the test, the water level was monitored to determine the amount of loss where the penetration rate can then gauged. The ingress rates were variable depending on their position upon the masonry panel.

Due to its simplicity, ease of operation and relative cheapness, the RILEM test may promote increased use of this technique in the testing of masonry walls for water penetration and permeability.

These testing techniques amongst others have concentrated on imitating realistic weather conditions but do not attempt to promote realistic masonry behaviour. Rain penetration at a unique point on a masonry panel can be gauged by a standing reservoir of water, though for a more realistic assessment, the test specimen should undergo some loading regime. Research of loaded masonry panels and their relationship with water ingress is very limited.

2.4 Summary

It is clear from this chapter that considerable efforts have been made in understanding water ingress and the factors that control this phenomena.

The effect of mortar type and factors such as w/c ratio and curing conditions, the influence of brick type and its pore size distribution and overall factors such as cracking at the brick/mortar interface and workmanship of the mason have all been considered influential. A number of testing techniques for measuring water ingress into brick, mortar and masonry panels have also been discussed.

However little attempt has been made to assess the true water penetration characteristics of a masonry structure. Investigations already undertaken have mainly concentrated on masonry exposed to a number of environmental conditions to assess likely deterioration characteristics of a variety of brick and mortar types. Although these research programmes provided invaluable data on ingress behaviour they do not consider the effect that applied stress has in creating micro-cracks likely to increase the deterioration rate in masonry via increased water ingress. The effect of bed orientation, although comprehensively studied for shear, would undoubtedly influence any ingress as differing failure modes were likely to induce variable crack patterns. So far no attempt has been made to determine the effect of this factor.

A reliable and adaptable test apparatus has therefore to be developed which would allow water ingress to be accurately measured and be able to quantify the influence of factors such as bed orientation and applied stress level on the water ingress characteristics of masonry.

CHAPTER 3

MATERIAL TESTING

3.1 Introduction

The testing described in this chapter was performed in order to establish various properties for the four brick and three mortar types that were anticipated to be used in the construction of the masonry panels within this research programme.

The individual brick and mortar properties were used to estimate the ultimate failure strength of a masonry panel. They were also used to gauge likely bond characteristics at the brick/mortar interface and their susceptibility to water ingress. Material tests also provided comparisons to the variability, or similarity, of the properties of brick and mortar. These factors were assessed and highlighted before any large scale masonry panel testing was undertaken.

The workability of a mortar mix was assessed using a number of retentivity tests that were followed by tests on mortar cubes. These cubes were produced to determine compressive strengths, elastic modulii and Poisson's ratio values.

The absorption rate of bricks, their compressive strengths, elastic modulii and Poisson's ratio was also determined.

3.2 Sieve Analysis of Sand

Investigators had found that the size distribution of sand, or sand grading, is influential in governing the water/cement ratio of mortar which in turn can control bond strength and permeability [26,27,123]. The sand grading also controls porosity, drying shrinkage and workability.

A sieve analysis test was undertaken in accordance with BS 812 [124,125] to ascertain the grading of the aggregate used in all mortar mixes throughout the investigation.

The findings are presented in Table 3.1 in accordance with recommendations as denoted in BS 1200 [126].

Table 3.1 Building sands for mortar used in masonry panels [126]

BS sieve	Percentage of mass passing BS sieves		
	Type S	Type G	Sand used
mm			
6.3	100	100	100
5.00	98-100	98-100	100
2.36	90-100	90-100	100
1.18	70-100	70-100	99
µm			
600	40-100	40-100	94
300	5-70	20-90	60
150	0-15	0-25	19
75	0-5	0-8	6

Table 3.1 indicates that the building sand used in the mortar mix conforms to Type G sand in accordance with BS 1200 [126].

3.3 Mortar Preparation and Testing

3.3.1 Test preparation

Ordinary Portland cement (OPC), which is used for all tests, and hydrated lime are both in accordance with current British Standards [127,128].

(a) Cube preparation:

Three different mortar mixes were anticipated to be used in the masonry test panels which would generate a variety of brick/mortar bond strengths. This would therefore induce variable failure loads and crack patterns and was initially expected to have a major controlling influence on water ingress into masonry.

Tests on fresh mortar concentrated on water content. Hardened mortar cubes were tested in compression to assess the strength of 1:1:6, 1:$^1/_2$:5 and 1:$^1/_4$:3 (cement:lime:sand) mortar mixes by volume. Additional cube tests were undertaken to calculate the modulus of elasticity E_m.

Cubes were prepared in accordance with BS 4551: 1980 [129].

(b) Testing:

Tests on fresh mortars were undertaken in accordance with BS 4551: 1980 [129]. These tests gave an indication of the workability and water content of the different mortar mixes.

Workability is an indication of the water/cement ratio (w/c) which has consistently proved to be one of the most influential factors affecting the properties of mortar, controlling the porosity of cement pastes and hence strength.

Both the consistence and water retentivity tests are also important. If the bricks used are of high suction, too much water may be lost from the mortar into the brick interior with a detrimental effect on the brick/mortar bond.

3.3.2 Fresh mortar tests

(a) Free water content:

Three fresh mortar samples were taken from each mix prior to the making of cubes. These were placed in three pre-weighed dishes and left to dry in an oven to a constant mass. The moisture contents were then calculated to the nearest 0.5%.

The water content of a mortar mix is subjective as it was left to the masons' expertise to decide on how much water was required to create a desirable consistency. These results can be seen in Table 3.2.

Table 3.2 Moisture contents for fresh mortar

Mortar type	Average moisture content (%)
1 : 1: 6	15.7
1 : $^1/_2$: 5	17.0
1 : $^1/_4$: 3	14.8

Moisture contents can be seen as being approximately equal for all mixes.

(b) Workability tests:

The consistence, or ease of flow, of a mortar mix was measured using the dropping ball technique as described in BS 4551: 1980 [129]. This test, although measuring only the physical property of the mortar, was useful in indicating the ease by which mortar can be applied to the brick and its capacity to spread evenly without allowing any cavities to form.

Three tests were made on separate portions of each mortar mix with the average of three penetrations being noted to the nearest 0.1mm (Table 3.3).

Table 3.3 Average penetration depths using the dropping ball technique [129]

Mortar type	Average penetration (mm)
1:1:6	6.8
1:$^1/_2$:5	8.0
1:$^1/_4$:3	6.6

Although these tests were influenced by the free water content of the mortar all penetrations were approximately equal. This tended to indicate that the proposed mortar types behaved similarly in terms of consistence irrespective of their constituent materials.

Bowler et al [130,131] indicated that mortars with poor workability as defined by consistence tended to produce the least watertight masonry walls.

(c) Water retentivity test:

This test as described in BS 4551: 1980 [129] was used to gauge the possible tendency for mortars to lose free water by suction.

Water retentivity is measured by the mass of water retained by mortar after applying a standardised suction rate. This is usually expressed as a percentage of the mass of water originally present in the mortar (Table 3.4).

Table 3.4 Average water retentivity for mortar mixes

Mortar type	Average water retentivity (%)
1 : 1: 6	100
1 : $^1/_2$: 5	100
1 : $^1/_4$: 3	100

*BS 4551: 1980 [129] recommends that average values are rounded to the nearest 5%

The dropping ball test was then repeated on the mortar after suction. The corrected penetration of the ball after suction was a measure of the consistence retentivity (Table 3.5).

Table 3.5 Average consistence retentivity for mortar mixes after suction

Mortar type	Average consistence retentivity (%)
1 : 1: 6	62
1 : $^1/_2$: 5	44
1 : $^1/_4$: 3	71

These results vary markedly between mortar types. The free water content within each mix is thought to play a highly influential role in governing this test. Results showed that the mortar mix with the highest free water content (Table 3.2, mortar mix 1:$^1/_2$:5) also displayed the lowest consistence retentivity (Table 3.5).

3.3.3 Mortar cube testing

(a) Compressive strength ($f_{cu(m)}$):

Three cubes per mix were tested to failure in accordance with BS 4551: 1980 [129]. These tests would allow the assessment of masonry panel strength for the differing types of mortar.

Table 3.6 shows a summary of the average compressive strengths of the mortar mixes. Test results clearly showed that the 1:1:6 mix is the weakest of all the mortars tested and the strongest mix was the 1:$^1/_4$:3. The difference in strength between the extremes of these mix types is 12.7N/mm^2.

Increased durability tended to be obtained with stronger mortars containing the greater proportion of cement, though this should be counterbalanced by the greater tendency of cracking in masonry due to settlement and thermal and moisture movements.

(b) Modulus of elasticity of mortar (E_m):

Samples were tested in accordance with BS 1881: Part 121: 1983 [132].

Three test specimens of 3-cube stacks were used in the assessment of the modulus of elasticity of mortar (E_m). The three cubes were separated by 1-2mm of dental plaster. The dental plaster was mixed in a plastic bag to the desired workability and then placed between the cubes. The dental plaster had been shown to have no influence over any final results [133,134].

Dental plaster was applied to the top and bottom of the specimens in contact with the loading platens. Two 10mm rosette strain gauges were then attached at mid-cube height to the middle cube, and on two opposite sides whereupon they were then attached to a data logger (Fig. 3.1).

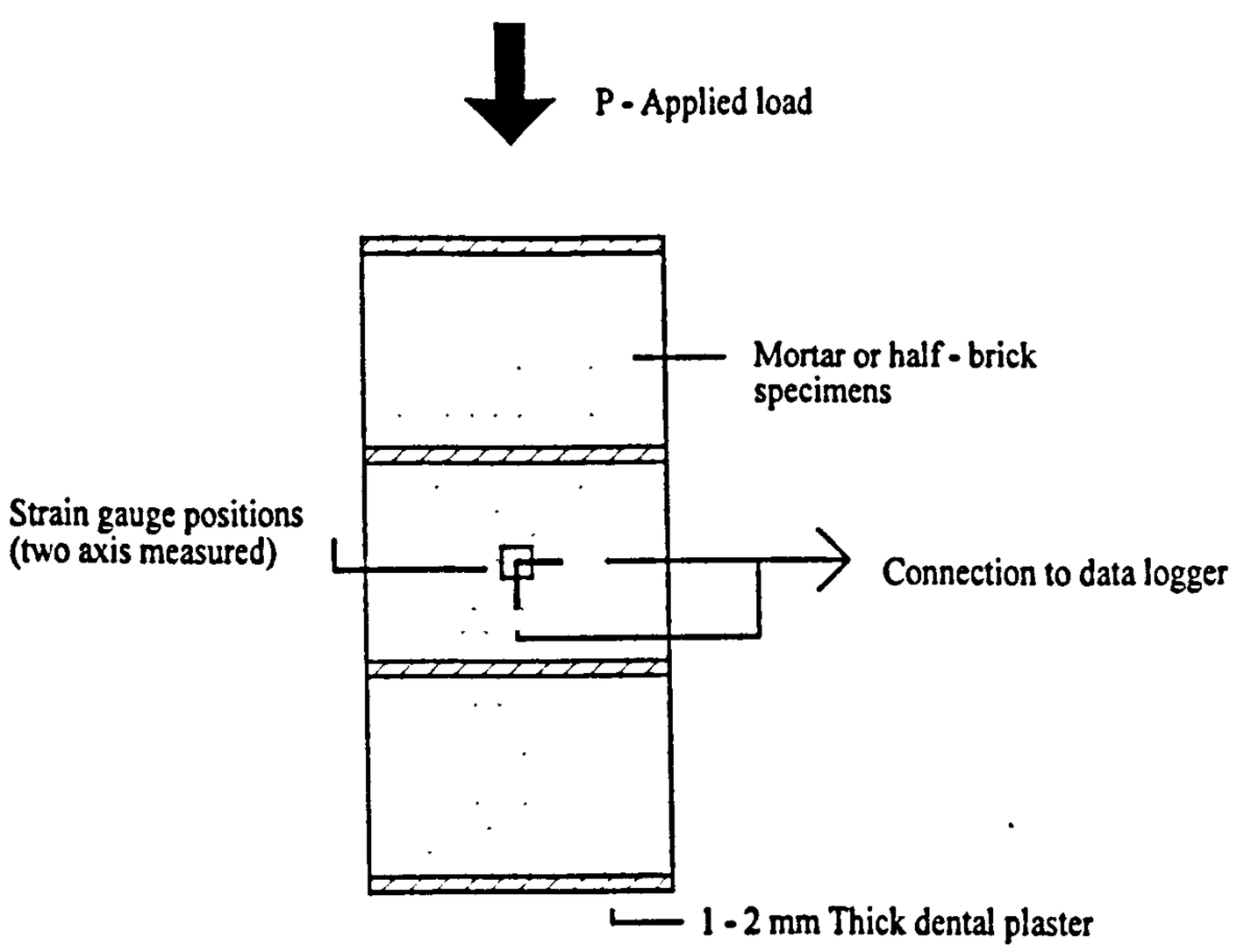

Fig. 3.1 Specimen arrangement for measuring elastic modulus (E_m)

The data logger measured strain and applied stress in increments until failure was reached. From the data recorded the elastic modulii of each mortar mix (E_m) was estimated.

In conjunction with these modulii tests, data was also used to assess the relationship between lateral and axial strain (Poisson's ratio, υ_m). Results from these tests are shown in Table 3.6

Table 3.6 Summary of mortar cube test results

Mortar type	Compressive strength, $f_{cu(m)}$ (N/mm^2)	Elastic modulus E_m (N/mm^2)	Poisson's ratio, υ_m
1 : 1 : 6	12.7	5400	0.33
1 : $^1/_2$: 5	15.1	9180	0.26
1 : $^1/_4$: 3	25.4	17500	0.25

3.4 Brick Testing

Four brick types were used in the investigation. Calcium silicate or Type 1 bricks have a grey lustre and are solid with a small frog on one face. Type 2 bricks are yellowish in colour which have relatively smooth surfaces on all faces and have three centrally positioned cores. Type 3 bricks are red in colour with particularly rough vertical surfaces on all but one face and have 10 small centrally positioned cores. Type 4 bricks are also yellowish in colour with a rough surface on only one vertical face and five centrally located slits (Fig. 3.2).

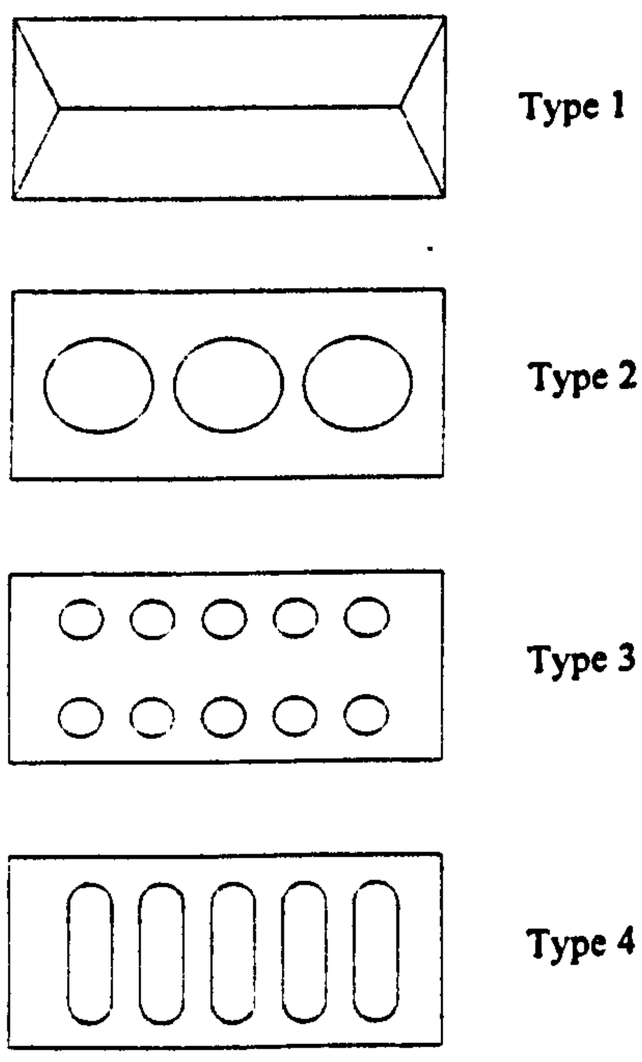

Fig. 3.2 Sketches of cored brick types used in testing

Calcium silicate bricks are manufactured using silica sand and hydrated lime mechanically pressed into shape and autoclaved. Type 2-4 bricks have clay as their main constituent and are kiln fired.

(a) Absorption rate:

Ten bricks are used from each brick type in the test for absorption. Testing was carried out in accordance with BS 3921: 1985 [59].

The average absorption rates for clay bricks are broadly similar. Absorption rates for Type 1 (calcium silicate) bricks were higher than those exhibited by the clay bricks by almost a factor of 2 (Table 3.7).

Table 3.7 Average results of water absorption for bricks

Brick type	Average absorption (%)
1	11.3
2	7.0
3	6.2
4	7.0

Using these experimental results it may be concluded that bricks, with the exception of Type 1 (calcium silicate), are unlikely to be too influential in governing both permeability and brick/mortar bond strength. The scatter of absorption rates between bricks of the same type were found to be just as variable as differences between actual brick types.

(b) Compressive strength:

As with mortar compression results, these tests allowed for an indication of the contribution of the brick to the overall test panel strength to be gauged. Some relationships do exist between the compressive strength of bricks and their relative absorption rates (Fig. 3.3).

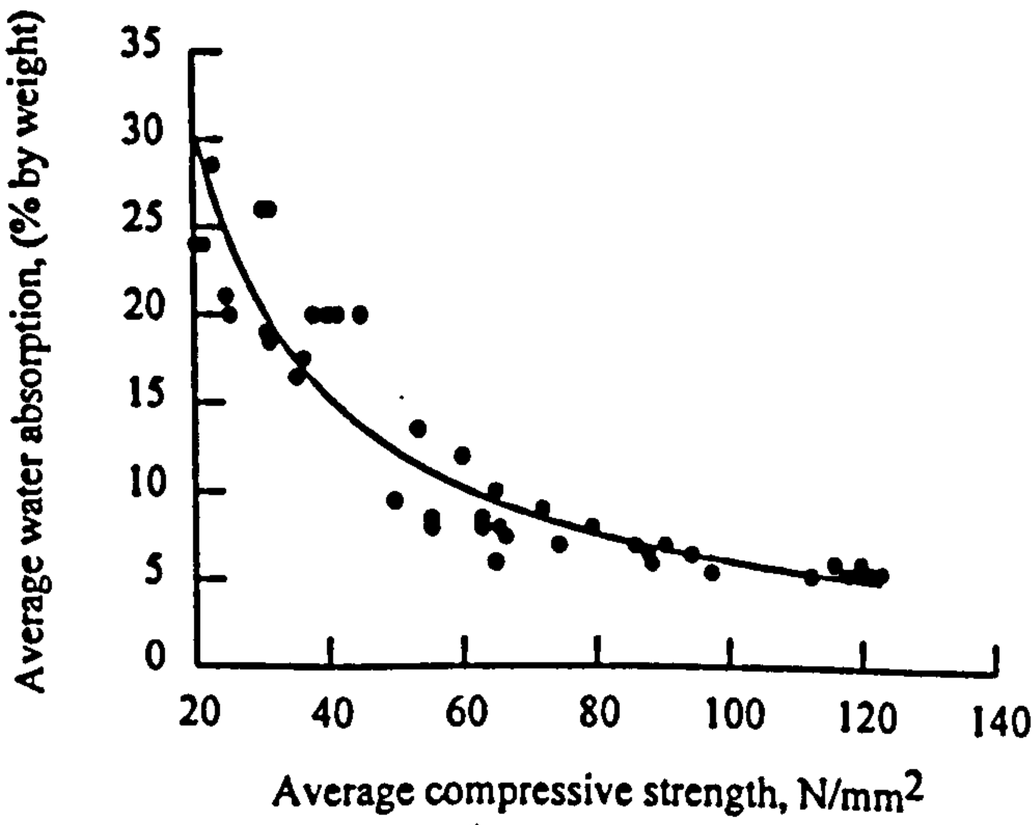

Fig. 3.3 Typical relationship between average absorption and compressive strength [135]

Table 3.8 gives an indication of the compressive strengths of brick.

(c) Modulus of elasticity of brick (E_b):

Similar to the mortar tests, the modulus of elasticity of bricks (E_b) was determined by tests on 3-brick stacks. The test followed the same procedure as that for mortar. The test was carried out in accordance with BS 1881: 1983 [132] which is commonly used to determine the modulus of elasticity of concrete.

Three samples of each brick type were tested, the average results being shown in Table 3.8. These results indicated that the higher the compressive strength of brick the higher the elastic modulii.

Poisson's ratio results for brick (υ_b) can also be seen in Table 3.8. These results showed that there is very little change in Poisson's ratio values between a basic stress and failure stress. This indicated that lateral and axial strain increased linearly.

Table 3.8 Average brick properties

Brick type	Compressive strength, f_b (N/mm^2)	Elasticmodulus, E_b (N/mm^2)	Poisson's ratio υ_b at plateau level	Poisson's ratio υ_b at peak level
1	24	—	—	—
2	59	12650	0.16	0.19
3	81	43550	0.21	0.21
4	54	13200	0.41	0.42

3.5 Conclusions

The testing of fresh mortars showed that consistency and retentivity was similar irrespective of the mortar type. This implied that when bricks were placed upon the mortar bed, then all mortar mixes would behave broadly similarly with respect to having water drawn from them by a brick and that the ease by which mortar could be applied to the brick and be spread evenly without cavities forming.

Experimental work further showed:

- Testing 3-cube and 3-brick stacks proved to be an effective and easy test to determine the modulus of elasticity and Poisson's ratio for mortar and brick. It was found that increasingly higher cube crushing strengths for mortar mixes also corresponded with increasingly higher modulii of elasticity.

- For the range of clay bricks tested, very little change was observed in the values of Poisson's ratio at basic stress and failure stress levels.

- Calcium silicate bricks exhibited higher water absorption rates compared to those of clay bricks, this being quantified as being between 1.6-1.8 times more absorbent.

CHAPTER 4

PERMEAMETER DEVELOPMENT

4.1 Introduction

To assess the likely water ingress characteristics of stressed masonry panels, a new permeameter was developed to measure water ingress. This chapter describes a typical experiment on bricks and mortar specimens using the new permeameter.

In developing the test permeameter a number of influential factors were considered. The permeameter should allow a head of water to ingress effectively into a masonry panel and for data to be generated that showed the influence of factors such as applied load and bed orientation. The permeameter should also be adaptable, light, robust and be capable of generating repeatable tests results. It also should have a large enough wetted contact area with the test specimen that would allow realistic ingress results to be measured.

4.2 Permeameter Development

Using direct methods of testing (i.e. measuring water ingress and comparing this with a volume of egress) are time consuming due to the small volumes of water measured, longevity of test and the complex equipment required to undertake these types of test. A practical method of testing is measuring only the water ingress to indicate the relative water ingress characteristics of a masonry panel.

Choosing an indirect method of testing would reduce problems of measurement and allow relatively simple tests to be carried out on masonry panels and repeated frequently.

Due to the variability in workmanship at an individual mortar joint it became obvious from an early stage that any test permeameter would have to be fixed to a particular mortar joint position on a panel for the duration of the test programme. However, once a particular test programme was completed these permeameters could be removed from the panel and fixed to another thus limiting manufacturing time, number and cost.

Permeameters were initially made of grey PVC. They incorporated an inlet valve that allowed water entry and an air valve that allowed entrapped air to escape. The permeameter had an internal diameter of 40mm. This allowed the permeameters to sit over an effective area of brick/mortar interface. Tapered side walls were also incorporated which allowed a sealant to be smeared easily onto the permeameter wall and masonry panel (Permeameter A, Fig. 4.1).

For consistent results to be gathered, any moisture content was removed from the masonry panels prior to testing.

Moisture blocks pores and cavities within the panel limiting water ingress. The moisture content can vary throughout an individual panel and differ considerably for the duration of the test programme. Removal of any moisture provided a datum that allowed comparisons to be made between water ingress for panels when loaded and unloaded.

To remove the moisture, test panels were dried in a temperature controlled oven for a minimum of 24hrs prior to testing. However due to space limitations within the oven, more screw-in joints for the inlet valve had to be manufactured and the airlock position was brought forward, closer to the masonry surface. This ensured that there would be a complete wetted area impinging on the wall surface (Permeameter B, Fig. 4.1).

Further development followed with a change in permeameter material to clear perspex. This proved to be equally effective in gaining repeatable results. However these required more individual parts to be manufactured and glued into position using chloroform. Due to perspex permeameters having these additional parts, more areas were prone to leakage. This was solved by smearing a water resistant sealant to the joints of the manufactured parts (Permeameter C, Fig. 4.1).

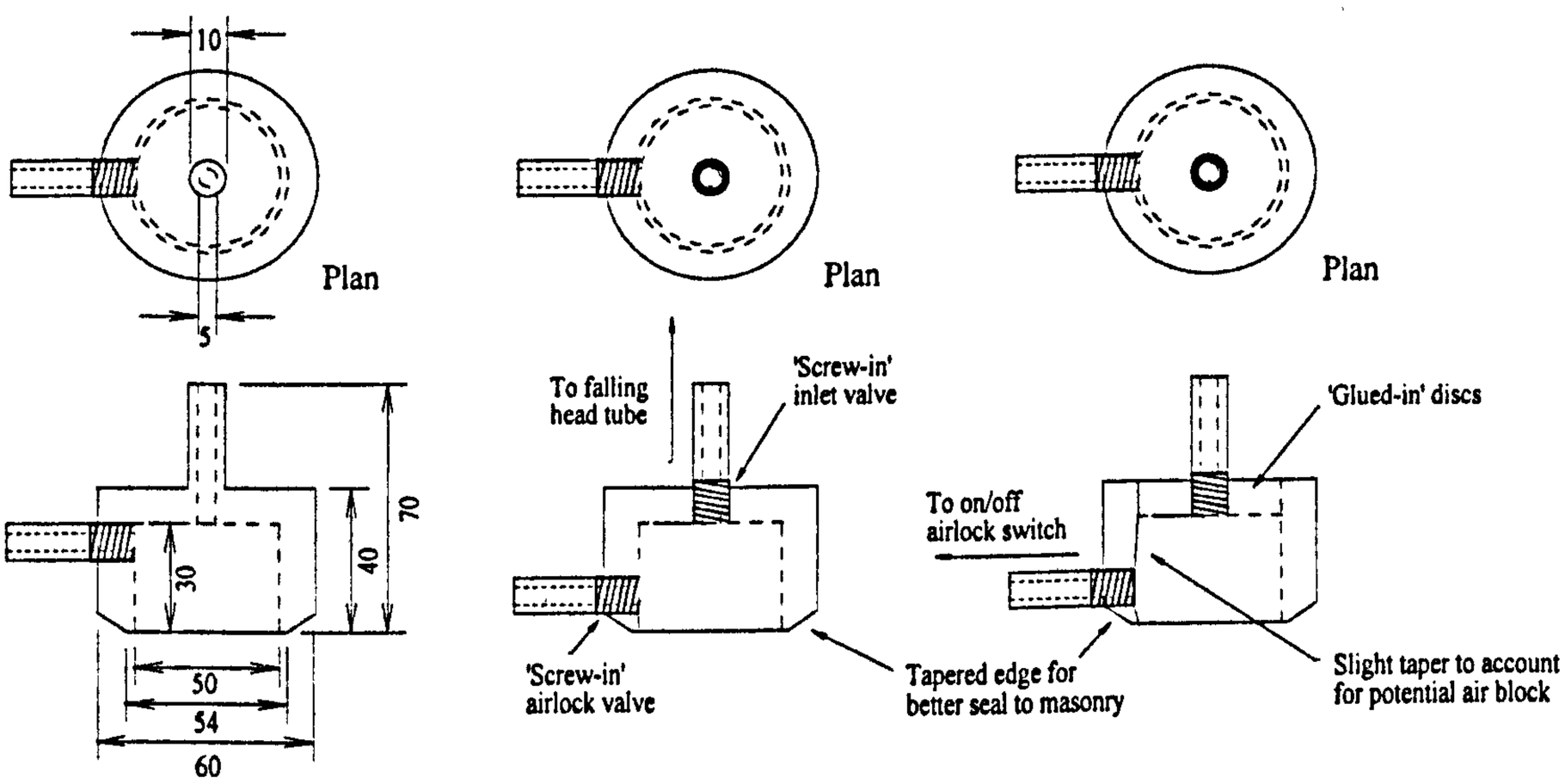

Fig. 4.1 Development of permeameters during testing

Figure 4.2 shows a range of permeameter types attached to Type 4 test panels.

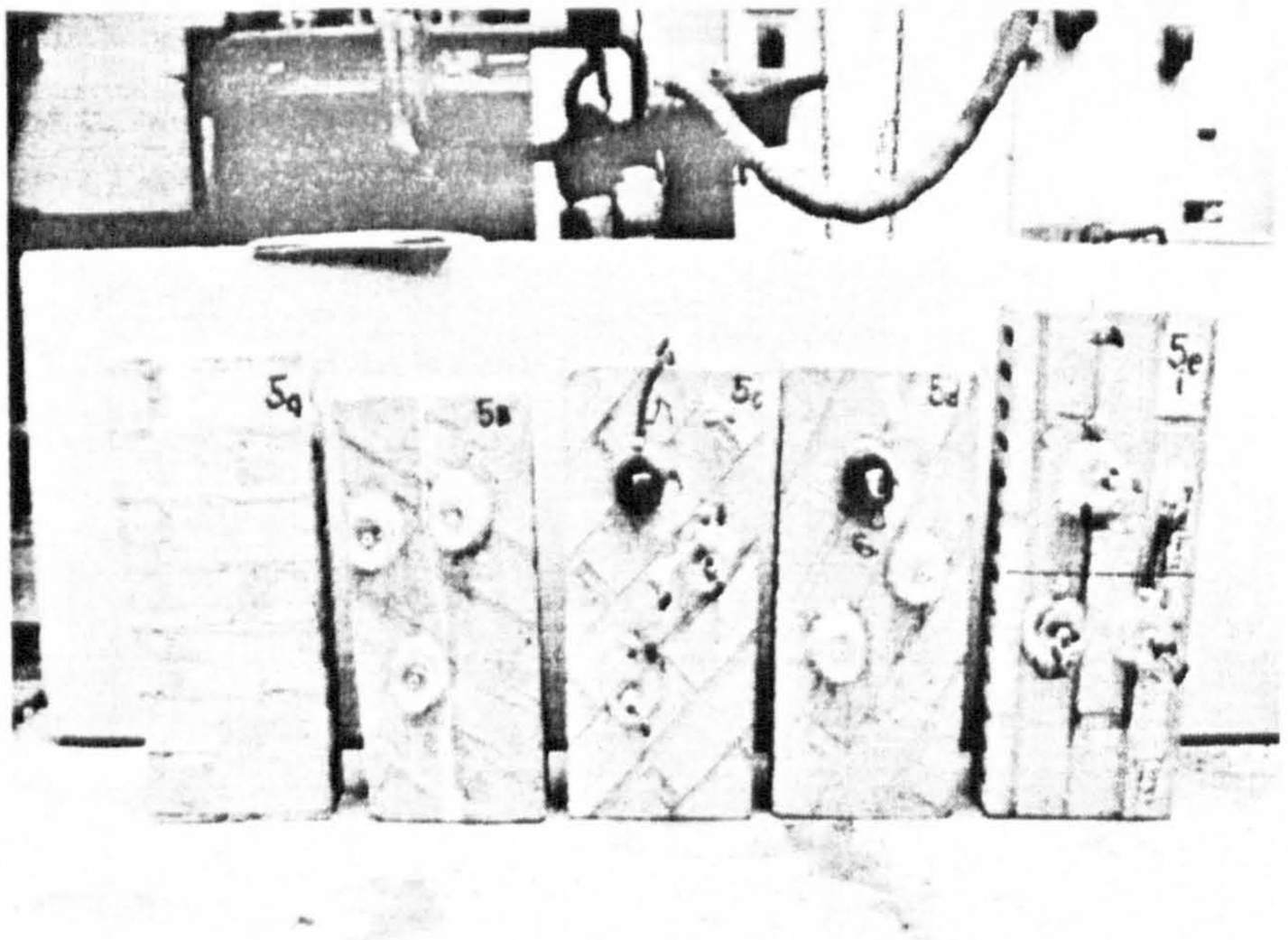

Fig. 4.2 Typical permeameters attached to Type 4 test panels

4.3 Permeameter Attachment

Three permeameters were attached to each wall. These were situated at distinct mortar joints on the panel and were at a horizontal bed (Joint 1), a vertical bed (Joint 2) and the cross over position of both (Joint 3) (Fig. 4.3).

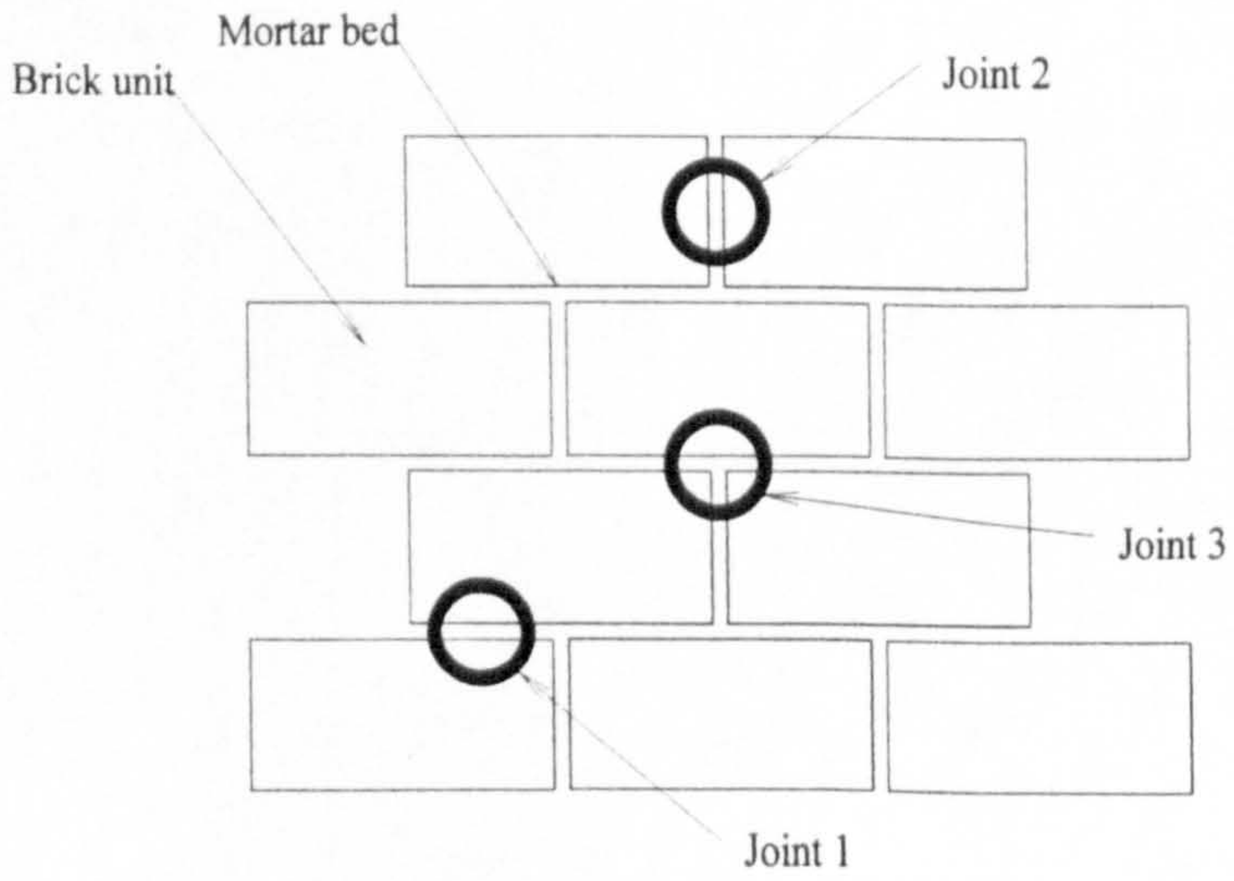

Fig. 4.3 Typical permeameter positions on masonry test panel

The permeameters were placed as close as possible to the centre of the masonry panel and always positioned, where possible, one brick course apart to avoid any water ingress interaction.

Permeameters were attached to panels using RS 550-230, a commercially available silicone rubber sealant.

Airlock valves were generally screwed into position. The threads for these valves were covered in PTFE tape to ensure a watertight seal. In a relatively few cases, the airlock valve was glued into position and sealed using the silicone rubber sealant.

The airlock valve was 105mm high from the top of the permeameter. Once this valve was open and air escaped, water was allowed to rise to a height of 100mm before the valve was closed. Sealing around the airlock valve using PTFE tape and jubilee clips prevented further air escape.

4.4 Procedure for Testing Using Permeameters

Time taken for the removal of the test panel from the oven to time of test via fabrication of permeameters and load to be applied would be the same for all panels (approximately 1hr). This would allow any thermal movements to be accommodated within results.

Four initial falling water heads were chosen for full scale masonry panel testing. An initial head of 200mm was chosen to match any possible ISAT values. A final head of 1500mm was chosen as this would be the worst possible case within a weather driven scenario and would also give good and concise results over a relatively short space of time. The 600mm and 1000mm heads were chosen as they would indicate any potential trends developing within the characteristics of water ingress dependant upon the applied pressure head.

Once a wall and its attached permeameters had been removed from the oven and fabricated with any inlet and/or airlock valves required, the permeameters were attached to plastic tubes that acted as the reservoir for the falling head. These plastic tubes had an internal diameter of 10mm and therefore allowed the volume of water ingress to be calculated. The volume of ingress (within a given time) would be the fall in head in the test reservoir multiplied by its face area.

Water in these tubes were checked for airlocks and bubbles. Any bubbles were tapped and squeezed until the tube was clear. Evaporation from these tubes was controlled by placing a spot of oil on its surface. However with a relatively small surface area and the short period of test time, it was felt that evaporation effects could be neglected.

Originally methylene blue dye powder was used to make the falling head easier to identify through the tubing. However, some permeameters had been removed after early testing and deposits were found which may have clogged pores and restricted crack widths. The use of dye powder was therefore discontinued.

Once the inlet valve was switched on, the falling head was measured at 0.25, 0.5, 0.75, 1.0, 1.25, 1.5, 1.75, 2.0, 2.5, 3.0, 3.5, 4.0, 5.0, 10, 20, 30, 45 and 60mins or until there was no change in water level. This enabled the volume of water ingress to be measured with respect to time.

The changes in falling head during testing was noted on the tubing using a wipe clean marker. Notes were also taken of the head at 15secs, height in the airlock and any areas of leakage around the permeameter. Figure 4.4 shows a typical falling head test arrangement.

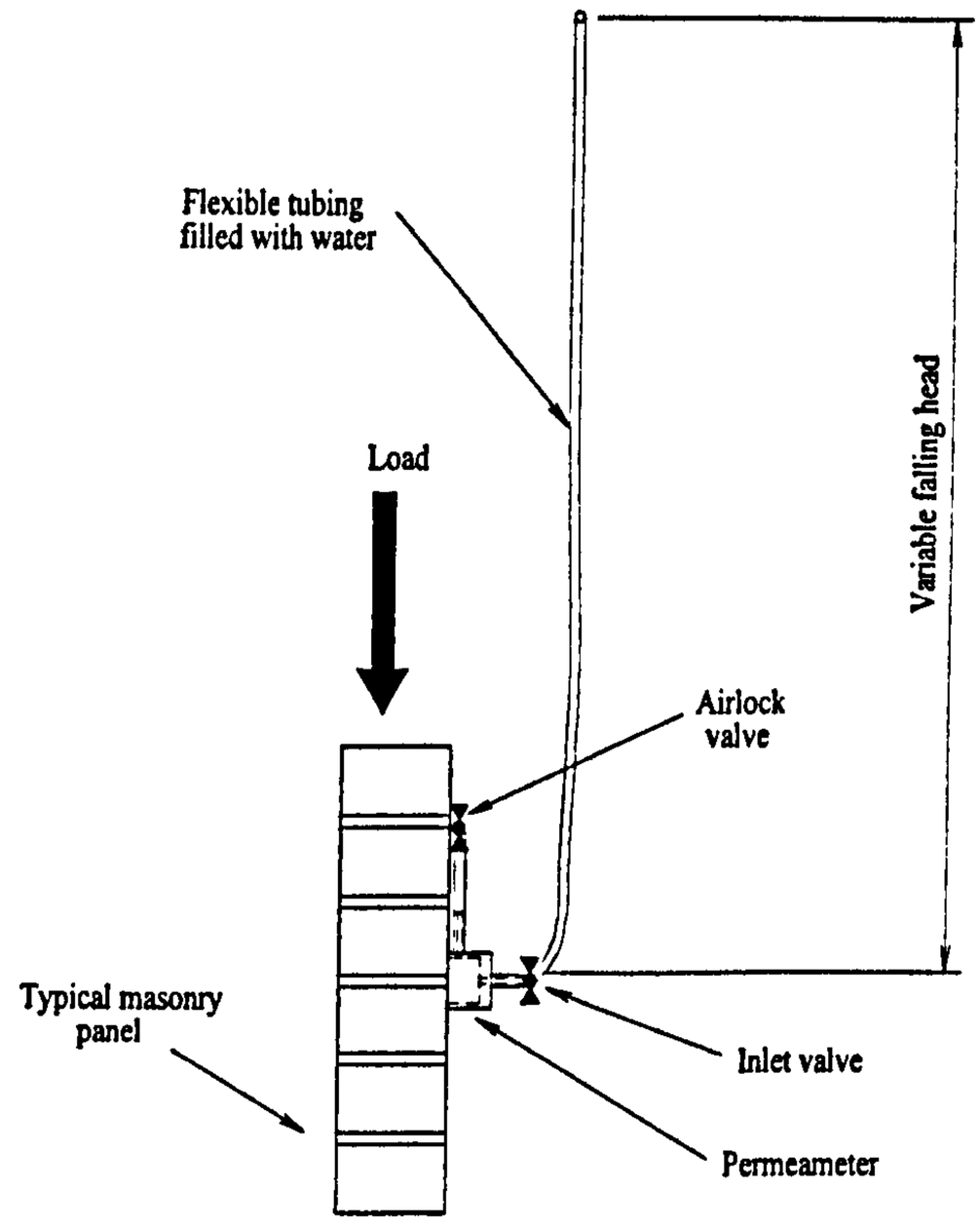

Fig. 4.4 Typical falling head test for measuring water ingress rates using a permeameter

A 'background' permeameter test was undertaken for each joint position (Fig. 4.3) at the four initial head levels for all panels when unstressed. This allowed an ingress datum to be set by which the effect of stressing a panels can be gauged by any subsequent increase or decrease in water ingress rates.

If during testing the permeameter or sealant surround exhibited water leakage then the test was immediately discontinued, a note made of the points of leakage and the test re-programmed for 24hrs later.

Figure 4.5 shows a summary of the test technique for measuring water ingress into a masonry panel.

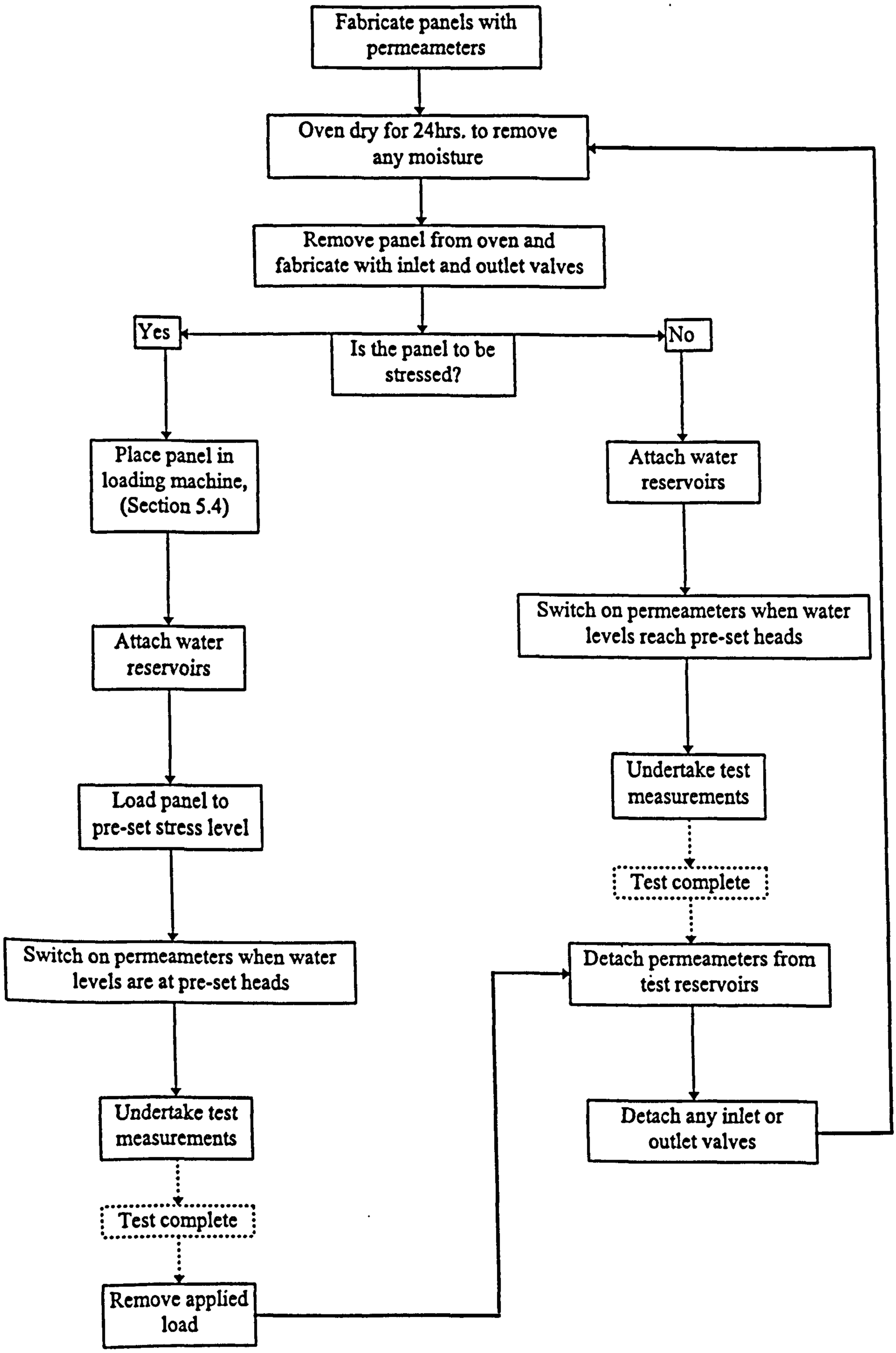

Fig. 4.5 Summary of test technique for measuring water ingress into a masonry panel

4.5 Testing of Bricks and Mortars Using Permeameters

Initially it was envisioned that mortar and brick type would play a large part in governing water ingress. Results from Chapter 3 showed that mortar tended to behave relatively similarly irrespective of its constituent materials. Clay based bricks showed roughly the same absorption rate though can be considered more influential as they are likely to control the bond strength.

The water ingress rates for brick and mortar was determined under varying initial heads using the permeameter technique. The data gathered would also allow comparisons to be made with full scale masonry tests. Five bricks per type and five mortar cubes per mix were used as the test sample size.

4.5.1 Permeameter assessment - brick

Figure 4.6 shows the average ingress rates for each brick type at all test heads of water.

These relationships show clearly that there is little water ingress over time for all initial test heads. The clay bricks (Types 2, 3 and 4) appear almost impermeable to water ingress. Type 1 (calcium silicate) bricks perform poorly due to their constituent materials and relative density. It should be noted that Type 1 bricks do not have a glassy face like many of the oven fired clay bricks which aid the resistance to water penetration.

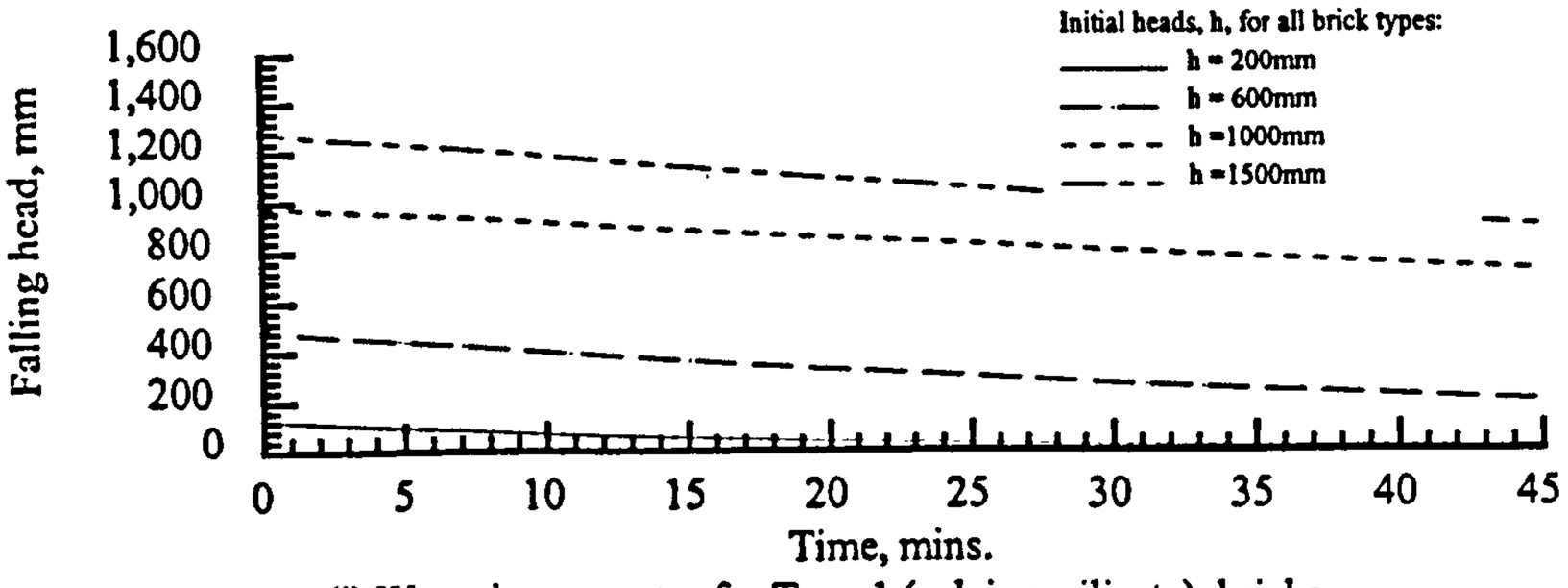

(i) Water ingress rates for Type 1 (calcium silicate) bricks

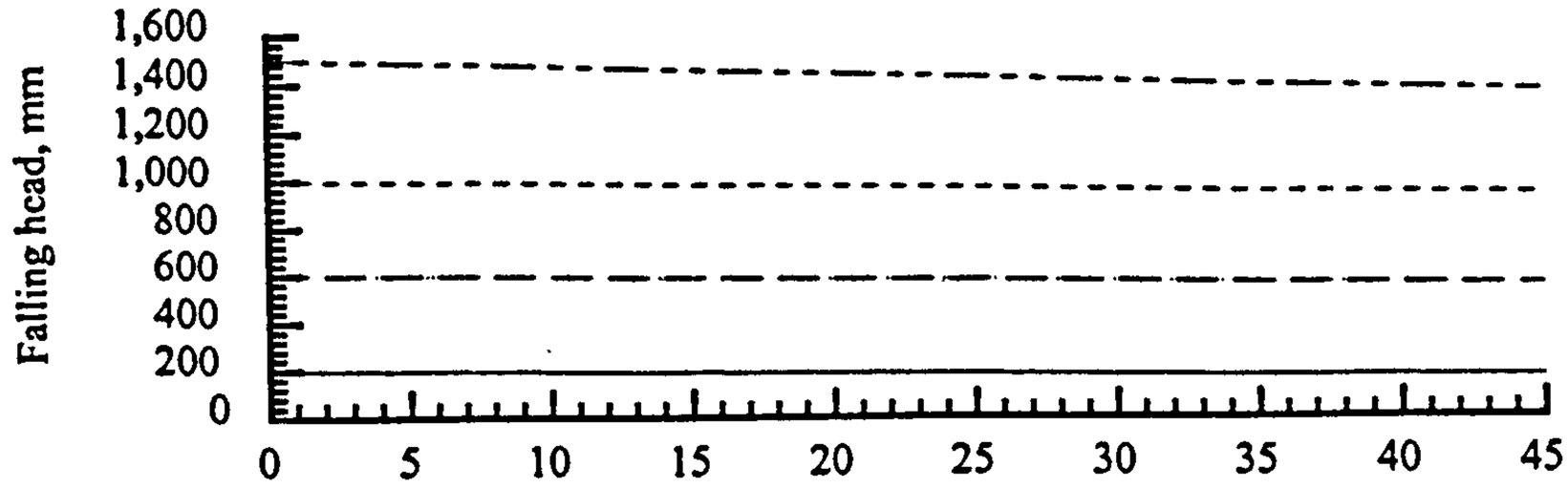

(ii) Water ingress rates for Type 2 bricks

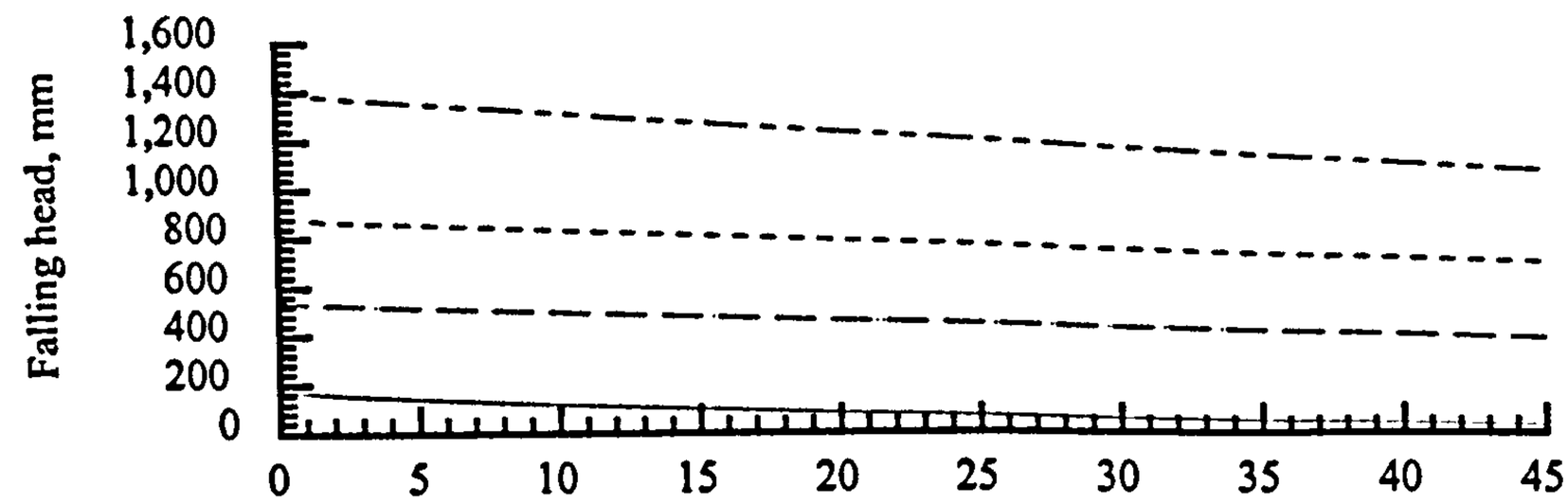

(iii) Water ingress rates for Type 3 bricks

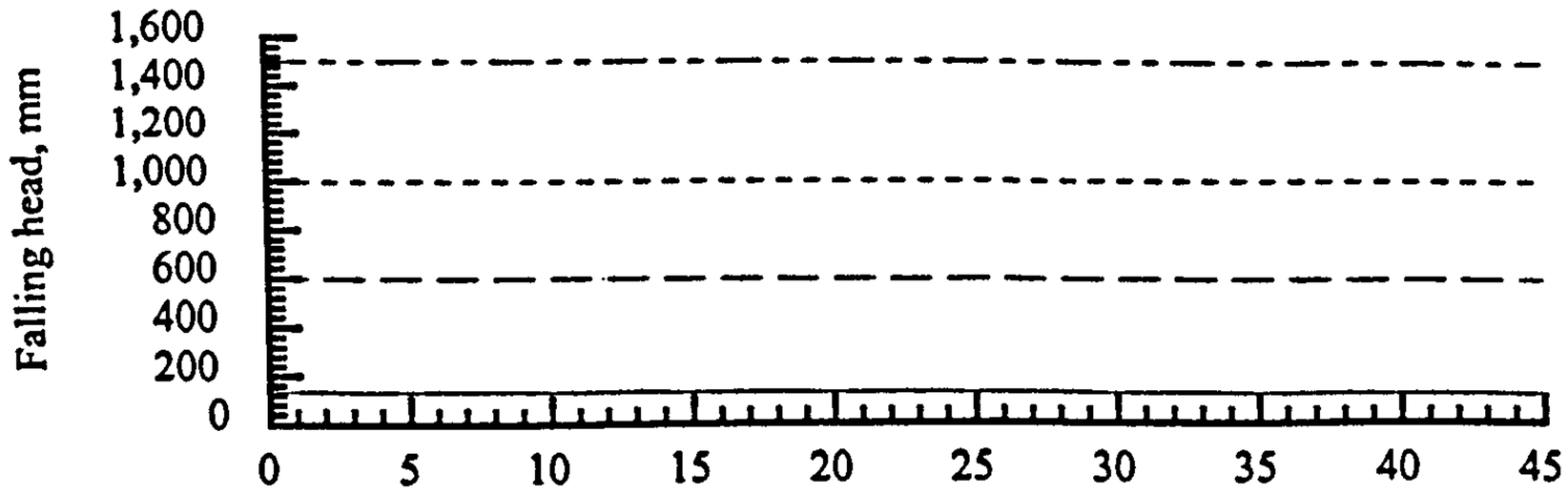

(iv) Water ingress rates for Type 4 bricks

Fig. 4.6 (i-iv) Water ingress rates for Type 1-4 bricks for all initial water heads

Table 4.1 shows the average decay best-fit curves based on experimental results for all brick types at all heads. These decay relationships were calculated using Microsoft Excel.

Table 4.1 Water ingress curves for test bricks

Initial head, h (mm)	Type 1	Type 2	Type 3	Type 4
200	$y = 128e^{-0.0610t}$	$y = 200e^{-0.0038t}$	$y = 172e^{-0.0383t}$	$y = 136e^{-0\ 0036t}$
600	$y = 486e^{-0.0198t}$	$y = 600e^{-0.0019t}$	$y = 534e^{-0.0074t}$	$y = 598e^{-0\ 0009t}$
1000	$y = 980e^{-0.0068t}$	$y = 1000e^{-0.0016t}$	$y = 877e^{-0\ 0053t}$	$y = 996e^{-0.0005t}$
1500	$y = 1280e^{-0\ 0079t}$	$y = 1500e^{-0.0022t}$	$y = 1391e^{-0.0059t}$	$y = 1500e^{-0.0005t}$

y - head in reservoir
t - time from commencement of test

Absorption rates for clay bricks (Table 3.8) showed similar average results for Type 2 and 4 bricks, with Type 3 bricks having the lowest value. In terms of water ingress using the permeameter technique, brick Types 2 and 4 have broadly similar rates with Type 3 bricks now having the quickest of the absorption rates. However due to the differing test time, technique and sample size no real comparisons can be drawn.

These results were helpful however when full scale testing was undertaken on masonry panels indicating that very little water will ingress through the brick alone.

4.5.2 Permeameter assessment - mortar

Figure 4.7 shows the relative ingress rates for each mortar type at all initial water heads.

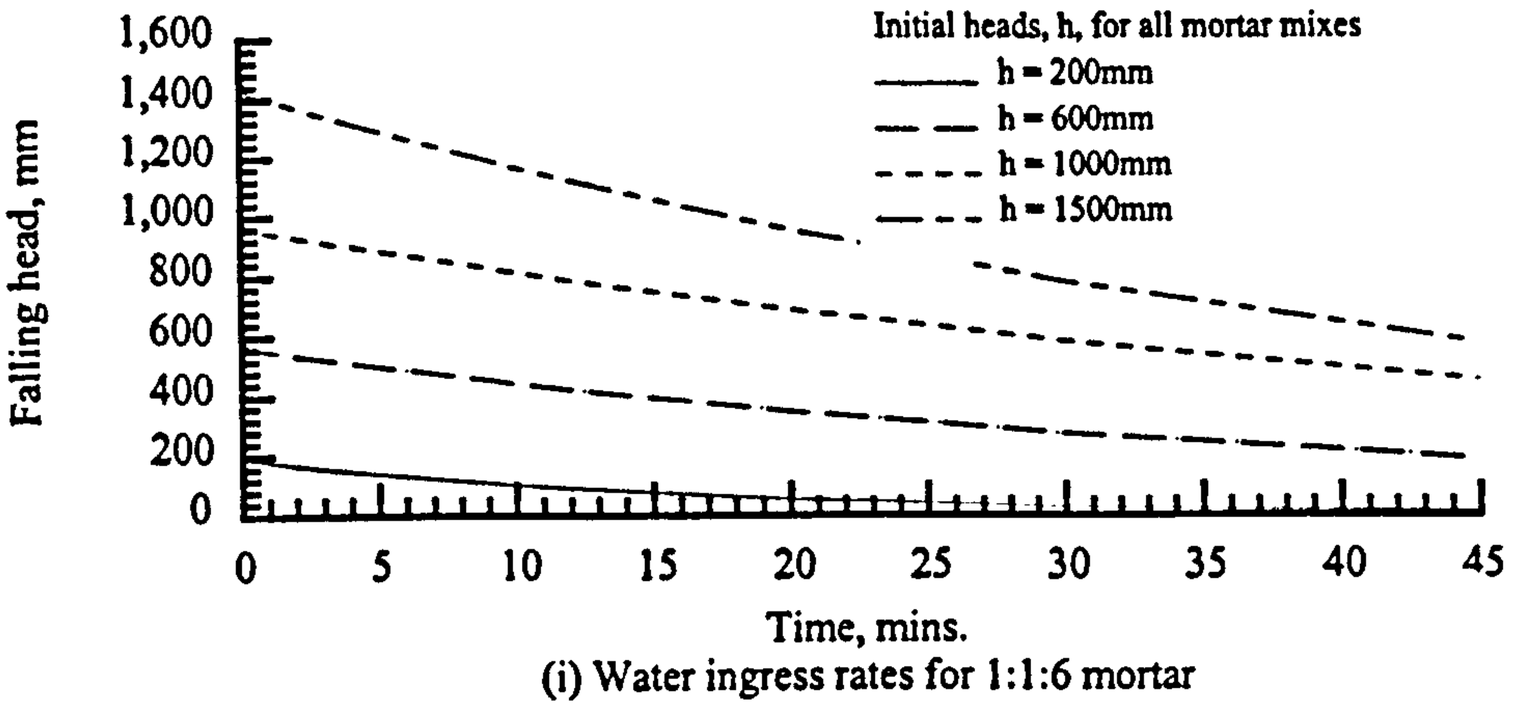

(i) Water ingress rates for 1:1:6 mortar

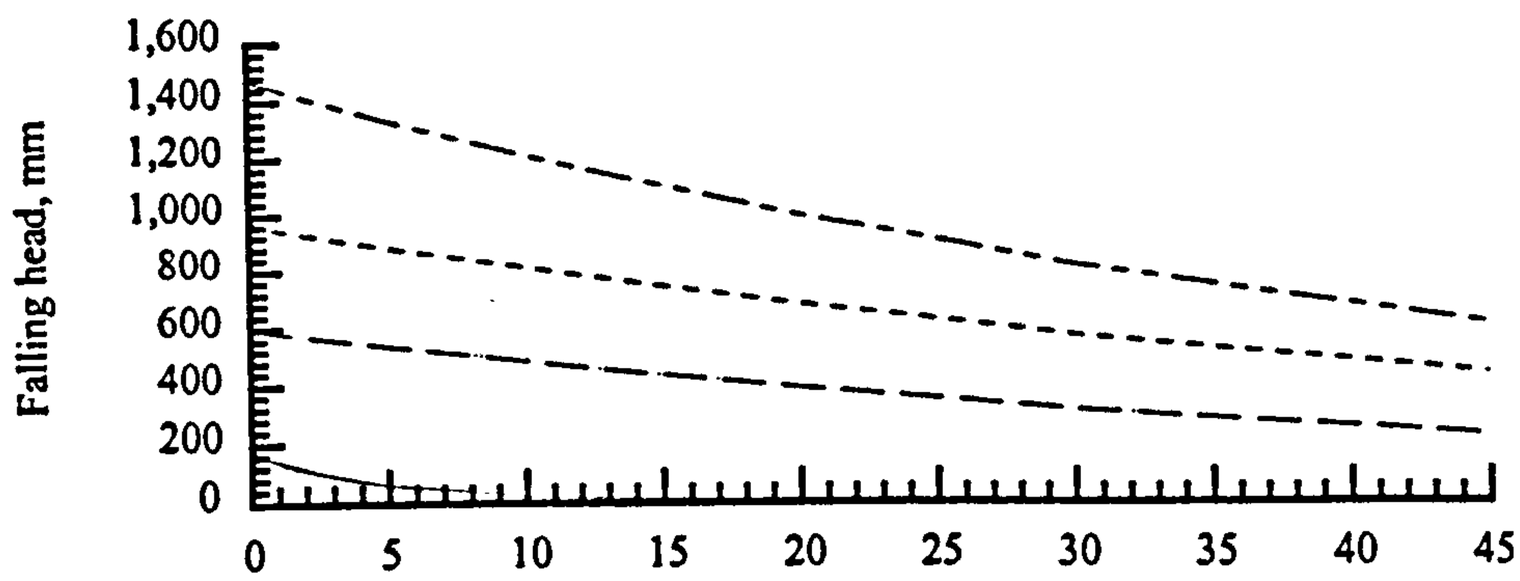

(ii) Water ingress rates for 1:1/2:5 mortar

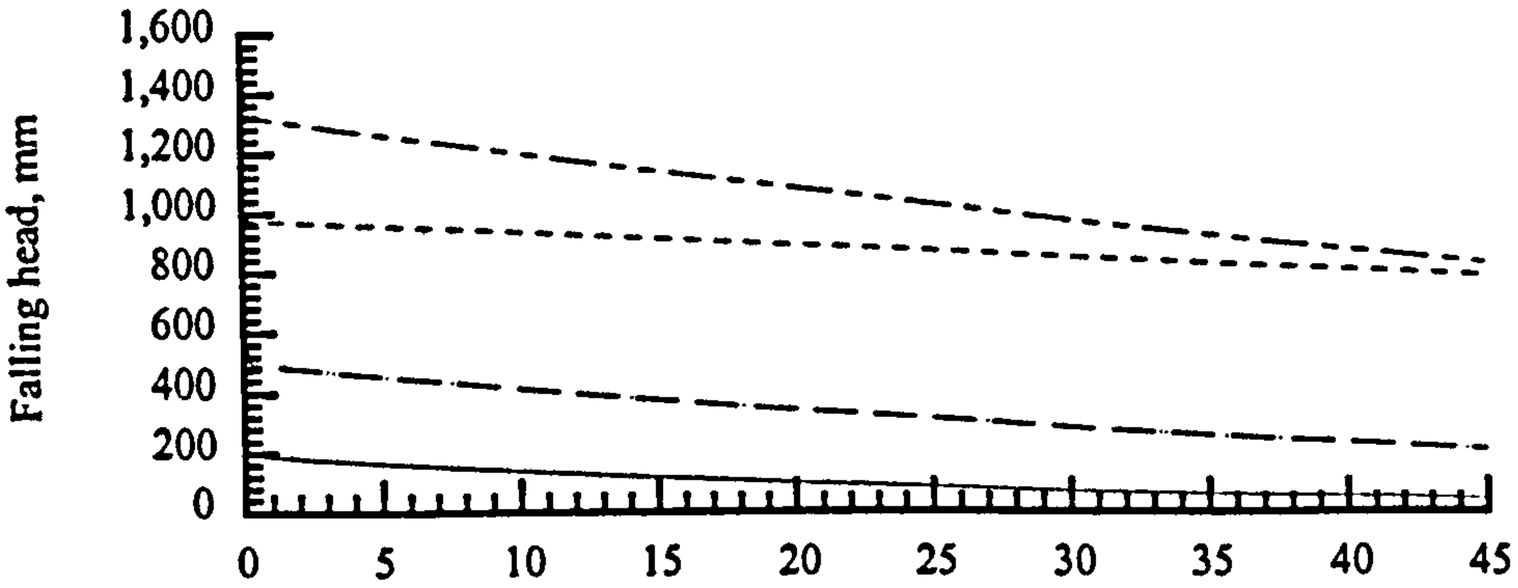

(iii) Water ingress rates for 1:1/4:3 mortar

Fig. 4.7 (i-iii) Water ingress rates for all mortar types

The water ingress rates exhibited are quicker than that of brick due to the variability of mortar. It may be concluded that as the best-fit decay equations (Table 4.2) were broadly similar for all mixes then the mortars tested had no real influence in governing water ingress.

Table 4.2 shows these best-fit decay curves for all mortar mixes at all heads.

Table 4.2 Water ingress curves for mortar cubes

Initial head, h (mm)	1:1:6	1:$^1/_2$:5	1:$^1/_4$:3
200	$y = 194e^{-0.0633t}$	$y = 171e^{-0\ 0204t}$	$y = 196e^{-0\ 0350t}$
600	$y = 566e^{-0.0242t}$	$y = 599e^{-0.0216t}$	$y = 500e^{-0\ 0194t}$
1000	$y = 920e^{-0.0166t}$	$y = 964e^{-0\ 0174t}$	$y = 975e^{-0.0049t}$
1500	$y = 1427e^{-0.0200t}$	$y = 1471e^{-0\ 0195t}$	$y = 1325e^{-0\ 0106t}$

y - head in reservoir
t - time from commencement of test

The decay curves in Table 4.2 show that ingress rates are quicker than that of brick, approximately by a factor of 10.

4.6 Conclusions

This chapter showed the development of an adaptable, easy to use permeameter that produced concise results and can be used repeatedly.

From the experimental investigations carried out in this chapter a number of conclusions can be drawn.

- Tests on brick and mortar using permeameters showed that clay bricks (Types 2-4) exhibited similar water ingress results and were much less encouraging of water ingress than calcium silicate bricks (Type 1).

- Permeameter testing indicated that water ingress rates were broadly similar for all mortar mixes irrespective of their mix constituents.

- Comparisons of results showed that water ingress rates for mortar were found to be quicker than that for clay bricks, approximately by a factor of 10.

Brick absorption is highly influential in governing brick/mortar bond and in creating fissures and cavities at the interface. The water ingress rates as indicated by the permeameters combined with results in Chapter 3, showed that the mortar types, irrespective of their constituent materials, behaved similarly in factors relating to water ingress.

Therefore only one mortar mix (1:$^1/_2$:5) was used in full scale masonry panel tests. All brick types indicated within this chapter were used.

CHAPTER 5

INSTRUMENTATION AND PRELIMINARY TESTING FOR THE ULTIMATE STRENGTH OF MASONRY PANELS

5.1 Introduction

Panels were initially tested to observe the behaviour of masonry as it was loaded and particularly as it approached an ultimate failure load. Using these panels, the influence of bed orientation was investigated.

The permeameter testing technique was used to study the effect of applied stress, water head, joint position and bed orientation on water ingress into masonry panels.

This chapter discusses the development of the masonry test panels and the accompanying preliminary tests. Positions of permeameters and demec points are also indicated for all test panels.

5.2 Details of Test Panels

Forty-seven panels were constructed for testing. These were 7 Type 1 (calcium silicate), 8 Type 2, 16 Type 3 and 16 Type 4 panels. The specimen sizes were all approximately 550x505mm or $2^1/_2$ bricks wide by 7 courses high prior to panels being cut to variable bed orientations. The cut panels had a height to width ratio of 2:1.

The mason was instructed to build according to his normal practice although special emphasis was undertaken in ensuring that specimens were built plumb. The panels were built on small plywood plinths, the bricks being bedded on top of this by mortar. As noted in both Chapters 3 and 4, a mortar mix of $1:^1/_2:5$ was used in all panels.

After these panels were built they were covered in polythene and left to cure for 7 days after which the polythene was removed and the panels were further allowed to cure in the laboratory until time of test.

5.3 Specimen Preparation

It is rare that walls are only loaded perpendicular to their horizontal beds. Wind loads, raking forces and a variety of dead or live loads can transmit their stress through masonry at a variety of angles. To assess the importance of the applied stress at an angle to the horizontal bed and its effect on the rate of water ingress, a variety of specimens were cut to a required shape.

Masonry panels were therefore cut to pre-defined angles of 0°, 30°, 45°, 60° and 90° with reference to the horizontal bed joint, i.e. 0° (Fig. 5.1).

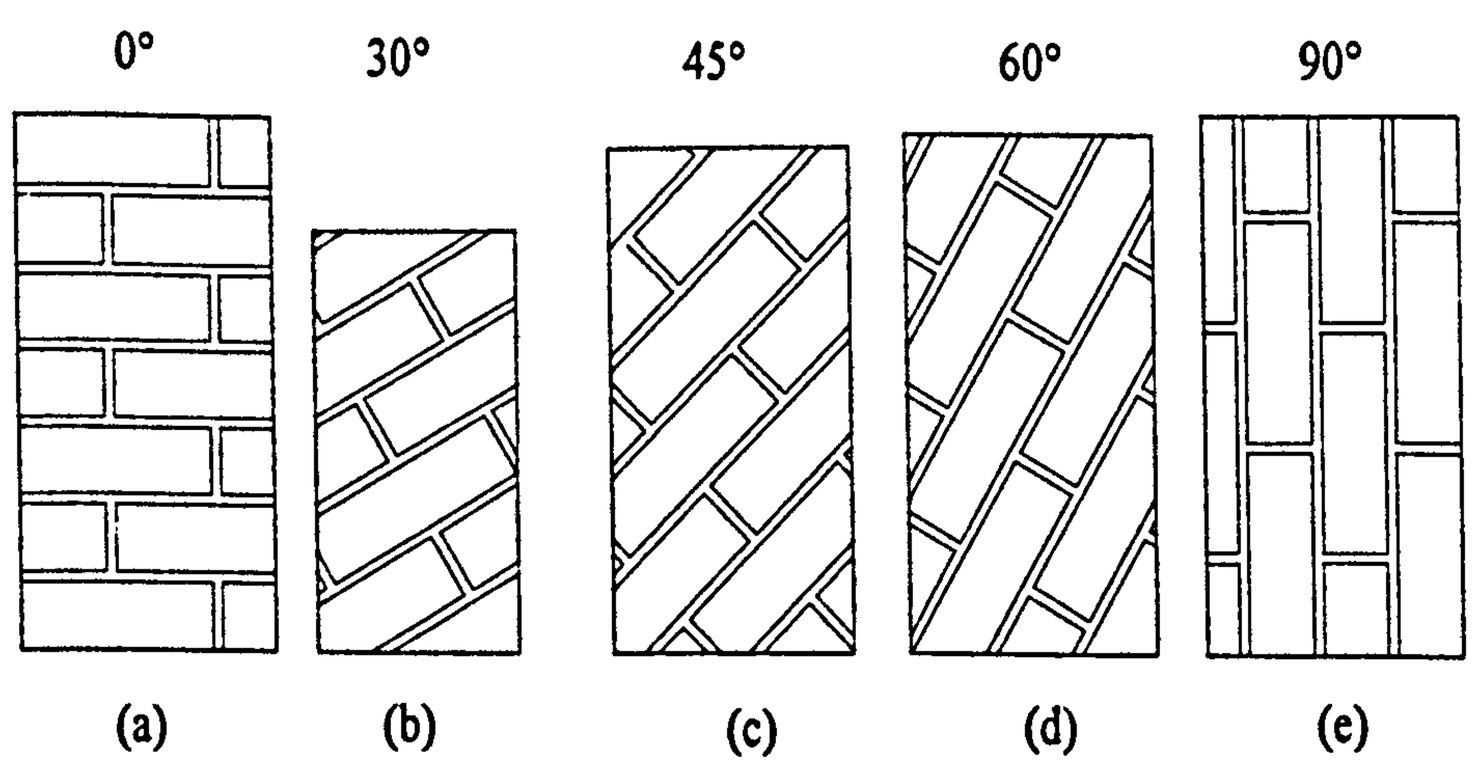

Fig. 5.1 Typical wall cut angles: 0°, 30°, 45°, 60° and 90° to original bed angle

To assess if any microcracking had occurred during cutting to these bed orientations, demec buttons were attached across mortar joints and measured before and after cutting. Initially, there were very slight differences in readings. This was probably caused by the coolant water from the saw causing the brick and mortar to expand. After the panels dried no differences in demec readings was recorded.

5.4 Experimental Testing of Masonry Panels

(a) Loading of test panels:

Prior to loading of any masonry panel, each was capped at both bottom and top with 1-2mm layer of dental plaster followed by a 10mm thick steel spreader plate.

The loading frame used during testing was an Avery-Dennison hydraulic rig of 1000kN (100 Tonne) capacity. The frame is controlled by a microcomputer which allowed the rate of load increase to be specified in either load or extension terms. Pauses in load application could be pre-set to allow strain measurements to be taken.

Loading of the test panels to failure followed closely the procedure in BS 1881: Part 121: 1983 [132].

Initially a basic stress (σ_b) of 0.5N/mm^2 was applied. The load was then increased at a constant rate of 0.6N/mm^2/s until the designated load level of $F_w/3$ was reached, where F_w is the predicted panel failure load. The loading remained constant at $F_w/3$ then reduced until σ_b was reached. This cycle was repeated twice. After these cycles were completed test panels were loaded to failure.

If a measurement for water ingress under load was to be made, then the load was increased from σ_b to a predetermined percentage of the predicted failure load without any cyclic loading. For all water ingress tests the predetermined test levels were at 0.3, 0.45 and 0.6 of the ultimate failure strength (f_{ult}) of the panel.

Demec readings were taken at regular intervals during both the cyclic loading and when loading remained constant. This allowed the crack development across the mortar bed joint or vertical (perpend) joint to be assessed. Strain was also measured parallel to the load direction irrespective of bed orientation.

(b) Ultimate failure load of masonry panel (F_{ult}):

Once the masonry panels had been cut to their pre-defined dimensions and orientation, an assessment of the ultimate failure strength (F_{ult}) was made.

Experimental panels were assessed in conjunction with Hendry's empirical equation for predicting ultimate panel failure stress (f) with a bed orientation of $\theta=0°$ [113]:

$$f = 1.242 f_b^{0.531} f_{cu(m)}^{0.208} \qquad \text{Eqn. 5.1}$$

$f_{cu(m)}$ - cube crushing stress of mortar, (Table 3.6, Chapter 3)

f_b - ultimate compressive strength of brick, (Table 3.8, Chapter 3)

Note: Eqn. 5.1 is only suitable for masonry of thickness 102.5mm

Table 5.1 shows the relationship between actual and predicted failure loads using Eqn. 5.1.

Table 5.1 Actual and predicted failure loads for masonry under uniaxial compression

Brick type	Actual failure load, F_{ult} (kN)	Predicted failure load* (kN)
Type 1	224	325
Type 2	545	524
Type 3	430	619
Type 4	561	565

* see Eqn. 5.1

The predicted failure loads for masonry panel were generally higher than actual values though Type 2 and 4 panel results showed good agreement. Differences may be caused by variability in the brick and mortar, together with possible eccentricities built within the panel and poor workmanship.

This empirical formula may only be appropriate for clay bricks. Type 1 (calcium silicate) panels can be deemed unsuitable for this equation as seen by the large discrepancy between predicted and actual values.

The relationships between the ultimate failure load (F_{ult}) and bed orientation for the tested panel specimens is shown in Fig. 5.2.

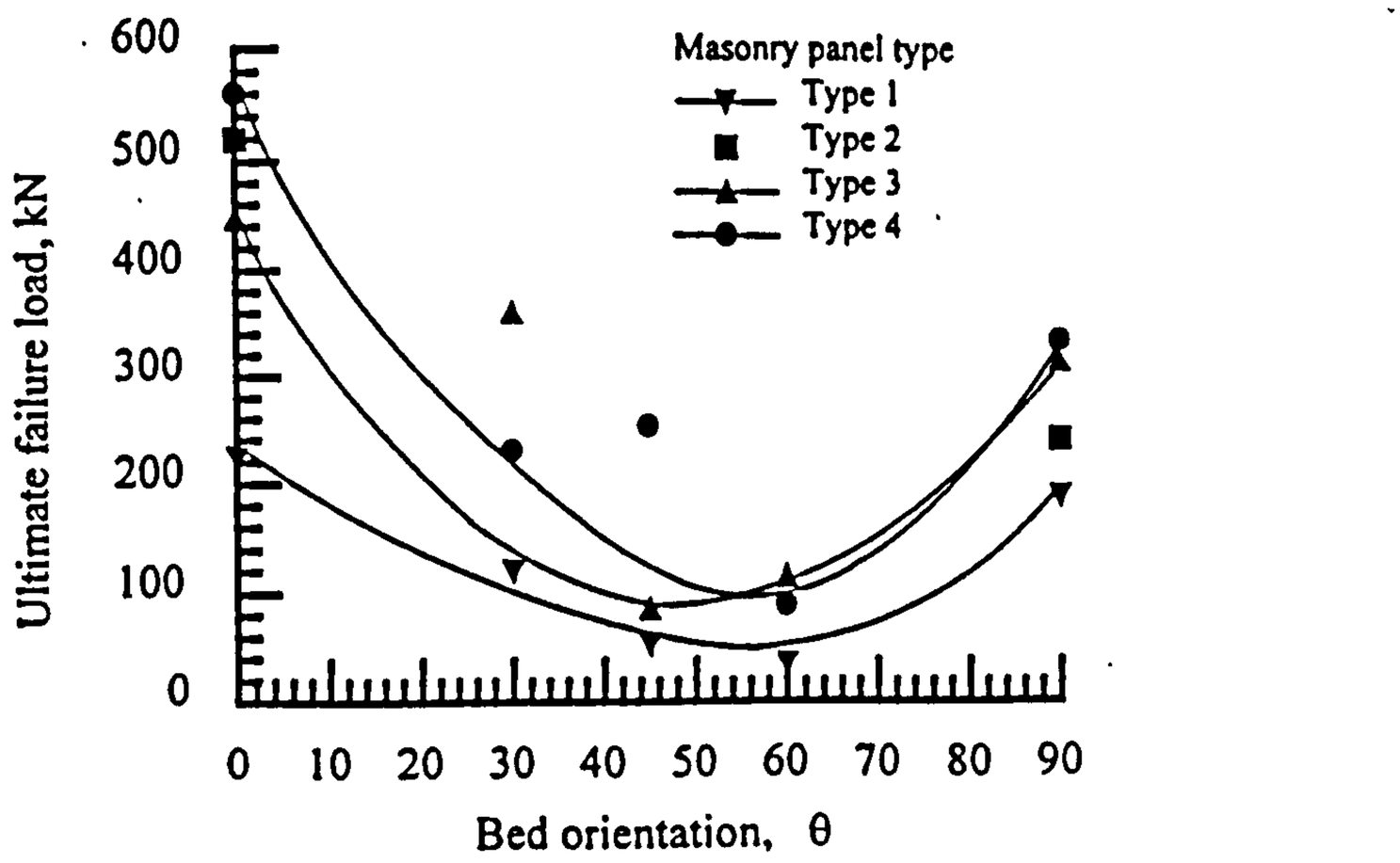

Fig. 5.2 Effect of principal stress angle on the compressive capacity of a masonry panel

This relationship showed that as the bed angle increased then the ultimate failure load decreased. This is true for all panel types. However, due to the inherently large variability in brick/mortar bond strengths it is likely that F_{ult} for Type 4 panel at 45° and Type 3 at 30° are higher than may be expected.

When the panels were orientated, failure occurred at the brick/mortar interface where the applied shear stress was greater than the bond strength between these materials. Generally the minimum failure load occurred when the bed orientation lay between 45° and 60°.

An increase in ultimate load was noted at higher bed orientations. Although major debonding occurred along the brick/mortar interfaces due to high tensile stresses, the bed orientation allowed the masonry panel to effectively act as a number of distinct columns which combined to carry load independently.

As bed orientation varied from θ=0° to θ=90° then a change in failure mode was recorded. The test panels were found to change from a compression form of failure at low bed orientations through a shear failure of combined tensile-compressive stresses before finally failing in pure tension at bed orientations, θ= 90°. Each form of failure exhibited unique cracking patterns (Fig. 5.3).

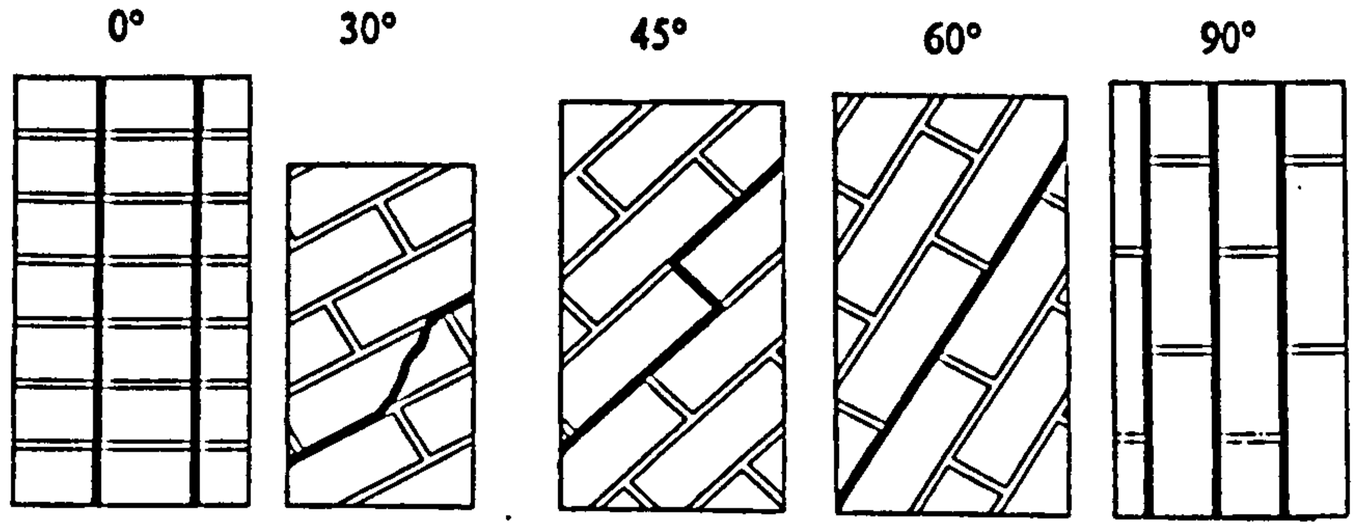

Fig. 5.3 Failure modes for test panel with variable bed orientations

Low bed orientated panels exhibited large vertical cracking through both mortar bed and brick before failure occurred. This progressed to a shear failure for higher bed orientations where the weakest brick/mortar bond was exploited to produce a 'sliding' failure along a bed. Finally large tensile cracks at the brick/mortar interface were produced at higher bed orientations before failure was reached.

The results exhibited for these test panels were similar to those of previous investigators [101-108].

5.5 Strain Measurement and Permeameter Positions on Test Panels

Strain had to be measured as quickly and efficiently as possible, as the specimens were under a load and being subjected to creep when these results were taken. The measurement technique would also have to consider the ease of installation, accuracy of readings and volume of strain measurements required.

Although wire resistance strain gauges were used successfully in the determination of elastic modulii for bricks and mortar (Chapter 3), due to their preparation and difficulty in attaching to masonry panels, their relative cost and their inability to measure strain across a joint, it was decided that strain measurement via demec buttons would be the most appropriate solution.

Demec buttons were used for all tests to measure the strain and hence potential crack development within test panels. These demec points were located at positions relative to the attached permeameter, allowing strain to be measured concomitantly with water ingress and were also used to provide an indication of any slippage across a mortar bed.

These strain buttons were positioned on the opposite face of the panel than that of the permeameter. Permeameters were positioned on panel faces that would most likely face an external environment. Most masonry panels had demec buttons orientated parallel and perpendicular to the particular joint that was considered for water ingress.

Figures 5.4-5.7 shows the demec button and permeameter arrangement for typical test panels.

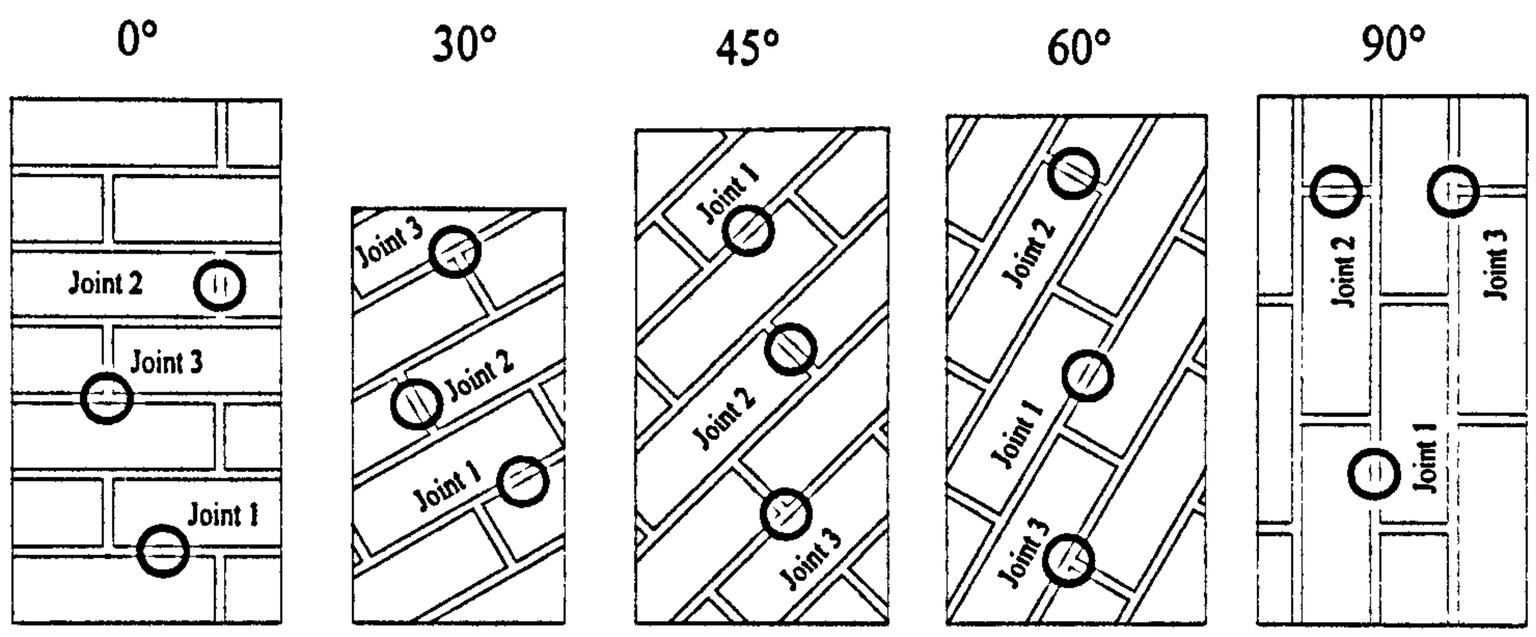

Fig. 5.4 Permeameter details for Type 1 (calcium silicate) panels

During testing it was found that Type 1 (calcium silicate) panels were particularly fragile and difficult to use as loaded test specimens. Full loading tests for Type 1 panels were stopped after some initial trials. However assessing water ingress for stressed masonry continued with other brick types. These are shown in Figs 5.5-5.7.

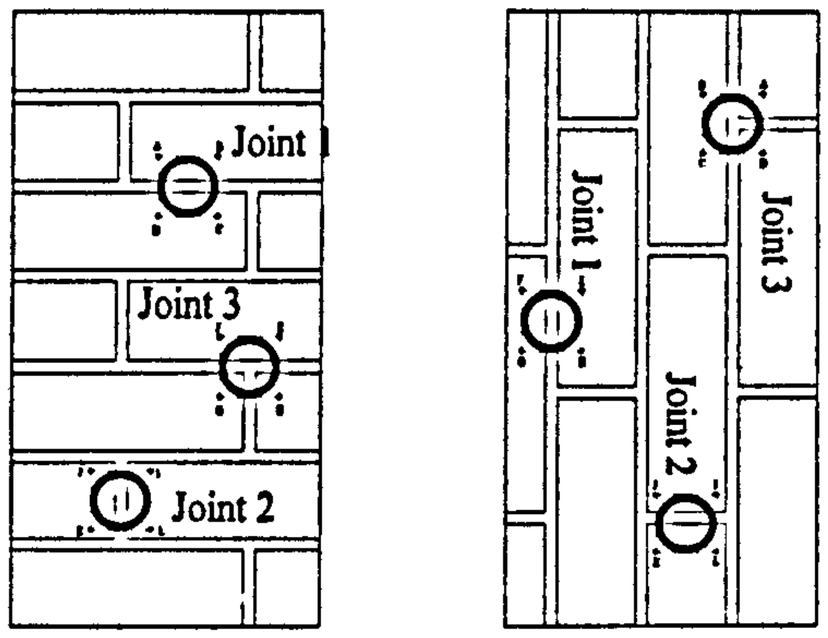

Fig. 5.5 Demec button locations and permeameter details for Type 2 panels

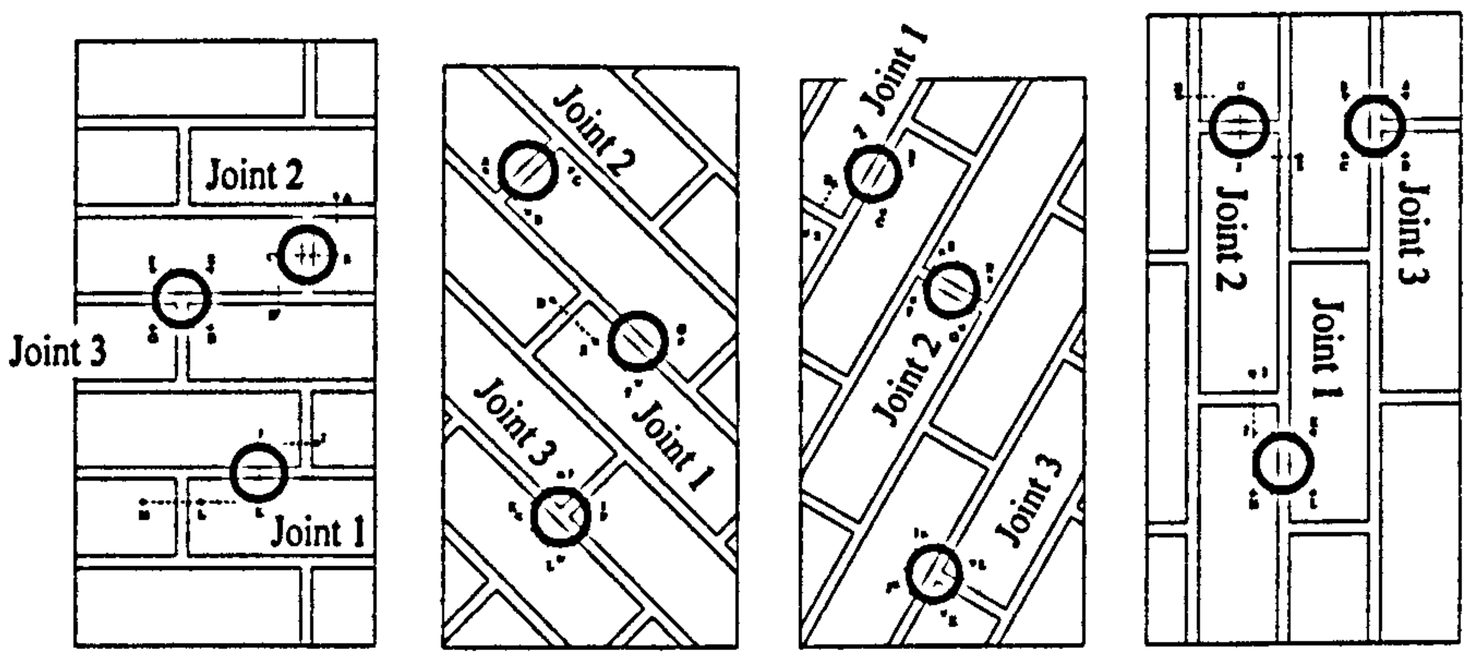

Fig. 5.6 Demec button locations and permeameter details for Type 3 panels

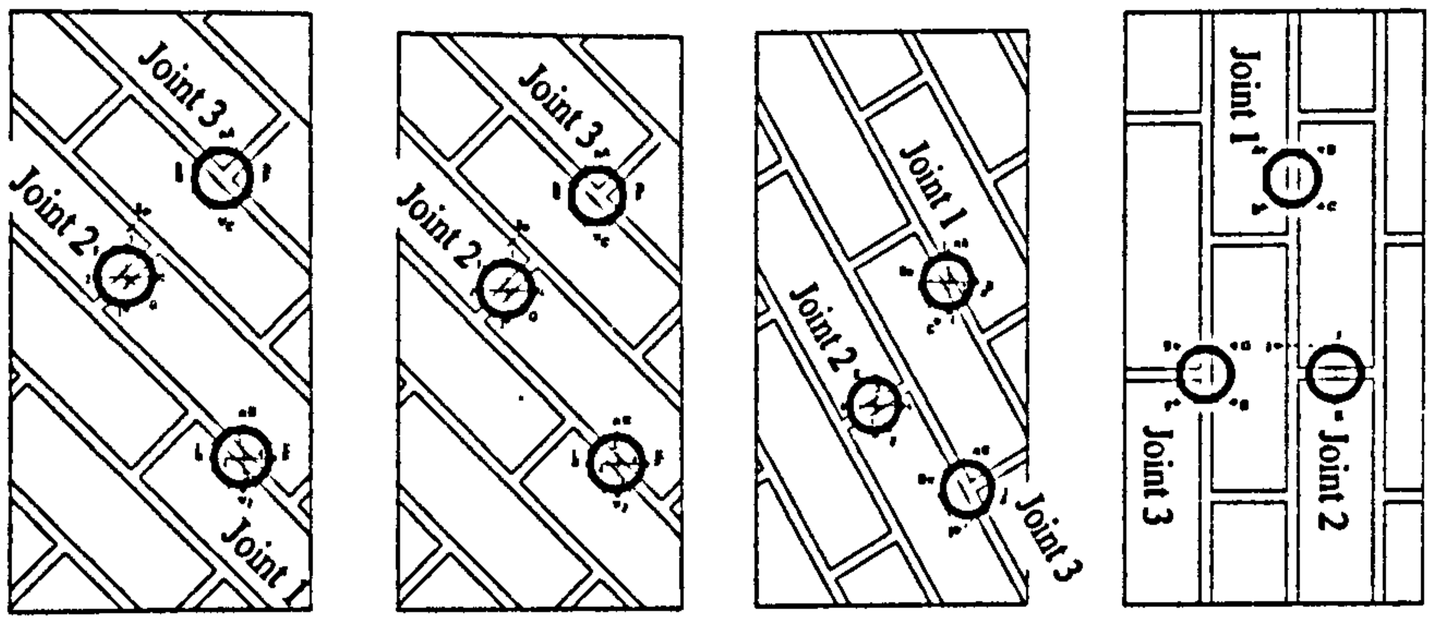

Fig. 5.7 Demec button locations and permeameter details for Type 4 panels

Type 4 test panels had demec buttons that allowed strain development to be measured both parallel and perpendicular to the applied load.

5.6 Conclusions

A number of sacrificial panels were used to build a picture of panel failure dependant upon bed orientation. Panels were found to undergo compression to combined tension-compression to total tension failure as bed orientation changed from $\theta=0°$ to $\theta=90°$. From panel testing it was found:

- When the bed angle of a masonry panel increased then the ultimate failure load decreased. The minimum failure load occurred for panels with bed orientations between 45° and 60°. Panels which exhibited greatest resistance to load were those with bed orientations of $\theta=0°$.

- Changes in bed orientation of the panels exhibited corresponding changes in their failure mode and crack development. Low bed orientated panels exhibited large vertical cracking through both mortar bed and brick prior to failure. Shear failure was exhibited for higher bed orientations where the weakest brick/mortar bond was exploited to produce sliding failure along a bed. Large tensile cracks at the brick/mortar interface were generated at higher bed orientations before failure was reached.

- Calcium silicate masonry panels were found to be fragile and difficult to use as loaded test specimens due to their relatively weak brick/mortar bond.

The panel failure loads and modes of failure gave a valuable indication of potential crack development. This was used to develop a stressing regime for individual panels that allowed water ingress to be measured at variable applied stress levels.

CHAPTER 6

WATER INGRESS CHARACTERISTICS FOR CONCENTRICALLY LOADED MASONRY PANELS

6.1 Introduction

The aim of this chapter is to assess the main factors that affect the deterioration of masonry and its susceptibility to water penetration. Forty-seven masonry panels were tested in order to assess the following:

- The effect of varying the initial water head on water penetration through stressed and unstressed masonry panels;

- The effect of applying different levels of vertical stress on water ingress through masonry;

- The influence of bed orientation on the failure mechanism of masonry under vertical stress and ultimately on the water ingress characteristics of masonry;

- Which mortar joints were prone to high levels of water penetration and hence likely to exhibit the most deterioration;

- Which brick panels were prone to increased water penetration under these variable conditions.

Using the new permeameter technique developed for and during the course of this experimental study, water ingress rates were measured to assess the effects of the above variables.

Masonry panels tested were identified in terms of their bed orientation, θ. These orientations were 0°, 30°, 45°, 60° and 90°, where θ represents the angle between the main mortar bed joint and the horizontal plane.

Water ingress into individual masonry panels was measured and identified at distinct joints. These joint positions were detailed in Fig. 4.2 and shown again here for information as Fig. 6.1.

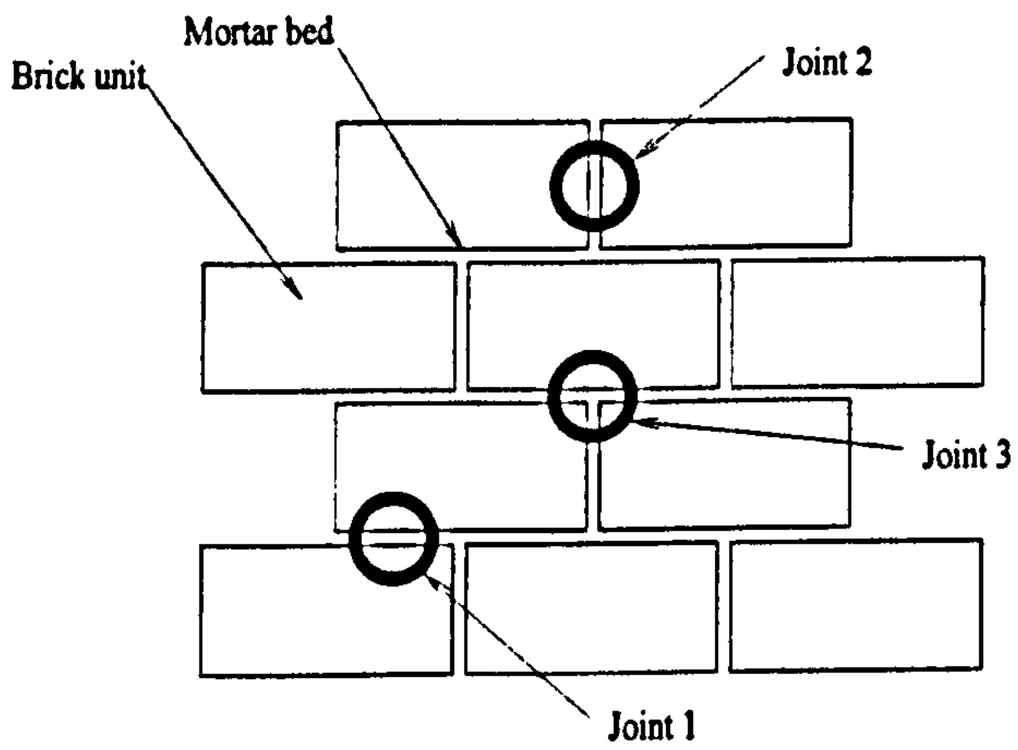

Fig. 6.1 Typical permeameter positions on masonry test panels

6.2 General Remarks on Tests and Measurements

Full details relating to test technique and the development of the permeameters can be consulted within Chapter 4. The salient points are presented here for discussion.

(a) Water ingress:

Water ingress into test panels was measured using permeameters at variable initial water heads. These were 200mm, 600mm, 1000mm and 1500mm. Ingress was indicated during the experimental investigation as the drop in water head within the test reservoir. This was converted to a volume of ingress by multiplying the head drop by the reservoir face area. For all tests, this area was based on a reservoir diameter of 10mm.

Generally, all tests had a large initial head drop in the test reservoir on immediate commencement of testing. This was caused by quick initial absorption, large cavities at the brick/mortar interface under consideration or 'settling' within the reservoir.

The initial volume of water required to give a pre-set initial head prior to the start of any test assumed a level surface between permeameter and masonry panel, Fig. 6.2(a). Due to the variability in constructing masonry panels, this level surface was difficult to achieve and so a difference or 'settling' was encountered between the initial assumption and actual condition, Fig. 6.2(b).

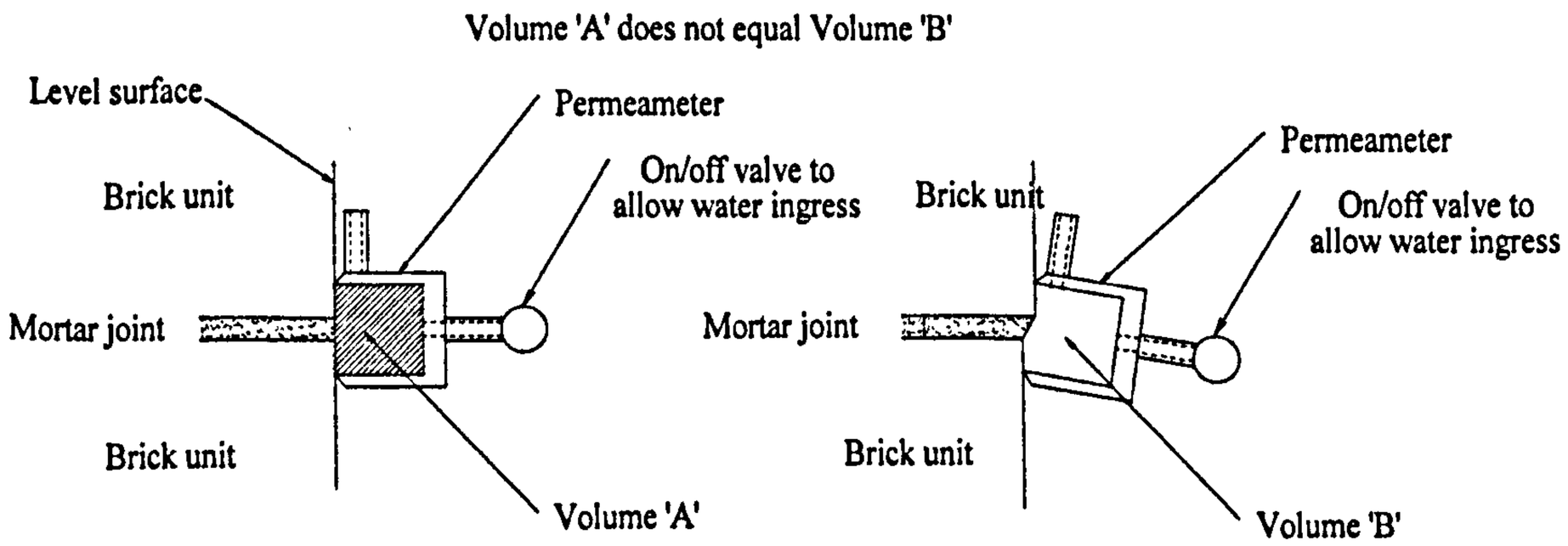

(a) Idealised attachment of permeameter to masonry panel

(b) Actual attachment of permeameter to masonry panel

Fig. 6.2 Idealisation of 'settling' effects encountered in permeameter attachment

These initial effects were considered consistent as results were compared using the same permeameter and joint position throughout the whole test programme. In most cases water ingress was assessed and used for comparison purposes when 'settling' effects were ignored. These settling effects were ignored after the initial 15secs of testing.

Due to the variability of a masonry panel, the measurement of water ingress could vary from almost instantaneous to a test which lasted longer than 24hrs due to the impermeability of a joints' position. Accordingly, ingress rates were recorded over differing test durations.

(b) Strain measurement:

Water ingress was measured at $0.0f_{ult}$, $0.3f_{ult}$, $0.45f_{ult}$ and $0.6f_{ult}$ where f_{ult} was a pre-determined ultimate failure stress as discussed in Chapter 5.

For simplification of results, only strain generated directly across mortar joints was presented in all figures. This strain was measured using demec gauges which were placed across a mortar joint but in effect measured any strain within the brick, mortar and any change at the interface. In effect, the strain measured was of a composite material.

At joint positions 1 and 2 (Fig. 6.1), this presented little problem. At Joint 3, the brick/mortar interface considered had both horizontal (main bed joint) and vertical (perpend joint) components. It was found that the strain across the main bed joint was more influential than that generated across the perpend joint. Therefore, where applicable for Joint 3, only strain generated across its main bed joint component would be presented in any relevant figures.

6.3 Water Ingress Characteristics when Bed Orientation, $\theta=0°$

For a panel with this bed orientation, the applied stress level would fundamentally control water ingress rates by its ability to open or close cavities at all brick/mortar interfaces. The loading of this type of panel allowed large compressive strains to be accommodated before vertical tensile cracks occurred which denoted the onset of structural failure.

6.3.1 Panel testing

Both Type 2 and 3 brick panels were used in this study. Type 2 panel (denoted as 2A) had a cross-section of 105x300mm and a predicted failure load (F_{ult}) of 541kN, corresponding to an ultimate stress level (f_{ult}) of 17.1N/mm^2. This allowed water ingress to be measured at 5.1N/mm^2 ($0.3f_{ult}$), 7.7N/mm^2 ($0.45f_{ult}$) and 10.3N/mm^2 ($0.6f_{ult}$). Similarly, the Type 3 panel (3A) had a cross section of 100x275mm and a predicted failure load of 430kN. This allowed water ingress rates to be measured when applied stress levels were 4.7N/mm^2 ($0.3f_{ult}$), 7.0N/mm^2 ($0.45f_{ult}$) and 9.4N/mm^2 ($0.6f_{ult}$).

Failure loads indicated for panels with bed orientation θ=0° and all subsequent panels with variable bed orientations was based on experimental assessment of sacrificial test panels as indicated in Chapter 5.

For information, the location of demec buttons to measure strain and permeameter positions on the test panels are shown in Fig. 6.3.

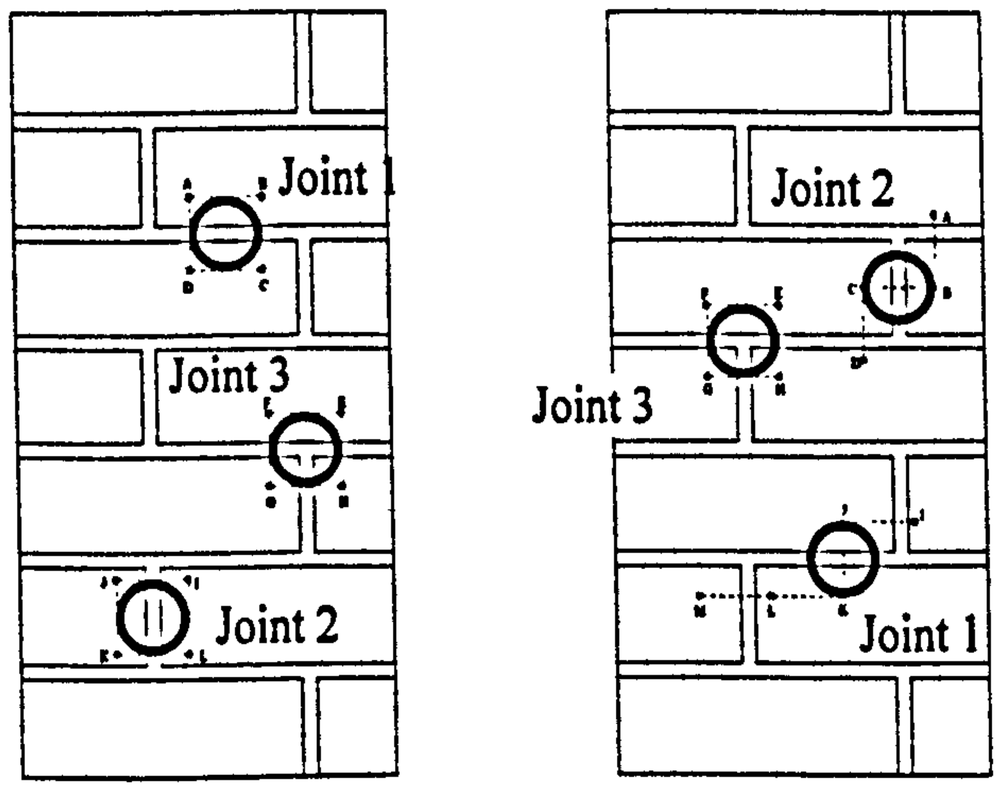

Fig. 6.3 Permeameter and demec positions for panels with bed orientation θ=0°

The average water ingress rates for panels 2A and 3A are shown in Figs 6.4-6.6. These relationships indicate the influence of applied stress level and initial head (h) on water ingress with time. For simplification the relationships presented are identified in terms of joint positions.

These fundamental relationships were the basis of study that relate the volume of water ingress into a panel to the applied stress levels, strain measurements and bed orientations of the panels. For ease of discussion, the effect of these factors were considered in individual sections within this chapter.

Figures 6.4-6.6 show that at Joint 1 there is a noticeable improvement in its resistance to water ingress as applied stress levels increased from $0.0f_{ult}$ (i.e. unstressed) to $0.6f_{ult}$. Joint 2 indicated a slight deterioration in its resistance to water penetration as stress levels increased. At Joint 3, an immediate indication of the variability of brick and mortar jointing is shown by the large decrease in test duration. Compare Joints 1 and 2 test duration of 45mins with only 10mins for Joint 3.

The data generated from these tests would be developed later to form relationships between strain and initial head. This is discussed in subsequent sections.

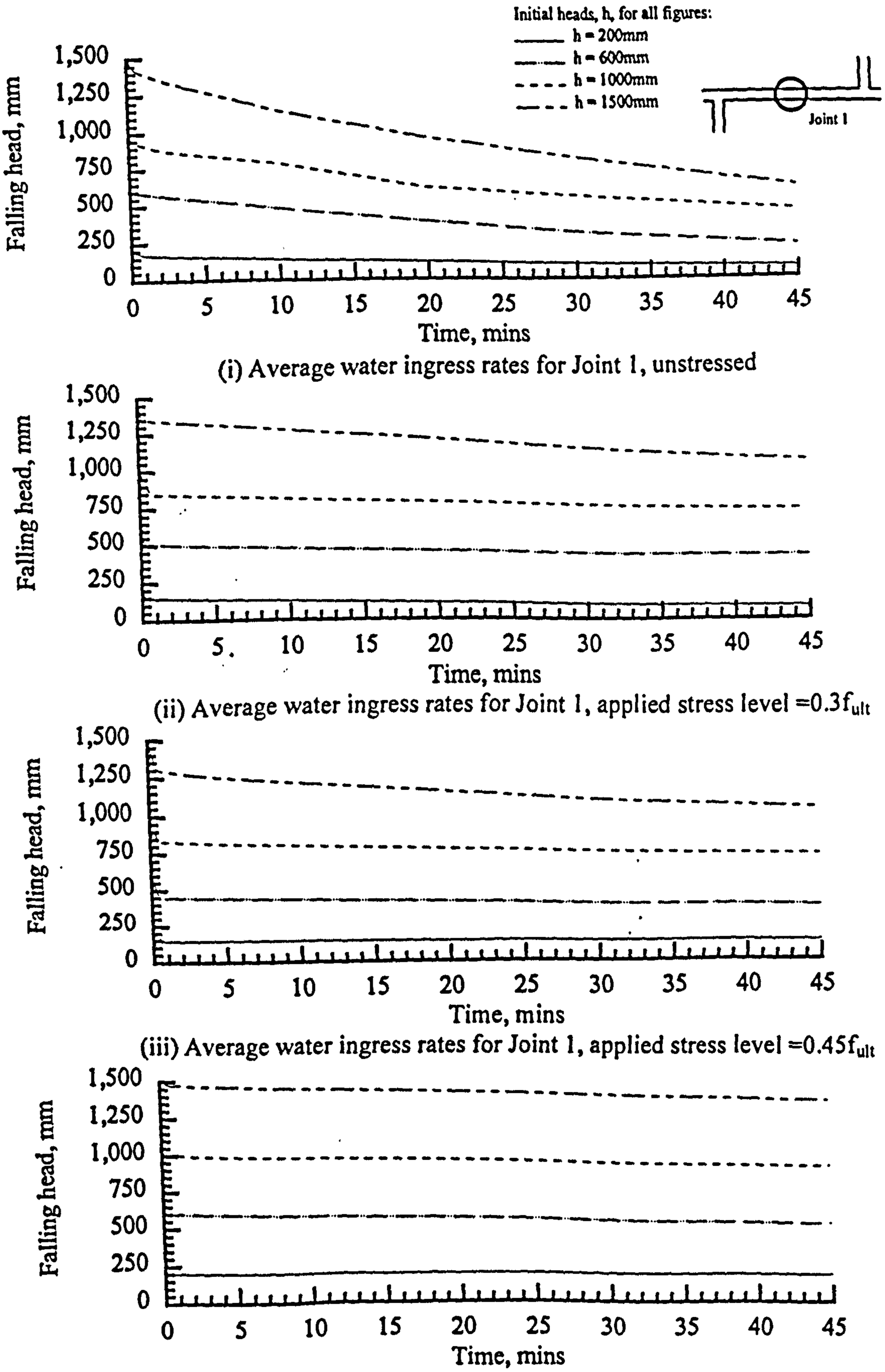

Fig. 6.4 Average water ingress rates at Joint 1, bed orientation θ=0°

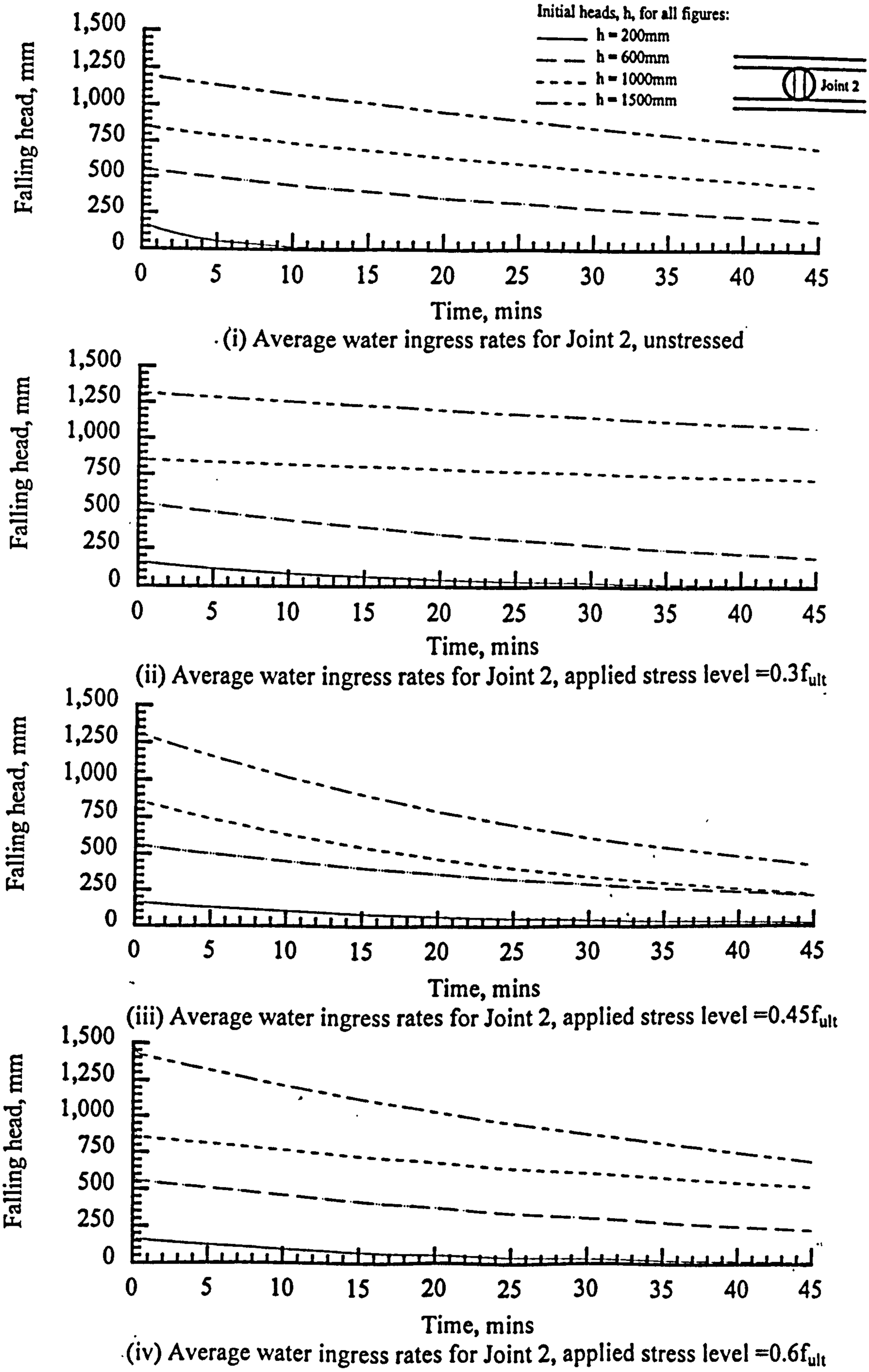

Fig. 6.5 Average water ingress rates at Joint 2, bed orientation θ=0°

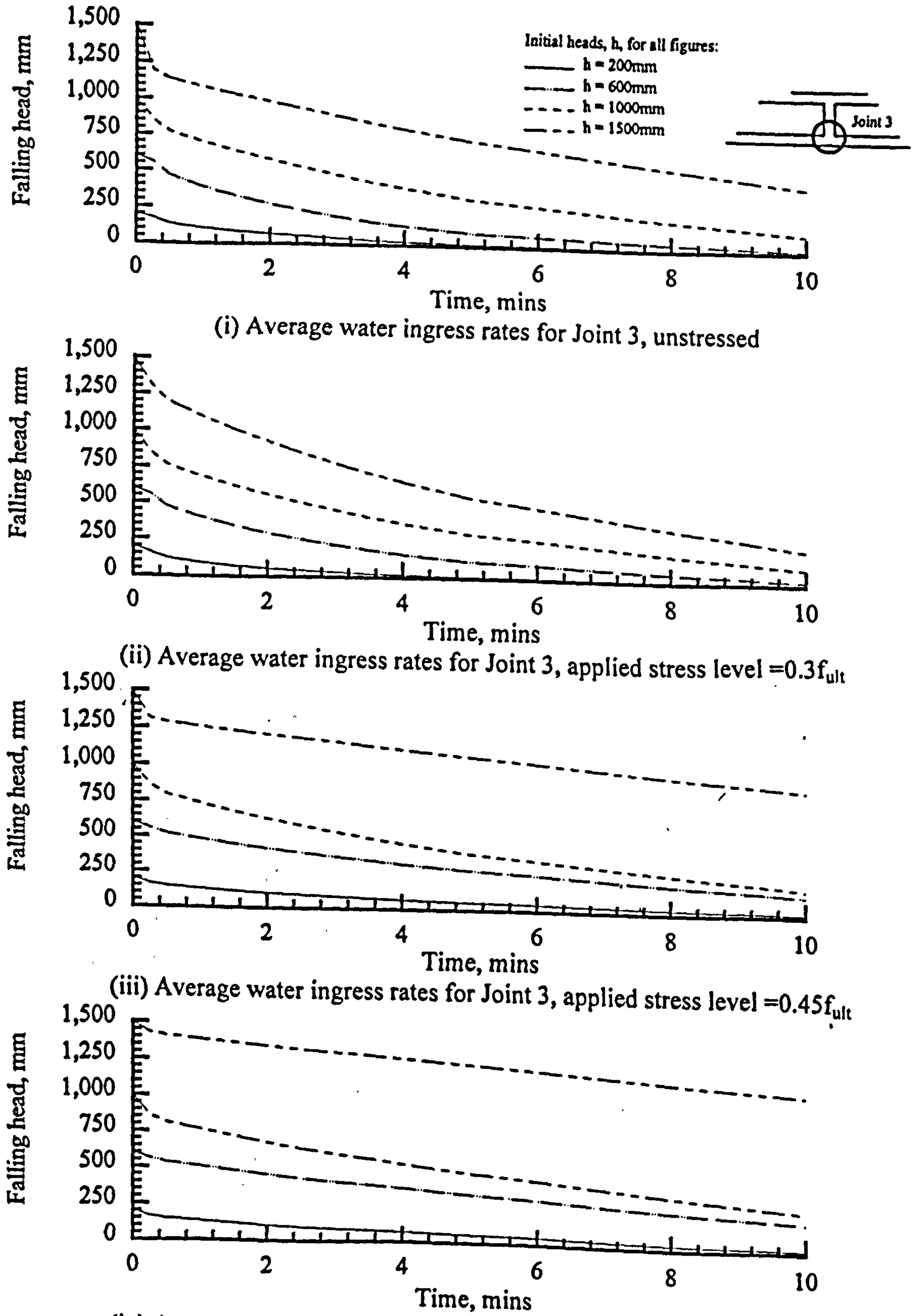

(i) Average water ingress rates for Joint 3, unstressed

(ii) Average water ingress rates for Joint 3, applied stress level $=0.3f_{ult}$

(iii) Average water ingress rates for Joint 3, applied stress level $=0.45f_{ult}$

(iv) Average water ingress rates for Joint 3, applied stress level $=0.6f_{ult}$

Fig. 6.6 Average water ingress rates at Joint 3, bed orientation $\theta=0°$

6.3.2 Modelling of water ingress rate results

The average ingress rates found during experimentation and shown in Figs 6.4-6.6 were found to best-fit theoretical decay curves using Microsoft Excel. These are shown in Table 6.1.

These relationship were used to develop an empirical model of water ingress rates under load. This is discussed in detail in Chapter 8.

Table 6.1 Average decay curves and coefficient of correlation values for panels with bed orientation $\theta = 0°$

Initial head, h (mm)	Applied stress, (N/mm^2)	Joint 1		Joint 2		Joint 3	
		y =	R^2	y =	R^2	y =	R^2
200	0.00 f_{ult}	$139e^{-0.0299t}$	0.99	$173e^{-0.2350t}$	0.98	$180e^{-0.4710t}$	0.98
	0.30 f_{ult}	$149e^{-0.0134t}$	1.0	$159e^{-0.0650t}$	0.96	$200e^{-0.5388t}$	1.0
	0.45 f_{ult}	$151e^{-0.0024t}$	1.0	$164e^{-0.0479t}$	0.96	$188e^{-0.2244t}$	0.99
	0.60 f_{ult}	$151e^{-0.0024t}$	1.0	$165e^{-0.0588t}$	0.97	$188e^{-0.2191t}$	1.0
600	0.00 f_{ult}	$529e^{-0.0171t}$	1.0	$554e^{-0.0223t}$	1.0	$492e^{-0.3568t}$	0.97
	0.30 f_{ult}	$470e^{-0.0049t}$	0.98	$555e^{-0.0235t}$	0.94	$559e^{-0.3151t}$	0.99
	0.45 f_{ult}	$474e^{-0.0041t}$	0.99	$560e^{-0.0220t}$	0.94	$508e^{-0.1393t}$	0.98
	0.60 f_{ult}	$476e^{-0.0034t}$	1.0	$563e^{-0.0204t}$	0.95	$530e^{-0.1041t}$	0.99
1000	0.00 f_{ult}	$851e^{-0.0144t}$	0.99	$850e^{-0.0143t}$	0.99	$753e^{-0.1945t}$	0.85
	0.30 f_{ult}	$847e^{-0.0038t}$	0.95	$848e^{-0.0037t}$	0.97	$767e^{-0.2084t}$	0.90
	0.45 f_{ult}	$863e^{-0.0031t}$	0.98	$864e^{-0.0031t}$	0.98	$872e^{-0.1547t}$	0.99
	0.60 f_{ult}	$859e^{-0.0023t}$	0.98	$860e^{-0.0023t}$	0.97	$869e^{-0.1154t}$	0.98
1500	0.00 f_{ult}	$1358e^{-0.0194t}$	1.0	$1298e^{-0.0114t}$	0.84	$1050e^{-0.1005t}$	0.97
	0.30 f_{ult}	$1351e^{-0.0056t}$	0.98	$1315e^{-0.0045t}$	1.0	$1033e^{-0.1735t}$	0.90
	0.45 f_{ult}	$1349e^{-0.0046t}$	0.98	$1315e^{-0.0135t}$	0.92	$1127e^{-0.0404t}$	0.89
	0.60 f_{ult}	$1361e^{-0.0020t}$	0.97	$1430e^{-0.0162t}$	0.97	$1185e^{-0.0290t}$	0.91

y - Water head in reservoir

t - Time from the commencement of testing

f_{ult} - Average predicted failure stress for panels; for $\theta=0°$ panels, $f_{ult} = 16.4 N/mm^2$

The best-fit decay relationships were based on experimental water ingress rates after the initial 15secs of testing. This was to avoid the large initial drop in water head caused by settling effects as discussed in Section 6.2.

6.3.3 Effect of varying applied stress level on strain for θ=0°panels

Figure 6.7 shows the average stress-strain relationships for masonry joints using experimental data from panels 2A and 3A. These relationships are for the horizontal joint (Joint 1) and the perpend joint (Joint 2). Strain generated at Joint 3 exhibited both these strain levels and for purposes of simplification is not shown. Applied stress levels are shown only up to and including $0.6f_{ult}$.

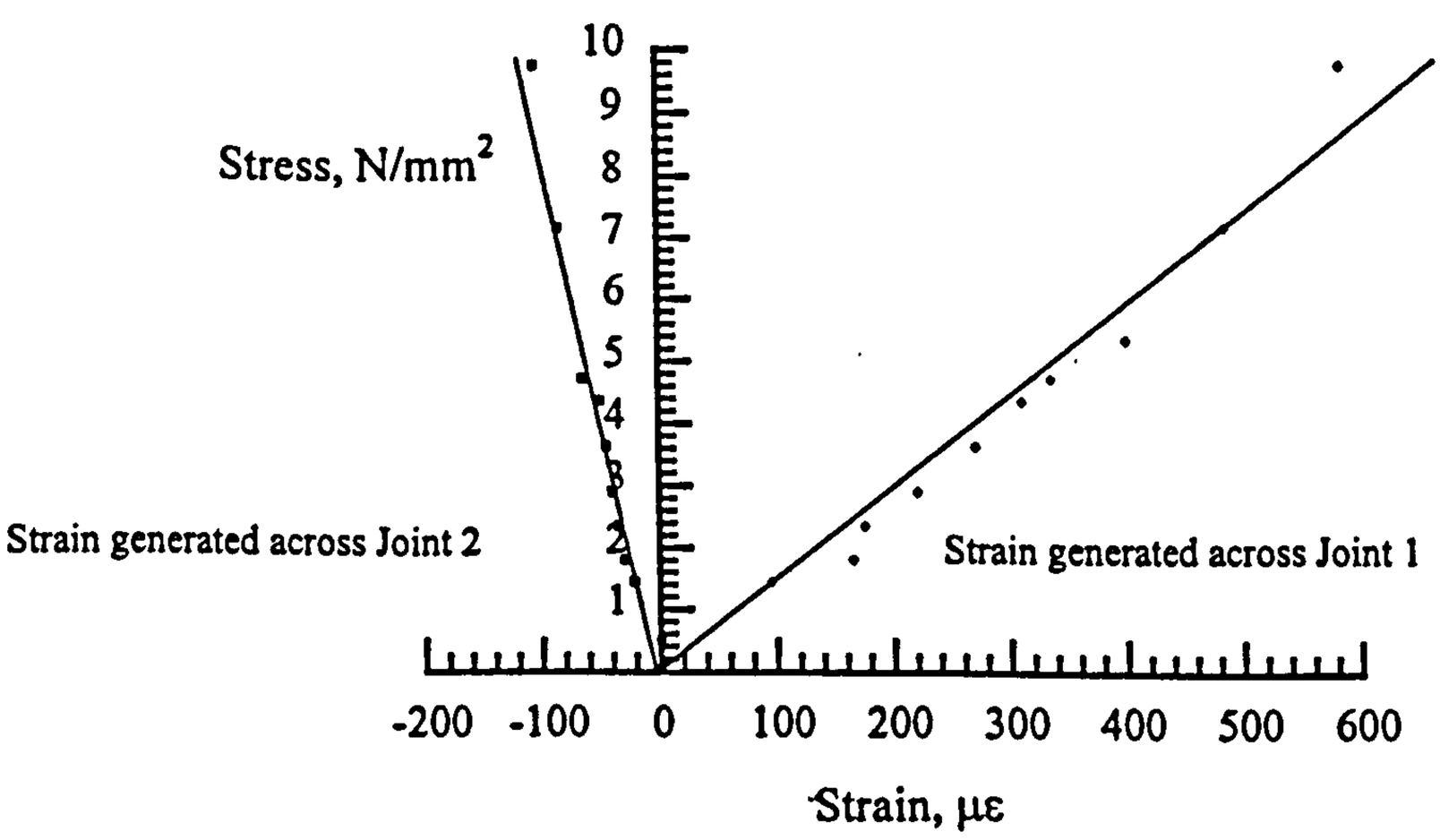

Fig. 6.7 Average stress-strain relationship for masonry joints, bed orientation θ=0°

Note that the strain measured here and for all subsequent related figures, strain is measured across both brick, mortar and interface. A fuller explanation can be seen in Section 6.2(b)

The stress-strain relationship for both masonry joints were found to be approximately linear. A more parabolic relationship would be formed as the panel approached failure.

Figure 6.7 shows that stressing across bed joints (Joint 1) produced compressive strains of 400-550με at $0.3\text{-}0.45f_{ult}$ and 600-650με at $0.6f_{ult}$ respectively. These strains would produce an effectively more watertight brick/mortar interface as more cavities closed.

For perpend joints (Joint 2), tensile strains of between -75με and -95με were recorded for panels stressed to 0.3-0.45f_{ult} respectively. Tensile strains of -160με were recorded when applied stress was 0.6f_{ult}.

These tensile strains were initially thought to promote an opening out of the perpend joints and would initiate debonding at the brick/mortar interface. This would result in an increase in water ingress.

Joint 3 would compress along its horizontal mortar bed component and debond at its perpend component.

As the applied stress to the panel was uniform, then each mortar joint in the panel would undergo the same vertical and horizontal strain. Strains generated at Joint 3 across both its horizontal and vertical component were similar to those at Joint 1 and 2.

6.3.4 Effect of varying initial water head and applied stress level on water ingress through θ=0° panels

The value in varying the initial head was to assess the worst case of rain water penetration through masonry. Low initial heads of magnitudes up to 200mm can be similar to wind driven rain in an external environment. Higher initial heads correspond to worst possible weather driven scenarios and may exploit more fully any cavities at the brick/mortar interface.

When panels were unstressed this hypothesis is true at all joint positions. When stressed however, the panels ingress behaviour was largely controlled by the value of stress and the corresponding strain across the mortar joints.

This is exhibited in typical experimental results given in Table 6.2 for θ=0° panels which shows that the drop in the water head within the initial 45mins of testing at Joints 1 and 2 and after 10mins at Joint 3, is dependent on both initial head and applied stress.

Table 6.2 Typical results of water head drop within 45mins of test commencing for Joint 1 and 2 and within 10mins for Joint 3 for θ=0° panels as influenced by applied stress and initial water head

Applied stress, (N/mm^2)	Joint 1				Joint 2				Joint 3			
	Initial head (mm)				Initial head (mm)				Initial head (mm)			
	200	600	1000	1500	200	600	1000	1500	200	600	1000	1500
$0.00f_{ult}$	97	154	263	381	183	169	263	431	171	586	906	1317
$0.30f_{ult}$	69	152	184	222	116	160	182	242	158	576	904	1115
$0.45f_{ult}$	52	145	163	211	98	150	159	283	147	473	814	747
$0.60f_{ult}$	50	139	160	162	108	156	162	351	127	469	725	613

f_{ult} - Average predicted failure stress for panels; for θ=0°, f_{ult} =16.4N/mm²

The results in Table 6.2 for unstressed panels, i.e. at $0.0f_{ult}$, showed an increase in ingress rate as the initial water head increased. The drop in water head was however found to be over 25% of all values of initial heads at Joints 1 and 2 after 45mins. At Joint 3 the corresponding drop was approximately 90% with again little ingress being recorded after 10mins.

For the initial head to be considered influential irrespective of applied stress level then the drop in water as indicated above should remain constant. Water ingress results in Table 6.2 show a decrease which indicated that stress (and therefore strain) would be the controlling factor rather than the magnitude of initial head.

As the applied stress increased to $0.6f_{ult}$ across Joint 1, cavities start to close which improved the resistance to water penetration.

At Joint 2, the initial water head was not found influential in governing water ingress at low levels of applied stress. However, as tensile strains were expected at Joint 2 which indicated the occurrence of debonding, then it may be expected that initial water heads would prove increasingly influential. Table 6.2 indicated that there was a reduction in water ingress indicating a closing of the brick/mortar interface. This is clearly shown by the decrease in the head drop at stress levels $0.3f_{ult}$-$0.45f_{ult}$. Table 6.2 therefore shows that stress levels and not the initial water heads was found to be more influential in controlling water ingress through masonry.

The results also show that the effect on ingress rates for panels stressed to $0.6f_{ult}$ was marginal, with only a slight increase in ingress noted compared to panels stressed to $0.45f_{ult}$ at each initial head.

At Joint 3, the initial head was a factor in governing water ingress at unstressed and low applied stress levels. The magnitude of water ingress at this position was greater than at Joint 1 and 2, and occurred in a much smaller time span. This is clearly indicated by comparing 10mins for ingress measurements at Joint 3 to 45mins at Joints 1 and 2.

The reason that Joint 3 exhibited the largest volume of water ingress may be more than coincidence. When a mason forms Joint 1, mortar is laid and bricks pressed upon it. At Joint 2, a mason will spread mortar onto the brick and press this against another. The junction between these two (Joint 3) therefore has no direct mortar placed upon it and only later will mortar be pointed into position. This may leave large cavities behind the pointed 'skin' allowing easy access of water in the case of unstressed panels.

These cavities would be further enlarged by loading resulting in cracking/debonding at the brick/mortar interface and thus encouraging increasingly greater volumes of water to ingress. Also at this position, both lateral and axial strains act simultaneously creating both strain discontinuity and stress concentrations leading to large areas of debonding which can further lead to an increased water penetration.

The above factors suggest that Joint 3 is the worst mortar joint in a masonry wall to inhibit water ingress even for unstressed panels.

6.3.5 Relationship between water ingress and strain for θ=0° panels

(a) Joint 1:

Figure 6.8 shows the relationship between average volume ingress and strain across Joint 1. This figure was based on average results from test panels 2A and 3A. Strain indicated here and for all figures within this chapter, is strain measured perpendicular (across) the mortar joint.

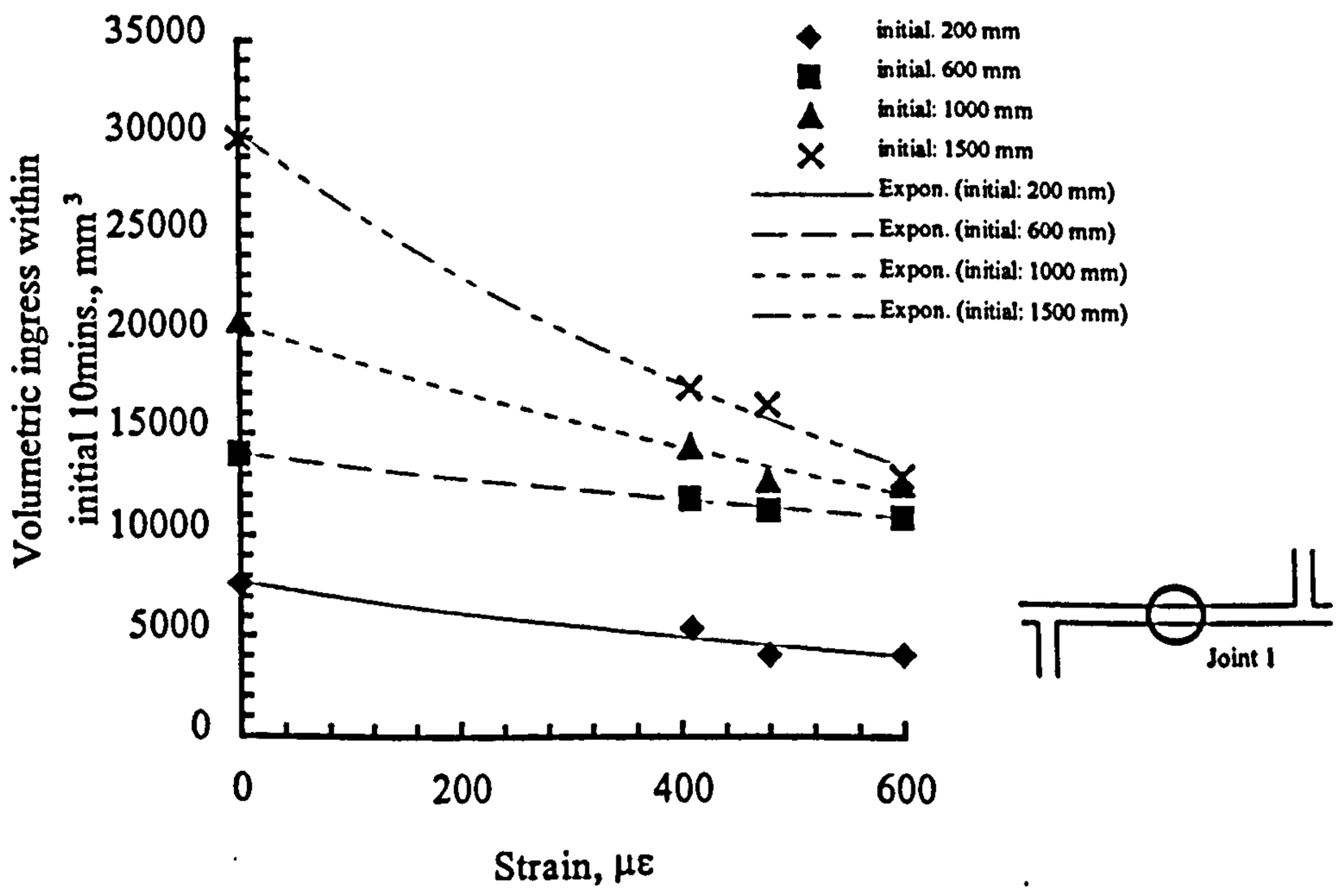

Fig. 6.8 Volume intake within initial 10mins at Joint 1 under four levels of stress for bed orientation θ=0°

The above figure shows an improvement in the resistance of Joint 1 to water ingress irrespective of initial head under stress. The effect of this improvement was most marked for high initial heads (1000mm and 1500mm).

Continued loading produced only a small improvement in the resistance to water ingress.

This indicates that a threshold compressive strain may be reached whereby any additional compressive strains had a negligible effect in reducing water ingress rates further. Once this threshold strain was reached, then all water accessible cavities were closed and the mortar beds were totally effective in resisting water penetration.

The relationships indicated in Fig. 6.8 can be expressed as a standard decay equation:

$$V_i = Ae^{-b\varepsilon} \qquad \text{Eqn. 6.1}$$

V_i - volume of water ingress when strain across joint was ε

A - coefficient dependant upon the volume of water ingress when panel was unstressed

b - decay coefficient

Using Microsoft Excel, standard decay equations were generated as best-fit curves to the experimental data points. Table 6.3 shows these standard decay equations based on Fig. 6.8.

Table 6.3 Standard decay equations for water ingress at Joint 1

Initial head, h (mm)	Joint 1	
	$V_i =$	R^2
200	$7682e^{-0.0011\varepsilon}$	0.99
600	$14014e^{-0.0004\varepsilon}$	0.97
1000	$20503e^{-0.0010\varepsilon}$	0.99
1500	$30232e^{-0.0013\varepsilon}$	0.94

These decay relationships exhibited good agreement with the experimental data points, this is reflected by the average coefficient of correlation for all results, R^2=0.97. These equations are plotted as best-fit curves against experimental data in Fig. 6.8.

These curves decreased to a minimal level, where this will be the combined absorption of brick and mortar with no cavities at their interface. Gradually this mechanism would become water saturated and the joint could not support further water ingress.

(b) Joint 2:

Figure 6.5 (Section 6.3.1) indicated that ingress rates reduced as the applied stress increased which would be at odds with the expected tensile cracking at the brick/mortar interface of Joint 2.

Figure 6.9 shows the average relationship between the volume intake based on these ingress rates and corresponding measured strain.

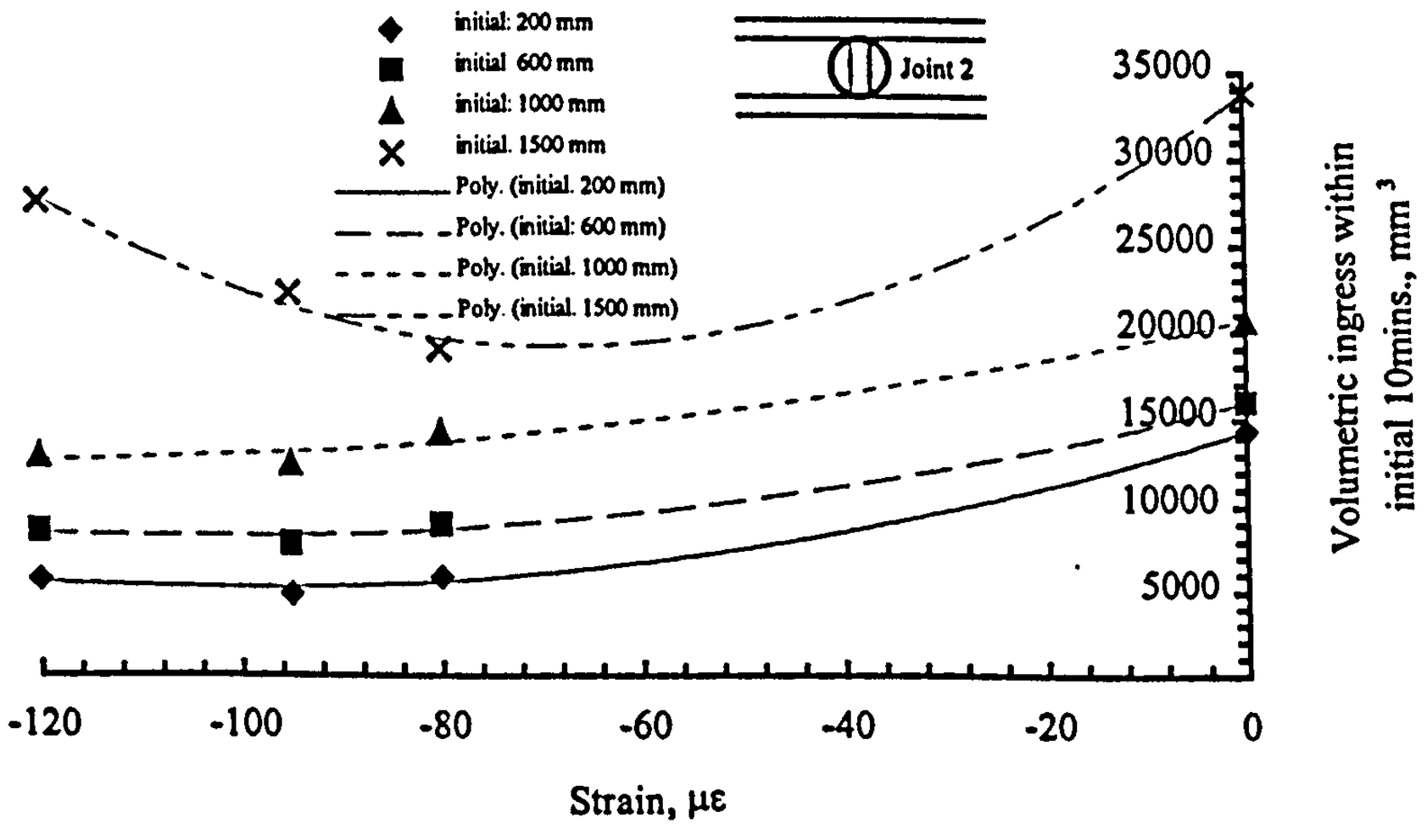

Fig. 6.9 Volume intake within initial 10mins at Joint 2 under four levels of stress for bed orientation θ=0°

The above figure shows that volume intake rates for the first three initial heads (200mm, 600mm and 1000mm) decreased as tensile strains across Joint 2 increased. However, for initial head of 1500mm, volume ingress increased once a threshold tensile strain had been surpassed. This indicates that water has exploited cracks created by high applied stress.

This unexpected behaviour can be explained as follows:

Due to the applied vertical load, the specimen was under uniform vertical compressive stress at any cross section along its height. The effect of the stress is to compress the horizontal bed joints closing any voids, .capillary pores, transverse cavities and cracks at the mortar joints and at the brick/mortar interfaces.

This is true for mortar, as it possess high deformation characteristics due to its high plasticity compared to the brick. The vertical perpendicular joints (Joint 2) are also under the same applied vertical compressive stress. The mortar at these joints underwent vertical and horizontal deformation or strain under the same applied vertical compressive stress. The vertical strain closed any voids, capillary pores, transverse cavities and cracks at the brick mortar interfaces. The horizontal deformation or strain is attributed to the high Poisson's ratio of mortar.

This special phenomenon continued under low levels of applied stress but at high levels, the strain at the mortar and at the interface reached high values. These high values of strain are usually associated with the ultimate tensile strength of mortar or the ultimate bond tensile strength of the brick/mortar interface. At this threshold point, cracks start to appear causing an increase in water ingress through both the mortar joints and brick/mortar interfaces. The threshold point for tensile strains using Fig. 6.9 was dependent upon initial head exploiting any strain generated cracks.

Due to the general increase in ingress rates at Joint 2 caused by the crack initiation at high strain levels, an exponential decay relationship similar to Eqn. 6.1 is not possible. This is exhibited most clearly for an initial head of 1500mm, though is exhibited for all lower initial heads (≤1000mm) to a lesser extent. However a second order polynomial relationship could be used to accurately predict the volume ingress rate for Joint 2 caused by a change in strain.

This standard second order polynomial is of the form:

$$V_i = A\varepsilon^2 + B\varepsilon + C \qquad \text{Eqn. 6.2}$$

V_i - volume of water ingress at a strain, ε

A, B, C - coefficients

Table 6.4 shows the standard polynomial equations as derived by Microsoft Excel. These equations were also plotted in Fig. 6.9 against experimental results as best-fit curves.

Table 6.4 Standard second order polynomial equations for water ingress at Joint 2

Initial head, h (mm)	Joint 1	
	V_i =	R^2
200	$0.50\varepsilon^2 + 182.50\varepsilon + 14419$	0.99
600	$0.72\varepsilon^2 + 148.40\varepsilon + 16019$	0.99
1000	$0.81\varepsilon^2 + 126.10\varepsilon + 20602$	0.98
1500	$3.17\varepsilon^2 + 431.00\varepsilon + 33809$	0.99

These equations exhibited good agreement with experimental data results, with an average coefficient of correlation, R^2=0.99.

The lowest volume ingress for each relationship occurred at the threshold tensile strain. Once this threshold strain was breached then ingress rates began to rise. By using the equations as shown in Table 6.4 and Fig. 6.9, threshold strain phenomena can be identified.

By differentiating volumetric ingress (V_i) with respect to strain (ε) in Table 6.4, i.e. $dV_i/d\varepsilon = 0$, an indication of a threshold tensile strain level with respect to the initial water head was found. This is shown in Fig. 6.10.

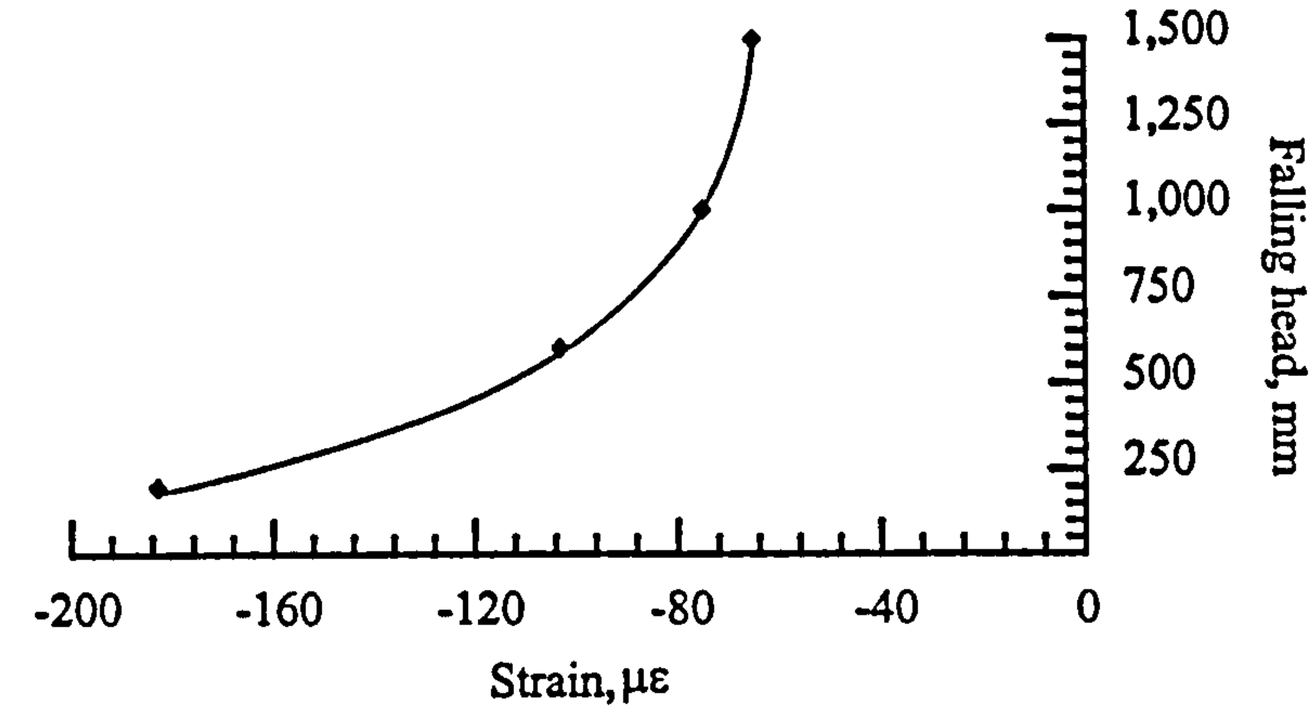

Fig. 6.10 Threshold strains for minimum water ingress as influenced by initial water head at Joint 2

Figure 6.10 shows that the threshold tensile strain is influenced by the height of the initial water head. For an initial head of 200mm, then the threshold strain was found to be -183με. Using Fig. 6.7 (Section 6.3.3) this would require an applied stress $>0.6f_{ult}$, i.e. outwith the test range. Conversely, an initial head of 1500mm requires a threshold strain of -63με, generated when applied stress was 4.8N/mm^2 ($\cong 0.3f_{ult}$).

(c) Joint 3:

Figure 6.11 shows the average volume intake-strain relationships for Joint 3 using panels 2A and 3A and was similar to that for Joint 1. Note that strain values shown are those generated across the main mortar bed component.

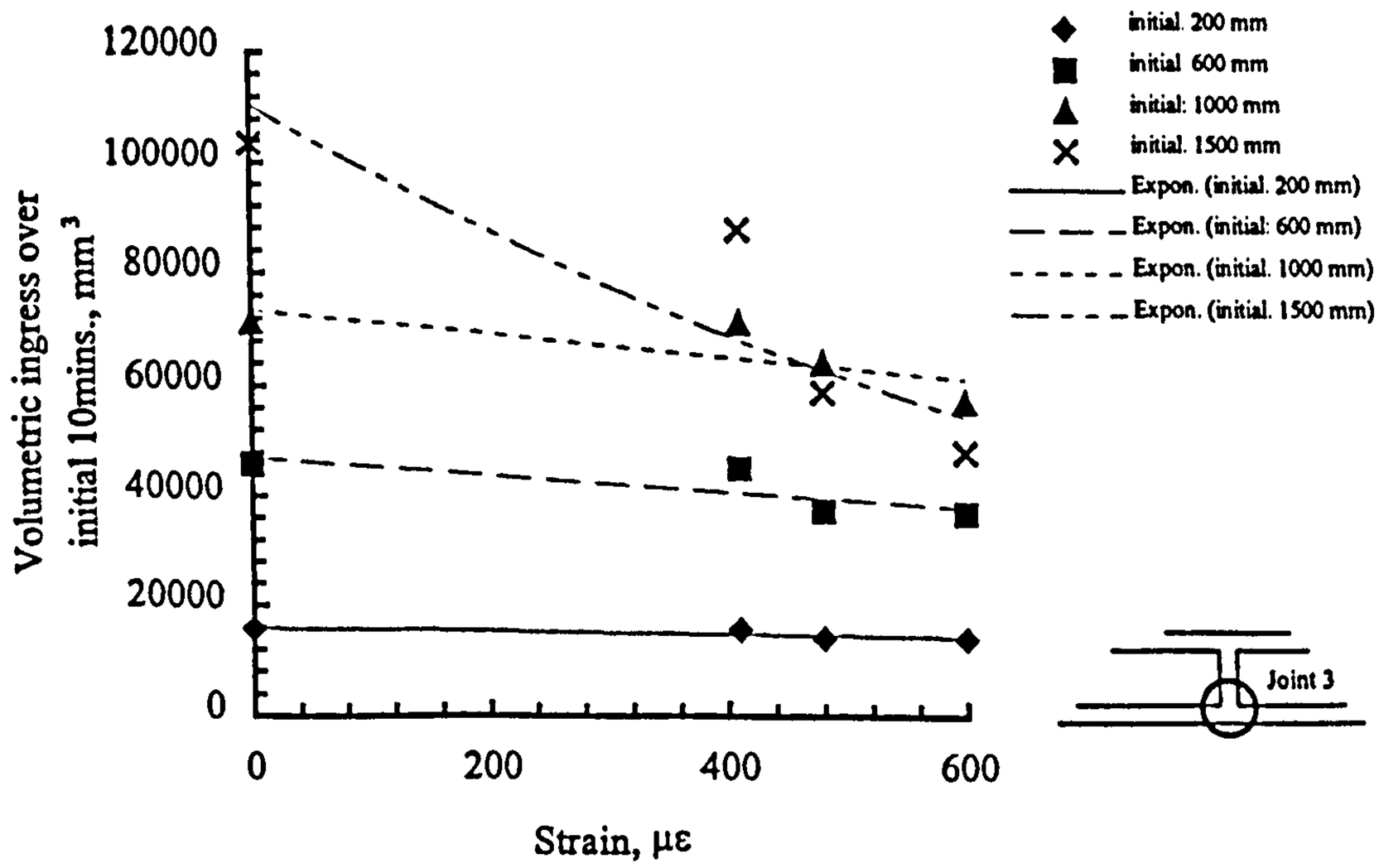

Fig. 6.11 Volume intake within initial 10mins at Joint 3 under four levels of stress for bed orientation θ=0°

These relationships showed decreasing water ingress as strain across the mortar bed increased. However there was very little change in volume of water ingress when measured at stress levels of $0.3f_{ult}$ (410με), $0.45f_{ult}$ (480με) and $0.6f_{ult}$ (600με) indicating that closure of cavities at the brick/mortar interface can be considered significant after only a stress level of $0.3f_{ult}$.

As with Joint 1, the volume intake-strain relationship can also be expressed as a decay relationship, (Eqn. 6.1), as the volume ingress decreased with increasing compressive strains. These relationships can be consulted in Table 6.5 and were already plotted in Fig. 6.11 as best-fit curves to the experimental results.

Table 6.5 Standard decay equations for water ingress at Joint 3

Initial head, h (mm)	Joint 1	
	$V_i =$	R^2
200	$15770e^{-0.0002\mu}$	0.85
600	$47057e^{-0.0004\mu}$	0.65
1000	$73402e^{-0.0003\mu}$	0.70
1500	$110600e^{-0.0012\mu}$	0.75

Equations exhibited in Table 6.5 showed reasonable agreement with experimental results, the average coefficient of correlation R^2=0.74.

The relationship exhibited at Joint 3 under an initial head of 1500mm showed a poor correlation with experimental results. This may be caused by an anomaly in the test result mainly at a strain level of ≅400με. For strain generated at this position it was expected that the volume of water ingress would be lower than what was indicated in Fig. 6.11.

Similar to that at Joint 1 (Table 6.3) these curves decrease to a minimal level, where this will be the combined absorption of brick and mortar with no fissures at the brick/mortar interface.

6.3.6 Effect of joint type on water ingress for θ=0° panels

By comparing joint types it was expected to state which joints were more prone to leakage under load.

Joint 1 is the most resistant to water ingress when loaded. Joint 2 proved to be the least resistant to water ingress when the panel was loaded. This was particularly pertinent when the stress level was $\geq 0.45 f_{ult}$ corresponding to load levels likely to generate higher strains than threshold tensile levels. Although Joint 3 in this case had the numerically highest volume of ingress, the general trend was for decreasing water ingress rates as the panel was stressed. However, it has already been discussed in Section 6.3.4 that the highest volume of ingress at Joint 3 may be no coincidence. It is felt that laying and pointing procedures combined with lateral and axial strains acting simultaneously at this joint contribute to the poor water resistance capability of Joint 3.

6.4 Water Ingress Characteristics when Bed Orientation θ=90°

When panels with this orientation were stressed, a tensile/splitting mode of failure occurred along the brick/mortar interface of the main mortar beds which lay parallel to the direction of loading, creating columns of brick and mortar. These columns would sustain considerable further loading independently prior to total structural failure.

This mode of failure and the related crack development would fundamentally control the ingress of water at all joint positions.

6.4.1 Panel testing

Type 2, 3 and 4 brick panels were used for this study. The Type 2 panel (2E) had a cross section of 100x245mm with a predicted failure load (F_{ult}) and failure stress (f_{ult}) of 240kN and 9.8N/mm^2 respectively. This failure load originated from panels previously tested within this research programme (Chapter 5). For this type of panel water ingress was monitored at 2.9N/mm^2 ($0.3f_{ult}$), 4.4N/mm^2 ($0.45f_{ult}$) and 5.9N/mm^2 ($0.6f_{ult}$). For Type 3 panel (3E) a predicted failure load (F_{ult}) of 330kN was used to generate a failure stress (f_{ult}) of 13N/mm^2. Water ingress was measured when stress levels were 3.9N/mm^2 ($0.3f_{ult}$), 5.8N/mm^2 ($0.45f_{ult}$) and 7.8N/mm^2 ($0.6f_{ult}$). For Type 4 panel (4E), water ingress was measured at 3.9N/mm^2 ($0.3f_{ult}$), 5.8N/mm^2 ($0.45f_{ult}$) and 7.8N/mm^2 ($0.6f_{ult}$) as the predicted failure load was 334kN. The cross sectional area for panels 3E and 4E was 100x255mm.

For information, the location of demec points and permeameter positions are shown in Fig. 6.12.

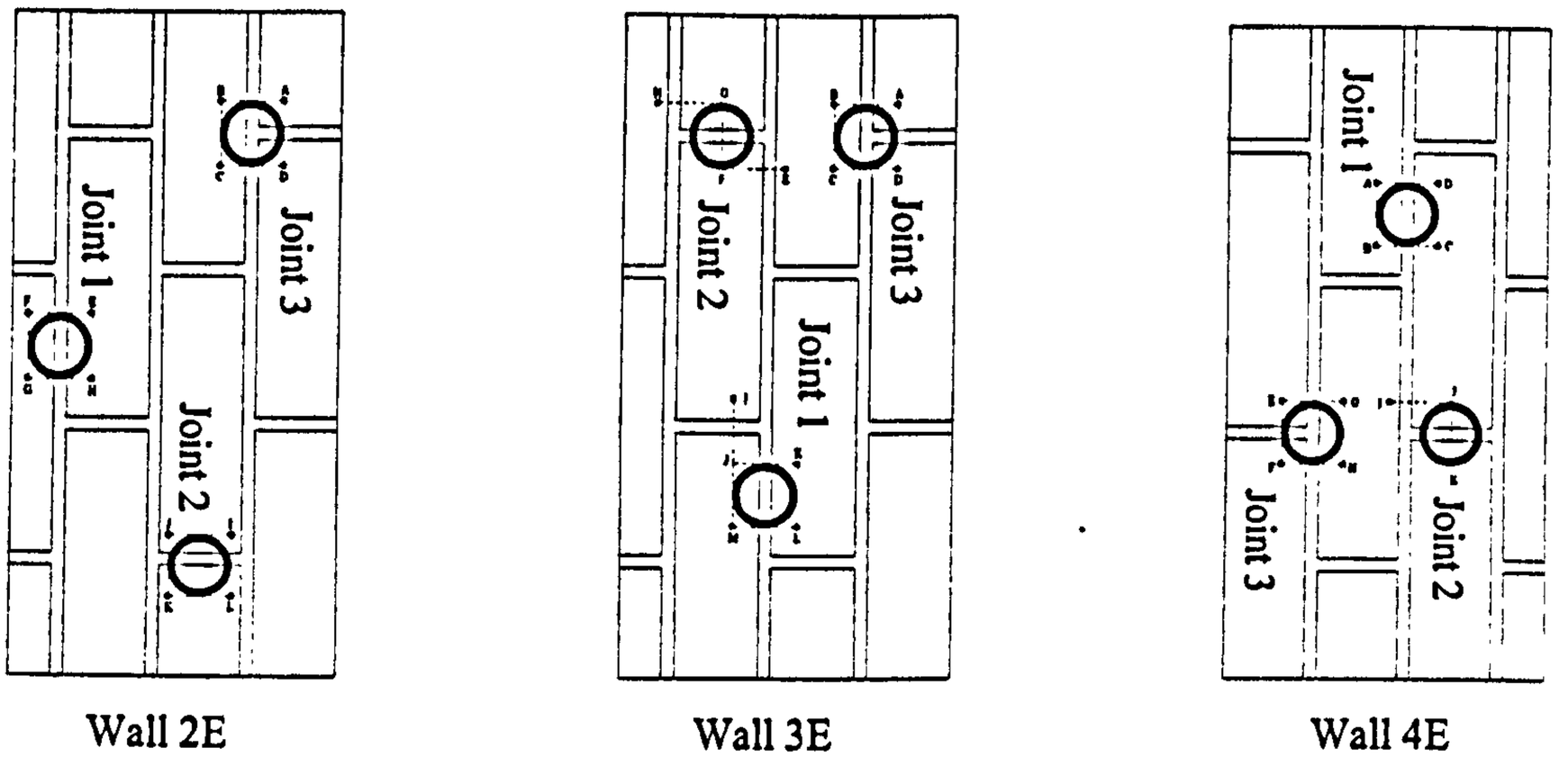

Fig. 6.12 Permeameter and demec positions for panels with bed orientation θ=90°

The average water ingress rates for panels 2E, 3E and 4E are shown in Figs 6.13-6.15. These relationships indicate the influence of applied stress level and initial head (h) on water ingress with time. For simplification, relationships shown here are identified in terms of joint position.

For all panels, a data set of water ingress rates could not be generated for applied stress levels up to $0.6f_{ult}$. This was due to early cracking of panels, even at low applied stress levels, resulting in water ingress often being instantaneous. The panel could however sustain considerable further loading.

For measuring water ingress at Joint 1, brick/mortar interface was fully compromised at applied stress levels $>0.3f_{ult}$.

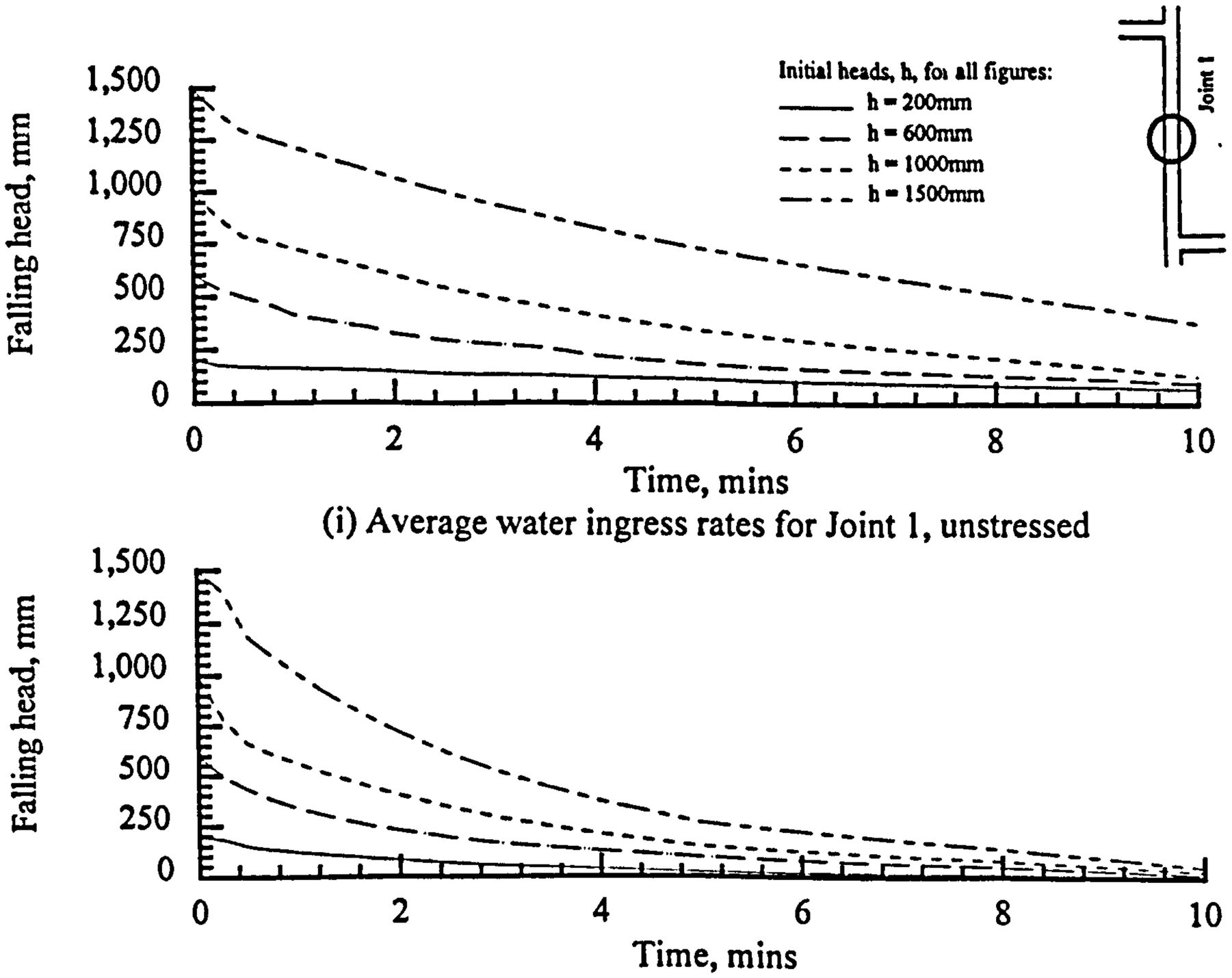

(i) Average water ingress rates for Joint 1, unstressed

(ii) Average water ingress rates for Joint 1, applied stress level $=0.3f_{ult}$

Note: Effectively instantaneous water ingress when panels were stressed to $0.45f_{ult}$ and $0.6f_{ult}$ for all panels.

Fig. 6.13 Average water ingress rates at Joint 1, bed orientation $\theta=90°$

The above falling head-time relationships for Joint 1 exhibited a rapid increase in ingress rates when panels were stressed compared to rates when panels were unstressed, with all water having penetrated the panels within the initial 10mins of test commencing, when applied stress level was $\geq 0.3f_{ult}$.

Figure 6.14 shows that water ingress rates at Joint 2 are dependant upon both applied stress level and initial water head. Due to purely compression stresses acting at this joint, debonding was minimum and water ingress was measured up to applied stress levels of $0.45f_{ult}$.

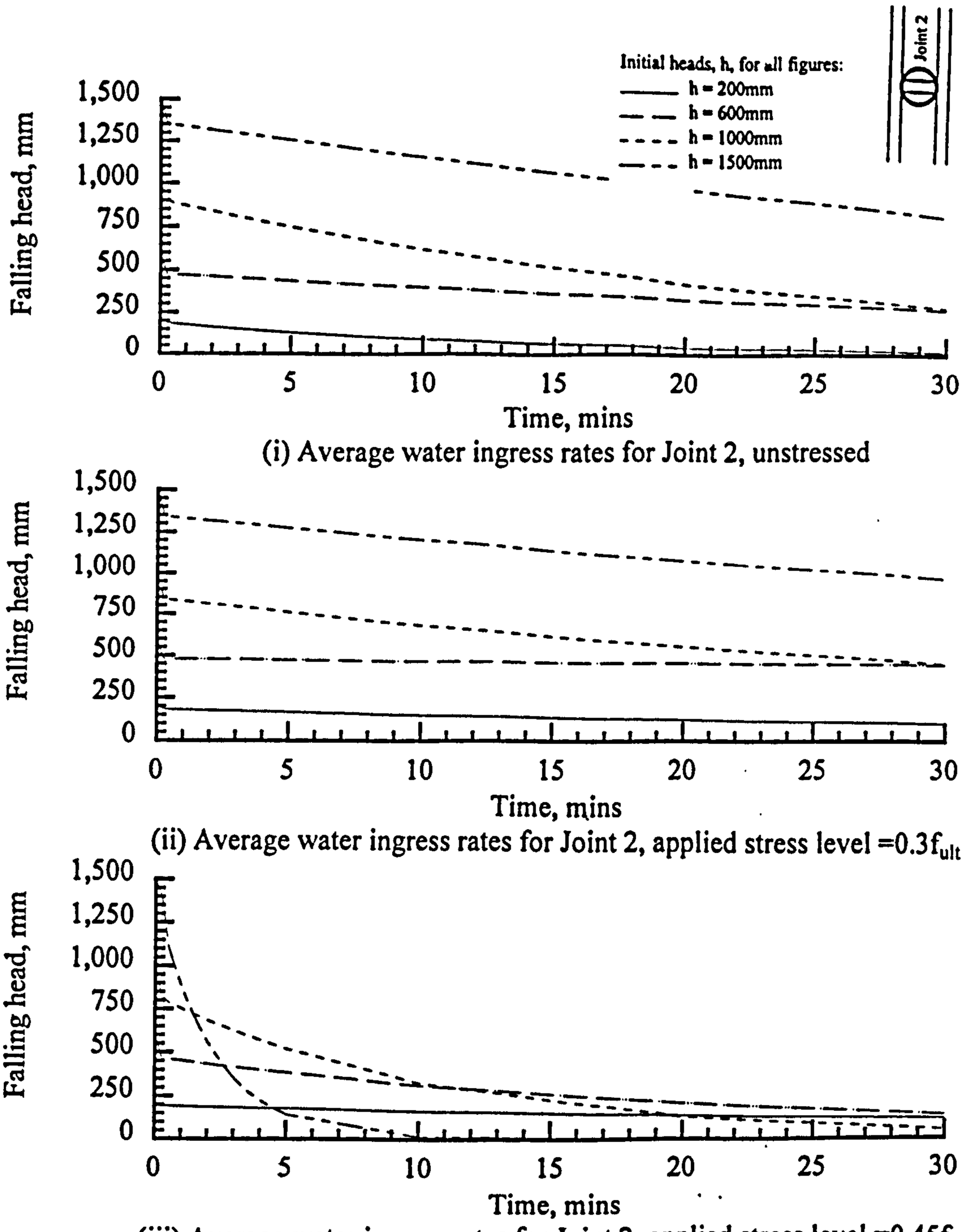

Note: Effectively instantaneous water ingress when panels were stressed to $0.6f_{ult}$ for all panels.

Fig. 6.14 Average water ingress rates at Joint 2, bed orientation $\theta=90°$

When panels were stressed to $0.3f_{ult}$, water ingress rates showed little sign of additional decay. In fact, Joint 2 improved its resistance to water ingress. Once applied stress levels were $>0.3f_{ult}$ then the panel became increasingly compromised to cracking within its own mortar bed and debonding at those mortar beds lying adjacent. This then lead to an increase in water ingress with time.

Figure 6.15 exhibits similar falling head-time relationships for Joint 3 as already indicated for Joint 1 (Fig. 6.13). At unstressed levels, water ingress into the panel continued after 10mins of the test commencing. However, water ingress rates increased dramatically for stress levels $\geq 0.3f_{ult}$. This is exhibited by full water ingress into the panel within the initial 5mins of test commencing irrespective of initial head.

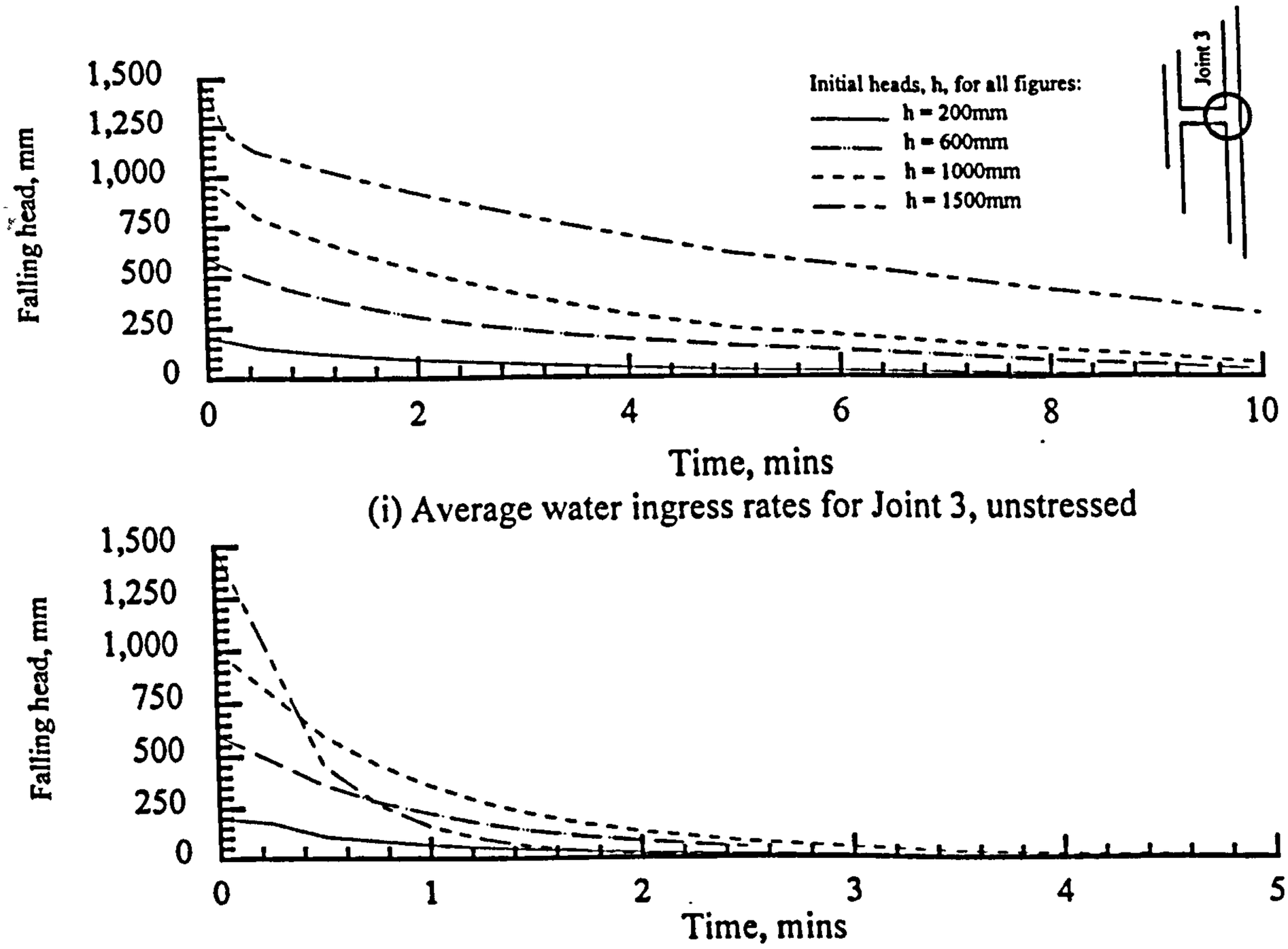

(i) Average water ingress rates for Joint 3, unstressed

(ii) Average water ingress rates for Joint 3, applied stress level $=0.3f_{ult}$

Note: Effectively instantaneous water ingress when panels were stressed to $0.45f_{ult}$ and $0.6f_{ult}$ for all panels.

Fig. 6.15 Average water ingress rates at Joint 3, bed orientation $\theta=90°$

6.4.2 Modelling of water ingress rate results

The average experimental ingress rates of panels 2E, 3E and 4E (Figs 6.13-6.15, Section 6.4.1) were found to best-fit theoretical decay curves as shown in Table 6.6.

Table 6.6 Average decay curves and coefficient of correlation values for panels with bed orientation θ=90°

Initial head, h (mm)	Applied stress, (N/mm^2)	Joint 1		Joint 2		Joint 3	
		y =	R^2	y =	R^2	y =	R^2
200	0.00 f_{ult}	$176e^{-0.0921t}$	0.99	$190e^{-0.0763t}$	0.99	$176e^{-0.3383t}$	0.99
	0.30 f_{ult}	$183e^{-0.4073t}$	1.0	$182e^{-0.0196t}$	0.86	$173e^{-0.9495t}$	0.97
	0.45 f_{ult}	*		$196e^{-0.0171t}$	0.96	*	
600	0.00 f_{ult}	$529e^{-0.0171t}$	1.0	$476e^{-0.0179t}$	0.97	$492e^{-0.3568t}$	0.98
	0.30 f_{ult}	$470e^{-0.0049t}$	0.98	$480e^{-0.0027t}$	0.84	$559e^{-0.3151t}$	1.0
	0.45 f_{ult}	*		$472e^{-0.0406t}$	0.99	*	
1000	0.00 f_{ult}	$872e^{-0.2038t}$	0.99	$902e^{-0.0380t}$	1.0	$909e^{-0.2684t}$	0.98
	0.30 f_{ult}	$779e^{-0.3302t}$	0.95	$843e^{-0.0210t}$	0.97	$990e^{-1.0199t}$	1.0
	0.45 f_{ult}	*		$826e^{-0.0923t}$	0.99	*	
1500	0.00 f_{ult}	$1380e^{-0.1290t}$	1.0	$1357e^{-0.0166t}$	0.98	$1207e^{-0.11376t}$	0.91
	0.30 f_{ult}	$1400e^{-0.3322t}$	0.98	$1315e^{-0.00113t}$	0.90	$1300e^{-2.1091t}$	1.0
	0.45 f_{ult}	*		$1315e^{-0.45621t}$	1.0	*	

* - Indicates that water ingress rates were effectively instantaneous. Ingress rates at $0.6f_{ult}$ were also instantaneous for all joint types.
y - Water head in reservoir
t - Time from the commencement of testing
f_{ult} - Average predicted failure stress for panels; for θ=90° panels, f_{ult} =12.0N/mm^2.

Although data is limited due to the early generation of cracks, these relationships were envisioned to be used in the mathematical modelling of ingress rates. This is discussed in Chapter 8.

6.4.3 Effect of varying applied stress level on strain for θ=90°panels

Figure 6.16 shows the average stress-strain relationship derived by testing panels 2E, 3E and 4E. These relationships represent the measurement of stress and strain across the horizontal joint (Joint 1) and the perpend joint (Joint 2). Strain generated at Joint 3 exhibited both these strain levels.

These relationships show the main mortar bed parallel to the applied load (Joint 1) undergoing tensile cracking whilst the perpend joint (Joint 2) underwent compression.

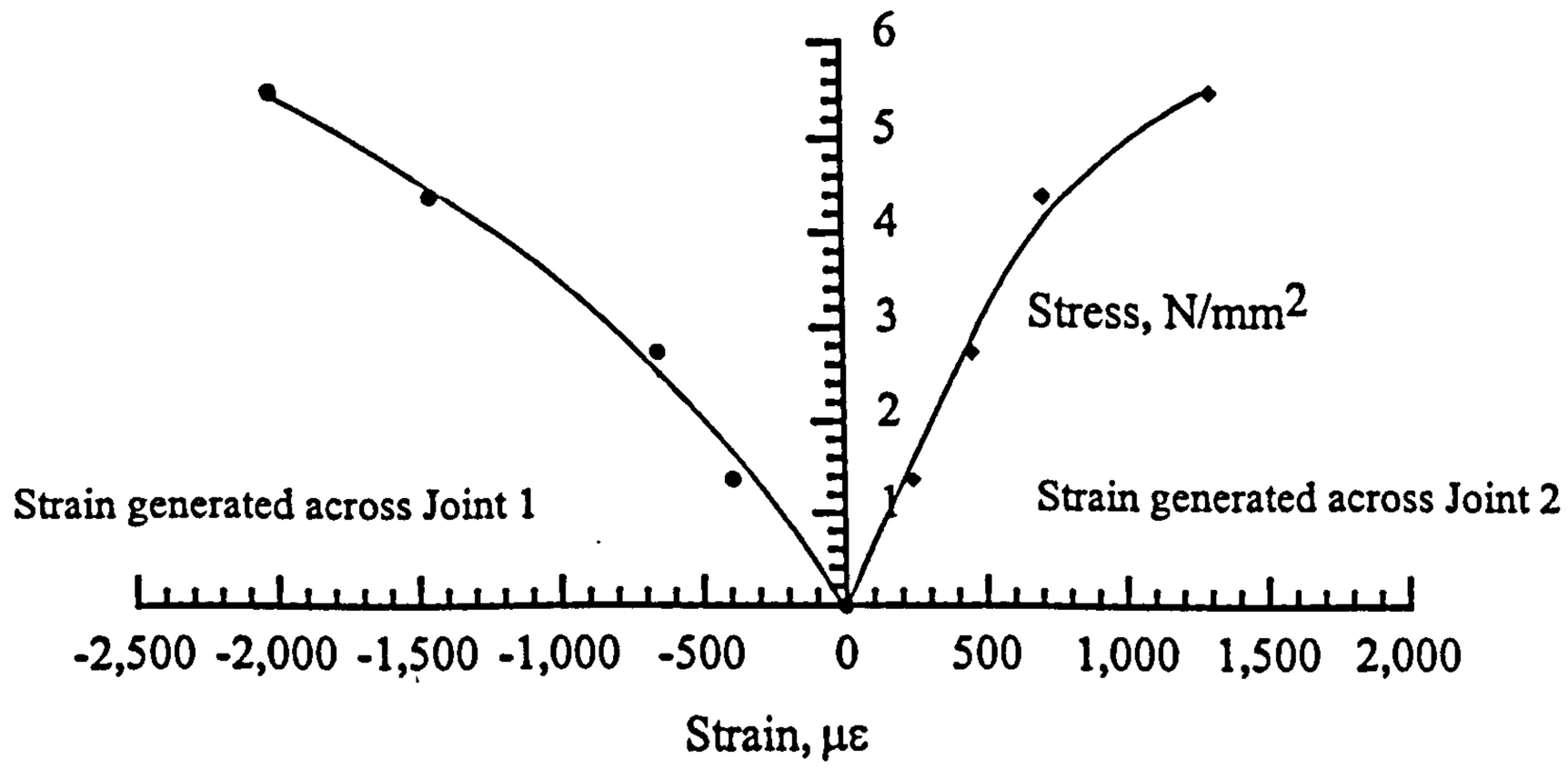

Fig. 6.16 Average stress-strain relationship for masonry joints, bed orientation θ=90°

Strains across Joint 1 showed that at low applied stress levels (≡0.3f_{ult}) a linear-elastic behaviour was exhibited. However as the applied stress level increased, a more parabolic relationship would be formed. This indicted that permanent displacements at Joint 1 had occurred which would lead to a deterioration in the mortar beds' resistance to water penetration.

Stressing across Joint 1 produced tensile strains of -400με at 0.3f_{ult} and -2500με at 0.45f_{ult}. Tensile strains of these higher magnitudes were equivalent to large cracks being developed at Joint 1. It was expected that debonding was not localised, and that it occurred along the entire mortar bed. This would have a serious effect on water ingress, with much higher rates being predicted than when panels were unstressed or orientated at θ=0°.

Joint 2 was subjected to purely compressive stress and exhibited approximately elastic behaviour at low applied stress levels $<0.3f_{ult}$. Increasing the applied stress level produced irrecoverable failure at Joint 2 with some cracking caused by the compression failure mode likely having occurred.

This loading generated compressive strains across Joint 2 of 1000με when panels were stressed to $0.3f_{ult}$ and upwards of 1800με when applied stress was $0.45f_{ult}$. This compared with tensile strains generated at this joint of between -75 and -95με for $\theta=0°$ panels. These high tensile strains ensured that Poisson's ratio effects (as discussed for $\theta=0°$) panels would not be considered.

At Joint 2 it was expected that these compressive strains would control water ingress. However, at higher applied stress levels ($\geq 0.45f_{ult}$), main mortar beds debonded and the panels were effectively split into distinct columns. These columns would carry considerable further loading, as indicated by high compressive strains shown in Fig. 6.16. These high strains indicate the onset of total structural failure, and in effect the failure mode for these distinct columns would be considered as compression, as for $\theta=0°$ panels. A compression failure mode generates cracking in both brick unit and mortar bed leading to an increase in water ingress.

Joint 3 would debond along the mortar bed component which lay parallel to the applied load and compress at its perpend component. The high levels of debonding and cracking along the main mortar bed component were likely to control the behaviour of water ingress of Joint 3. Increased ingress rates would be expected at all stress levels, following similar water ingress patterns as indicated at Joint 1 due to debonding. The magnitude of strains exhibited in Fig. 6.16 would occur across each component at Joint 3.

6.4.4 Effect of varying initial water head and applied stress levels on water ingress through θ=90° panels

Varying the initial head when panels were unstressed found that only a nominal influence was exerted at all joint positions. However, when panels were stressed to $0.3f_{ult}$, then debonding occurred along the main mortar beds resulting in very quick ingress rates at Joint 1 and 3, and effectively instantaneous rates when panels were stressed to $0.45f_{ult}$.

At Joint 2, an applied compressive stress resulted in an improved resistance to water ingress up to $0.3f_{ult}$. Associated cracking corresponding to applied stress levels of $0.45f_{ult}$ resulted in quick ingress rates.

Therefore, for all joints, the magnitude of the initial head was only found influential when applied stresses had caused cracking or debonding.

6.4.5 Relationship between water ingress and strain for θ=90° panels

(a) Joint 1 and Joint 3:

At Joint 1 and 3, the applied stress level was the dominant factor in governing ingress rates due to debonding at the main bed brick/mortar interface. Even low strains of $\leq$-350με generated when applied stress was $0.3f_{ult}$ heavily influenced water ingress rates.

Using average ingress results from panels 2E, 3E and 4E (Section 6.4.1), the relationship between the volume of water ingress within the initial 10mins of testing and the corresponding strain level across Joints 1 and 3 are shown in Figs 6.17 and 6.18 respectively.

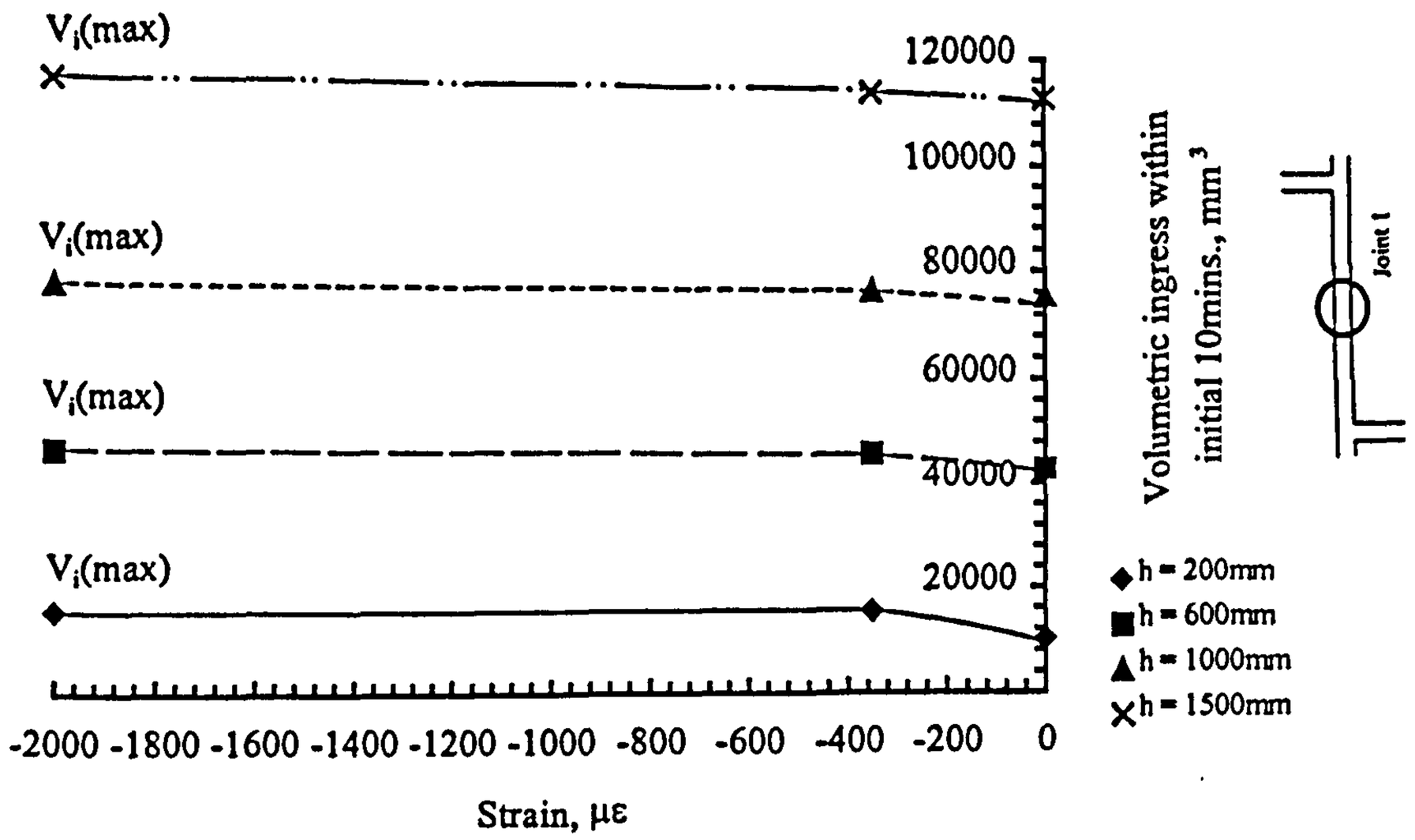

Fig. 6.17 Volume intake within initial 10mins at Joint 1 under three levels of stress for bed orientation θ=90°

Figure 6.17 showed that Joint 1 was particularly prone to water ingress. After the strain reached levels greater than -350με, Joint 1 provided little or no resistance to water ingress for any value of initial water head.

When applied stress levels were $\geq 0.45 f_{ult}$ water ingress was almost instantaneous at Joint 1. These ingress rates were represented in Fig. 6.17 as the initial head level multiplied by the reservoir face area and is indicative of the maximum possible volume of water ingress, V_i(max).

Figure 6.18 shows the volume ingress-strain relationships for Joint 3. These are of a similar form to those exhibited at Joint 1 (Fig. 6.17).

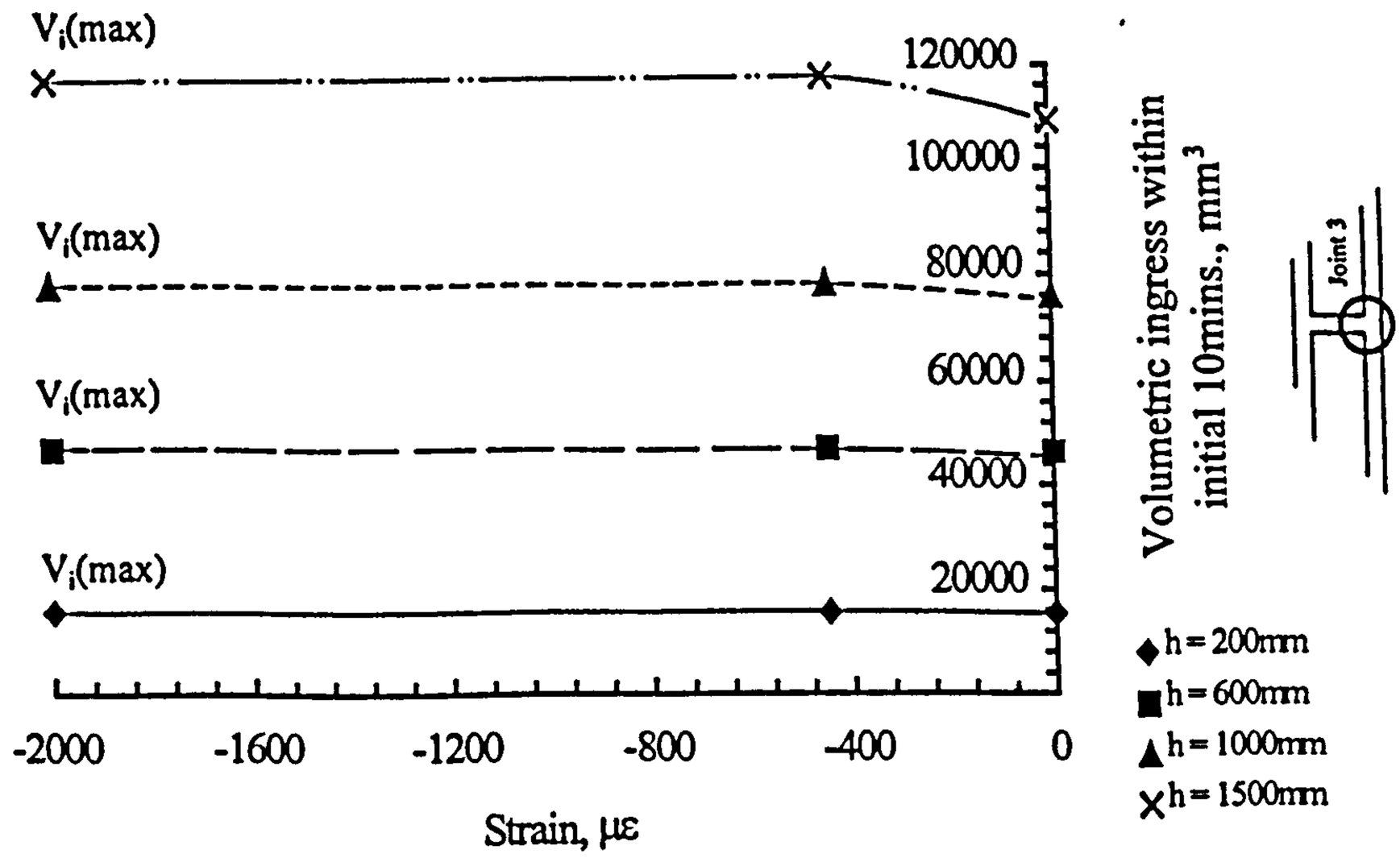

Fig. 6.18 Volume intake within initial 10mins at Joint 3 under three levels of stress for bed orientation $\theta = 90°$

Joint 3 behaved similarly to Joint 1, reaching maximum water ingress at approximately -450με, this strain being measured across the main mortar bed.

Ingress was slightly lower than that for Joint 1 due to the presence of the perpend component which resisted some, though relatively minor water ingress at low applied stress levels ($<0.3f_{ult}$). When applied stress levels were $\geq 0.45f_{ult}$ then almost instantaneous ingress was recorded.

The maximum volume ingress as exhibited in Figs 6.17 and 6.18 is a measure of the total volume of ingress that can occur dependent upon initial head, e.g. initial head h=1500mm, reservoir diameter =10mm, maximum volume ingress, $V_i = 117810mm^3$ (V_i(max)).

(b) Joint 2:

Figure 6.19 shows the average volume ingress-strain relationship for Joint 2.

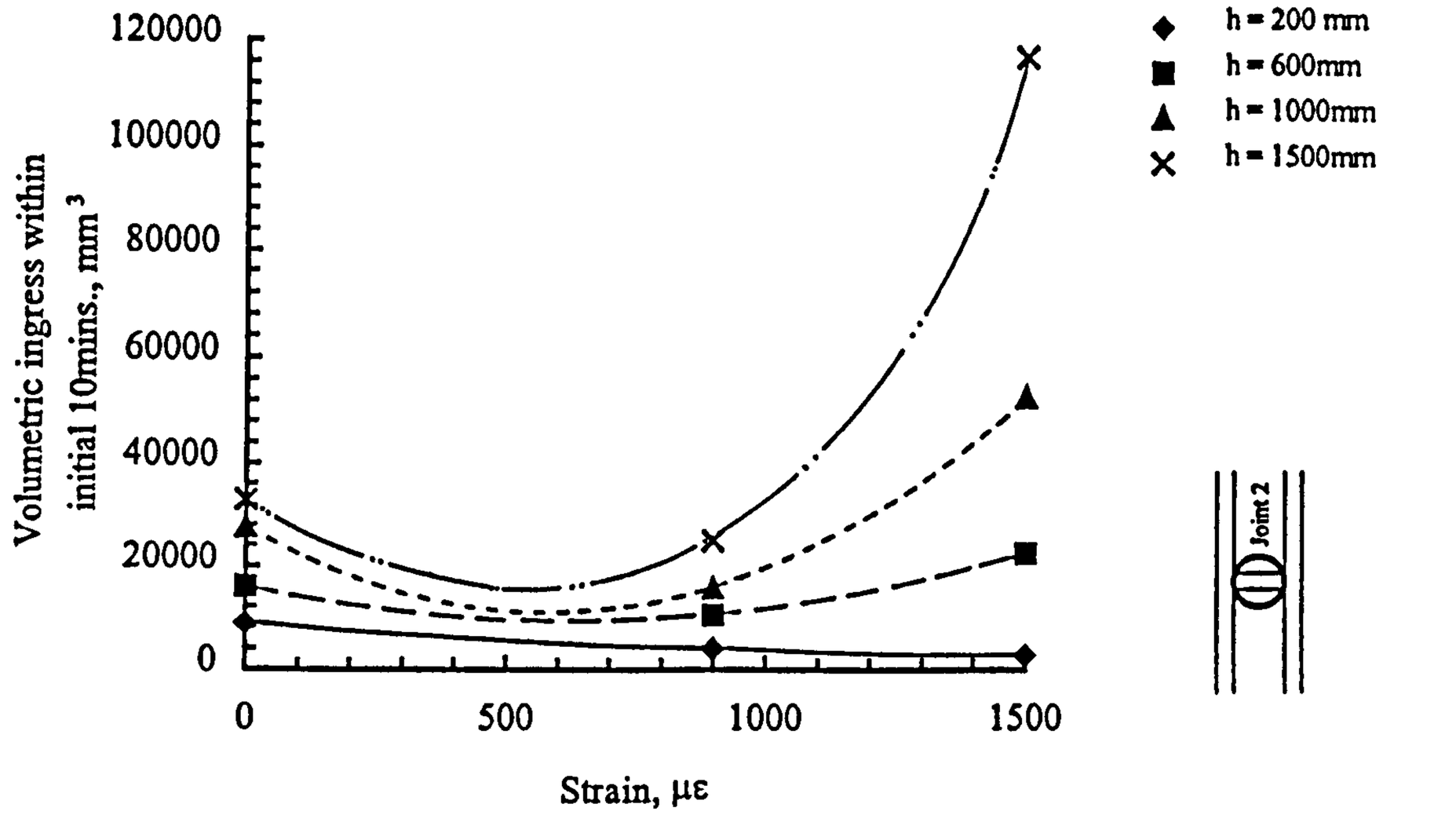

Fig. 6.19 Volume intake within initial 10mins at Joint 2 under three levels of stress for bed orientation $\theta = 90°$

Joint 2 showed an improvement in its resistance to water ingress up to a maximum compressive strain of between 450με and 550με. This was equivalent to an applied stress level of approximately $0.3f_{ult}$ or $3.8N/mm^2$. Thereafter the volumetric ingress-strain relationship showed a marked increase in water penetration.

High applied stresses caused $\theta=90°$ panels to form into a number of independent and distinct columns. Higher applied compressive stresses induced greater lateral stresses with accompanying lateral strains, creating vertical cracking in the mortar joint. This occurred for applied stress levels $\geq 0.45f_{ult}$ leading to an increase in water ingress. Eventually water ingress at Joint 2 would correspond to those at Joint 1 and 3, i.e. effectively instantaneous water ingress at high applied stress levels.

6.4.6 Effect of joint type on water ingress for θ=90° panels

Jcints 1 and 3 behaved similarly for all panels tested, each being dependent upon the extent of debonding at the brick/mortar interface at low stress levels. The critical stress level for Joints 1 and 3 is when an applied stress level of $0.3f_{ult}$ was reached. At this stress level, a rapid increase in water ingress was noted compared to those rates when panels were unstressed. After $0.3f_{ult}$ the panels largely fail in their ability to resist water ingress.

Joint 2 at stress levels $\leq 0.45f_{ult}$ performed better than Joints 1 and 3 in resisting water ingress. However at higher stress levels ($>0.45f_{ult}$) water ingress rates increased and it was predicted that as the panel neared failure there would be a breakdown in the mortar bed caused by cracking similar to that exhibited by a compression failure.

Therefore as applied stress increased to $>0.45f_{ult}$ and the onset of structural failure began then all joint positions became compromised to increased rates of ingress.

6.5 Water Ingress Characteristics When Bed Orientation θ=30°

For θ=0° and θ=90° panels, compression failure and tension failure occurred respectively. When the main mortar bed of a panel was orientated at 30° to the applied load, then a combination of both these failure modes occurred with compressive strains being the more dominant. Partial shearing along the brick/mortar interface of a main mortar bed would occur leading to the creation of cracks within these beds and prompting an increase in water ingress prior to total structural failure. Limited tensile cracking within the perpends would also occur and produce quicker water ingress rates though these would be inhibited at low load levels by Poisson's ratio effects.

6.5.1 Panel testing

A Type 4 panel (4B) was used for this experimental study. Panel 4B had a cross section of 230x100mm and a failure load (F_{ult}) of 230kN, with a corresponding failure stress (f_{ult}) of 10N/mm^2. This allowed water ingress characteristics to be measured at 3N/mm^2 ($0.3f_{ult}$), 4.5N/mm^2 ($0.45f_{ult}$) and 6N/mm^2 ($0.6f_{ult}$).

For information, the location of permeameters and demec points for panel 4B is shown in Fig. 6.20.

Demec points used in this experimental programme were able to note any slippage along a mortar bed. Figure 6.21 shows a simplified demonstration of demec movement denoting any slippage or likely compression.

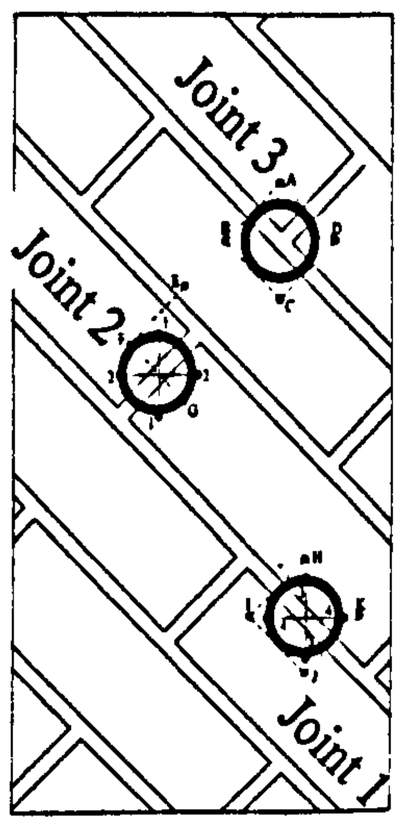

Fig. 6.20 Permeameter and demec positions for panel with bed orientation θ=30°

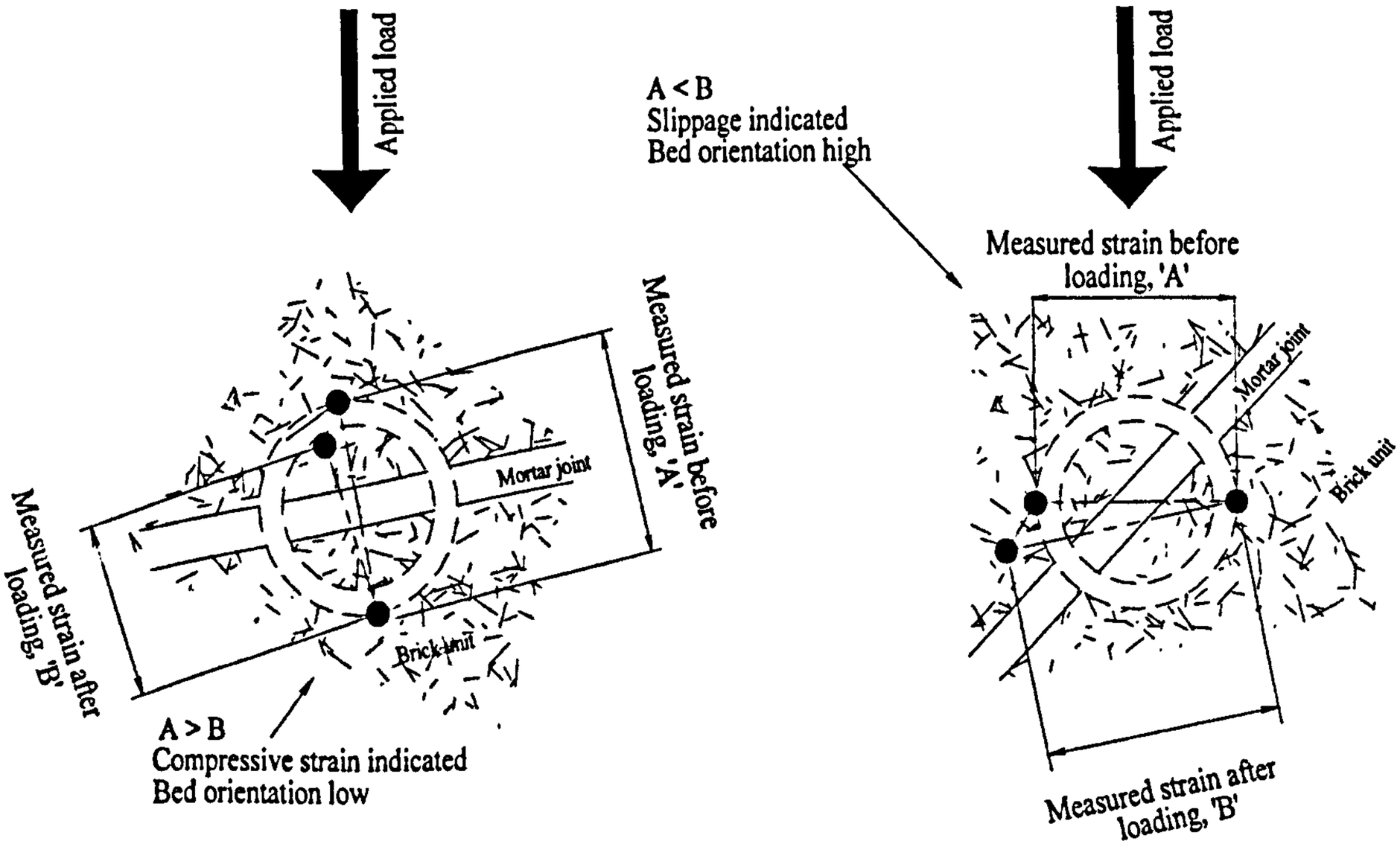

Fig. 6.21 Movement of demec buttons across Joint 1 leading to the measurement of both compressive and tensile strains

The measurement of strain exhibited in Fig. 6.21 is similar for all panels that have intermediate bed orientations.

The water ingress rates for panel 4B are shown in Figs 6.22-6.24. These relationships indicate the influence of applied stress level and initial head (h) on water ingress with time. For simplification, these relationships are identified in terms of their joint position.

At all joint positions, falling head-time relationships exhibited good decay characteristics and would be used to gauge the influence that applied stress level and initial head have in controlling ingress. It is likely that ingress rate for Joint 3, at $0.45f_{ult}$ and initial head of 1000mm is anomalous and that this rate would likely be lower.

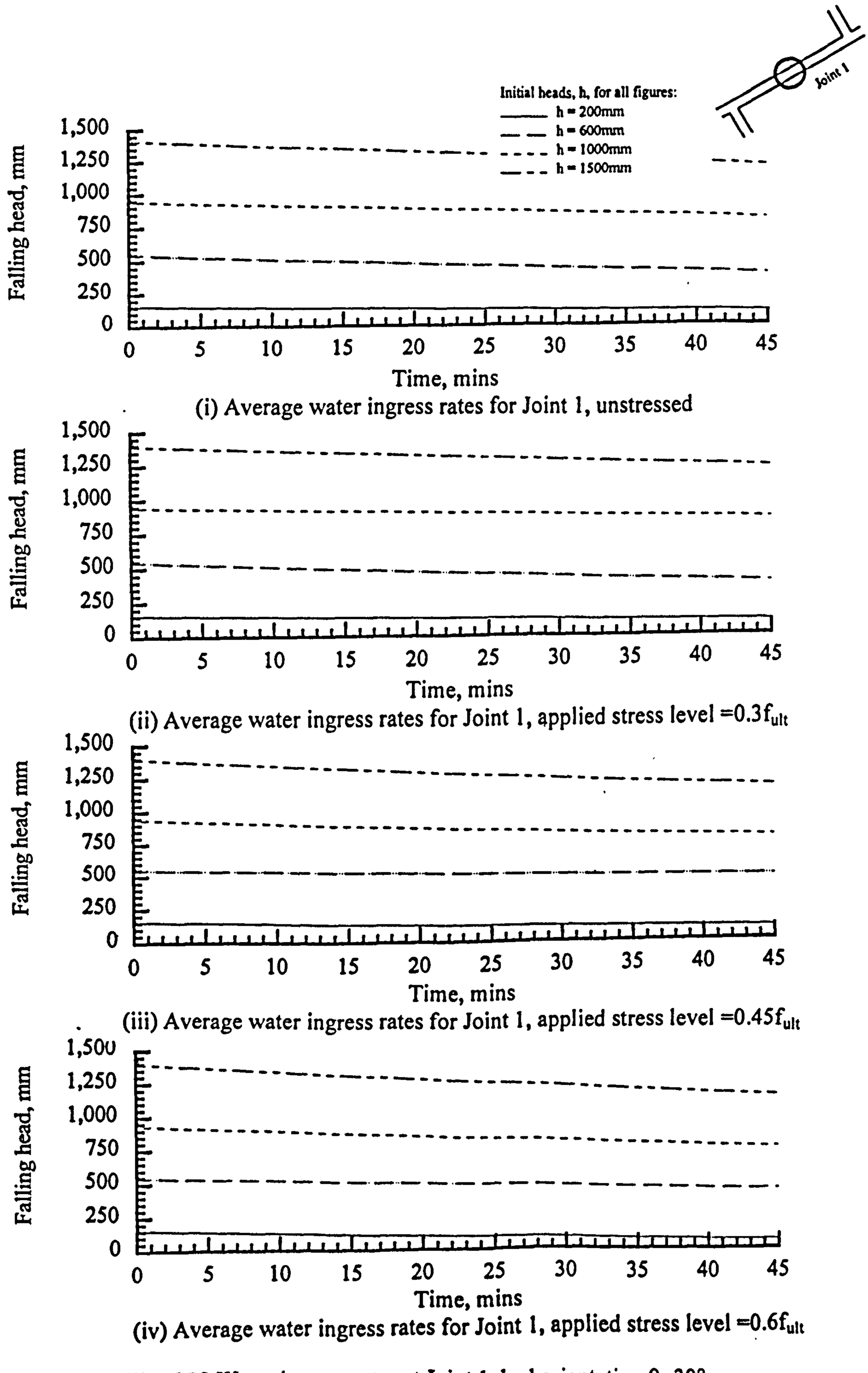

(i) Average water ingress rates for Joint 1, unstressed

(ii) Average water ingress rates for Joint 1, applied stress level $=0.3f_{ult}$

(iii) Average water ingress rates for Joint 1, applied stress level $=0.45f_{ult}$

(iv) Average water ingress rates for Joint 1, applied stress level $=0.6f_{ult}$

Fig. 6.22 Water ingress rates at Joint 1, bed orientation $\theta=30°$

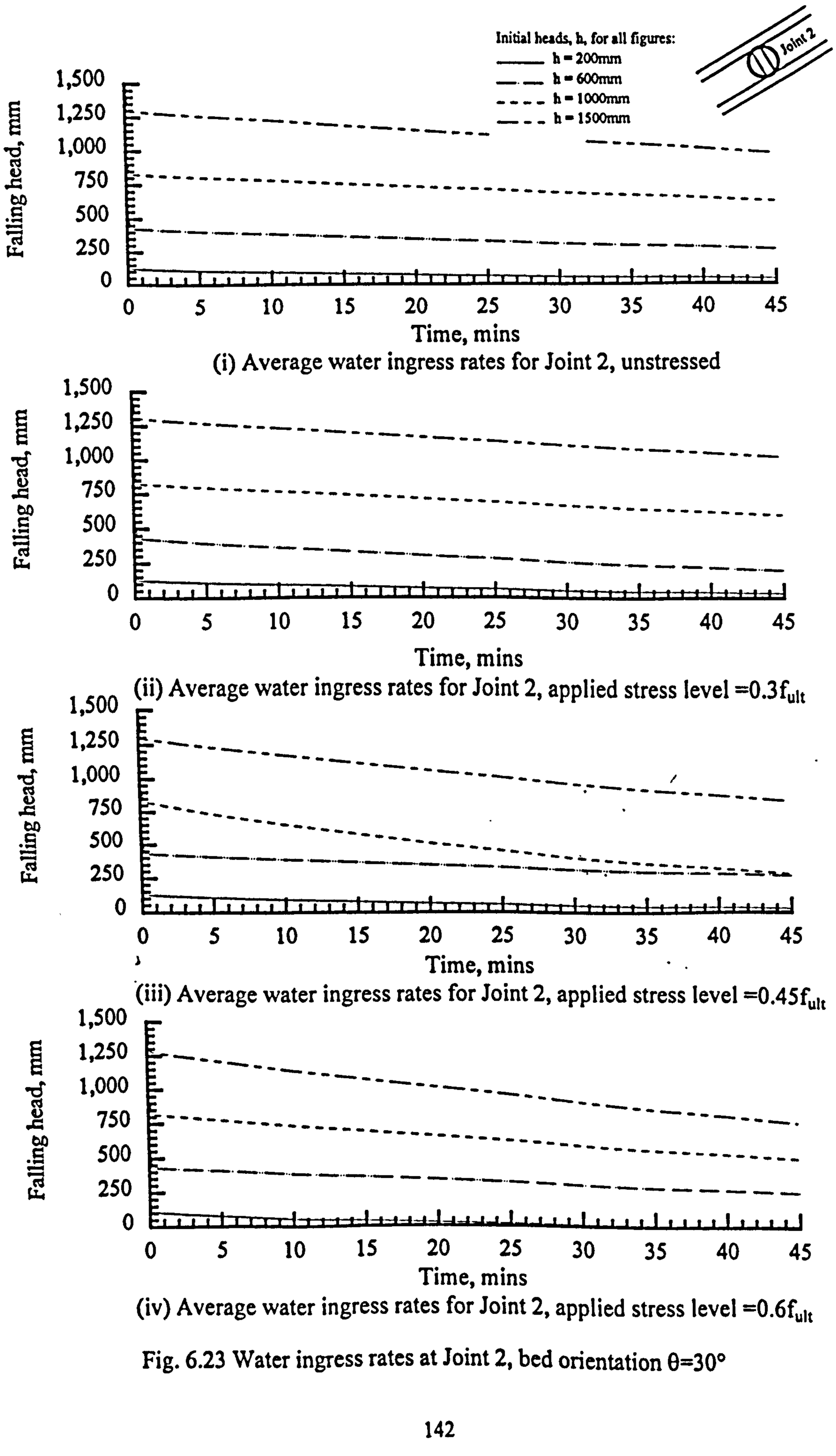

(i) Average water ingress rates for Joint 2, unstressed

(ii) Average water ingress rates for Joint 2, applied stress level =0.3f_{ult}

(iii) Average water ingress rates for Joint 2, applied stress level =0.45f_{ult}

(iv) Average water ingress rates for Joint 2, applied stress level =0.6f_{ult}

Fig. 6.23 Water ingress rates at Joint 2, bed orientation θ=30°

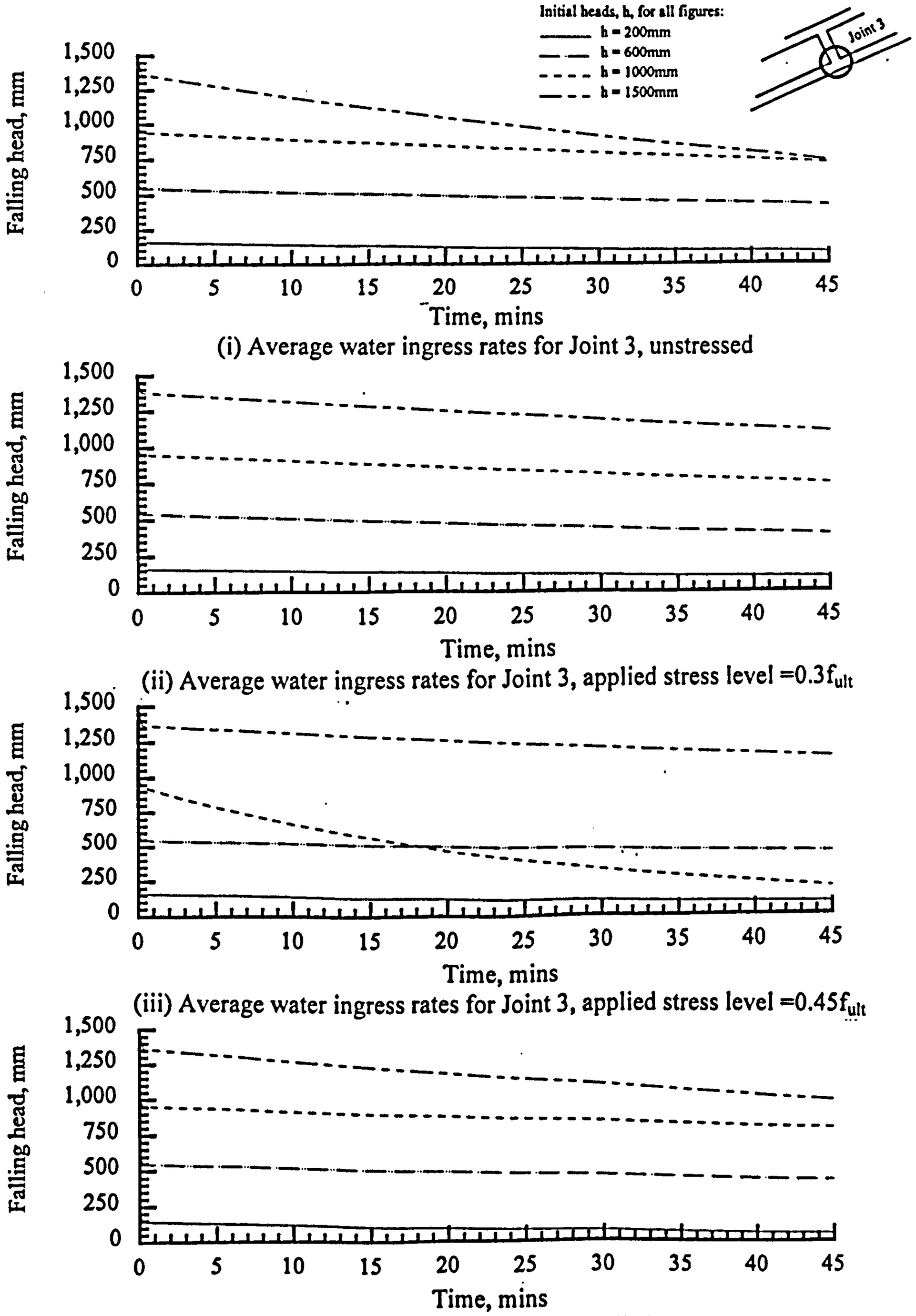

Fig. 6.24 Water ingress rates at Joint 3, bed orientation θ=30°

6.5.2 Modelling of water ingress rate results

Experimental results indicating ingress rates for panel 4B were found to best-fit decay relationships. These can be consulted in Table 6.7.

Table 6.7 Decay curves and coefficient of correlation values for panels with bed orientation θ=30°

Initial head, h (mm)	Applied stress, (N/mm^2)	Joint 1		Joint 2		Joint 3	
		y =	R^2	y =	R^2	y =	R^2
200	0.00 f_{ult}	$155e^{-0.0088t}$	0.99	$123e^{-0.0266t}$	1.0	$165e^{-0.0143t}$	1.0
	0.30 f_{ult}	$155e^{-0.0078t}$	1.0	$125e^{-0.0303t}$	0.98	$163e^{-0.0119t}$	1.0
	0.45 f_{ult}	$155e^{-0.0112t}$	1.0	$127e^{-0.0339t}$	0.98	$162e^{-0.0105t}$	1.0
	0.60 f_{ult}	$156e^{-0.0204t}$	0.98	$125e^{-0.0725t}$	0.98	$163e^{-0.0233t}$	0.90
600	0.00 f_{ult}	$547e^{-0.0072t}$	0.99	$426e^{-0.0109t}$	0.92	$546e^{-0.0056t}$	0.96
	0.30 f_{ult}	$548e^{-0.0074t}$	0.98	$430e^{-0.0172t}$	0.96	$540e^{-0.0068t}$	0.90
	0.45 f_{ult}	$547e^{-0.0032t}$	0.98	$432e^{-0.0108t}$	0.95	$545e^{-0.0047t}$	0.96
	0.60 f_{ult}	$544e^{-0.0047t}$	0.98	$431e^{-0.0120t}$	0.97	$546e^{-0.0056t}$	0.95
1000	0.00 f_{ult}	$942e^{-0.0031t}$	0.99	$828e^{-0.0065t}$	0.94	$941e^{-0.0058t}$	0.95
	0.30 f_{ult}	$942e^{-0.0020t}$	0.95	$826e^{-0.0072t}$	0.94	$952e^{-0.0053t}$	0.95
	0.45 f_{ult}	$940e^{-0.0043t}$	0.97	$832e^{-0.0243t}$	0.99	$941e^{-0.0355t}$	0.99
	0.60 f_{ult}	$931e^{-0.0048t}$	0.94	$830e^{-0.0110t}$	0.92	$953e^{-0.0043t}$	0.93
1500	0.00 f_{ult}	$1410e^{-0.0032t}$	1.0	$1297e^{-0.0064t}$	0.91	$1366e^{-0.0136t}$	0.99
	0.30 f_{ult}	$1394e^{-0.0026t}$	0.94	$1306e^{-0.0055t}$	0.93	$1381e^{-0.0049t}$	0.94
	0.45 f_{ult}	$1397e^{-0.0041t}$	0.97	$1297e^{-0.0100t}$	0.94	$1371e^{-0.0044t}$	0.92
	0.60 f_{ult}	$1379e^{-0.0047t}$	0.96	$1280e^{-0.0116t}$	0.96	$1363e^{-0.0073t}$	0.93

y - Water head in reservoir
t - Time from the commencement of testing
f_{ult} - Average predicted failure stress for panel; for θ=30° panels, f_{ult} = 10N/mm^2

Each best-fit relationship was based on ingress after the initial 15secs to avoid any settling effects. These theoretical relationships showed good agreement with experimental data points, this being reflected by the average coefficient of correlation R^2=0.97 for all joints.

In Chapter 8, the above generated decay equations (Table 6.7) were used to form an empirical water ingress relationship based on applied stress, initial head and bed orientation.

6.5.3 Effect of varying applied stress level on strain for θ=30° panels

Figure 6.25 shows the average stress-strain relationship across the main mortar bed (Joint 1) and the perpend component (Joint 2). This average was based on 4 tests each to stress level of $0.3f_{ult}$, $0.45f_{ult}$ and $0.6f_{ult}$ for panel 4B. The strains exhibited across the main mortar bed and perpend component of Joint 3 were of similar magnitude to those measured across Joint 1 and 2. The stress-strain relationship for Joint 3 is omitted for clarity.

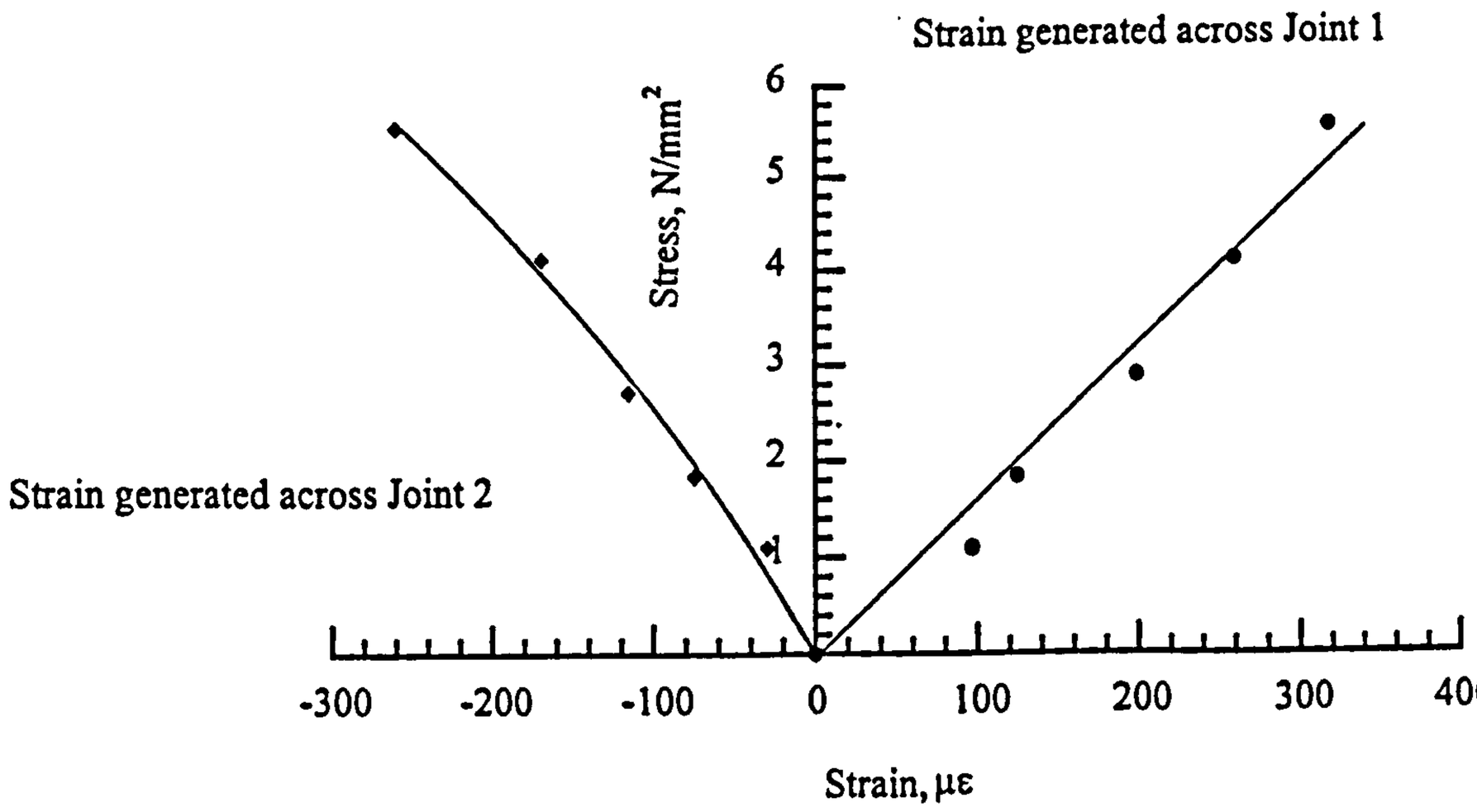

Fig. 6.25 Average stress-strain relationship for masonry joints, bed orientation θ=30°

Figure 6.25 indicates that the test positions along the main mortar bed (Joint 1 and part Joint 3) were compressed whilst the perpend joint (Joint 2 and part Joint 3) exhibited tensile strains.

As mortar beds orientated towards tensile failure (θ=90°) from compression failure (θ=0°) then the strain generated across all joints would have both a combination of compressive and tensile components.

For Joint 1 at low stress levels, no shear slip occurred. This was indicated by relatively low tensile strains (approximately -70με at $0.3f_{ult}$ corresponding to compressive strains of ≅200με at the same stress level as indicated in Fig. 6.25). At higher applied stress levels (≅$0.6f_{ult}$) the brick/mortar interface became increasingly compromised with cracking being created along potential shear planes. These stresses generated compressive strains ≥300με concomitantly with tensile strains of -170με.

At Joint 2, strain values increased from -120με at $0.3f_{ult}$ to -230με at $0.6f_{ult}$. The behaviour of this joint would be similar to that as discussed θ=0° panels. It was believed that any strains generated at low load levels were accommodated by Poisson's ratio effects. However as stress increased, a threshold tensile strain would be reached and surpassed, thereafter cracking and debonding would occur.

The behaviour of Joint 3 would be influenced, as for Joint 1, by compressive strains and latterly by shearing.

Comparing Fig. 6.25 with Fig. 6.7 (stress-strain relationship for θ=0° panels, Section 6.3.3) compression strains reduced from 600με at $0.6f_{ult}$ to 330με for θ=30° panels. Tensile strains increased from -120με at θ=0° to -230με for θ=30° panels. Compressive strains were generally found to halve when orientations increased from θ=0° to 30°. Conversely, tensile strains approximately doubled.

6.5.4 Effect of varying initial water head and applied stress level on water ingress through θ=30° panels

Considering the effect of the initial water head alone, the influence of this parameter can be gauged only when the panel was unstressed.

Table 6.8 shows the water head from a position after 15secs to a level after 10mins of testing for Joints 1 and 2 when the panel was unstressed.

Table 6.8 Head drop in test reservoir after 10mins of testing dependent upon initial head, h

	Initial head, h (mm)			
	200	**600**	**1000**	**1500**
Joint 1	40	48	44	50
Joint 2	78	70	110	188

Joint 1 exhibited a very slight increase in ingress rates when the panel was unstressed. However as the pressure head was increased from 200mm to 1500mm, the effect can be considered of only minor importance at this particular position.

Joint 2 showed increasingly larger head drops as initial head increased. However the increase was only two fold compared to the major increase in pressure head and was again considered of only minor significance.

Behaviour exhibited at Joint 3 was an amalgam of Joints 1 and 2, though the influence of the Joint 1 component would be the more dominant. A larger area of brick/mortar interface at the main bed component (Joint 1) is available for water ingress compared to the perpend component (Joint 2). This indicated that the main bed would be influential in controlling water ingress at Joint 3. However, the main bed component compressed (at low load levels) and the perpend component laterally expanded creating an area of high stress concentrations likely to induce cracking and influence water ingress.

Generally, the initial head would only become influential once the applied stress had extended or created new fissures for increasingly higher initial water heads to exploit.

6.5.5 Relationship between water ingress and strain for θ=30° panels

(a) Joint 1:

Figure 6.26 shows the volumetric intake-strain relationship at Joint 1 for panel 4B at all initial water heads.

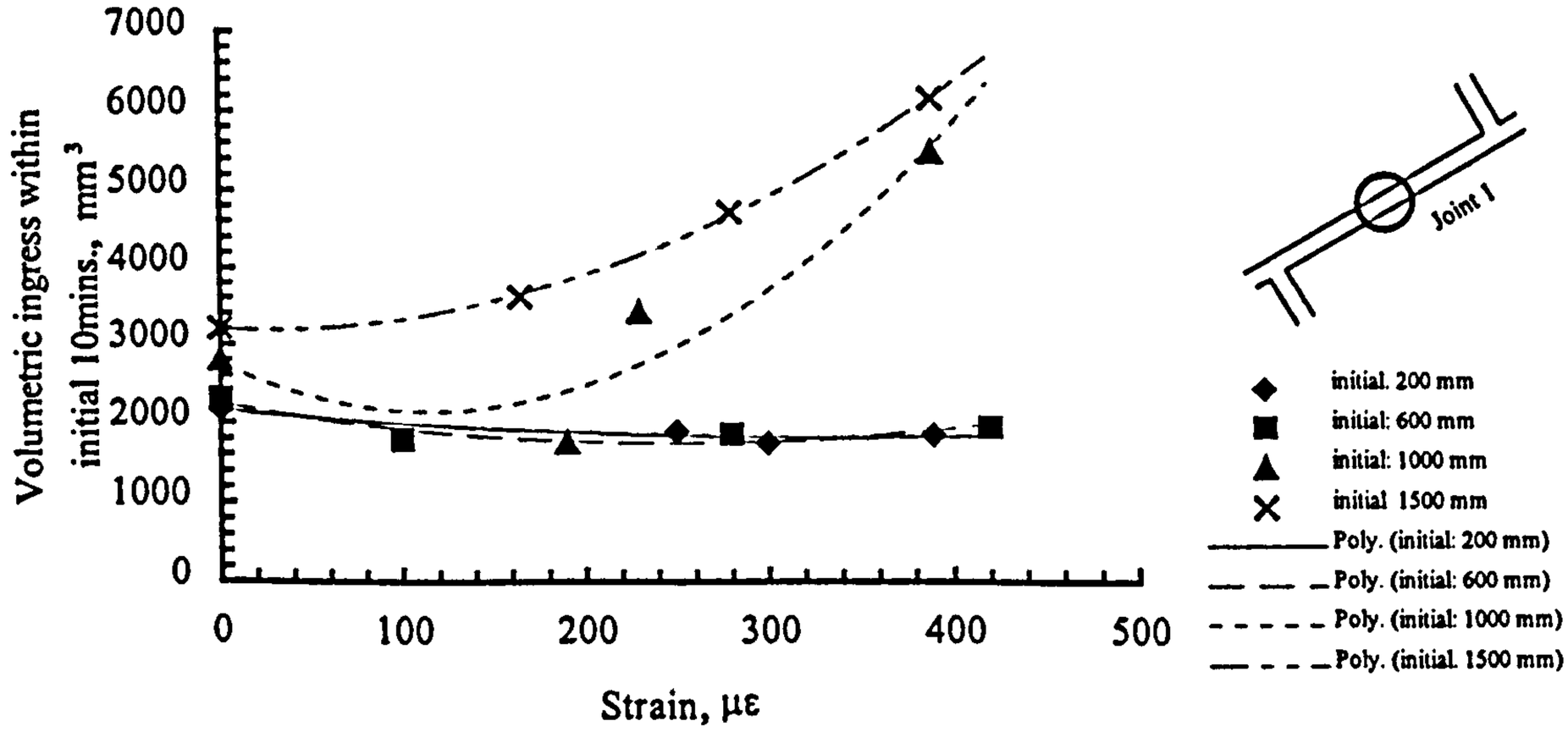

Fig. 6.26 Volume intake within initial 10mins at Joint 1 under four levels of stress for bed orientation θ=30°

The above figure shows strain across Joint 1 had little effect in improving or deteriorating water ingress rates at low initial heads (h≤600mm). However for strains across Joint 1 >175με, then ingress rates increased at higher heads (h≥1000mm).

High strains generated across Joint 1 when the applied stress was $0.6f_{ult}$ also indicated large tensile strains of the order -100με to -170με, which allowed the brick/mortar bond to be partially compromised promoting cracking. Only high initial heads can exploit these shear slips and so an increase in water ingress was measured.

It is likely that volumetric ingress for the initial head of 1000mm corresponding to a strain of 190με is anomalous and was caused by experimental error. It would be expected that water ingress rates were measured slightly higher than that indicated.

The relationships exhibited in Fig. 6.26 can be considered as best-fit second order polynomial equations of the general form as shown in Eqn. 6.2 (Section 6.3.5). Table 6.9 shows these best-fit relationships dependent upon initial water head.

Table 6.9 Standard second order polynomial equations for water ingress at Joint 1

Initial head, h (mm)	Joint 1	
	$V_i =$	R^2
200	$0.003\varepsilon^2 - 2.00\varepsilon + 2163$	0.90
600	$0.008\varepsilon^2 - 4.00\varepsilon + 2242$	0.90
1000	$0.045\varepsilon^2 - 10.38\varepsilon + 2742$	0.90
1500	$0.022\varepsilon^2 - 0.78\varepsilon + 3191$	0.99

The relationships shown in Table 6.9 exhibit good agreement with the experimental data points, with an average coefficient of correlation R^2=0.92.

Figure 6.26 shows that the volume of ingress is lowest immediately prior to the breakdown in water resistance. By differentiating volumetric ingress (V_i) with respect to strain (ε) in Table 6.8, i.e. $dV_i/d\varepsilon$=0, an indication of a threshold compression strain level with respect to the initial water head is found. This is shown in Fig. 6.27.

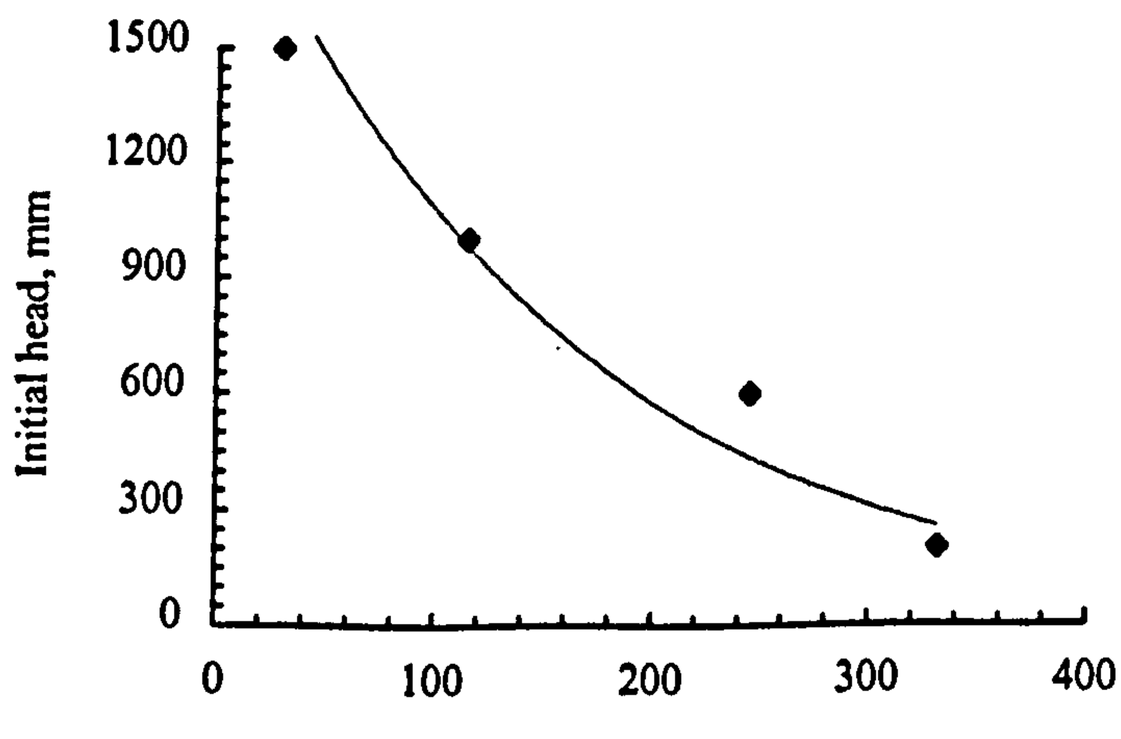

Fig. 6.27 Threshold strains for minimum water ingress dependant upon initial head of water at Joint 1

Figure 6.27 shows that debonding at the brick/mortar interface caused by low applied stress level and hence relatively small strains would be exploited by high initial water heads. When an initial head was 200mm then a threshold compression strain of 330με was required. By considering Fig. 6.25 (stress-strain relationship, Section 6.5.3) this was generated by a stress of 6.0N/mm^2 which is equivalent to $0.6f_{ult}$. For h=1500mm, a compression strain of 20με was required generated at applied stress level $<0.3f_{ult}$.

(b) Joint 2:

Figure 6.28 shows the volume ingress-strain relationship for Joint 2.

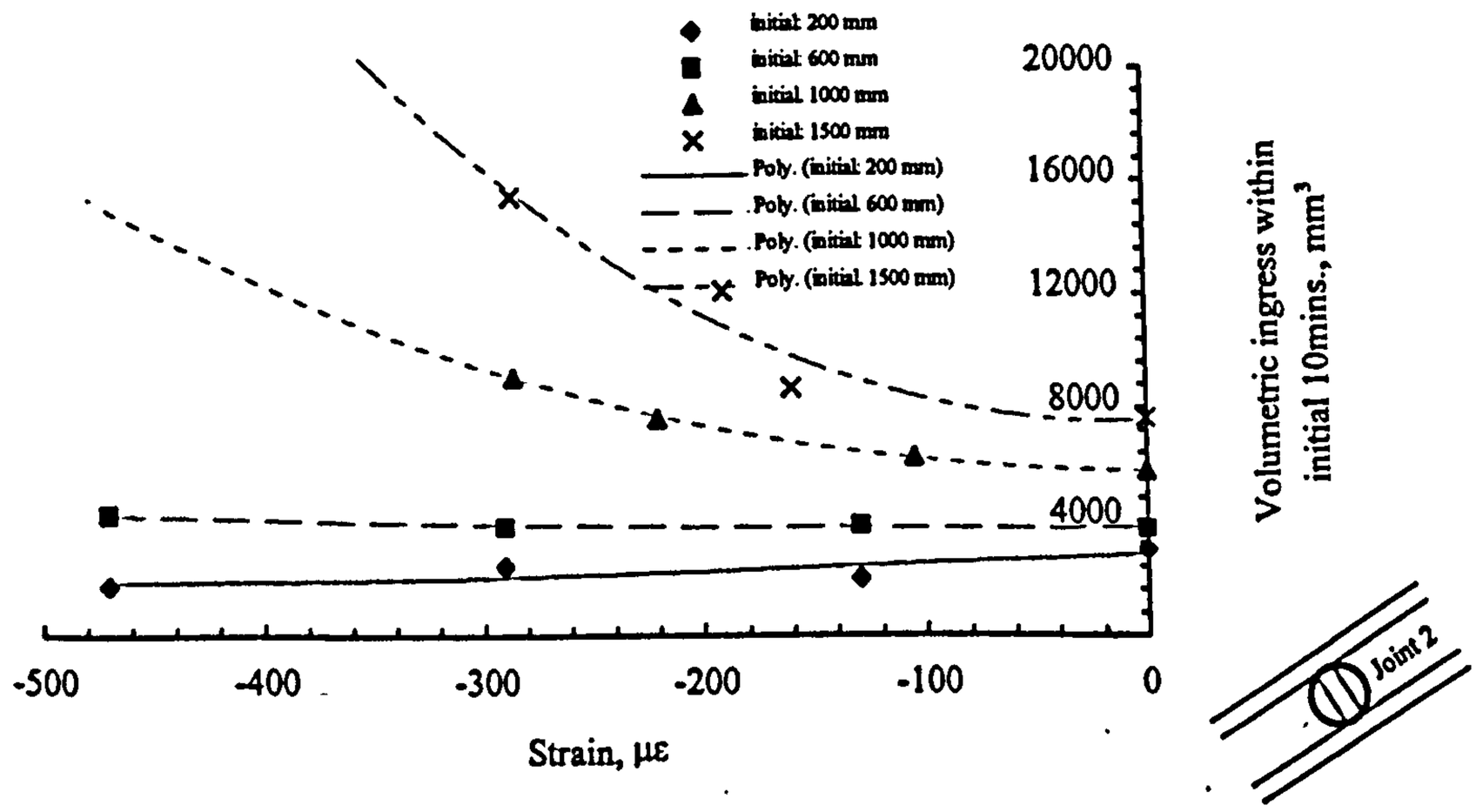

Fig. 6.28 Volume intake within initial 10mins at Joint 2 under four levels of stress for bed orientation θ=30°

The above figure shows that at low initial heads there was a reduction in water ingress rates depending on strain generated across the joint. At h=600mm, the water ingress volume matched almost exactly that of the unstressed panel, i.e. 0με. Thereafter the initial head proved highly influential in exploiting any debonding and cracking. At high head levels of 1000mm and 1500mm, water ingress was shown to increase considerably.

When the panel is loaded, Poisson's ratio effects created a deformation of the mortar, expanding the mortar into cavities at the brick/mortar interface which resulted in the reduction in water ingress. Where these deformations reach a maximum, minimum water ingress would occur. The maximum deformation occurs at the threshold tensile strain. Further loading would generate strains too large to be accommodated by Poisson's effects with the result that debonding occurs and water ingress rates begin to rise. This was similar to the phenomena at Joint 2 for $\theta=0°$ panels and was discussed at length in Section 6.3.5.

Table 6.10 shows the relationships exhibited in Fig. 6.28 as best-fit second order polynomial equations. These were used to estimate the threshold tensile strain across Joint 2.

Table 6.10 Standard second order polynomial equations for water ingress at Joint 2

Initial head, h (mm)	Joint 1	
	$V_i =$	R^2
200	$0.004\varepsilon^2 + 3.77\varepsilon + 2825$	0.80
600	$0.003\varepsilon^2 + 0.51\varepsilon + 3729$	0.89
1000	$0.043\varepsilon^2 + 3.30\varepsilon + 5793$	0.90
1500	$0.1147\varepsilon^2 + 4.41\varepsilon + 7538$	0.92

The relationships shown in Table 6.10 exhibited good agreement with the experimental data points, with an average coefficient of correlation $R^2=0.87$.

Having allowed that the threshold tensile strain would occur when there was a minimum ingress of water, i.e. $dV_i/d\varepsilon=0$, then Fig. 6.29 indicates that this threshold tensile strain is influenced by the initial water head.

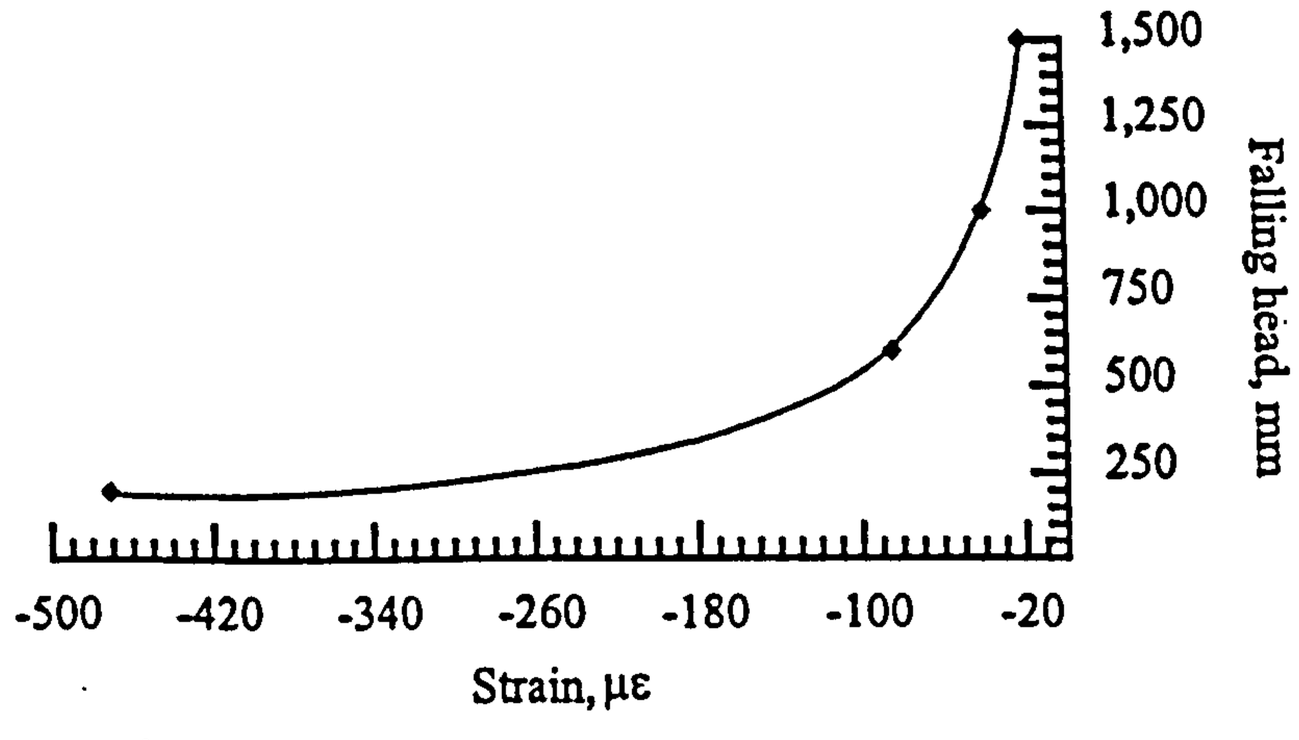

Fig. 6.29 Threshold strains for minimum water ingress as influenced by initial water head at Joint 2

Similar to the relationship exhibited at Joint 1 (Fig. 6.27), the threshold tensile strain is influenced by the height of the initial water head. When an initial head was 200mm then the threshold tensile strain was -470με. Using Fig. 6.25, this would require an equivalent stress value outwith the test range, i.e. $>0.6f_{ult}$. A threshold strain of 20με was generated when initial head was 1500mm. Low strains of this magnitude would be generated for applied stress levels $<0.3f_{ult}$.

As initial water heads increased then any extended fissures or additional cracking would be exploited by the increase in water head. Hence high initial heads required smaller threshold tensile strains.

(c) Joint 3:

Figure 6.30 shows the volumetric ingress-strain relationship for Joint 3. Strain values in this figure were measured across the main bed component of Joint 3.

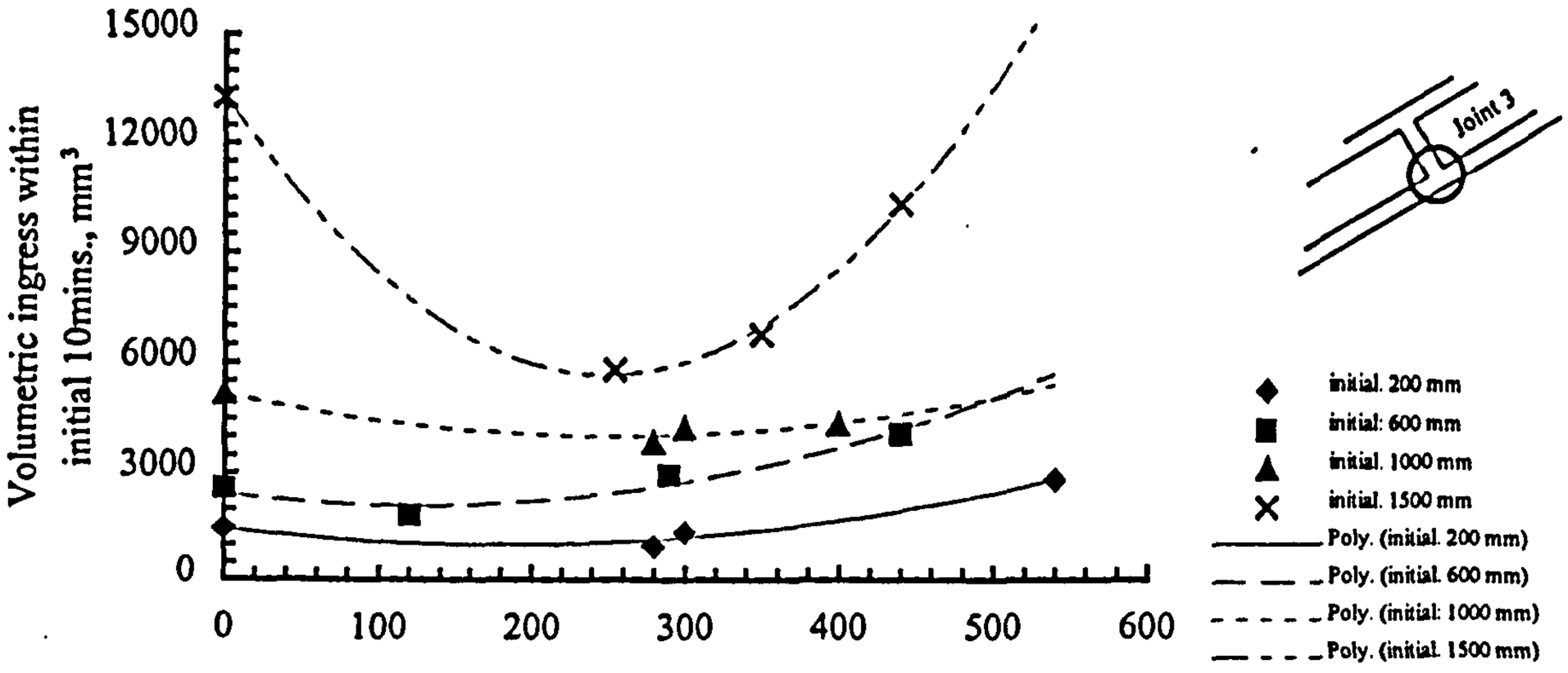

Fig. 6.30 Volume intake within initial 10mins at Joint 3 under four levels of stress for bed orientation θ=30°

The relationships as shown in Fig. 6.30 indicated an improvement in water ingress rates at low levels of strain. This was found to occur for strains between 140με-180με when applied stress level was a maximum at $0.45f_{ult}$. After these strain values were surpassed then volume of water ingress would increase.

The volume ingress relationship for the initial head of 1500mm is felt to be anomalous as a gradual increase in water ingress after the threshold (tensile) strain was surpassed would be expected. Although it is recognised that initial water heads play an important part in influencing ingress rates particularly when considered in conjunction with strain, it is felt that this relationship is too onerous and a less pronounced ingress would be more appropriate. Experimental error was felt to be responsible for these data points.

6.5.6 Effect of joint type on water ingress through θ=30°

Joint 1 was originally found to grow increasingly resistant to water ingress at low applied stress levels ($\leq 0.3f_{ult}$). As applied stress increased then the brick/mortar interface became prone to debonding which corresponded with high water ingress rates. This was likely caused by Joint 1 lying on a probable slip plane and therefore was increasingly influenced by shear forces.

Poisson's ratio effects were found influential across Joint 2 when the applied stress level was low. However, applied stress levels $>0.3f_{ult}$ generated high tensile strains causing incompatible deformations between the brick and mortar which allowed some debonding to occur. This had the effect of increasing water ingress rates particularly for high initial water heads (h≥1000mm).

Joint 3 was relatively unaffected by both shear slip (Joint 1) or the breakdown in Poisson's ratio effect (Joint 2). Shear failure can occur in all orientated mortar beds assuming a constant bond strength. However this factor is highly variable throughout a masonry panel, with failure only occurring at the weakest bond. Therefore Joint 3 may resist further loading whereas Joint 1 had already failed. This is emphasised in the water ingress results whereby Joint 1 exhibited increasingly larger ingress rates at high initial heads (1000mm, 1500mm) and stress levels compared to those exhibited at Joint 3 (Figs 6.26, 6.28).

Therefore, Joints 1 and Joint 3, (assuming the same brick/mortar bond strength was exhibited in all beds), would be the main areas of water ingress when panels were loaded due to the shear slip failure associated with θ=30° panels.

6.6 Water Ingress Characteristics when Bed Orientation θ=45°

When the test panel was orientated at 45° then this would generate both tensile and compressive strains perpendicular and parallel to the applied load at low stress levels. High applied stresses would also induce shearing along the main orientated mortar bed (Joint 1 and part of Joint 3). The perpend joints (Joint 2 and part of Joint 3) were now orientated so that they were subjected to more direct compressive forces.

The prospective failure mode would have a fundamental controlling factor in governing water ingress. Increased loading produced extensive shear slippage at the brick/mortar interface and debonding at the perpendicular mortar joints, both promoting increased water ingress.

6.6.1 Panel testing

Both Type 3 and 4 brick panels were used for this assessment. Type 3 panels (3C) had a cross section of 100x275mm with an ultimate failure load (F_{ult}) of 90kN, generating a predicted failure stress (f_{ult}) of 3.3N/mm^2. For this panel, water ingress was monitored when applied stress was 1.0N/mm^2 ($0.3f_{ult}$), 1.5N/mm^2 ($0.45f_{ult}$) and 2N/mm^2 ($0.6f_{ult}$). Type 4 panel (4C) had a cross section of 100x250mm with a predicted failure load of 253kN, which allowed water ingress to be measured when applied stress levels were 3.0N/mm^2 ($0.3f_{ult}$), 4.5N/mm^2 ($0.45f_{ult}$) and 6.0N/mm^2 ($0.6f_{ult}$). A predicted failure stress (f_{ult}) of 10N/mm^2 was assumed for panel 4C.

For information the location of permeameters and demec gauges are shown in Fig. 6.31 for panels 3C and 4C.

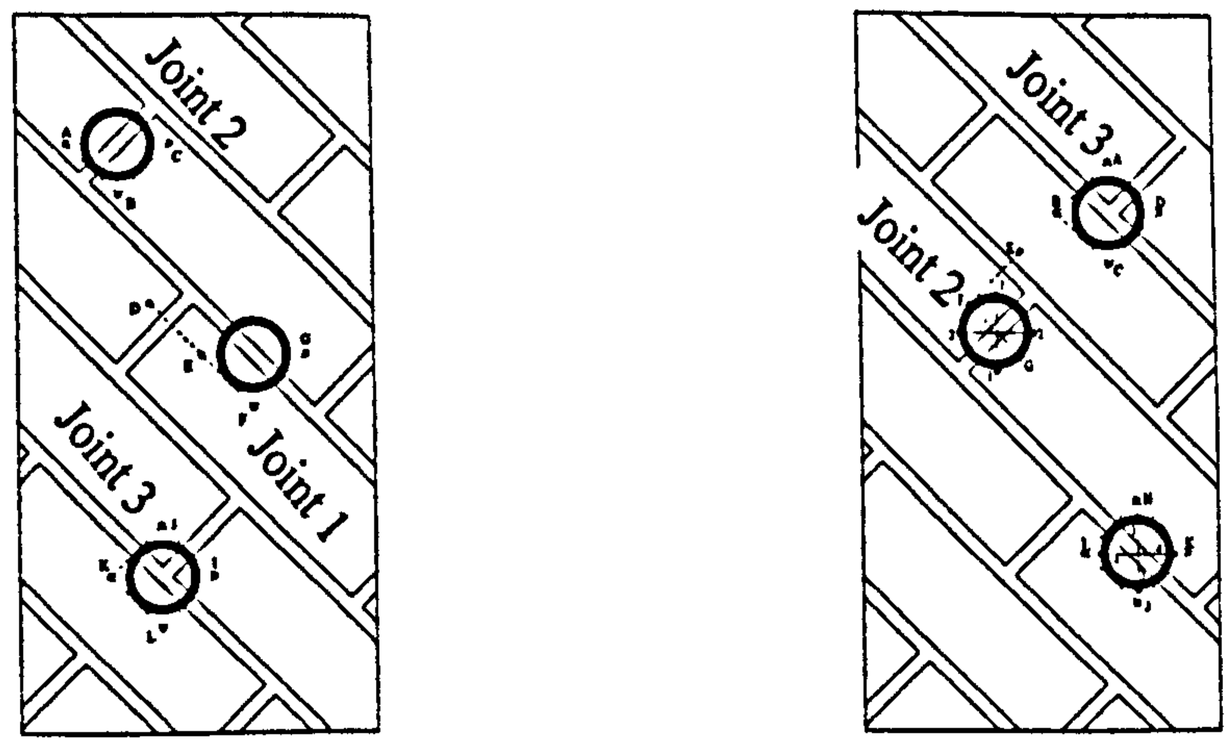

3C 4C

Fig. 6.31 Permeameter and demec positions for panels with bed orientation θ=45°

The average water ingress rates using panels 3C and 4C are shown in Figs 6.32-6.34 and indicates the influence of applied stress level and initial head on water ingress with time. For simplification, relationships generated here are identified in terms of joint position.

At Joint 1 (Fig. 6.32) as stress levels increased to $0.6f_{ult}$ there was an obvious increase in water ingress rates. Joint 2 (Fig. 6.33) exhibited similar water ingress rates throughout the whole stress range. Joint 3 (Fig. 6.34) water ingress rates were very poor irrespective of applied stress level, this being indicated by the very small duration of test. Generally as stress level increased, ingress rates quickened.

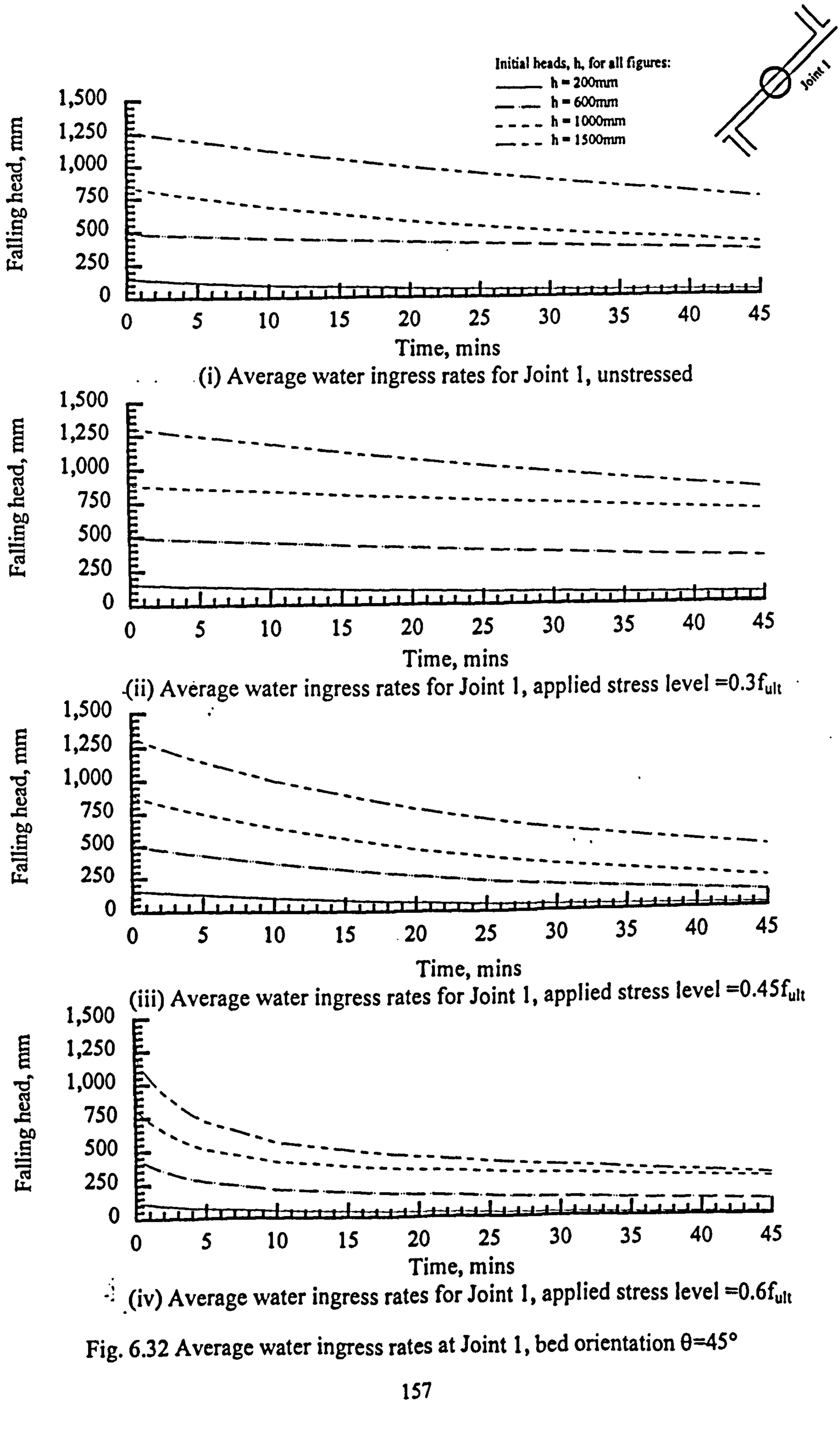

(i) Average water ingress rates for Joint 1, unstressed

(ii) Average water ingress rates for Joint 1, applied stress level =0.3f_{ult}

(iii) Average water ingress rates for Joint 1, applied stress level =0.45f_{ult}

(iv) Average water ingress rates for Joint 1, applied stress level =0.6f_{ult}

Fig. 6.32 Average water ingress rates at Joint 1, bed orientation θ=45°

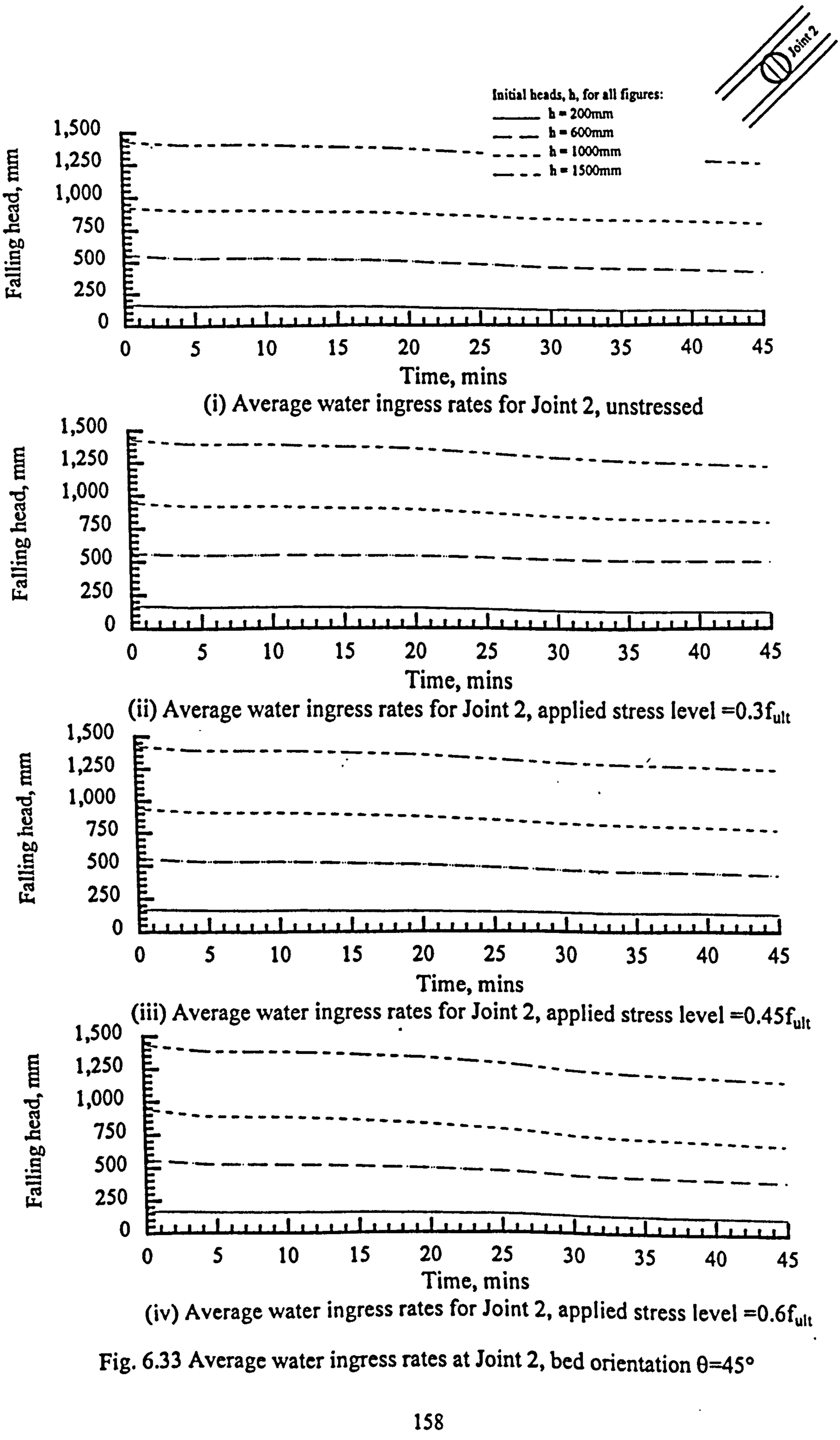

Fig. 6.33 Average water ingress rates at Joint 2, bed orientation θ=45°

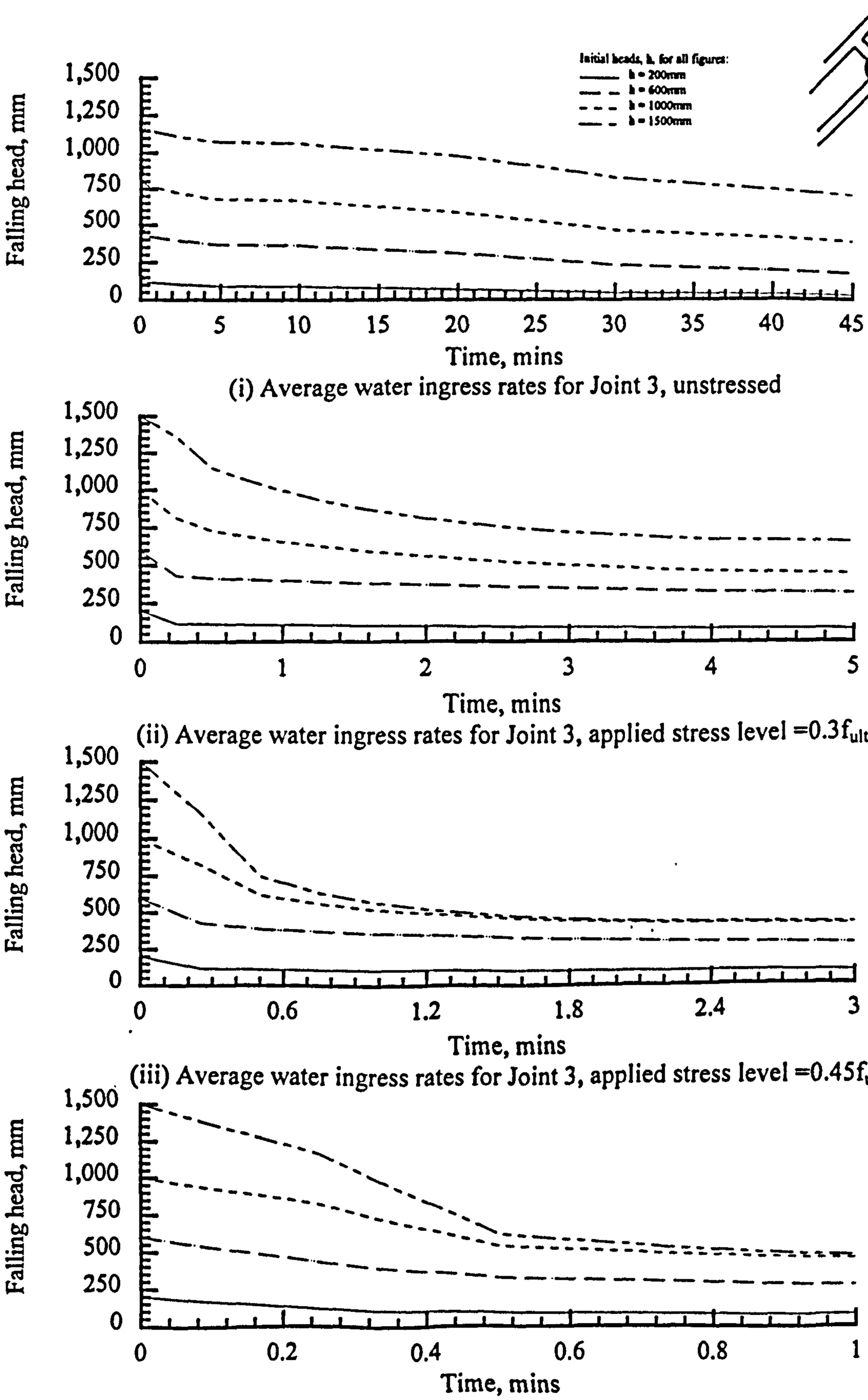

Fig. 6.34 Average water ingress rates at Joint 3, bed orientation θ=45°

6.6.2 Modelling of water ingress rate results

Similar to previous panels, average water ingress rates as measured experimentally for panels 3C and 4C were found to best-fit decay relationships. These are shown in Table 6.11.

These relationships showed good agreement with experimental data points, with the average coefficient of correlation R^2=0.95.

Table 6.11 Average decay curves and coefficient of correlation values for panels with bed orientation θ=45°

Initial head, h (mm)	Applied stress, (N/mm²)	Joint 1		Joint 2		Joint 3	
		y =	R²	y =	R²	y =	R²
200	0.00f_{ult}	$148e^{-0.0462t}$	1.0	$165e^{-0.0171t}$	1.0	$116e^{-0.0447t}$	0.98
	0.30 f_{ult}	$151e^{-0.0183t}$	1.0	$168e^{-0.0121t}$	1.0	$120e^{-0.0283t}$	1.0
	0.45 f_{ult}	$157e^{-0.0436t}$	1.0	$169e^{-0.0085t}$	1.0	$123e^{-0.0208t}$	1.0
	0.60 f_{ult}	$158e^{-0.0464t}$	1.0	$168e^{-0.0109t}$	1.0	$116e^{-0.0162t}$	1.0
600	0.00 f_{ult}	$486e^{-0.0078t}$	1.0	$559e^{-0.0160t}$	1.0	$580e^{-0.0322t}$	0.94
	0.30 f_{ult}	$495e^{-0.0090t}$	1.0	$559e^{-0.0040t}$	1.0	$570e^{-0.0261t}$	0.84
	0.45 f_{ult}	$505e^{-0.0323t}$	1.0	$553e^{-0.0089t}$	1.0	$573e^{-0.0186t}$	0.80
	0.60 f_{ult}	$510e^{-0.0311t}$	1.0	$554e^{-0.0104t}$	1.0	$572e^{-0.0157t}$	0.75
1000	0.00 f_{ult}	$838e^{-0.0209t}$	1.0	$923e^{-0.0054t}$	1.0	$911e^{-0.0671t}$	0.95
	0.30 f_{ult}	$881e^{-0.0058t}$	1.0	$941e^{-0.0057t}$	1.0	$908e^{-0.0875t}$	0.89
	0.45 f_{ult}	$877e^{-0.0305t}$	1.0	$938e^{-0.0069t}$	1.0	$908e^{-0.0614t}$	0.44
	0.60 f_{ult}	$872e^{-0.0238t}$	1.0	$935e^{-0.0105t}$	1.0	$899e^{-0.0743t}$	0.37
1500	0.00 f_{ult}	$1269e^{-0.0129t}$	0.98	$1432e^{-0.0047t}$	1.0	$1481e^{-0.0670t}$	0.58
	0.30 f_{ult}	$1305e^{-0.0099t}$	0.90	$1431e^{-0.0055t}$	1.0	$1481e^{-0.0518t}$	0.43
	0.45 f_{ult}	$1302e^{-0.0239t}$	0.88	$1424e^{-0.0050t}$	1.0	$1479e^{-0.0411t}$	0.28
	0.60 f_{ult}	$1281e^{-0.0300t}$	0.90	$1433e^{-0.0071t}$	1.0	$1466e^{-0.0533t}$	0.23

y - Water head in reservoir
t - Time from the commencement of testing
f_{ult} - Average predicted failure stress for panels; for θ=45° panel, f_{ult} = 6.7N/mm²

Note that for accuracy the initial 15secs of test data were neglected to avoid any problems with settling or large initial absorption rates. Settling effects were discussed in Section 6.3.

6.6.3 Effect of varying applied stress level on strain for θ=45° panels

Figure 6.35 shows the average stress-strain relationship for θ=45° panels. This figure presents the experimental strain results for panel 3C though panel 4C exhibited similar behaviour.

Only the stress-strain relationship generated across the main mortar bed (Joint 1) and the perpendicular component (Joint 2) is shown. These relationships were based on average results from a total of 12 loading cycles each to $0.3f_{ult}$, $0.45f_{ult}$ and $0.6f_{ult}$ stress levels. Joint 3 exhibited similar stress-strain relationships for each of its components and is omitted here for clarity .

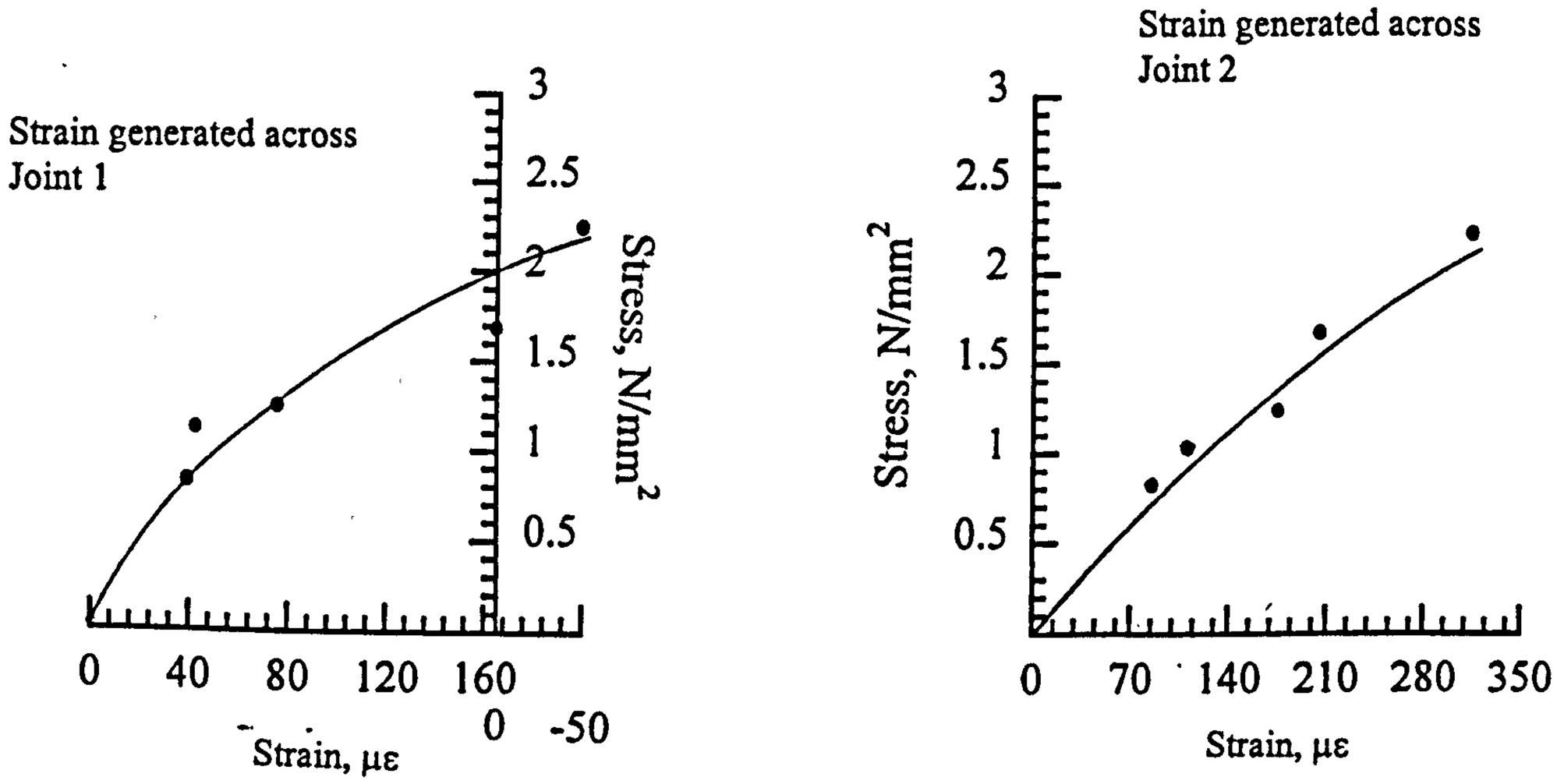

Fig. 6.35 Average stress-strain relationship for masonry joints, bed orientation θ=45°

Using Fig. 6.35, at Joint 1 and at low applied stress levels (<$0.3f_{ult}$) compression strains were generated which effectively closed any fissures at the brick/mortar interface. Shear generated along the main mortar beds at these stress levels was less than the brick/mortar bond capacity. However as applied loads increased then correspondingly the shear component at Joint 1 also increased.

This caused the brick/mortar bond to be compromised and sliding would occur along the bed; this being indicated by the relationship in Fig. 6.35 tending towards tensile strains (-ve) at high stress levels ($\geq 0.6f_{ult}$). This would be the controlling mechanism in governing ingress characteristics.

The stress-strain relationship for Joint 2 indicated that no shearing would occur at all applied stress levels (Fig. 6.35). Therefore only compression strains were generated across this joint. Bed orientations <45° had indicated that Poisson's ratio effects were important in governing debonding at the brick/mortar interface. This would become less influential for panels ≥45°, as Joint 2 was orientated closer to direct compression loads.

Broadly, up to stress levels of $0.45f_{ult}$, the stress-strain relationship for Joint 1 and 2 would be considered similar, thereafter the shearing mechanism at Joint 1 caused a fundamental difference in structural behaviour.

6.6.4 Effect of varying applied initial water head and stress level on water ingress through θ=45° panels

At all joint positions, low initial heads (≤600mm) at constant stress levels consistently exhibited little influence irrespective of joint type. Higher initial heads were found to exploit any extended or newly created cavities or fissures particularly at high stress levels.

This is consistent with phenomena exhibited for θ=0°, 30° and 90° panels.

6.6.5 Relationship between water ingress and strain for θ=45° panels

(a) Joint 1:

Fig. 6.36 shows the relationship between water ingress and strain level across Joint 1 when bed orientation θ=45°. This used average strain and ingress rates from panels 3C and 4C.

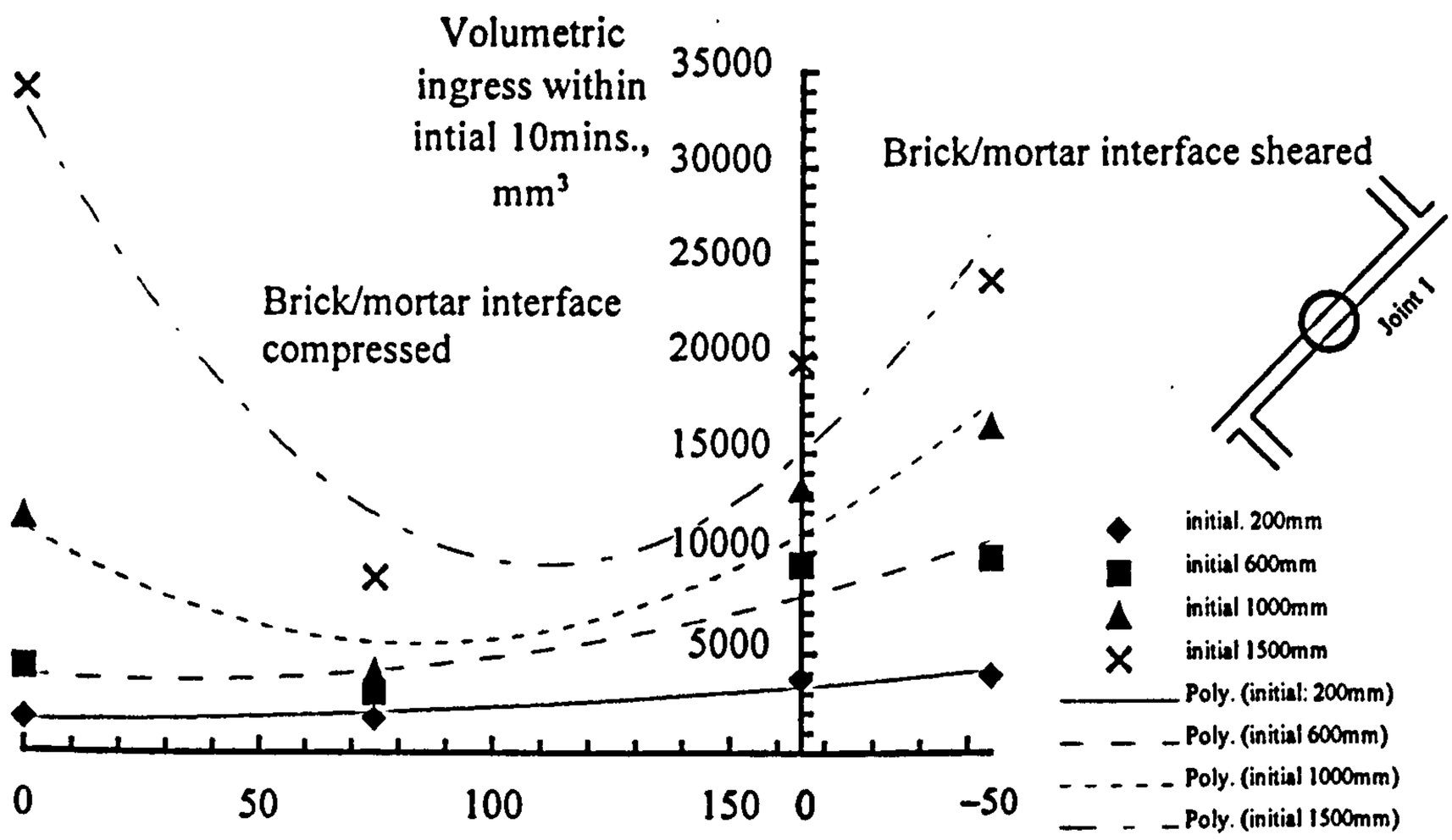

Fig. 6.36 Volume intake within initial 10mins at Joint 1 under four levels of stress for bed orientation θ=45°

Figure 6.36 shows the effect of shear failure on overall ingress rates. At low levels of applied stress ($\leq 0.3f_{ult}$) where strains generated were low (<100με), the mortar bed showed an improvement in its resistance to water ingress. As applied stress levels increased ($\geq 0.45f_{ult}$), then shear failure occurred causing slippage along the bed interface. This was indicated in Fig. 6.36 by -ve (tensile) strains.

For compression strains of 165με generated at an applied stress of $0.45f_{ult}$, then water ingress began to increase. Although no shear slip has occurred, it is suggested that microcracks are beginning to form at the brick/mortar interface encouraging quicker ingress rates, particularly for water under a larger pressure head.

At applied stress levels of $0.6f_{ult}$, tensile strains (≅-45με) and hence cracks were generated leading to an increase in water ingress to a maximum.

Due to the applied stresses having caused strains to fluctuate between compression and tension values, a theoretical formulation could not be matched accurately with the experimental results.

(b) Joint 2:

Figure 6.37 shows the relationship between water intake and strain at Joint 2. This was based on average ingress rates and strains for panels 3C and 4C.

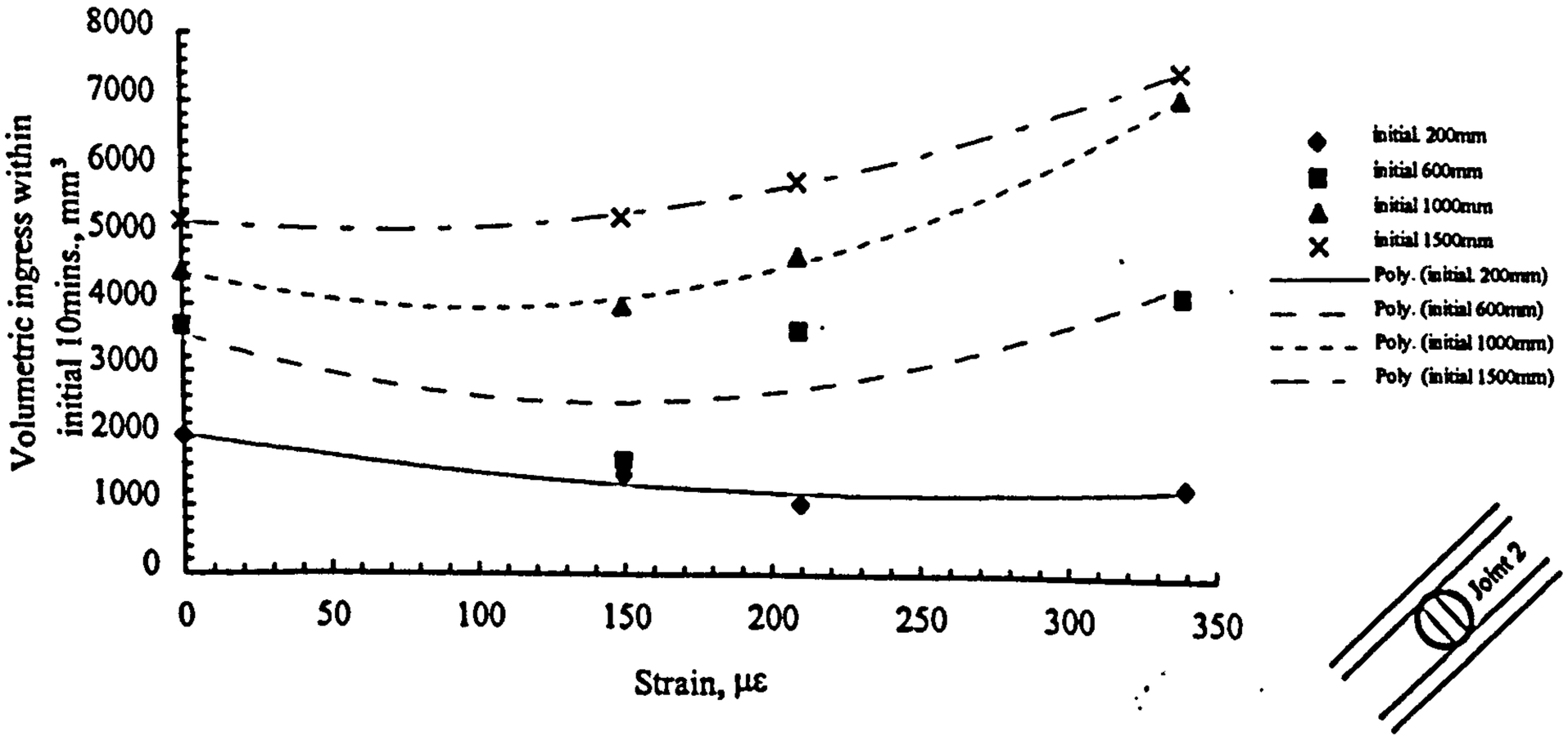

Fig. 6.37 Volume intake within initial 10mins at Joint 2 under four levels of stress for bed orientation θ=45°

The above relationships showed that Joint 2 decreased only slightly in its resistance to water ingress at low values of strain (≤150με) at applied stress levels ≤$0.3f_{ult}$.

Water ingress rates started to increase after this strain values at differing rates depending upon initial water head. Higher ingress rates were noted at higher initial water heads.

Strain generated across Joint 2 of 340με at $0.6f_{ult}$, produced tensile and compressive strains perpendicular and parallel to loading direction of approximately equal magnitude (280με). It would be expected that some perpend debonding occurred due to these high strain values leading to an increase in water ingress.

Relationships exhibited in Fig. 6.37 were found to follow closely that of second order polynomial equations. Table 6.12 shows these equations.

Table 6.12 Standard second order polynomial equations for water ingress at Joint 2

Initial head, h (mm)	Joint 2	
	$V_i =$	R^2
200	$0.0139\varepsilon^2 - 6.92\varepsilon + 2040$	0.91
600	$0.005\varepsilon^2 - 14.00\varepsilon + 3541$	0.58
1000	$0.054\varepsilon^2 - 10.58\varepsilon + 4481$	0.90
1500	$0.030\varepsilon^2 - 3.51\varepsilon + 5231$	0.99

By differentiating volumetric ingress (V_i) with respect to strain (ε) in Table 6.12, i.e. $dV_i/d\varepsilon=0$, an indication of threshold strain level with respect to initial water head was found. At this stress level, minimum water ingress would be exhibited. This is shown in Fig. 6.38.

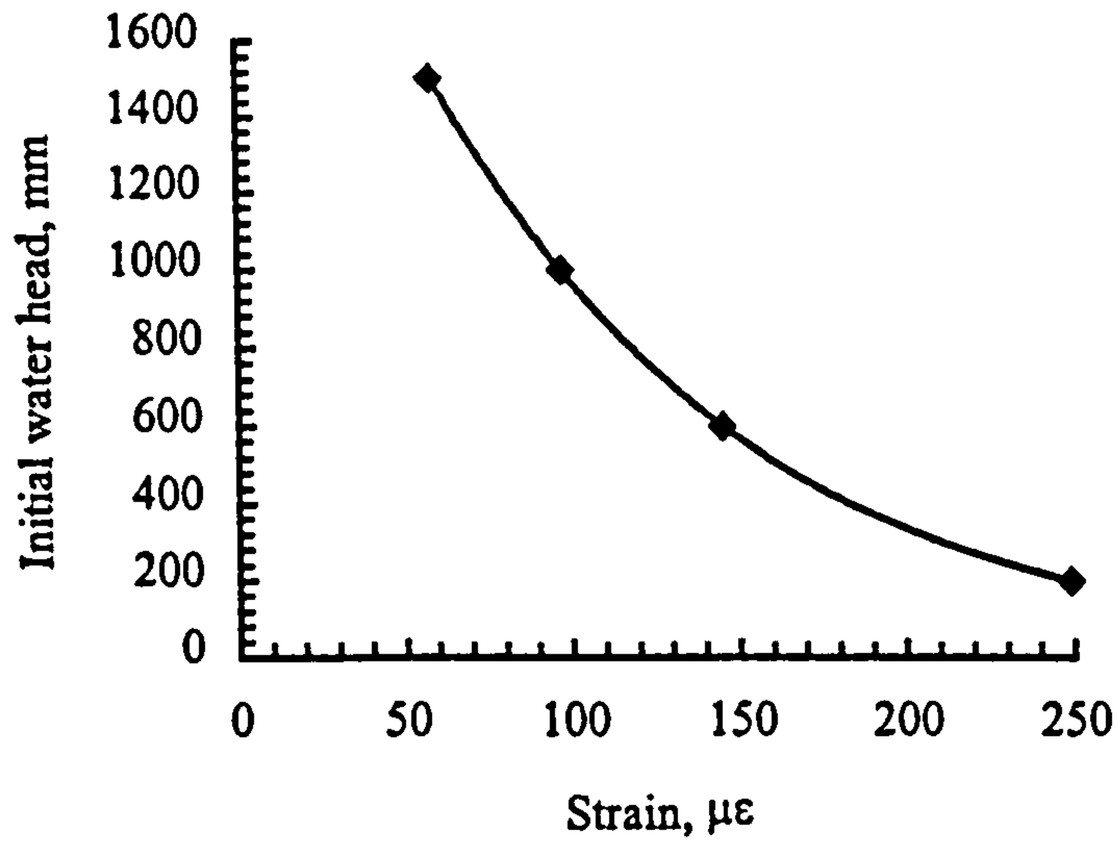

Fig. 6.38 Threshold strain across Joint 2 to induce minimum water ingress dependent upon initial water head

Figure 6.38 indicates that as the initial head decreased, larger strains were required to produce minimum water ingress. For a high initial head (h=1500mm), an optimum strain value of 60με was required which occur at low applied stresses of $\leq 0.3f_{ult}$. Low initial heads (h=200mm) would require a strain value of 250με generated at an applied stress $\equiv 0.6f_{ult}$.

(c) Joint 3:

Figure 6.39 shows the average volume intake-strain relationship for panels 3C and 4C at Joint 3.

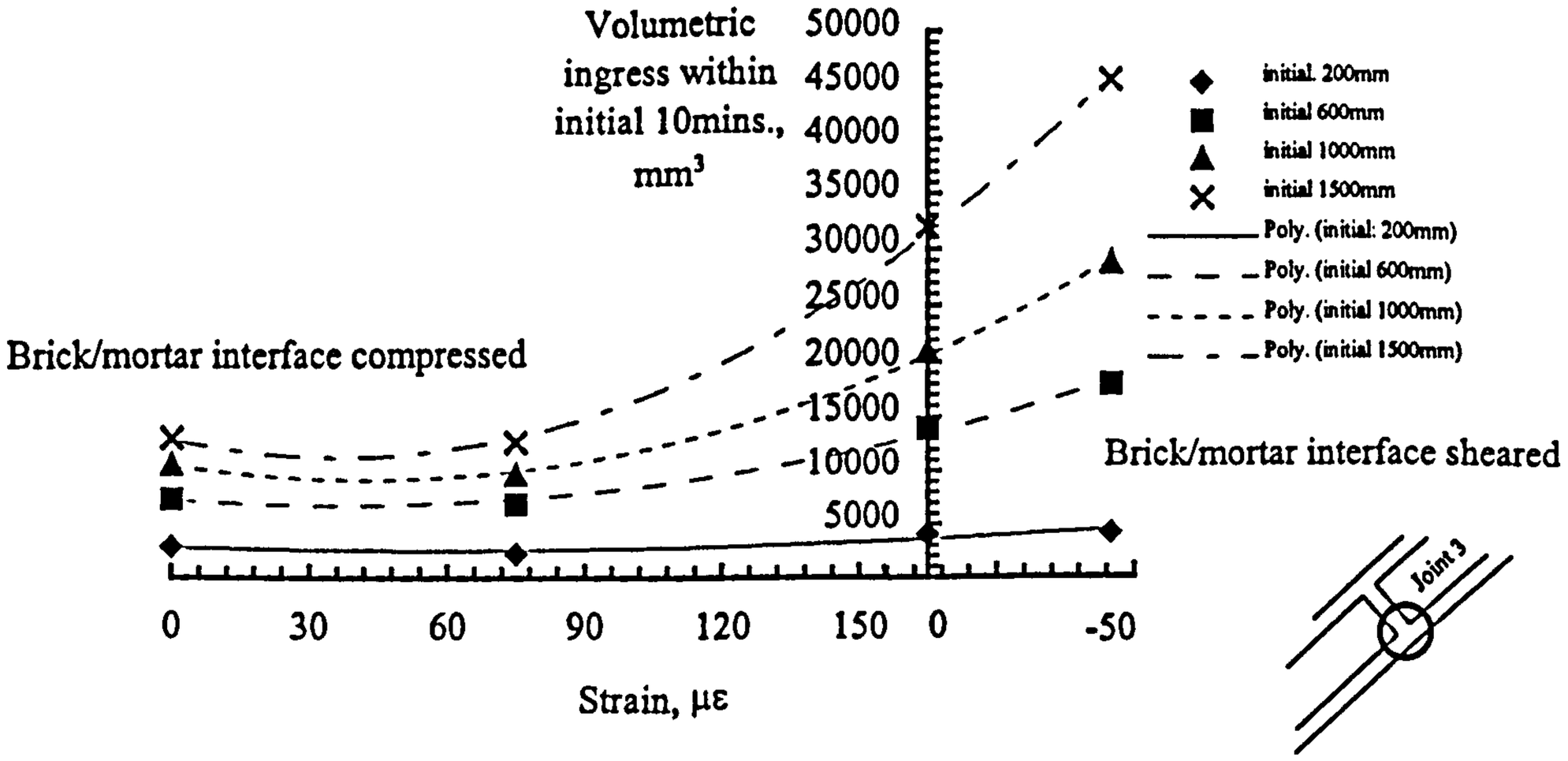

Fig 6.39 Volume intake within initial 10mins at Joint 3 under four levels of stress for bed orientation θ=45°

For an applied stress of $0.3f_{ult}$, compressive strains of 75με were generated. At $0.45f_{ult}$, compressive strains of 165με were generated which corresponded with an increase in water ingress. This was likely caused by microcracks forming at the brick/mortar interface prior to any shear slip. Slip was shown to occur at $0.6f_{ult}$ due to tensile strains of -45με being exhibited.

The behaviour of Joint 3 is similar to that exhibited at Joint 1 (Fig. 6.36). These relationships indicate that tensile cracks caused by shear slip is influential.

Due to the applied stress causing strains to fluctuate between compression and tension and due to the shear slip associated with the failure mode, a theoretical formulation could not be matched accurately with experimental results.

6.6.6 Effect of joint type on water ingress through θ=45° panels

The water ingress at Joints 1 and 3 under stress, as exhibited in Figs 6.37 and 6.39 respectively, are similar. Both joints fail by shear along the main brick/mortar interface which is very influential in governing water ingress. The large increase in water ingress rates at high stress levels ($\geq 0.6f_{ult}$) at Joint 1 and 3 indicated their likelihood as areas of water penetration.

Generally, Joint 2 exhibited smaller ingress rate increases at higher stress levels and would be considered the most resistant of mortar beds to water penetration.

6.7 Water Ingress Characteristics When Bed Orientation θ=60°

For θ=60° panels, the load direction caused shear slip along the main mortar bed. It would be expected that some initial compression of this mortar bed takes place prior to the shear component along the bed compromising the brick/mortar bond strength.

Assuming water ingress rates were measured at a shear plane, then these results were expected to show a rapid increase in ingress rates as the brick and mortar debond and slide against each other at high applied stress levels.

The perpend mortar joints would undergo increasingly direct compressive loading, with a corresponding closure of fissures at the brick/mortar interface. Water ingress rates would decrease at these positions. Tensile debonding at these beds is not an indication of the failure mechanism for bed orientations, θ = 60°.

6.7.1 Panel testing

Both Type 3 and 4 masonry panels were used for this assessment. Type 3 panel (3D) had a cross section of 100x245mm and a predicted ultimate failure load (F_{ult}) of 117kN. This corresponded to a failure stress (f_{ult}) of 4.8N/mm^2 and allowed water ingress to be measured at 1.4N/mm^2 ($0.3f_{ult}$), 2.1N/mm^2 ($0.45f_{ult}$) and 2.9N/mm^2 ($0.6f_{ult}$). Type 4 panel (4D) had the same cross sectional area as 3D with a corresponding predicted failure load (F_{ult}) of 88kN. Water ingress was measured at 1.1N/mm^2 ($0.3f_{ult}$), 1.6N/mm^2 ($0.45f_{ult}$) and 2.2N/mm^2 ($0.6f_{ult}$).

For information, the location of demec gauges and positions where ingress was measured is shown in Fig. 6.40.

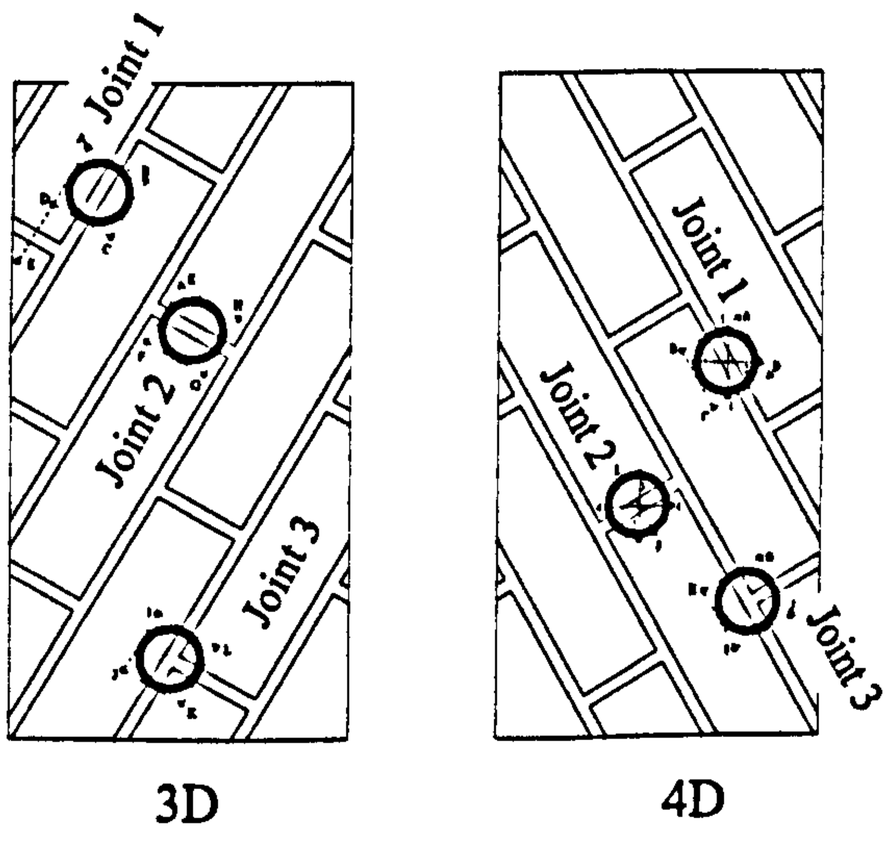

Fig. 6.40 Permeameter and demec positions for θ=60° panels

The average water ingress rates as measured experimentally for panels 3D and 4D are shown in Figs 6.41-6.43. These relationships indicate the influence of applied stress level and initial head (h) on water ingress with time. For simplification, relationships presented here are identified in terms of their joint position.

(i) Average water ingress rates for Joint 1, unstressed

(ii) Average water ingress rates for Joint 1, applied stress level $=0.3f_{ult}$

(iii) Average water ingress rates for Joint 1, applied stress level $=0.45f_{ult}$

(iv) Average water ingress rates for Joint 1, applied stress level $=0.6f_{ult}$

Fig. 6.41 Average water ingress rates at Joint 1, bed orientation $\theta=60°$

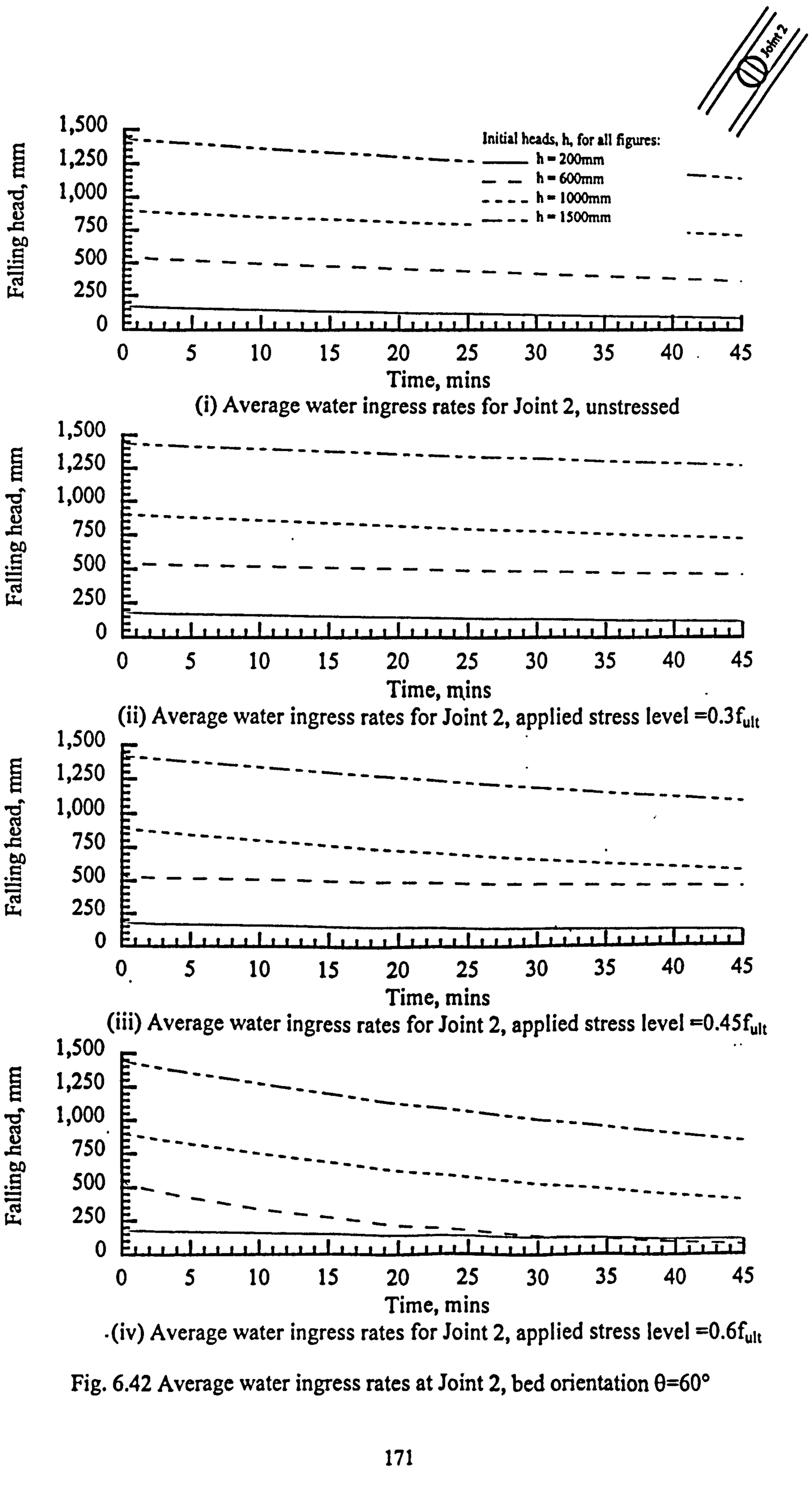

Fig. 6.42 Average water ingress rates at Joint 2, bed orientation θ=60°

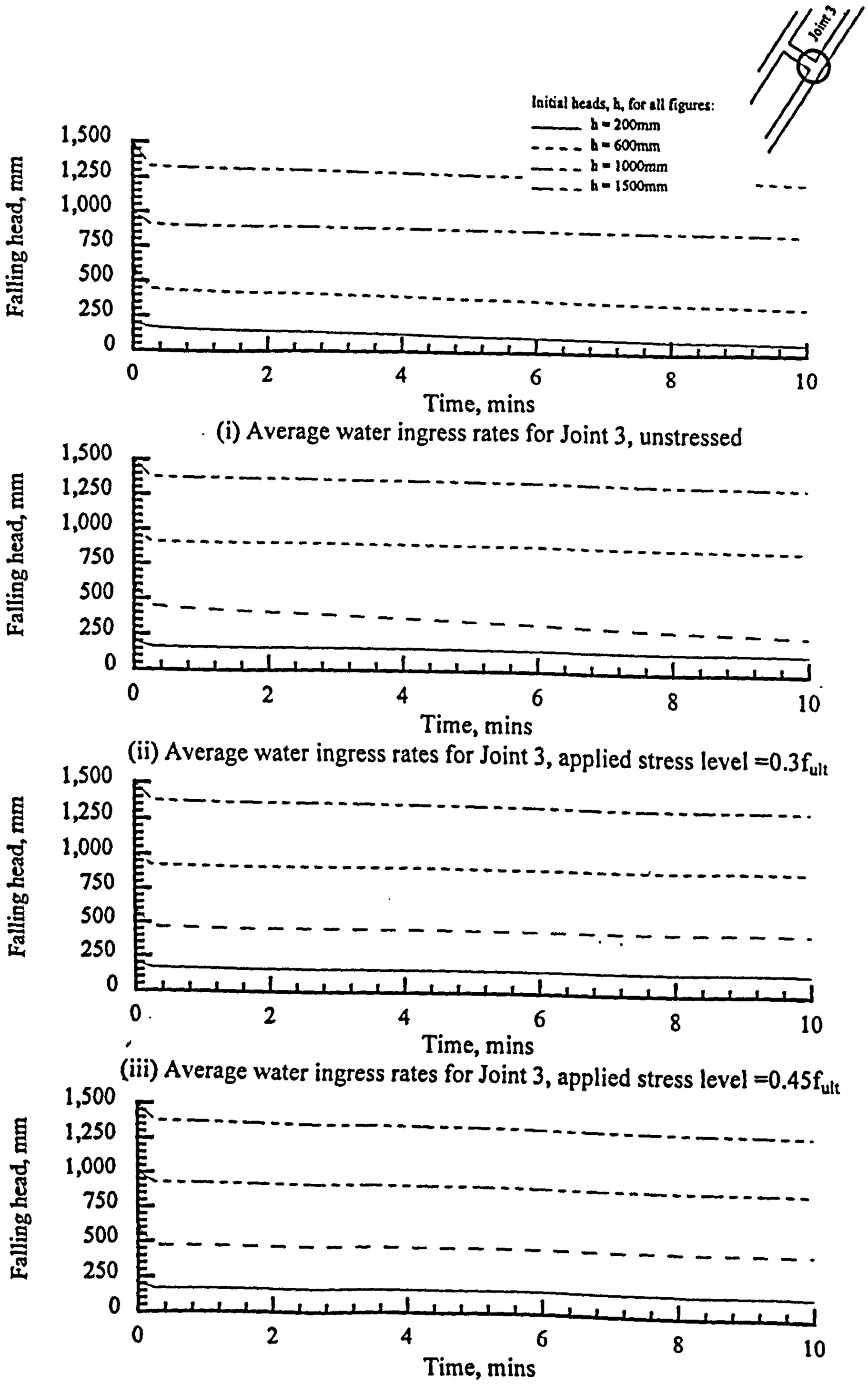

(i) Average water ingress rates for Joint 3, unstressed

(ii) Average water ingress rates for Joint 3, applied stress level $=0.3f_{ult}$

(iii) Average water ingress rates for Joint 3, applied stress level $=0.45f_{ult}$

– (iv) Average water ingress rates for Joint 3, applied stress level $=0.6f_{ult}$

Fig. 6.43 Average water ingress rates at Joint 3, bed orientation $\theta=60°$

Joint 1 (Fig. 6.41) exhibited increasingly quicker ingress rates as applied stress level was increased. This was likely caused by the brick/mortar bond capacity being compromised at high stress levels. At Joint 2 (Fig. 6.42) at stress levels of $0.3f_{ult}$ and $0.45f_{ult}$, ingress rates decreased. However perpend debonding at high stress levels resulted in quicker ingress rates. Figure 6.43 showed that Joint 3 had generally stable ingress rates as its brick/mortar capacity and was not compromised by any of the applied stress levels

6.7.2 Modelling of water ingress rate results

The average ingress rates found during experimentation and shown in Figs 6.41-6.43 were found to best-fit decay curves. These are shown in Table 6.13,

Table 6.13 Average decay curves and coefficient of correlation for panels with bed orientation θ=60°

Initial head, h (mm)	Applied stress, (N/mm^2)	Joint 1		Joint 2		Joint 3	
		y =	R^2	y =	R^2	y =	R^2
200	$0.00f_{ult}$	$123e^{-0.0174t}$	0.99	$174e^{-0.0156t}$	1.0	$175e^{-0.0834t}$	1.0
	$0.30\ f_{ult}$	$123e^{-0.0082t}$	1.0	$179e^{-0.0103t}$	1.0	$167e^{-0.0306t}$	1.0
	$0.45\ f_{ult}$	$121e^{-0.0037t}$	1.0	$178e^{-0.0100t}$	0.98	$168e^{-0.0118t}$	1.0
	$0.60\ f_{ult}$	$115e^{-0.0626t}$	0.98	$178e^{-0.0110t}$	0.99	$168e^{-0.0087t}$	1.0
600	$0.00\ f_{ult}$	$470e^{-0.0069t}$	1.0	$544e^{-0.0090t}$	0.99	$449e^{-0.0306t}$	0.94
	$0.30\ f_{ult}$	$490e^{-0.0061t}$	1.0	$540e^{-0.0039t}$	0.98	$453e^{-0.0520t}$	1.0
	$0.45\ f_{ult}$	$471e^{-0.0413t}$	1.0	$530e^{-0.0039t}$	1.0	$469e^{-0.0068t}$	1.0
	$0.60\ f_{ult}$	$430e^{-0.0615t}$	1.0	$530e^{-0.0450t}$	1.0	$470e^{-0.0034t}$	0.99
1000	$0.00\ f_{ult}$	$824e^{-0.0139t}$	0.99	$898e^{-0.0049t}$	0.99	$912e^{-0.0067t}$	1.0
	$0.30\ f_{ult}$	$771e^{-0.0050t}$	1.0	$901e^{-0.0050t}$	0.98	$915e^{-0.0047t}$	1.0
	$0.45\ f_{ult}$	$770e^{-0.0491t}$	0.84	$885e^{-0.0100t}$	0.99	$924e^{-0.0033t}$	0.99
	$0.60\ f_{ult}$	$809e^{-0.1012t}$	0.85	$900e^{-0.0180t}$	0.92	$930e^{-0.0045t}$	1.0
	$0.00\ f_{ult}$	$1334e^{-0.0067t}$	0.99	$1429e^{-0.0047t}$	0.96	$1335e^{-0.0079t}$	0.99
	$0.30\ f_{ult}$	$1121e^{-0.0558t}$	0.85	$1435e^{-0.0028t}$	0.96	$1381e^{-0.0044t}$	1.0
	$0.45\ f_{ult}$	$1120e^{-0.0543t}$	0.92	$1420e^{-0.0060t}$	0.94	$1379e^{-0.0041t}$	1.0
	$0.60\ f_{ult}$	$1050e^{-0.2510t}$	0.84	$1440e^{-0.0120t}$	0.95	$1379e^{-0.0054t}$	0.93

y - Water head in reservoir
t - Time from the commencement of testing
f_{ult} - Average predicted failure stress for masonry panel; for θ=60° panels, $f_{ult} = 4.2N/mm^2$

Good agreement was found between experimental and theoretical results, this was indicated by an average coefficient of correlation, $R^2= 0.97$.

6.7.3 Effect of varying applied stress level on strain for θ=60° panels

Figure 6.44 shows the average stress-strain relationship for panels 3D and 4D at the main mortar bed (Joint 1) and the perpendicular bed (Joint 2). Strain across the respective components of Joint 3 were of similar magnitude and are omitted here for clarity. This relationship only shows strain generated up to applied stress level of $0.6f_{ult}$.

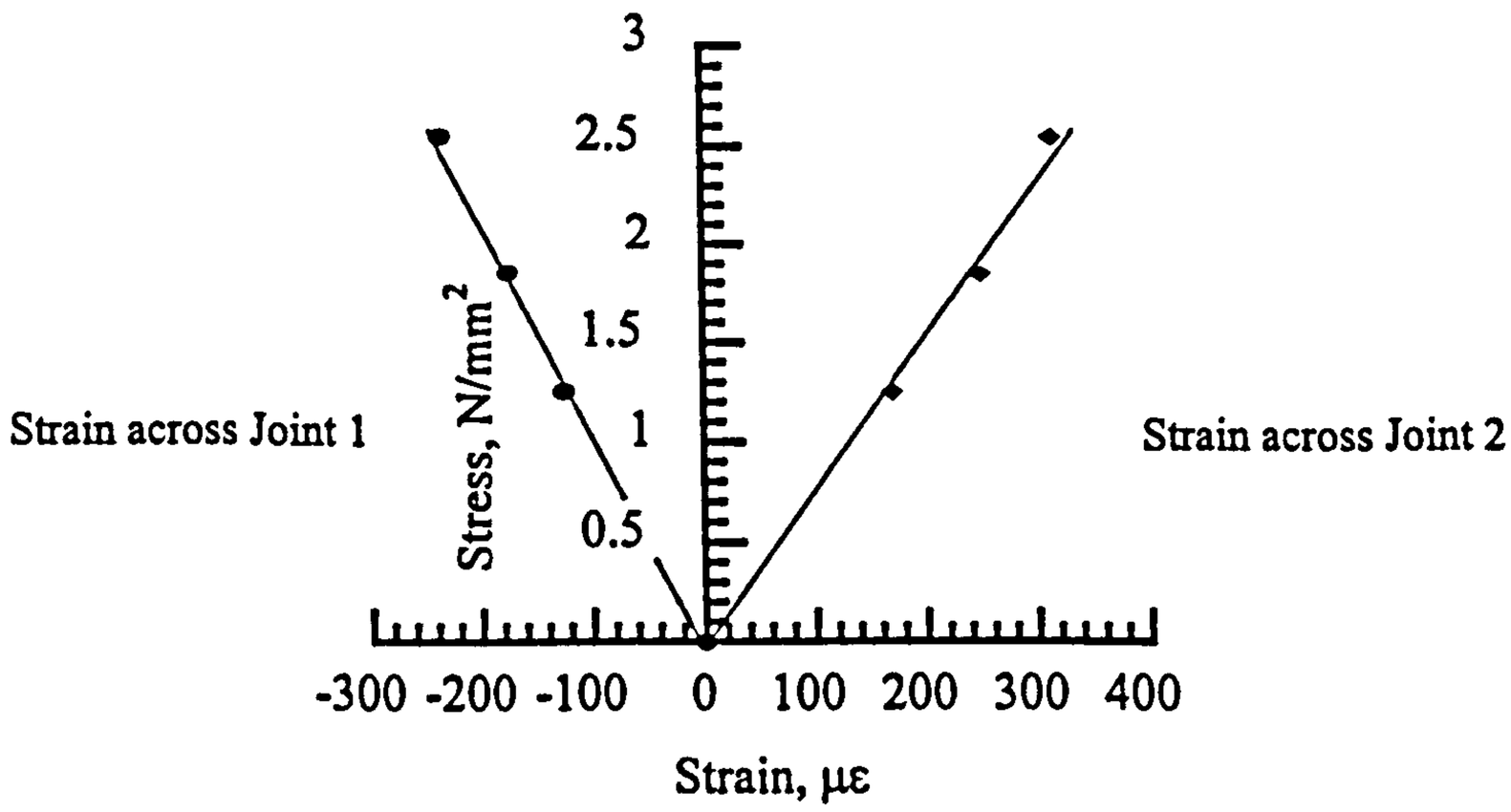

Fig. 6.44 Average stress-strain relationship for masonry joints, bed orientation θ=60°

These relationships exhibited two different types of behaviour with tensile strains being generated at Joint 1 and compressive strains at Joint 2.

At Joint 1, average tensile strains increased from -125με at $0.3f_{ult}$, to -175με at $0.45f_{ult}$ to finally -235με at $0.6f_{ult}$. These high strains would increasingly compromise the brick/mortar bond strength leading to increased water ingress.

Strains generated across Joint 2 were of the same order, (approximately 300με when applied stress was $0.6f_{ult}$), to those across Joint 1. These strains were compressive and in effect would close any cavities at the brick/mortar interface.

Only relatively small tensile strains were generated across this joint and were expected to have little effect in the overall behaviour in resisting water ingress. The tensile cracking of perpend joints was not a failure mechanism associated with θ=60° panels.

The strains generated across both the main bed and the perpend bed (Fig. 6.44) were similar at Joint 3. The behaviour at this joint position was expected to be controlled by the strain generated across the main bed component, i.e. Joint 1.

6.7.4 Effect of varying initial water head and applied stress level on water ingress through θ=60° panels

At all joint positions, all initial heads irrespective of their magnitude displayed little influence in governing water ingress when panels were unstressed. However, when stressing caused shear slip at the main bed or extended any fissures, then high initial heads correspondingly increased the water ingress levels.

This phenomena is consistent with that found at θ=0°, 30°, 45° and 90° panels.

6.7.5 Relationship between water ingress and strain for θ=60° panels

(a) Joint 1:

Figure 6.45 indicates the influence that both strain and initial head has in controlling water ingress. Experimental data points for Figs 6.45-6.47 were based on the average water ingress rates and strain levels for panels 3D and 4D.

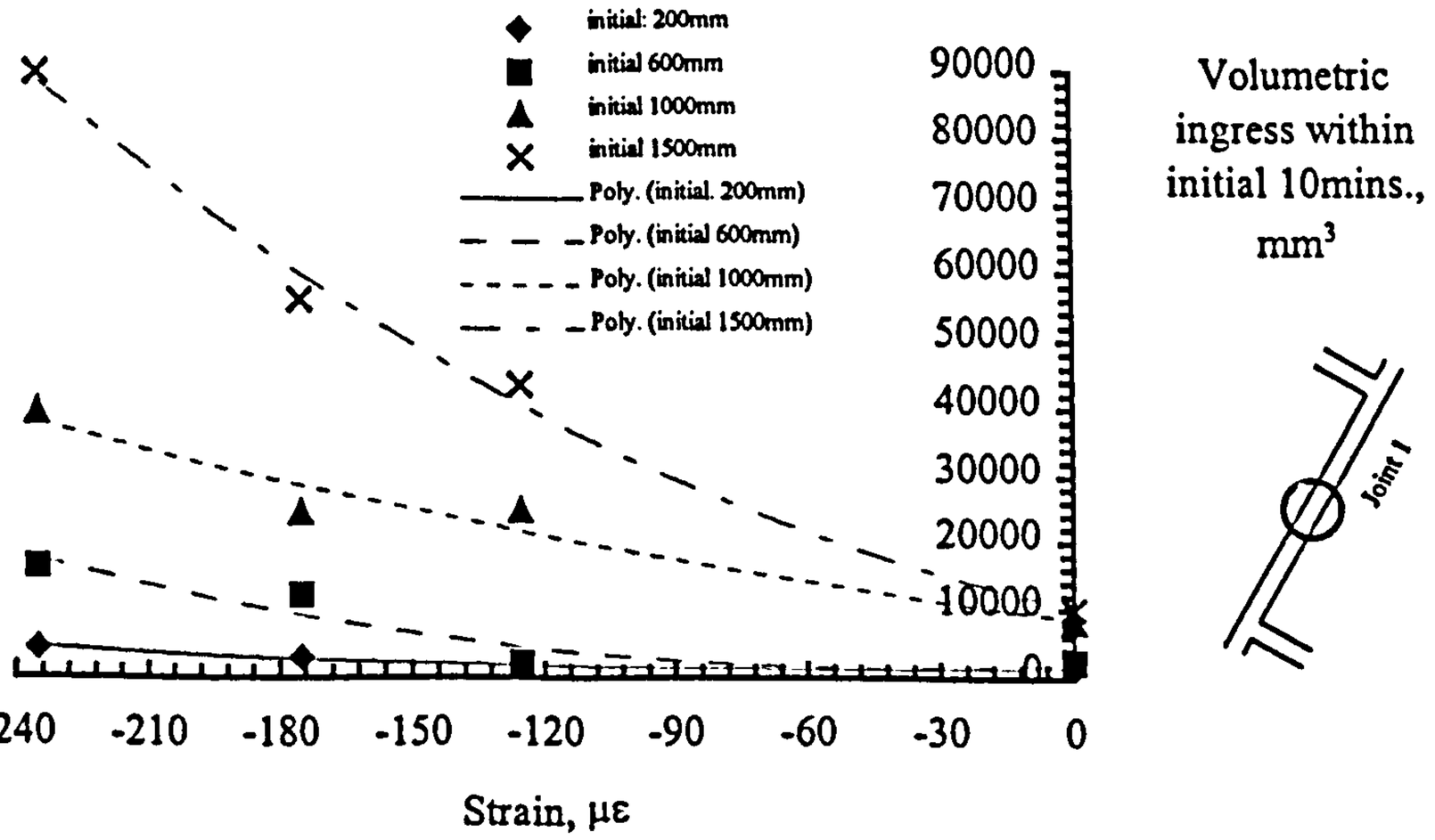

Fig. 6.45 Volume intake within initial 10mins at Joint 1 under four levels of stress for bed orientation $\theta = 60°$

The relationship exhibited above show the effect of both initial head and strain level on ingress behaviour. As the applied stress level increased to $0.6f_{ult}$ (with a corresponding tensile strain of -240με) ingress rates also increased for all initial heads.

These water ingress rates fit closely those of a second order polynomial equation, Eqn. 6.2 and can be consulted in Table 6.14.

Table 6.14 Theoretical formulation for water ingress at Joint 1 dependant upon strain level and initial water head

Initial head, h (mm)	Joint 2	
	$V_i =$	R^2
200	$0.094\varepsilon^2 + 9.42\varepsilon + 1474$	0.98
600	$0.421\varepsilon^2 + 33.80\varepsilon + 2090$	0.90
1000	$0.191\varepsilon^2 - 79.9\varepsilon + 8599$	0.94
1500	$0.837\varepsilon^2 - 135.8\varepsilon + 10390$	0.99

The relationships shown in Table 6.14 exhibit good agreement with the experimental values, with an average coefficient of correlation, R^2=0.94.

By differentiating the polynomial equations given in Table 6.14 with respect to strain (ε), then for low initial heads (≤600mm) the ingress rates would improve up to tensile strains of approximately 40με. For higher initial water heads (≥1000mm) then ingress rates increased on immediate commencement of loading.

(b) Joint 2:

Figure 6.46 indicates the influence that both strain and initial head has in controlling water ingress at Joint 2.

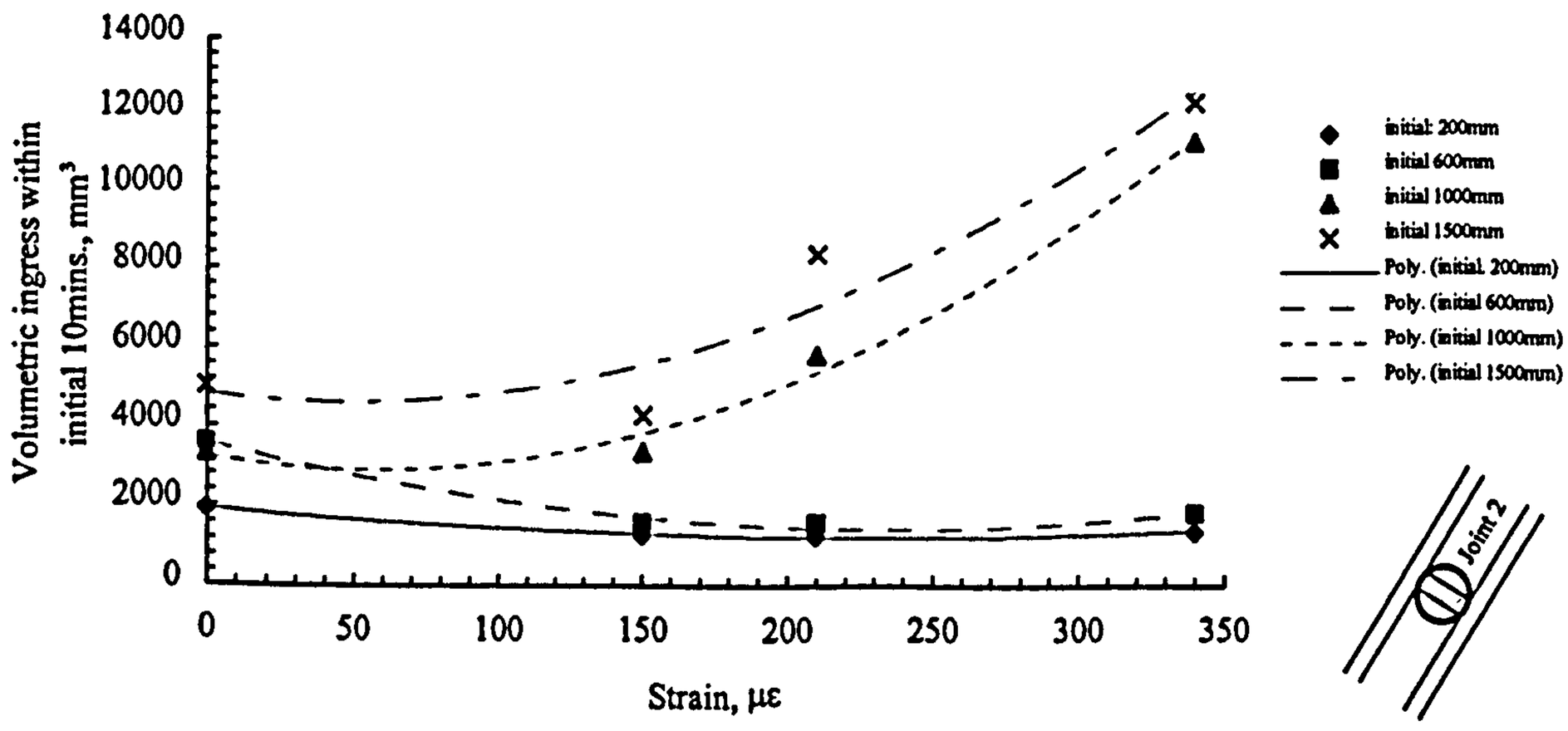

Fig. 6.46 Volume intake within initial 10mins at Joint 2 under four levels of stress for bed orientation θ=60°

Panels with a bed orientation of θ=60° were expected to undergo compression loading at Joint 2. Debonding of these joints leading to structural failure was not expected to have occurred.

At low initial heads (≤600mm) water ingress was found to decrease as compression strains increased to a maximum of 340με at $0.6f_{ult}$. Some debonding or small microcracks do appear to have formed across this joint, exhibited by increased water ingress at strains ≥150με at stress levels of $0.3f_{ult}$ for initial heads ≥1000mm.

Due to experimental error the data points for initial head of 1500mm and strains of 150με and 210με are anomalous.

(c) Joint 3:

Figure 6.47 indicates that at Joint 3 both strain and initial water head has a controlling influence on water ingress.

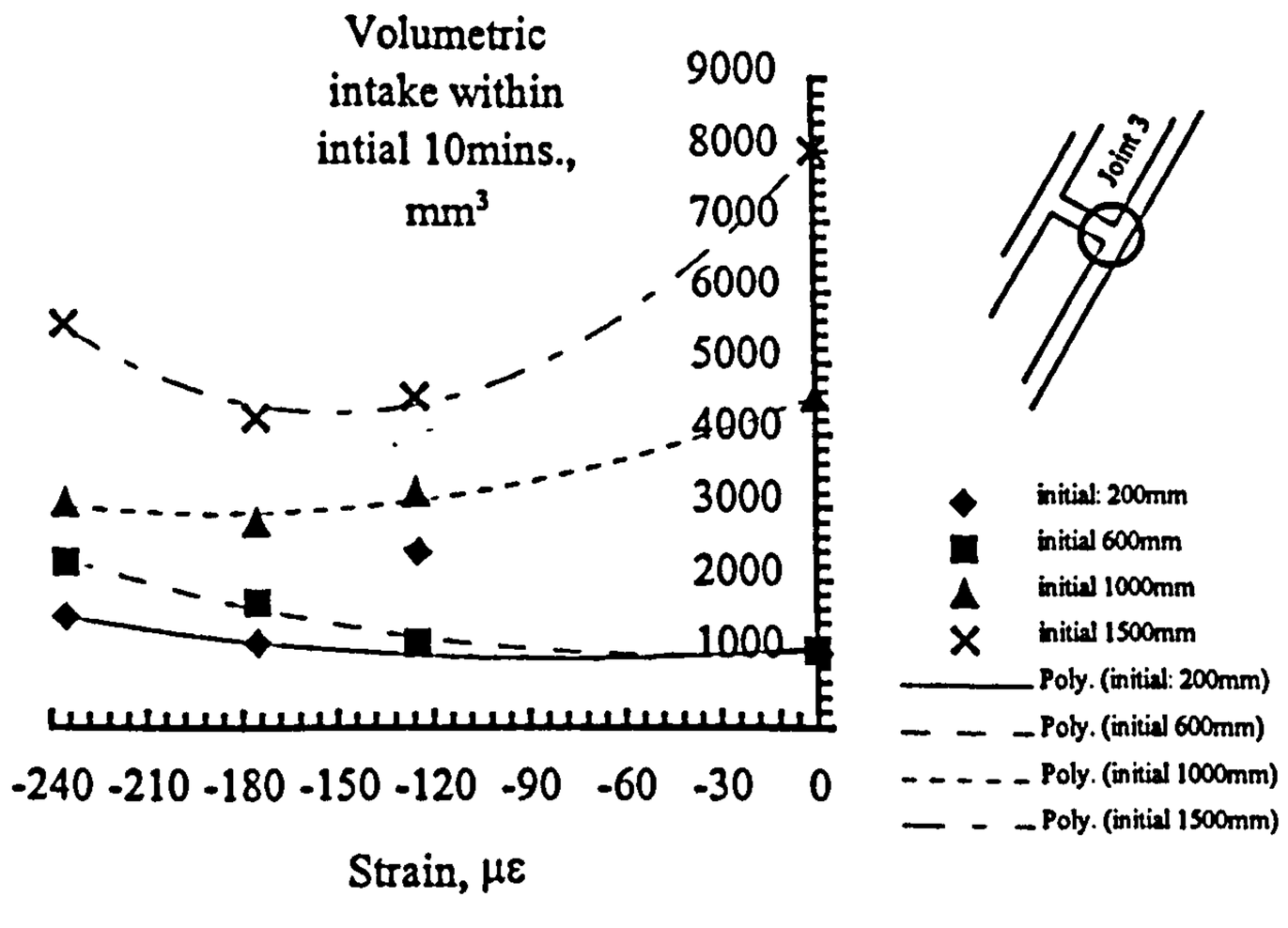

Fig. 6.47 Volume intake within initial 10mins at Joint 3 under four levels of stress for bed orientation θ=60°

The behaviour of Joint 3 as indicated by Fig. 6.48 initially shows an improvement in ingress rates as beds were compressed. This had generally occurred for strains up to ≅-130με (generated when applied stress was $0.3f_{ult}$). These strains had not compromised the brick/mortar bond capacity and in effect were closing any cavities due to the compressive component of the applied stress.

As the stress level increased to $0.6f_{ult}$ then an increase in water ingress was recorded. This cracking occurred along the brick/mortar interface, compromising the bond and encouraging water ingress particularly for initial head h=1500mm.

Water ingress rates for the initial head of 200mm and strain levels of -120με is anomalous and caused by experimental error. This ingress rate would be expected to be much lower.

6.7.6 Effect of joint type on water ingress through θ=60° panels

Water ingress rates at Joints 1 and 3 increased at applied stress level which compromised the brick/mortar bond capacity.

Joint 2 generally improved its resistance to water ingress at low stress levels. Only at higher stress levels where some debonding had taken place was this joint then prone to increased water ingress.

6.8 Effect of Bed Orientation on Water Ingress Characteristics

The preceding sections have indicated how water ingress was influenced by the applied stress level and related strain, initial head of water and bed orientation of the test panel.

The bed orientation was found to fundamentally control the failure mode of a masonry panel. This experimental programme had already demonstrated that strains at the main mortar beds (Joint 1) varied from compression to tension, with a corresponding effect on water ingress. A change in water ingress characteristics was also noted at the perpend joints (Joint 2) as the main mortar bed was orientated from θ=0° to θ=90°.

Water ingress resistance was measured either as an improvement or deterioration percentile by comparing ingress rates for unstressed and stressed panels. This is shown in Eqn. 6.3.

$$I_{wi} \text{ or } D_{wi} = \left(\frac{A-B}{A}\right) \times 100 \qquad \text{Eqn. 6.3}$$

I_{wi} - Improvement (or decrease) in water ingress

D_{wi} - Deterioration (or increase) in water ingress

A - Volume of water ingress after 10mins for unstressed panels

B - Volume of water ingress after 10mins for stressed panels

Figures 6.48-6.50(a-c) indicate the improvement or deterioration in water ingress for each joint position using Eqn. 6.3. These figures used average improvement or deterioration percentiles based on experimental data for all test panels contained within this chapter.

For ease of discussion, the relationships shown in Figs 6.48-6.50(a-c) are dependant upon the applied stress level and only indicate initial heads at 200mm and 1500mm. However this would be indicative of the large range in improvement or deterioration percentiles as bed orientation and stress level increased.

6.8.1 Effect of bed orientation at Joint 1

Figure 6.48(a-c) indicates the effect that bed orientation has in controlling water ingress behaviour at Joint 1 as the applied stress level increased from $0.3f_{ult}$ to $0.6f_{ult}$.

(a) Water ingress behaviour under applied stress level of $0.3f_{ult}$:

Fig. 6.48(a) shows the effect of bed orientation on water ingress at Joint 1 under an applied stress level of $0.3f_{ult}$. Note that for this figure and all subsequent figures a water ingress percentile of $I_{wi}=D_{wi}=0\%$ is equivalent to that of an unstressed panel.

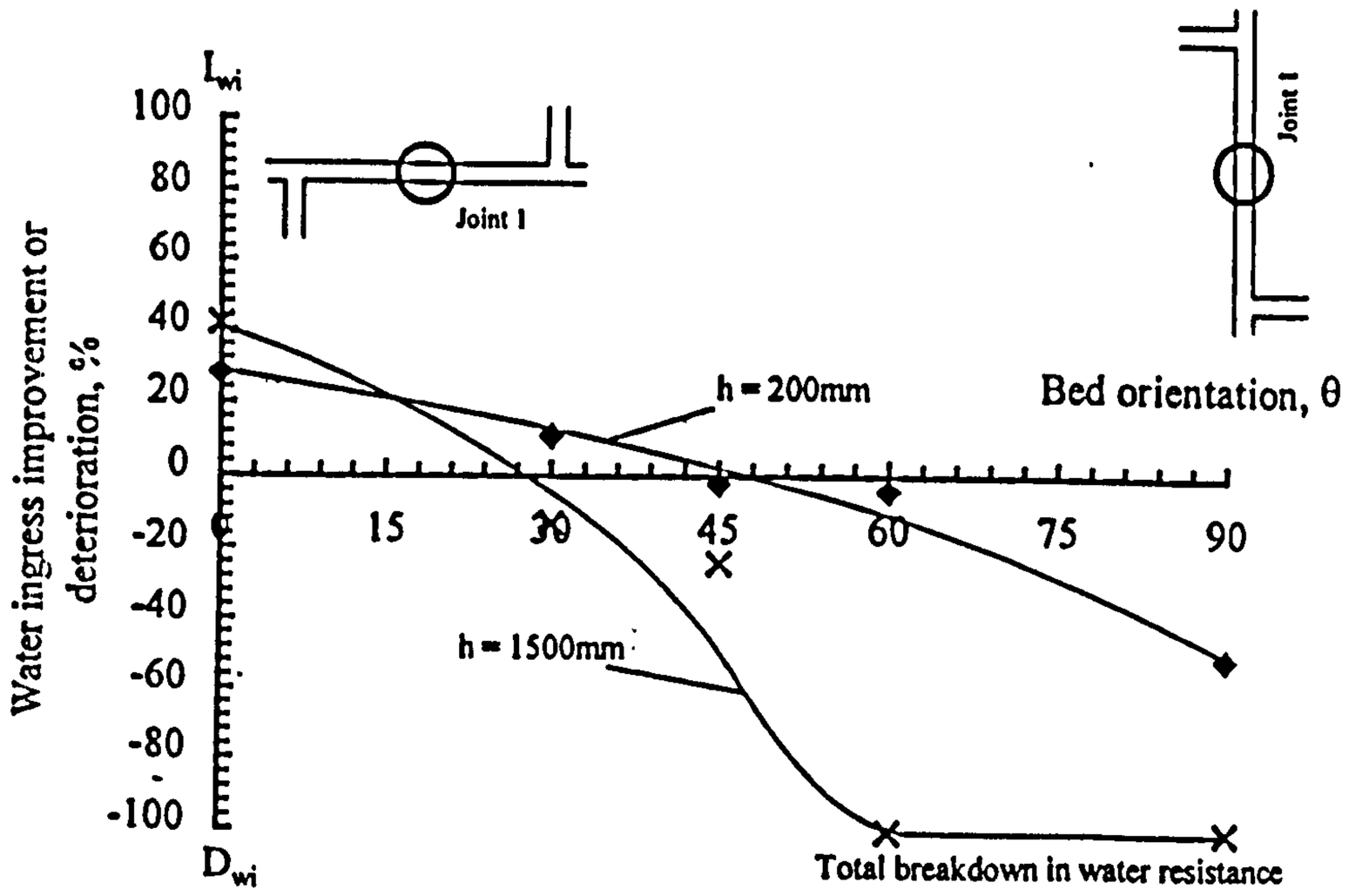

Fig. 6.48(a) Panel integrity relationship for Joint 1 as orientation increased, applied stress = $0.3f_{ult}$

The figure indicates that masonry panels stressed to $0.3f_{ult}$ were less prone to water ingress compared to unstressed panels. Water ingress started to increase above the value for unstressed panels (I_{wi}=D_{wi}=0%) at bed orientations of θ>20° and >45° for initial heads of 1500mm and 200mm respectively.

For high initial heads (h=1500mm), panels underwent total breakdown (D_{wi}=-100%) in its resistance to water ingress at θ=60°. This occurred when the total volume of ingress at any applied stress level was double that of panels when unstressed. Panel breakdown became increasingly pronounced after θ=45°. At this angle the shear component of stress along the brick/mortar interface became more dominant resulting in slippage along the bed.

At lower initial heads (h=200mm) total breakdown did not occur, though the bed became increasingly compromised to water ingress, particularly after θ=45°.

Intermediate initial heads (h=600mm and 1000mm) were generally found to lie within the limits as indicated by the two extreme test heads, Fig. 6.48(a). This would be similar for all subsequent figures independent of joint type.

(b) Water ingress behaviour under applied stress of 0.45_{ult}:

Figure 6.48(b) exhibits a similar relationship to that shown in Fig. 6.48(a).

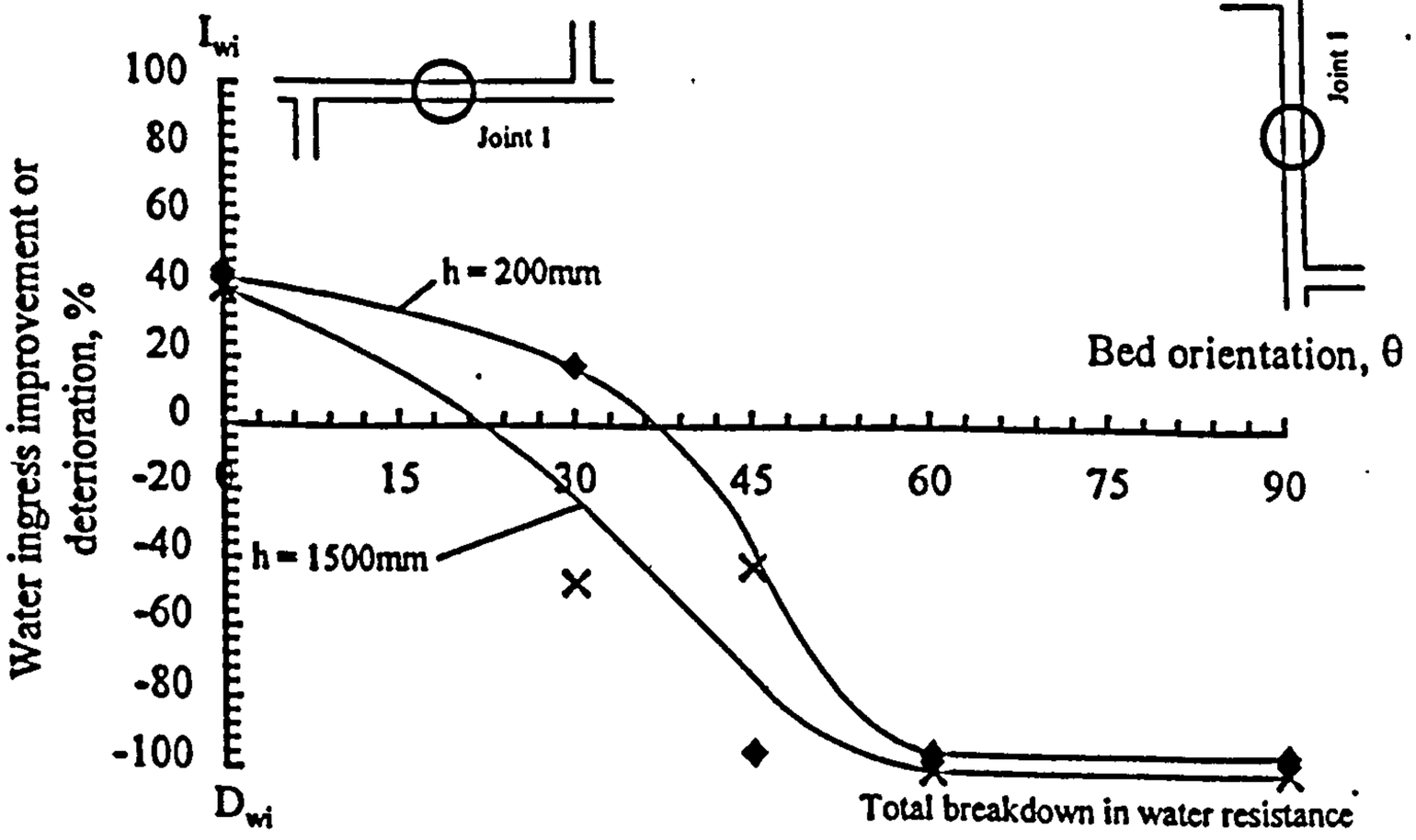

Fig. 6.48(b) Panel integrity relationship for Joint 1 as orientation increased, applied stress = $0.45f_{ult}$

At an initial head of h=1500mm, an improvement in panel resistance to water ingress was exhibited when $\theta \leq 22°$, thereafter it became increasingly compromised. Again total breakdown in the resistance to water ingress occurred at $\theta \geq 60°$. The deterioration percentile at $\theta=45°$ is likely to be anomalous due to experimental error; a larger D_{wi} value was expected closer to total breakdown.

Panels tested with an initial of head of h=200mm also exhibited total brick/mortar interface breakdown when $\theta=60°$. This indicated the sensitivity of a panel to applied stress levels as total breakdown in water resistance at Joint 1 did not occur when applied stress was $0.3f_{ult}$ (Fig. 6.48(a)). Total breakdown for $\theta=45°$ when h=200mm, is anomalous and a value of the order -20% (D_{wi}) would be appropriate.

(c) Water ingress under when applied stress level of $0.6f_{ult}$:

Figure 6.48(c) shows the effect of bed orientation when applied stress level was increased to $0.6f_{ult}$.

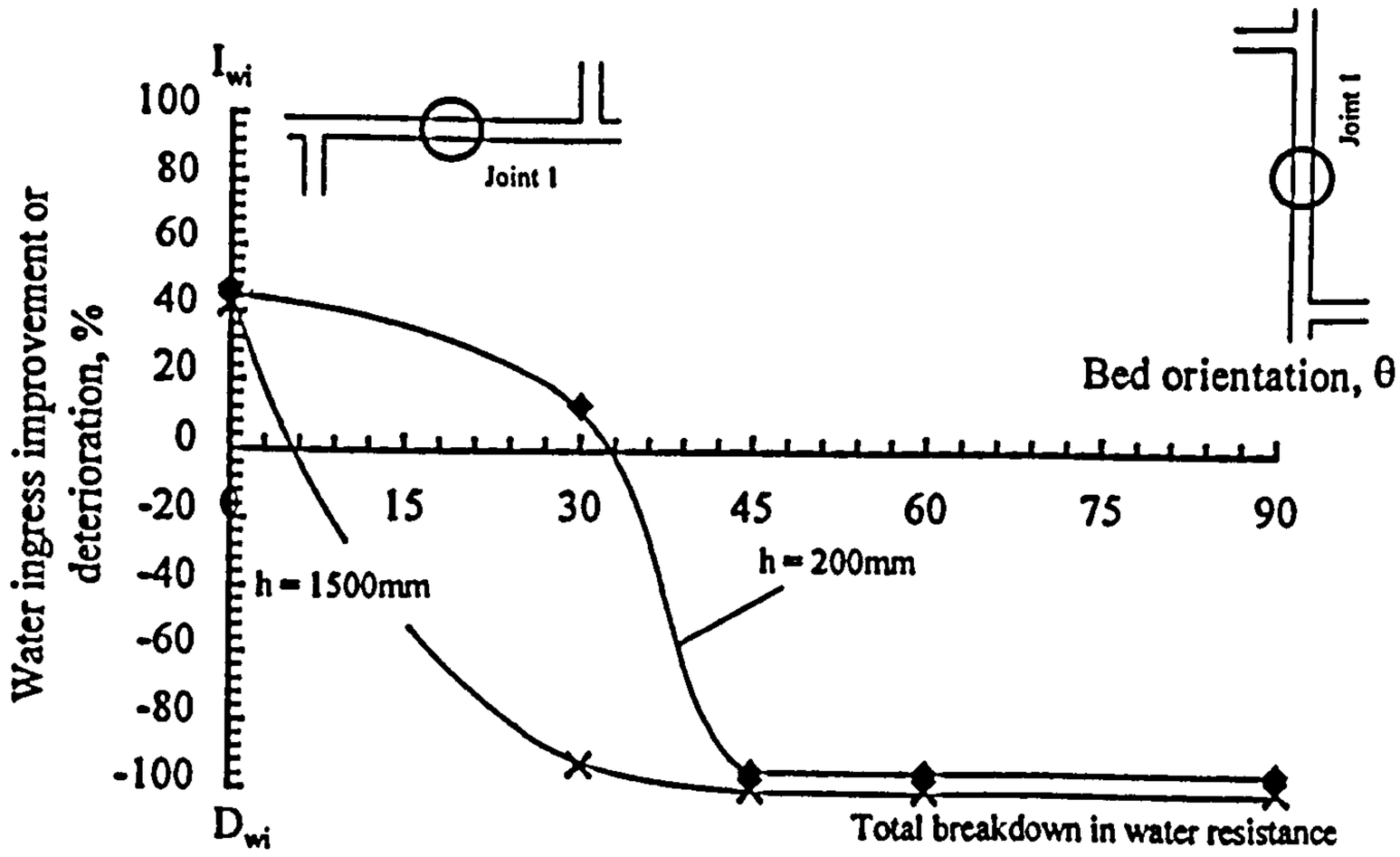

Fig. 6.48(c) Panel integrity relationship for Joint 1 as orientation increased, applied stress = $0.6f_{ult}$

This figure shows a total breakdown in the resistance of Joint 1 to water ingress when $\theta \geq 45°$. This occurred irrespective of the value of initial head.

For an initial head of h=200mm increased integrity of panels ($I_{wi}>0\%$) was only evident for $\theta \leq 33°$, thereafter a steep decline was noted as the brick/mortar bond became increasingly compromised to shear stresses and slip.

Panels under high initial heads (h=1500mm) showed improved resistance to water ingress only when $\theta<6°$. Thereafter, the structurally compromised brick/mortar bond allowed higher heads to exploit any tensile cracks or fissures which ensured full breakdown at bed orientations (θ) of between 30° and 45°.

(d) Overview of behaviour at Joint 1:

As bed orientation rotated towards θ=90°, then Joint 1 became increasingly prone to higher volumes of water ingress. This became further evident at higher applied stress and initial head levels.

As applied stress level increased, the range of bed orientations that would result in improved resistance characteristics (I_{wi} >0%) decreased. For an initial head h=200mm, this range was θ≤45° at $0.3f_{ult}$ to θ≤33° at $0.6f_{ult}$. Similarly for h=1500mm this range was θ≤27° decreasing to θ≤6° over the same applied stress range.

Total breakdown of Joint 1 resistance to water ingress varied with bed orientation, applied stress level and initial head. No total breakdown in joint resistance was encountered when h=200mm at $0.3f_{ult}$. This changed to breakdown at θ≥45° when applied stress was $0.6f_{ult}$. For initial head of h=1500mm the total breakdown occurred at angles of orientation of θ≥60° and θ≥30° when applied stress levels were $0.3f_{ult}$ and $0.6f_{ult}$ respectively.

6.8.2 Effect of bed orientation at Joint 2

Figure 6.49(a-c) indicates water ingress behaviour as the main bed was orientated closer to tensile failure and applied stress increased at the perpend joints (Joint 2).

(a) Water ingress behaviour under applied stress level of $0.3f_{ult}$:

Fig. 6.49(a) shows the improvement or deterioration in water ingress at Joint 2 as bed orientated to 90° and panel was stressed to $0.3f_{ult}$.

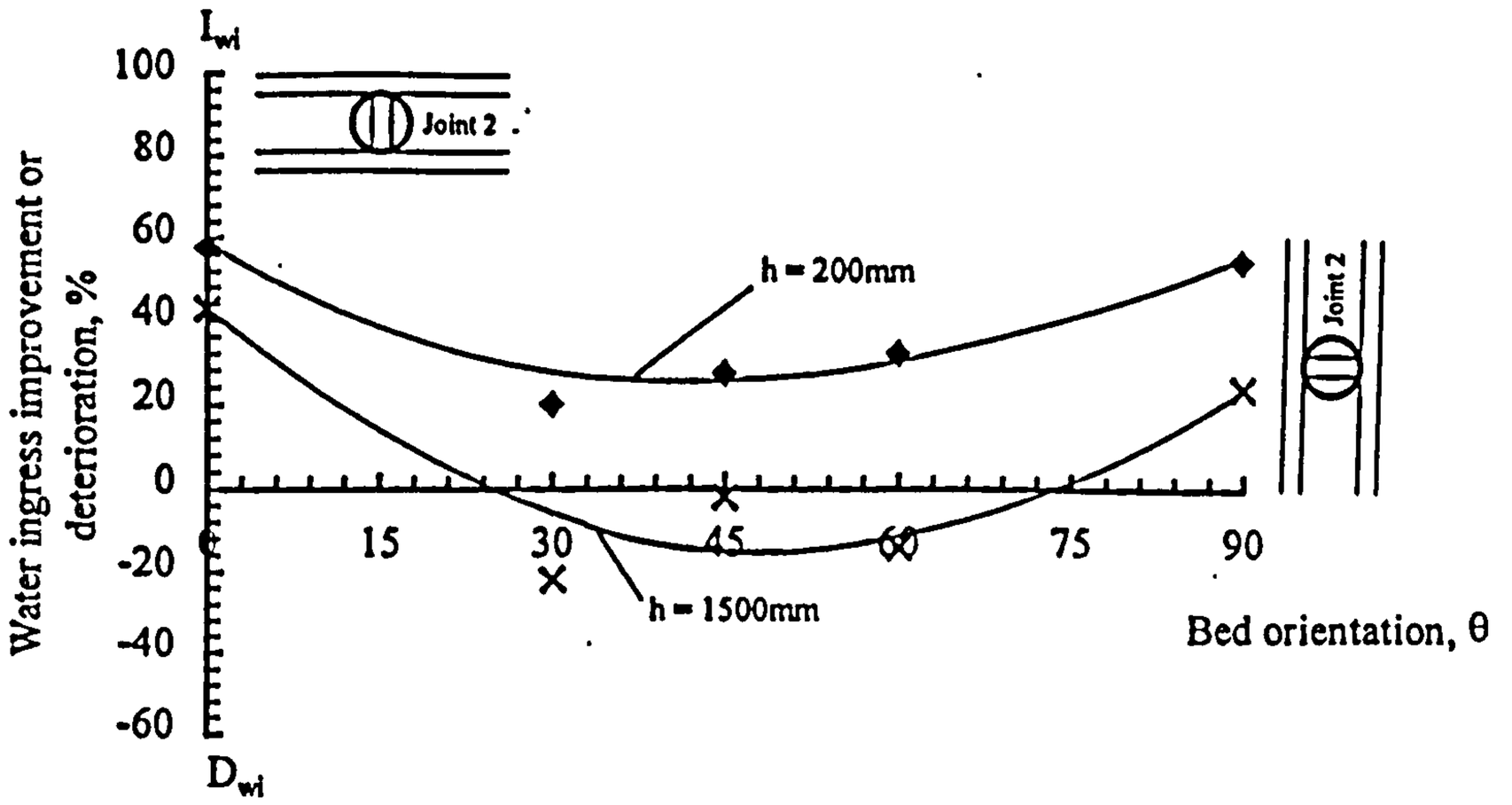

Fig. 6.49(a) Panel integrity relationship for Joint 2 as orientation increased, applied stress = $0.3f_{ult}$

At Joint 2 for low initial heads h=200mm, there was an improvement in the resistance of the joint to water ingress relative to unstressed panels (I_{wi}=D_{wi}=0%), at this applied stress level ($0.3f_{ult}$) irrespective of bed orientation.

Generally, at low bed orientations Poisson's ratio effects result in the closing of any fissures at the brick/mortar interface. As bed orientation approached θ=90° then this beneficial effect was replaced by large compression strains.

The minimum improvement in ingress occurred when bed orientation (θ) lay between 30°-60°. At this position neither Poisson's effects nor direct compression strains were dominant and surface microcracks were generated which increased water ingress.

These minimum values were also indicated at high initial heads of h=1500mm. Any tensile cracking at bed orientation (θ) between 25°-72° resulted in large ingress rates being present at these high heads.

Again an improvement generally occurred where Poisson's ratio effects or applied stress causing direct compression strains were dominant. Poisson's ratio effects have been discussed at length in Section 6.3.5.

Initial heads of 600mm and 1000mm were found to lie within those limits as already indicated in Fig. 6.49(a). These were omitted for both clarity and ease of discussion.

(b) Water ingress behaviour under applied stress level of $0.45f_{ult}$:

Figure 6.49(b) shows the behaviour of Joint 2 to water ingress as bed orientation rotated from $\theta=0°$ to $\theta=90°$ and the applied stress level was $0.45f_{ult}$.

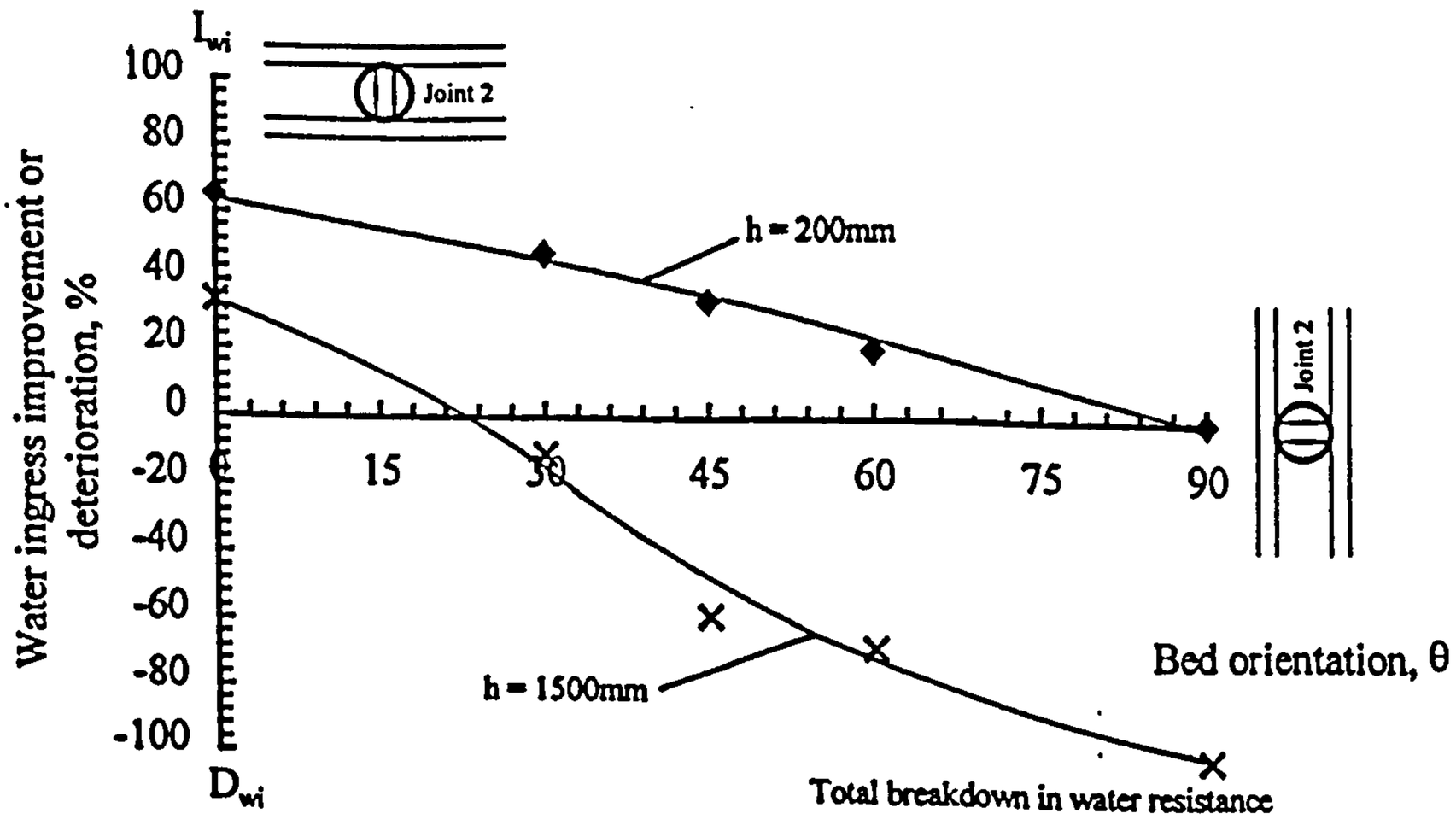

Fig. 6.49(b) Panel integrity relationship for Joint 2 as orientation increased, applied stress = $0.45f_{ult}$

Figure 6.49(b) shows that at $0.45f_{ult}$ and for low initial heads (h=200mm) there was always an improvement in panel resistance to water ingress though the magnitude of this improvement decreased from a maximum at $\theta=0°$ to a minimum at $\theta=90°$.

High initial heads (h=1500mm) exploited any tensile cracking or adjacent bed debonding to a greater effect, with the joints' resistance to water ingress effectively deteriorating after $\theta\cong18°$. Total breakdown was exhibited at $\theta=60°$.

(c) Water ingress behaviour under applied stress level of $0.6f_{ult}$:

High applied stresses $=0.6f_{ult}$ resulted in Poisson's ratio effects having little influence at low bed orientations, hence a much smaller improvement was exhibited in Fig. 6.49(c) compared to Fig. 6.49(a,b).

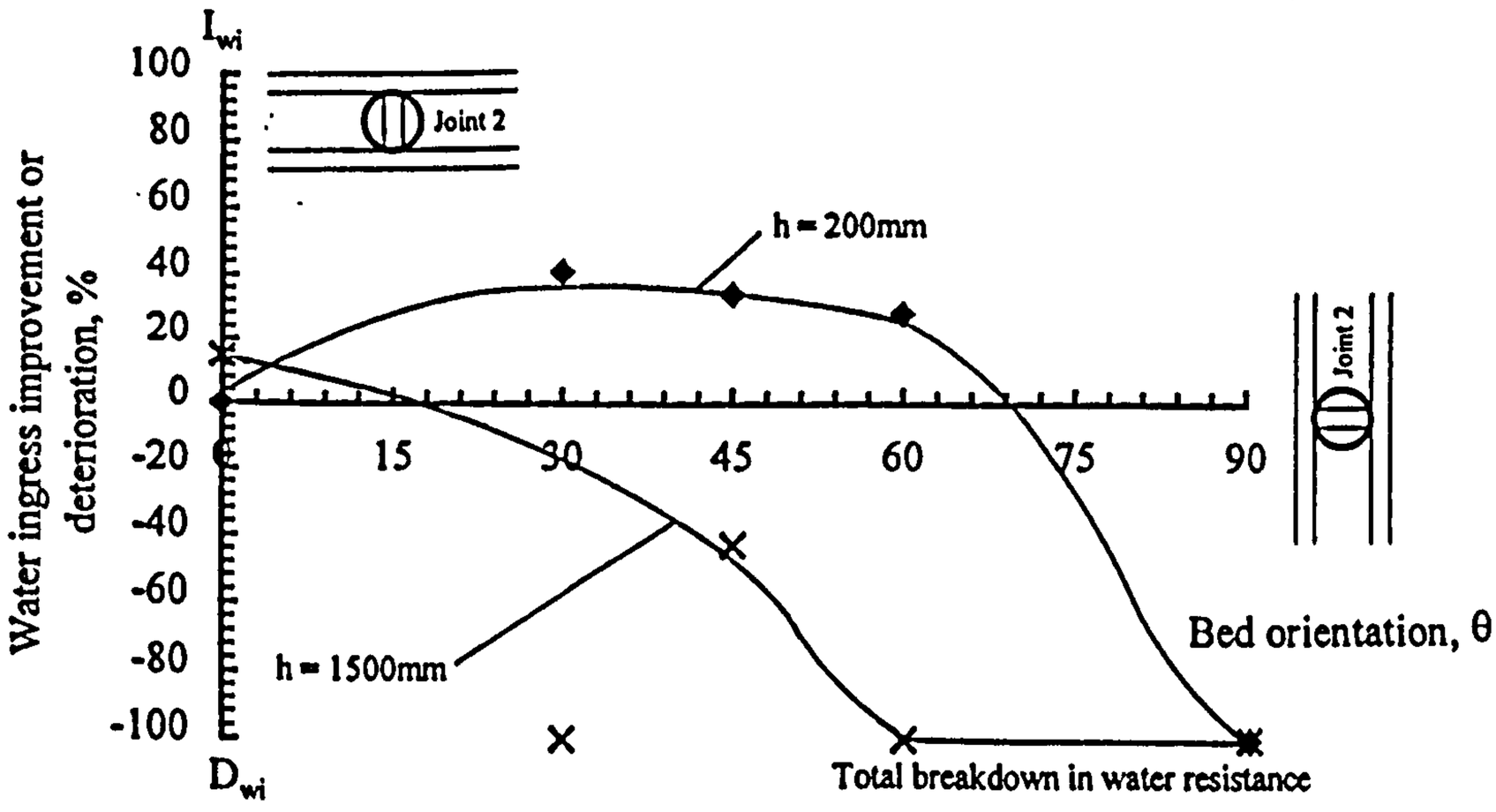

Fig. 6.49(c) Panel integrity relationship for Joint 2 as orientation increased, applied stress = $0.6f_{ult}$

For an initial head of h=1500mm total breakdown occurred when θ=60° as tensile splitting at Joint 2 would occur. This is not exhibited for lower head of h=200mm, where large improvements were noted at θ=30°, 45° and 60°. However when θ=90°, the failure mode changed to splitting and debonding of the brick/mortar interfaces of the main beds (Joint 1). The formation of these cracks at the sides of Joint 2 had a major contribution to the total breakdown in the resistance of Joint 2 to water ingress.

Average experimental result at θ=30° for h=1500mm is anomalous as a result of experimental error and total breakdown would not be expected at this position.

(d) Overview of behaviour at Joint 2:

Figures 6.49(a-c) have indicated the unique ingress characteristics of perpend bed joints as a masonry panel is rotated from θ=0° to θ=90°.

At low stress levels, Joint 2 can be generally assumed to improve its water resistance capacity. However as applied stress increased and the panel failure mode changed dependent upon bed orientation then Joint 2 became increasingly compromised. At high initial heads of h=1500mm, total breakdown was not encountered for $0.3f_{ult}$. However this changed to θ=60° for $0.6f_{ult}$ indicating the influence of bed orientation and its related failure mode.

6.8.3 Effect of bed orientation at Joint 3

Figure 6.50(a-c) indicate water ingress behaviour at Joint 3 which incorporated phenomena that occurred at both main bed and perpend mortar joint.

(a) Water ingress behaviour under applied stress level of $0.3f_{ult}$:

Figure 6.50(a) shows the effect of bed orientation on water ingress at Joint 3 under an applied stress level of $0.3f_{ult}$.

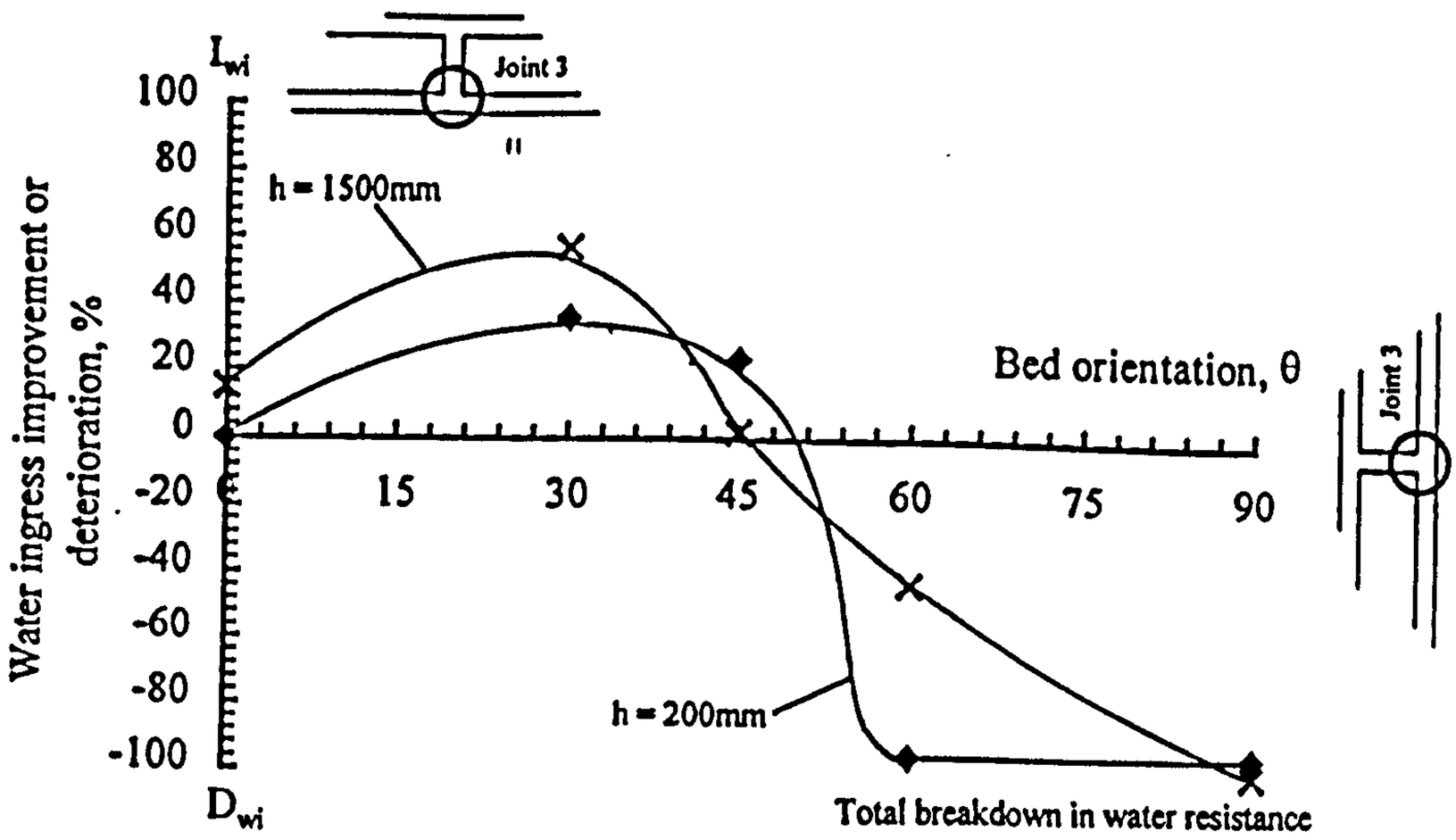

Fig. 6.50(a) Panel integrity relationship for Joint 3 as orientation increased, applied stress = $0.3f_{ult}$

At low bed orientations, large compressive strains improved the resistance of Joint 3 (I_{wi}>0%) to water ingress for both h=200mm and h=1500mm. As the bed orientation increased then shear strains would compromise the brick/mortar bond capacity, hence the resistance to water ingress deteriorates (D_{wi}<0%) after θ>50° at h=200mm and at θ>45° at h=1500mm. Total breakdown in resistance occurred at θ=60° for h=200mm and θ=90° at h=1500mm.

The average experimental result at θ=60° for h=1500mm is anomalous as a result of experimental error as total breakdown (D_{wi}=-100%) would be expected at this position.

(b) Water ingress behaviour under applied stress level of $0.45f_{ult}$:

The continued dependence of water ingress on bed orientation is indicated again in Fig. 6.50(b) when the applied stress level was $0.45f_{ult}$.

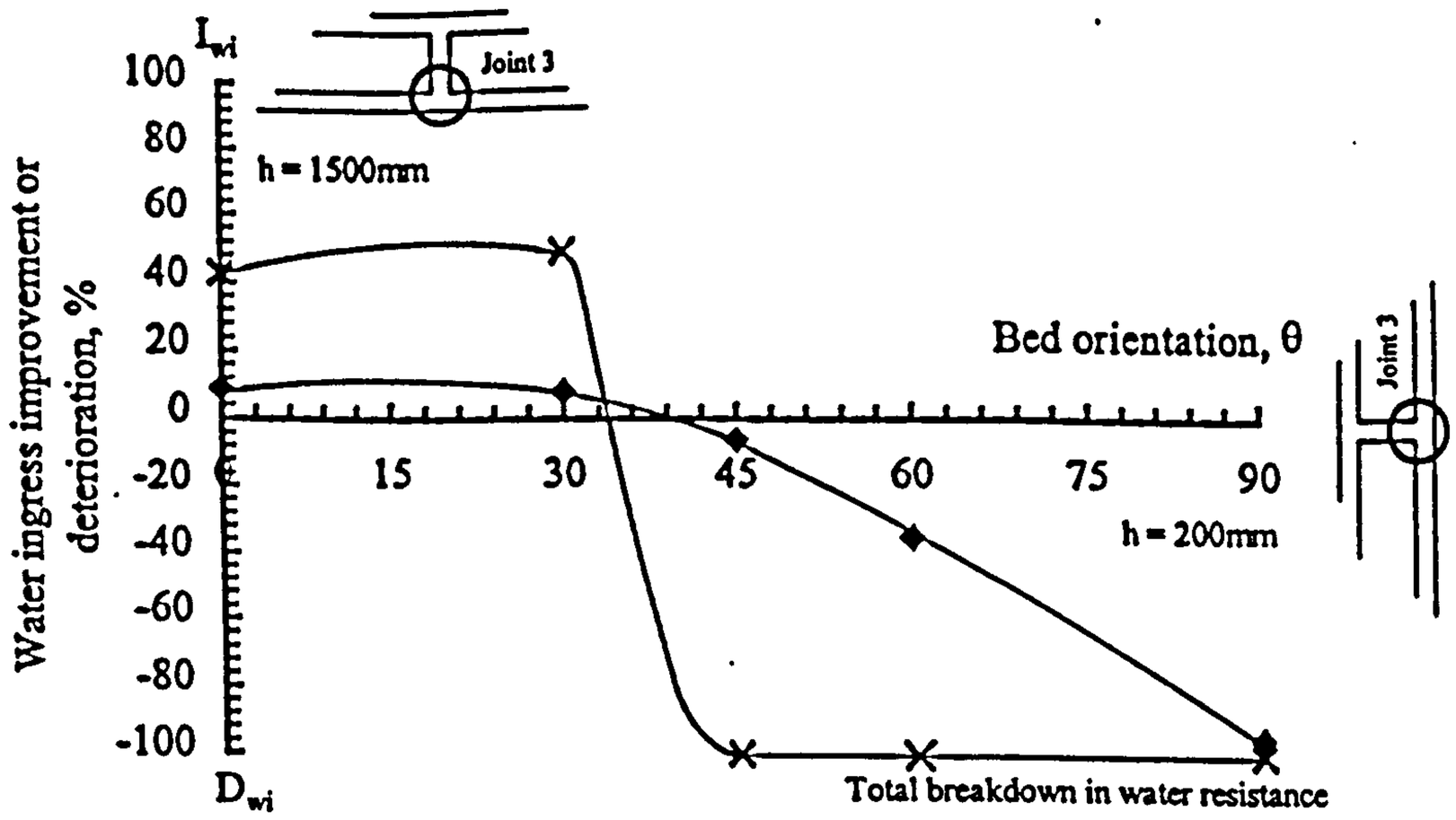

Fig. 6.50(b) Panel integrity relationship for Joint 3 as orientation increased, applied stress = $0.45f_{ult}$

Irrespective of initial head there was a small improvement in Joint 3 resistance to water ingress up to $\theta \cong 30°$ when shear stresses were small. Thereafter there was a sharp deterioration in Joint 3 resistance to water ingress indicated by total breakdown at $\theta = 45°$ for h=1500mm and 90° for h=200mm.

(c) Water ingress behaviour under applied stress level of $0.6f_{ult}$:

Figure 6.50(c) shows water ingress behaviour dependent upon bed orientation as stress level was increased to $0.6f_{ult}$.

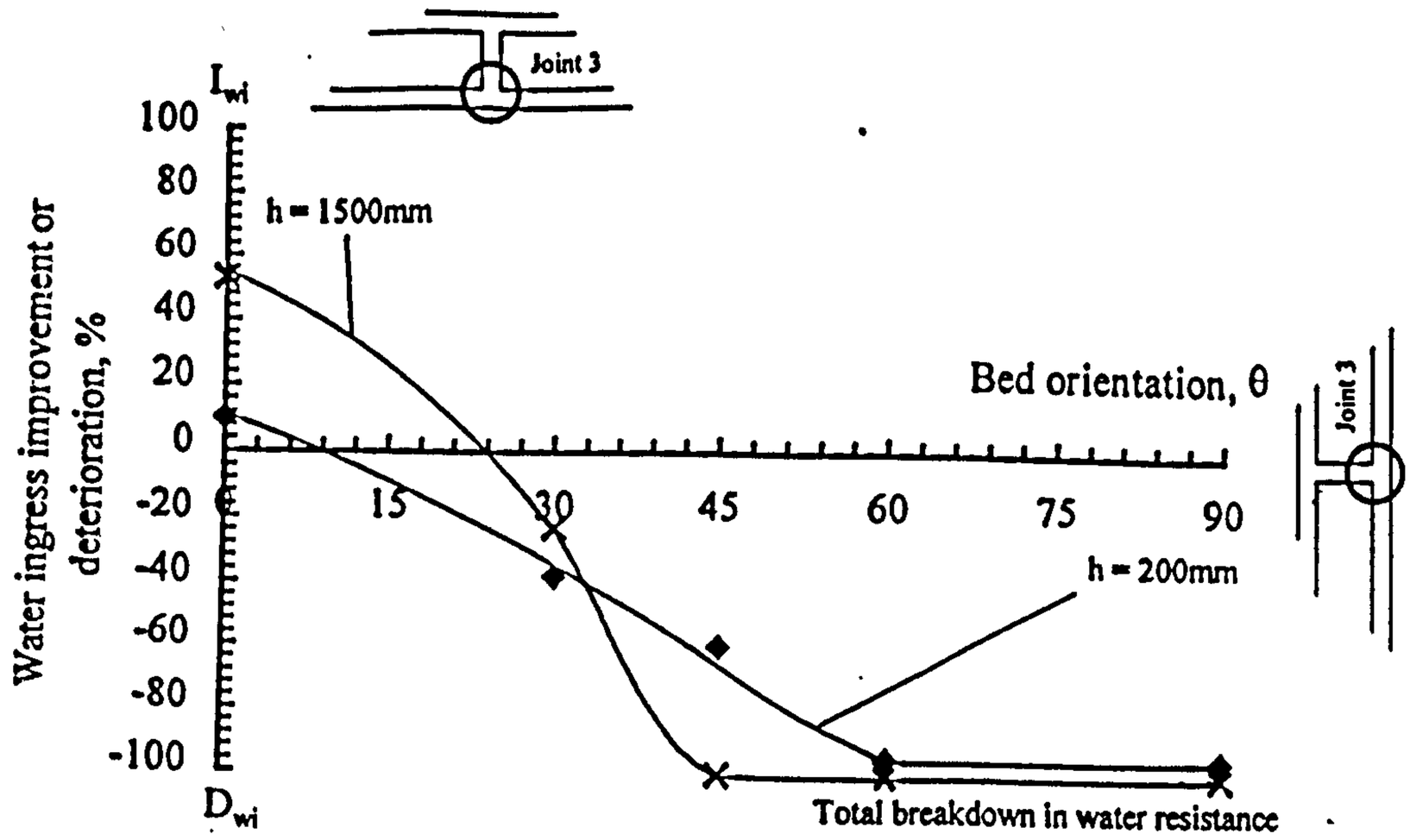

Fig. 6.50(c) Panel integrity relationship for Joint 3 as orientation increased, applied stress = $0.6f_{ult}$

As applied stress level increased to $0.6f_{ult}$ then Joint 3 resistance to water ingress deteriorated from 9°-24° dependent upon initial head.

Correspondingly, due to the brick/mortar bond capacity being compromised by large stresses, total breakdown was exhibited at θ=45° for h=1500mm and θ=60° for h=200mm.

(d) Overview of behaviour at Joint 3:

Figures 6.50(a-c) show the unique water ingress behaviour exhibited at Joint 3 when varying bed orientation.

Joint 3 ingress was controlled by the resistance that its main bed joint generated against water ingress. The vertical joint component was only partially influential, hence the total breakdown in resistance to water ingress occurred at higher bed orientations than at Joint 1.

However, behaviour at Joint 3 may be considered unique due to the method of construction of this joint and the influence of stress concentrations when the masonry panel was loaded.

6.9 Comparative Study of Water Ingress into Calcium Silicate and Clay Bricks Panels

The aesthetic properties of calcium silicate bricks make them a popular choice for masonry structures. Therefore, during their working life they encounter a full range of severe environmental conditions which can compromise their durability.

As the raw materials used to manufacture calcium silicate bricks differ from their clay brick counterparts then so do their physical properties and have the ability to resist water ingress. These differences are exhibited in Tables 3.6 and 3.7, Chapter 3.

By assessing water ingress rates into calcium silicate panels via permeameters and comparing this with corresponding ingress rates for clay brick panels then an indication as to the change in water ingress can be found.

6.9.1 Calcium silicate test panels

Five calcium silicate (Type 1) masonry panels were tested in this investigation. These panels were denoted as A-E, depending on bed orientation. Figure 6.51 shows the location of the permeameters on the test panels. No demec gauges were used as only unstressed panels were tested for water ingress.

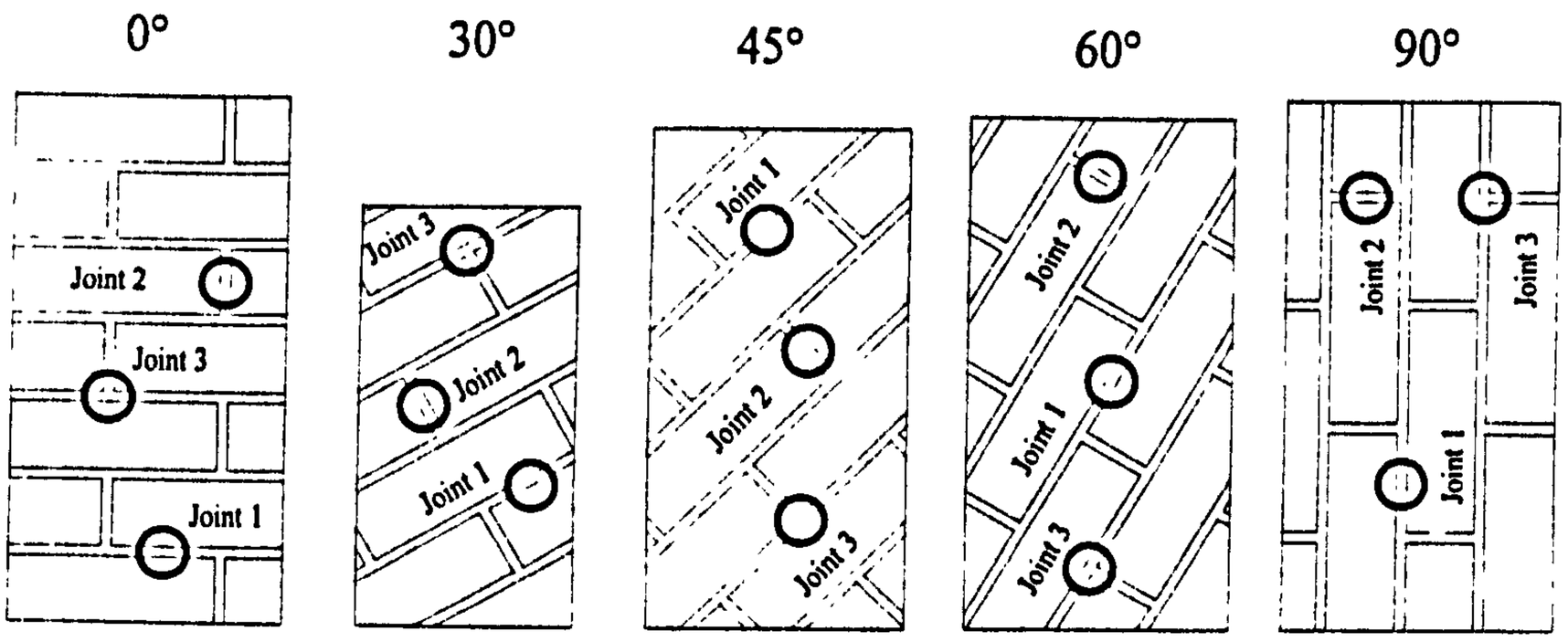

Fig. 6.51 Permeameter positions for calcium silicate (Type 1) test panels

Water ingress was measured using the same permeameter and technique as described in Chapter 4. Water ingress was measured at all mortar joint positions using initial heads of 200mm, 600mm, 1000mm and 1500mm.

6.9.2 Water ingress through calcium silicate (Type 1) and clay (Type 2, 3 and 4) brick panels

Using average water ingress rates for unstressed calcium silicate and clay brick panels allowed the study of the ability of each material to inhibit water ingress. The average ingress rates for clay brick panels as measured experimentally can be found in Figs 6.4-6.6, 6.13-6.15, 6.22-6.24, 6.32-6.34 and 6.41-6.43. These were dependent upon bed orientation and mortar joint position.

Figure 6.52 shows the average water ingress rates for unstressed calcium silicate and clay brick panels.

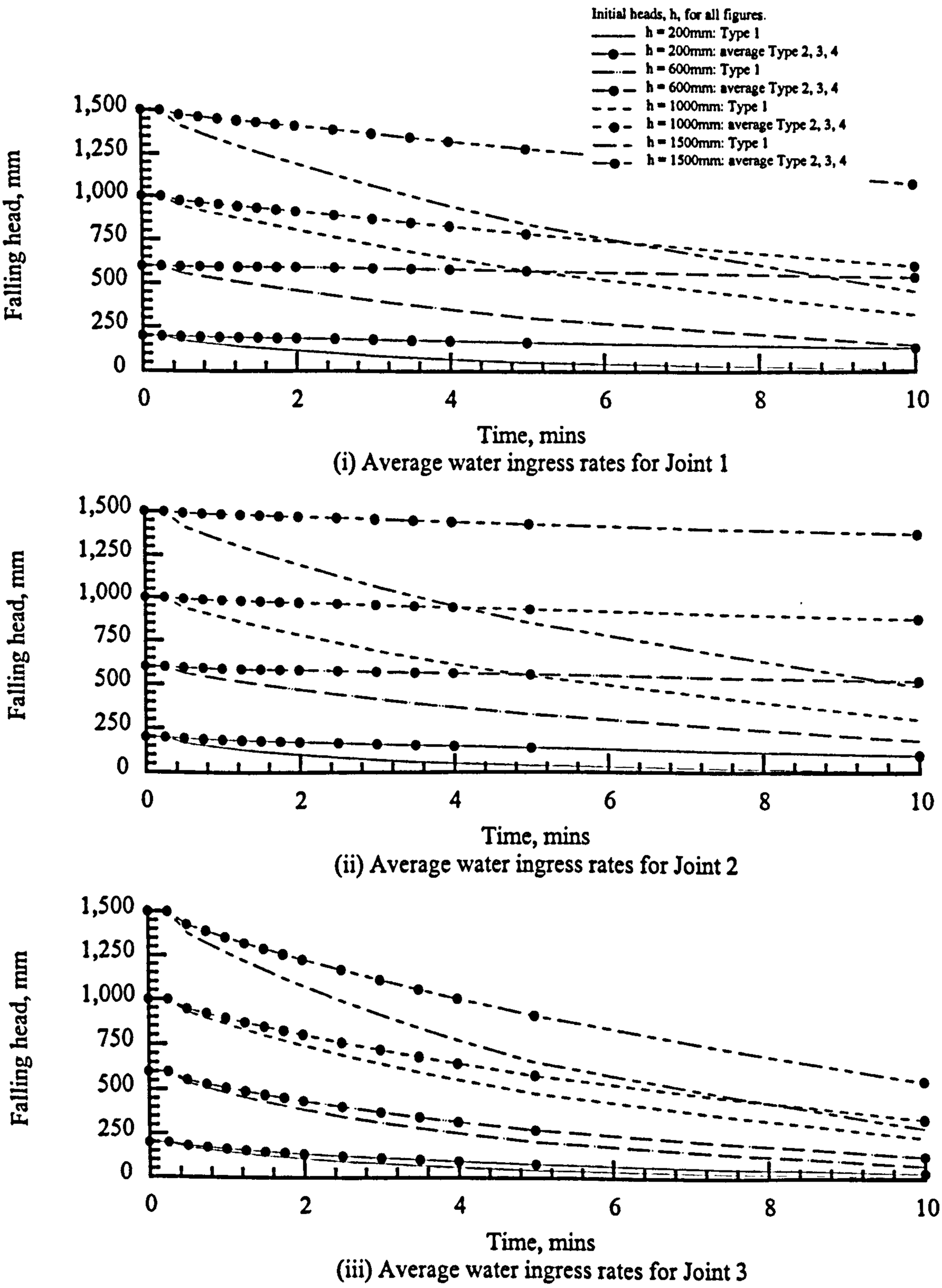

Fig. 6.52 Comparison of average water ingress rates for unstressed calcium silicate (Type 1) and clay brick (Type 2, 3 and 4) panels

Figure 6.52 shows that clay bricks are more resistant to water ingress irrespective of the initial water head or mortar joint position.

Table 6.15 shows the difference in the volume of water ingress within the initial 10mins of test commencing using data in Fig. 6.52 for calcium silicate and clay brick panels.

Table 6.15 Average volume of water ingress within initial 10mins of testing into unstressed calcium silicate and clay brick panels

Initial head, h (mm)	Volume ingress at Joint 1 (mm^3)			Volume ingress at Joint 2 (mm^3)			Volume ingress at Joint 3 (mm^3)		
	T1*	T2,3,4*	Z*	T1	T2,3,4	Z*	T1	T2,3,4	Z*
200	14372	4712	3.0	14922	4712	3.2	14922	13351	1.2
600	27488	10105	2.7	32986	7853	4.2	41626	37699	1.1
1000	53407	27489	1.9	54977	8639	6.4	60475	51836	1.2
1500	81681	31415	2.6	79325	10602	7.5	95033	74612	1.3

T1* - Average volume of ingress for calcium silicate (Type 1) brick panels
T2,3,4* - Average volume of ingress for clay (Types 2, 3 and 4) brick panels
Z* - Average volume of water ingress for calcium silicate brick (T1) panels / average volume of ingress for clay brick (T2,3,4) panels

Table 6.15 shows that irrespective of joint position and at low initial heads (h=200mm and h=600mm), calcium silicate panels were on average found to encourage 2.5 times more the volume of water ingress than that found in clay brick panels. This had risen to 3.2 times the volume for h=1000mm and 3.8 times for h=1500mm.

The variation in ingress between these two generic panel types was caused by the large difference in absorption rates between the two types of bricks. It was also recognised that calcium silicate bricks have a lower brick/mortar bond strength compared to clay bricks and hence were likely have a higher proportion of cavities at the brick/mortar interface which encouraged water ingress.

Both Fig. 6.52 and Table 6.15 show that Joint 3 was consistently found to be the least resistant to water ingress. This indicated that the laying method used to construct this joint proved highly influential in encouraging or inhibiting water ingress. This laying method has already been discussed at length in Section 6.3.6.

6.10 Conclusions

Based on the experimental results and observations presented in this chapter the following conclusions were made:

- For panels with bed orientation $\theta=0°$, the main mortar bed joint (Joint 1) was compressed under all levels of applied stress used in this investigation allowing the mortar bed to become less permeable to water ingress.

  Perpend joints (Joint 2) exhibited improved resistance to water ingress up to applied stress level of $0.45f_{ult}$ as a result of Poisson's ratio effects. At $0.6f_{ult}$, Poisson's ratio effects were negated and debonding occurred with a corresponding increase in water ingress.

  The present study showed that ingress was inhibited less at Joint 3 than at Joints 1 and 2. The main reason for this was possibly due to the process of laying adopted by the mason in forming Joint 3. For Joints 1 and 2 the mortar is applied directly to the brick and compressed against other bricks in the construction of the panels. This produces a good bond at the brick/mortar interface. The situation for Joint 3 is different in the sense that mortar is usually pointed into position later which may leave large cavities under the skin of the mortar. This thin layer is easily accessible by water when the panels are unstressed and the situation worsens under stress due to the resulting stress concentrations which creates incompatible deformations and strain discontinuity.

- Stressed panels with bed orientation $\theta=90°$ showed severe cracking at Joint 1 which occurred at the brick/mortar interface at low applied stress levels of $0.3f_{ult}$. This inhibited the resistance to water ingress and at high applied stress levels ($0.45f_{ult}$, $0.6f_{ult}$) total water ingress was complete after 15 seconds irrespective of the initial head of water.

Joint 2 was found to exhibit improved resistance to water ingress at applied stress levels of $0.3f_{ult}$ compared to the unstressed condition. Higher applied stress levels ($0.45f_{ult}$, $0.6f_{ult}$) caused microcracks in this mortar bed and surrounding brick and debonding of the adjacent mortar beds which resulted in increased water ingress rates.

- Stressed panels with bed orientation of $\theta=30°$ showed a shear slip at Joint 1 at an applied stress of $0.45f_{ult}$. This produced a less water resistant mortar bed compared to those exhibited for $\theta=0°$ panels.

  Joint 2 showed an increase in water resistance at low stress levels ($0.3f_{ult}$) due to Poisson's ratio effects. At higher applied stress levels ($\geq 0.45f_{ult}$) debonding occurred leading to an increase in water ingress.

- Stressed panels with bed orientation $\theta=45°$ showed an improvement in resistance to water ingress of Joint 1 under low levels of applied stress ($\leq 0.3f_{ult}$). As applied stress levels increased ($\geq 0.45f_{ult}$) shear slip occurred causing an increase in water ingress.

- Stressed panels with bed orientation of $\theta=60°$ exhibited some shear slip at Joint 1 on immediate commencement of loading indicated by an increase in water ingress at all initial heads compared to water ingress when panel were unstressed.

  Some tensile debonding and small microcrack formation was evident at Joint 2 particularly at higher applied stress levels than $0.3f_{ult}$. This was most evident by the increase in water ingress for initial heads ≥1000mm.

- For all panels, the magnitude of the initial head was not found influential at $0.0f_{ult}$ i.e. unstressed. When panels were loaded and cracking occurred at all joints under consideration, then higher initial heads produced higher rates of water ingress.

- The effect of bed orientation on water ingress was investigated by comparing the volume of ingressed water when panels were unstressed and stressed.

  This investigation found that Joint 1 decreased in its resistance to water ingress as both bed orientation rotated towards 90° and the stress level increased to $0.6f_{ult}$. An improvement in Joint 1 resistance to water ingress was only noted at $0.6f_{ult}$ when bed orientation was ≤30° at h=200mm and ≤10° at h=1500mm.

  Conversely Joint 2 generally improved its resistance to water ingress as bed orientated towards 90° though only up to and including applied stress levels of $0.45f_{ult}$. At $0.45f_{ult}$, an improved resistance to ingress at Joint 2 was noted when θ≤37° and θ≤27° for h=200mm and 1500mm respectively. Having increased the stress level to $0.6f_{ult}$, this changed to θ≤30° and θ≤15° over the same initial head range.

- Calcium silicate panels were found to be 2.5-3.8 times more likely to allow water ingress than clay brick counterparts this being dependent upon the applied pressure head of water. This was mainly due to differences in the material type, method of manufacture and brick/mortar bond strength.

CHAPTER 7

WATER INGRESS CHARACTERISTICS FOR ECCENTRICALLY LOADED PANELS AND CONCENTRICALLY LOADED PRE-SATURATED PANELS

7.1 Introduction

The water ingress characteristics of a masonry panel can be governed by both the eccentricity of loading and the level of inherent dampness.

Eccentricity of loading and the slenderness ratio (S_r) of a wall can govern its strength. The slenderness ratio is defined as:

$$S_r = \frac{h_p}{t_p} \qquad \text{Eqn. 7.1}$$

h_p - height of panel

t_p - thickness of panel

These factors are in turn dependent upon the geometry of the panel, its stiffness and the ability of a wall to distribute applied loads. Dependent upon the slenderness ratio, panels may fail by compression ($S_r<30$) or by buckling, exhibited by lateral deflection, prior to total structural failure ($S_r>30$).

Masonry structures can also be inherently damp due to a combination of repeated wetting and poor ventilation. Water is likely to be held in cavities and pores of the masonry and should reduce the likelihood of additional water ingress from rainfall.

This chapter examines the effect of the above factors on water ingress and attempts to quantify these.

7.2 Eccentric Loading on Masonry Panels

In walls subjected to bending and a small axial compression load, the angle of rotation is concentrated in one mortar joint only, with large cracks occurring at this joint. Under bending and large compression loads, the rotation occurs over several mortar joints [136].

Chapman and Slatford [113,137] considered the 'line of thrust' theory when developing a model for brittle masonry wall failure due to eccentric loading. If the load is applied within the middle third of a panel width, then no tension exists within the panel. Only when an applied load acts outwith the middle third is tension generated on a panel face. This leads to a cracked zone being formed, with this gradually extending over the height of the panel (Fig. 7.1(a)). Failure occurs when the cracked zone reaches the line of thrust and forms a hinge, usually at mid-height of the panel (Fig. 7.1(b)).

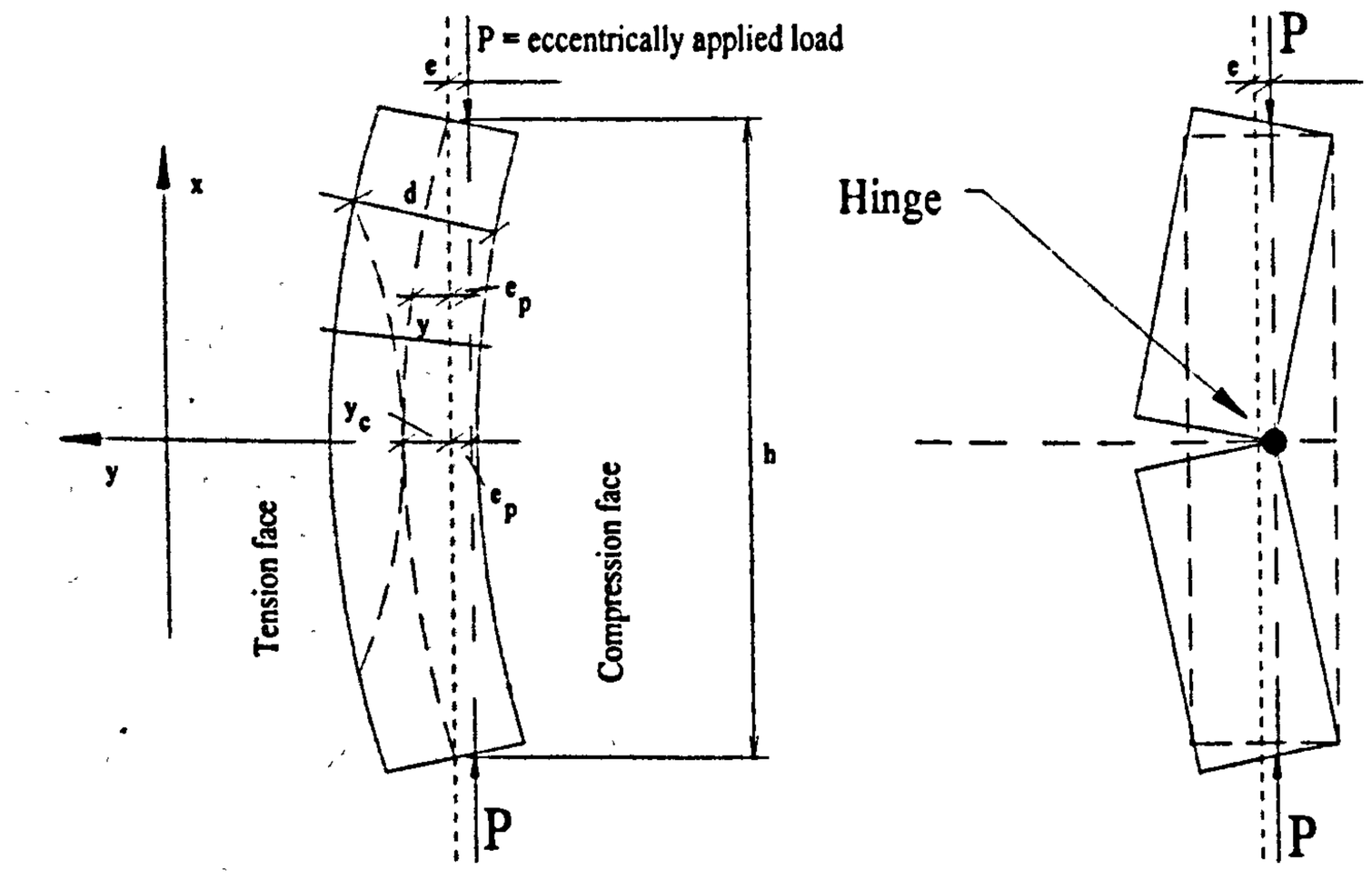

(a) (b)

Fig. 7.1 Eccentrically loaded pinned-end column of brittle material [113]

Eccentric loading is considered in BS 5628: Part 1 'Structural Use of Masonry' [138, 139]. Using simple eccentric loading positions (Fig 7.2) together with an additional value that allows for an increased moment due to slenderness (e_a) then a maximum eccentricity (e_t) can be calculated (Fig. 7.3).

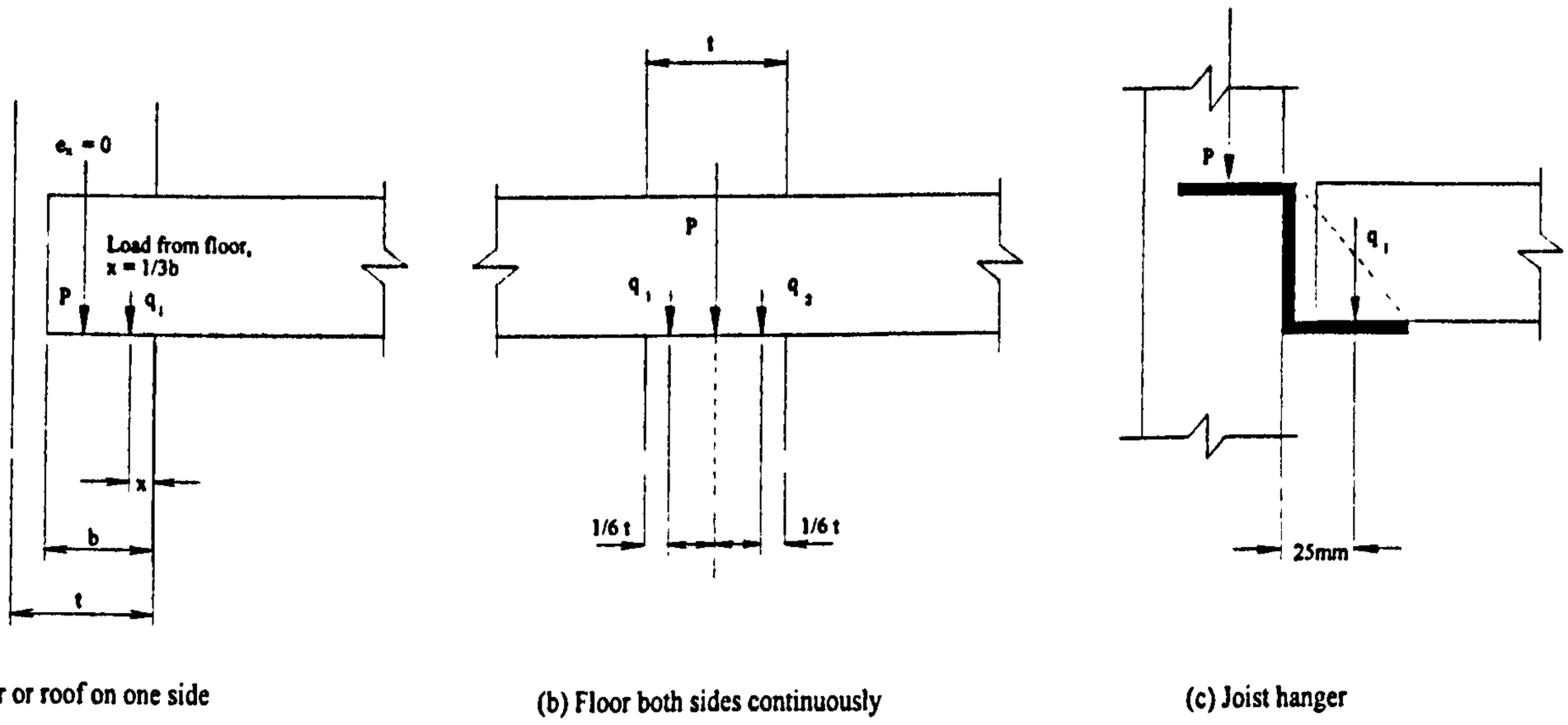

(a) Floor or roof on one side

(b) Floor both sides continuously

(c) Joist hanger

Note: q_1 and q_2 are loads from the floor
P is the load from the walls and above floors

Fig. 7.2 Standard eccentric loading positions [138]

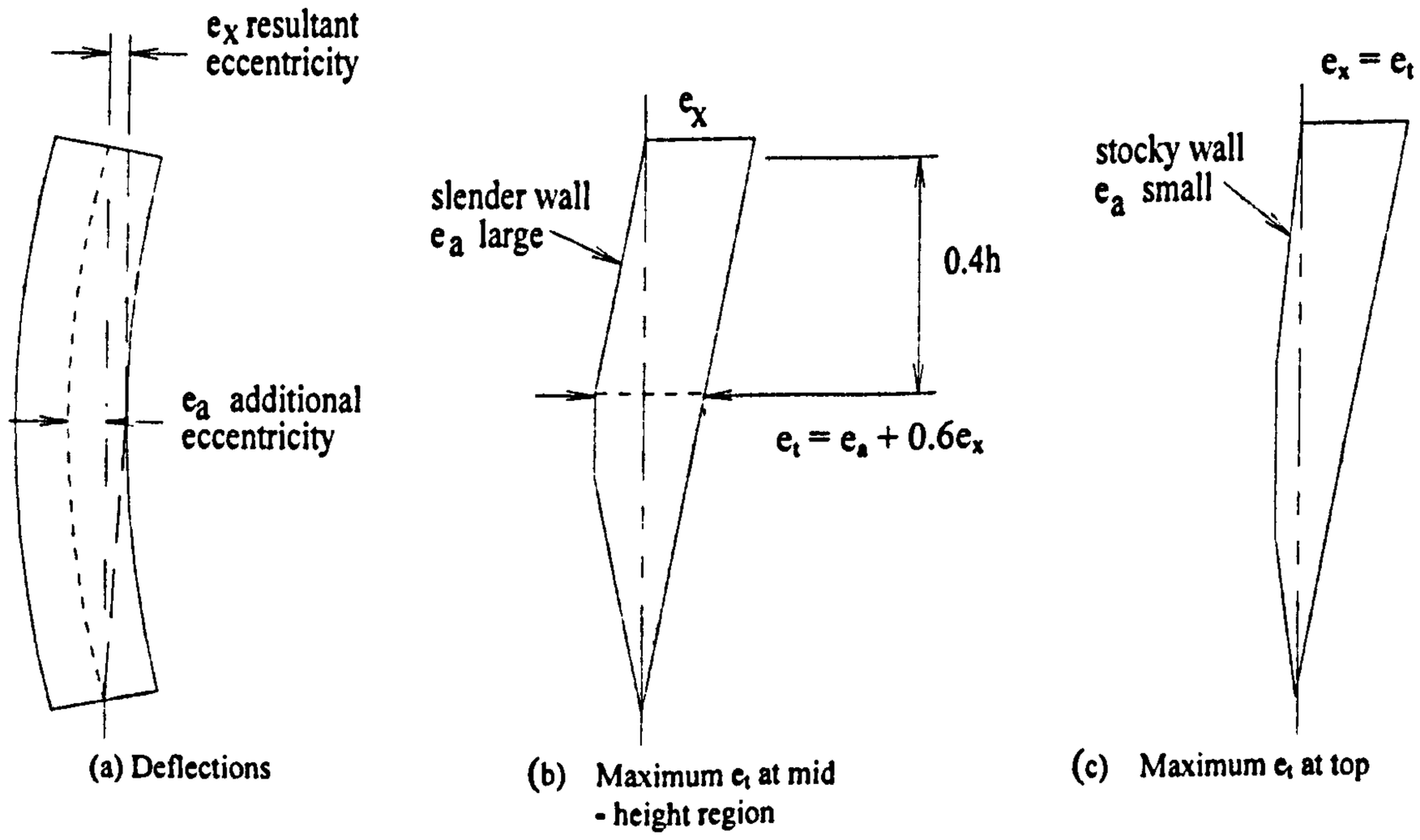

(a) Deflections

(b) Maximum e_t at mid - height region

(c) Maximum e_t at top

Fig. 7.3 Design eccentricity [139]

$$e_t = e_a + 0.6e_x \qquad \text{Eqn. 7.2}$$

where:

$$e_a = t_p\left[\frac{1}{2400}\left(\frac{h_{ef}}{t_{ef}}\right) - 0.015\right] \qquad \text{Eqn. 7.3}$$

t_p - panel thickness

t_{ef} - effective panel thickness

h_{ef} - effective panel height

e_x - resultant eccentricity

By considering both this maximum eccentricity value (e_t) and the characteristic masonry strength (f_k) then a capacity reduction factor (C_R) can be deduced to yield a wall load capacity. This leads to a design vertical load (Q_k), which can be calculated as:

$$Q_k = C_R t_p f_k \qquad \text{Eqn. 7.4}$$

The design vertical load (Q_k) would normally be multiplied by safety factors to accommodate any material variability and possible differences between site built and laboratory built panels.

7.3 Water Ingress Characteristics for Eccentrically Loaded Masonry Panels

When a panel bends under eccentric loading then the brick and mortar debond. The largest debonding and cracking would occur along the main horizontal bed, particularly at the centre sections of the panel, and would increase the likelihood of water ingress.

Permeameters and the accompanying test technique (Chapter 4) was used to investigate water ingress into eccentrically loaded masonry panels.

7.3.1 Panel testing

Two Type 4 panels with bed orientation $\theta=0°$. These were denoted as panels 4Ai and 4Aii. A bed orientation of $\theta=0°$ was chosen as this was the most realistic panel loading orientation and avoided any shear failure.

Panels 4Ai and 4Aii both had a cross section of 100x275mm and a predicted concentric failure load (F_{ult}) of 565kN. Water ingress was measured when eccentrically applied load was 170kN ($0.3F_{ult}$), 254kN ($0.45F_{ult}$) and 339kN ($0.6F_{ult}$). The slenderness ratio (S_r) for these panel was 5.

The location of permeameters and demec points are shown in Fig. 7.4.

Permeameters were attached to Face A (tension) only and were expected to measure changes in water ingress in panels under an eccentric load and where cracking occurred. Figure 7.4 also indicates that demec buttons were attached to both faces of the test panel which allowed potential tensile and compressive strains to be measured.

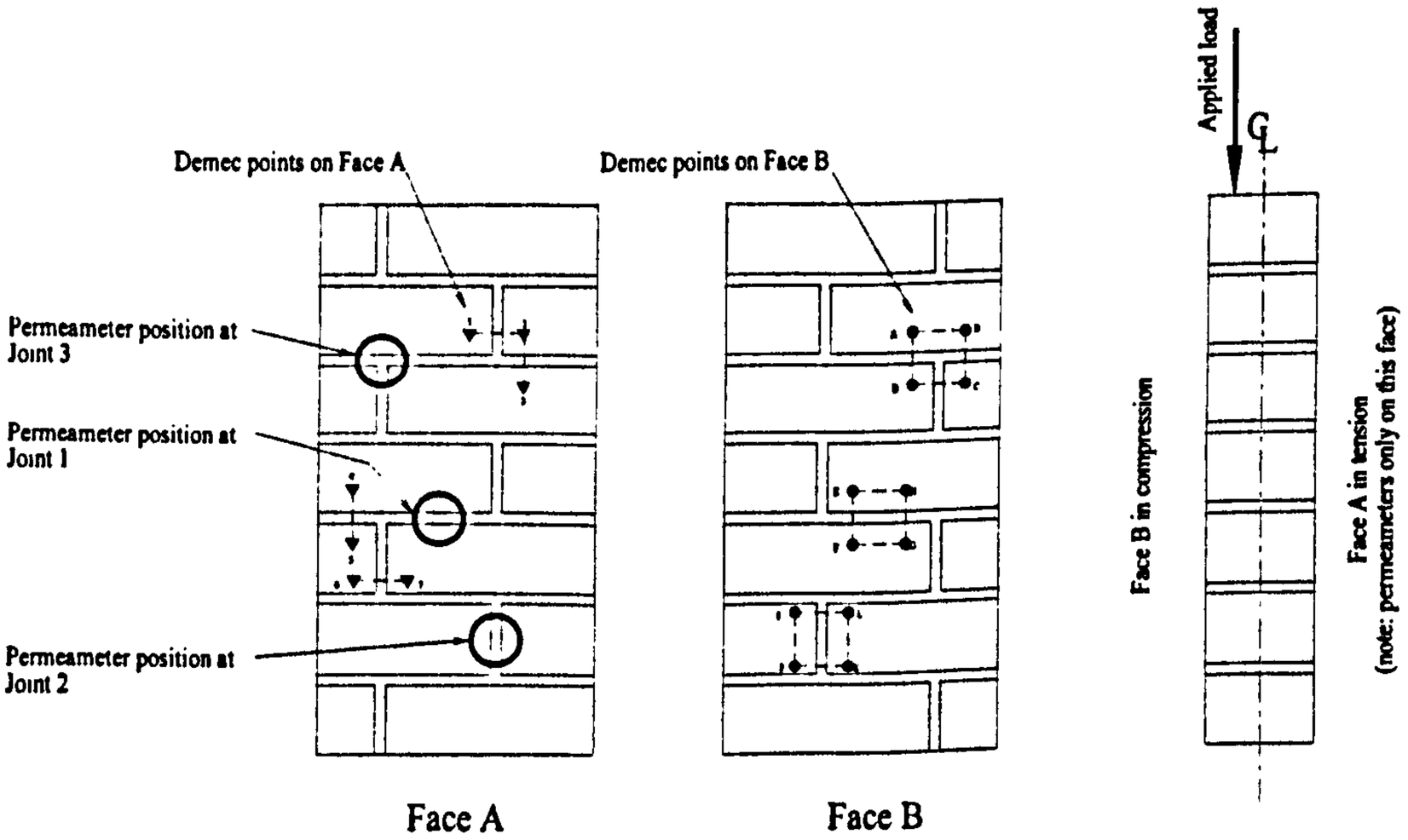

Fig. 7.4 Demec and permeameter position for eccentrically loaded panels: (4Ai, 4Aii)

Water ingress rates were initially measured when the panels were unstressed. Only one initial head (h) of 1000mm was chosen. This head provided a large enough water reservoir to give good, concise results over a reasonable length of time. All loads were increased incrementally to assess strain development on both panel faces.

Two positions of eccentricity (e) were chosen; $e = t_p/6$ and $e = t_p/3$.

The load was applied through hinges (placed at the bottom and top of the panel) made of circular steel rods inserted into a grooved steel capping plate. A swivel head bearing plate ensured accurate positioning of the top hinge which could then deform to take up minor variations in the loading surface. The eccentric loads were applied to panels 4Ai and 4Aii using the same test method as described in Chapter 5.

7.3.2 The load-strain relationship for eccentrically loaded masonry panels

The low slenderness ratio of the panel (S_r=5) meant that lateral buckling would not occur, and the failure mode would be compression. This is indicated in the load-strain relationship for panels 4Ai and 4Aii dependent upon the location of eccentrically applied load and joint position (Fig. 7.5). The strain shown in Fig. 7.5 is that developed on the face that permeameters were attached. For ease of discussion this is denoted as Face 'A' (Fig. 7.4). Strains measured at Joint 3 were of similar magnitude to those shown in Fig. 7.5 and are omitted here for clarity.

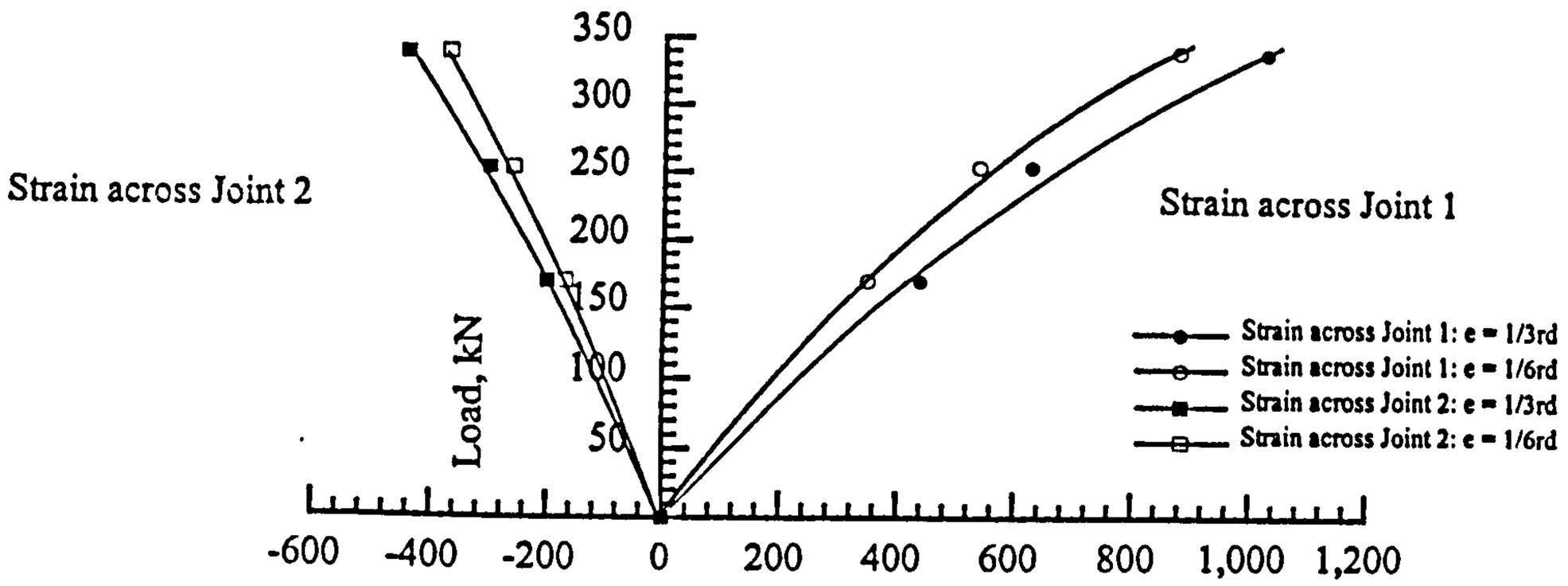

Fig. 7.5 Average load-strain relationship for masonry joints

Figure 7.5 shows clearly that compression strains developed within the panel were affected by the location of the eccentric loading. When e was $t_p/3$, both compressive and tensile strains were approximately 20% greater than when $e = t_p/6$ for all applied load levels.

Assuming that the distribution of stress is both linear and maximum on the compression face, (Face B, Fig. 7.6), then applying an eccentric load at $t_p/3$ and $t_p/6$ would coincide with the resultant of a triangular stress distribution. This is indicated in Fig. 7.6.

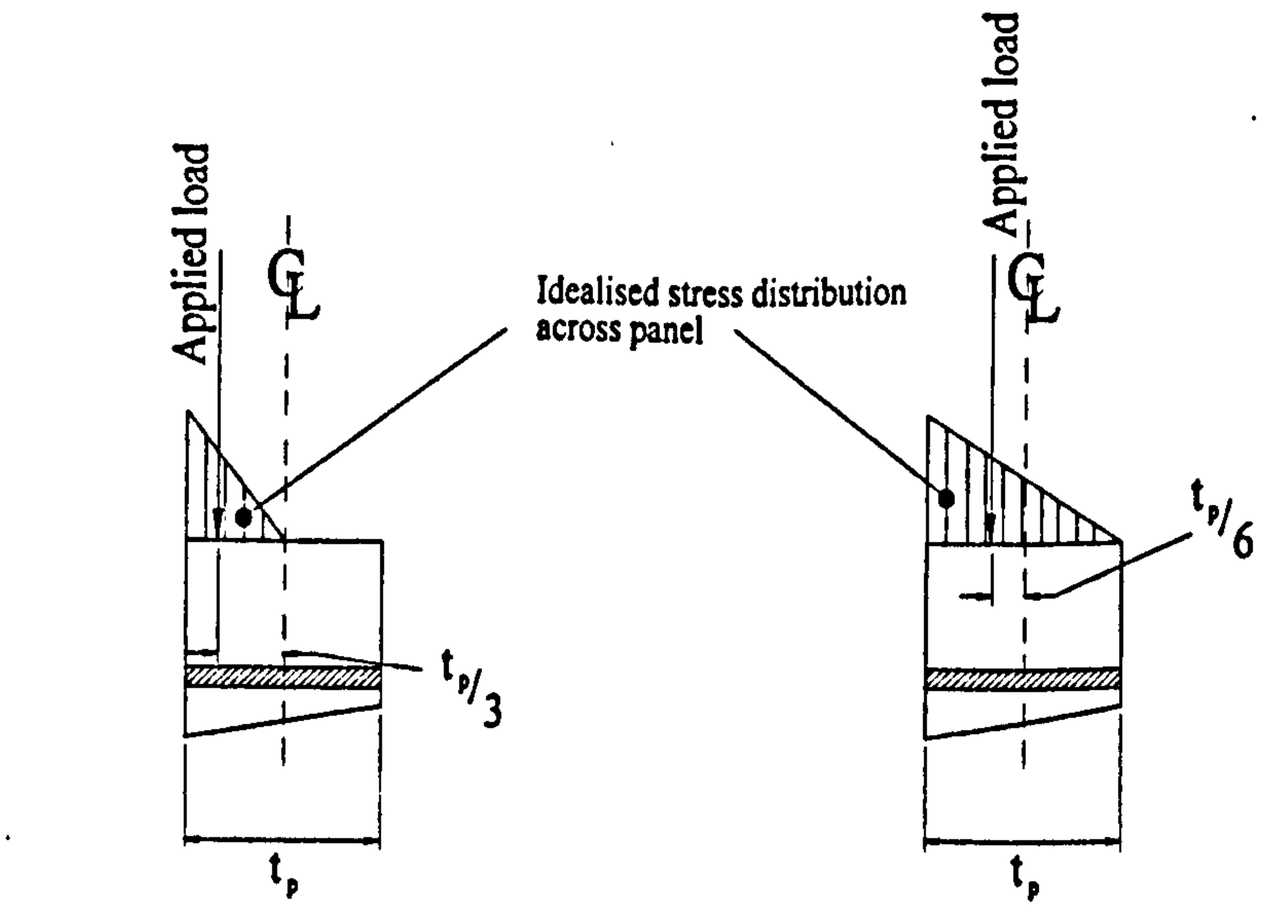

Fig. 7.6 Stress distribution across panel caused by eccentric loading

Some small lateral buckling would occur prior to total structural failure. However compression failure mode controls the behaviour of these panels and generates splitting of the brick units and mortar joints, thus influencing water ingress.

7.3.3 The influence of eccentric loading on water ingress

Figures 7.7-7.9 show the influence of eccentrically applied loads in encouraging or inhibiting water ingress at each joint position. These figures were based on results averaged from experimental data for four tests each on panels 4Ai and 4Aii.

(a) Joint 1:

Figure 7.7 shows water ingress behaviour dependent upon the applied load. This was identified at the two pre-set eccentric load positions.

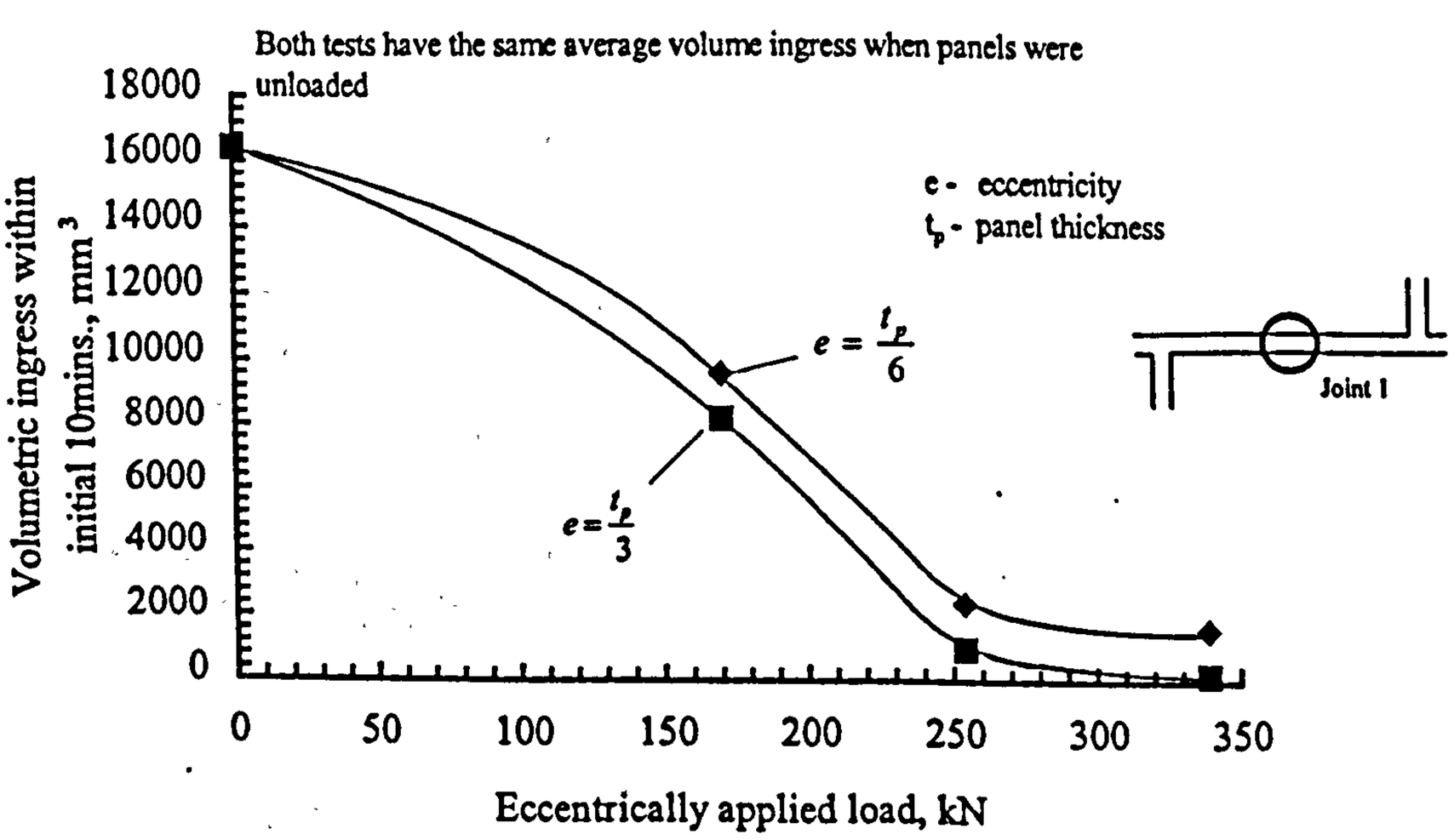

Fig. 7.7 Volume ingress under load at Joint 1 dependent upon eccentricity

The above figure shows similar volume ingress-eccentric load relationships irrespective of the magnitude of eccentricity. This was caused by purely compressive strains being generated across Joint 1.

Figure 7.6 indicates that compressive strains were slightly greater at $e = t_p/3$ which is reflected by the marginal improvement in its corresponding volume of ingress compared to those when $e = t_p/6$ (Fig. 7.7).

(b) Joint 2:

Figure 7.8 shows water ingress behaviour under load at Joint 2 dependent upon eccentric load positions.

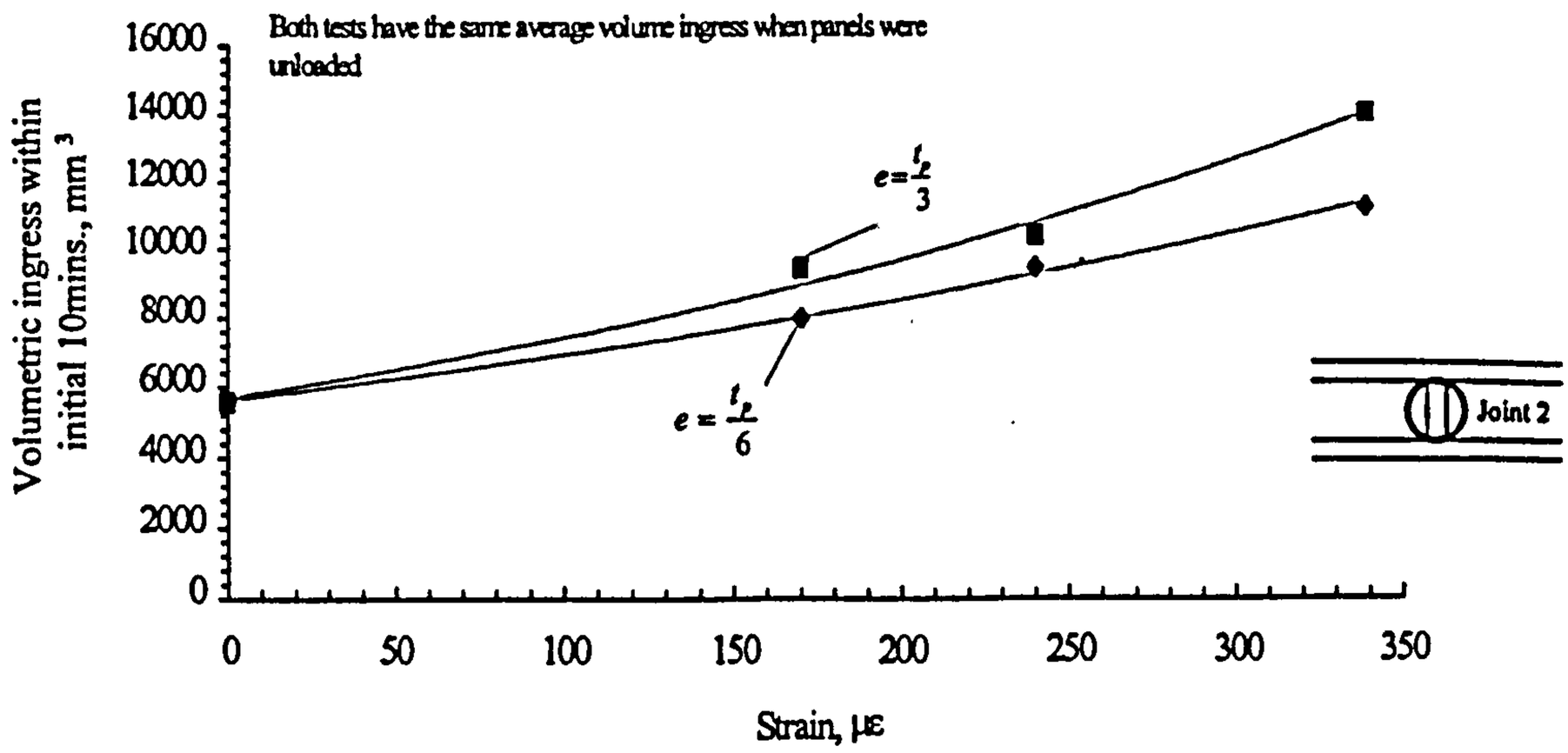

Fig. 7.8 Volume ingress under load at Joint 2 dependent upon eccentricity

The above figure showed that as the applied load level increased to 339kN (equivalent to $0.6F_{ult}$ where F_{ult} is the concentrically applied failure load of the panel) then the panel became increasingly prone to higher levels of water ingress.

Tensile strains were generated across Joint 2 when loaded. These large tensile strains occurred concomitantly with large compressive strains. Figure 7.6 (load-strain relationship) indicated that larger tensile strains occurred at $e = t_p/3$ rather than at $e = t_p/6$ with correspondingly more brick/mortar debonding having occurred. This concurs with the slightly higher volume of ingress when compared to the panel loaded at $e = t_p/6$.

(c) Joint 3:

Figure 7.9 shows water ingress behaviour dependent upon eccentric load.

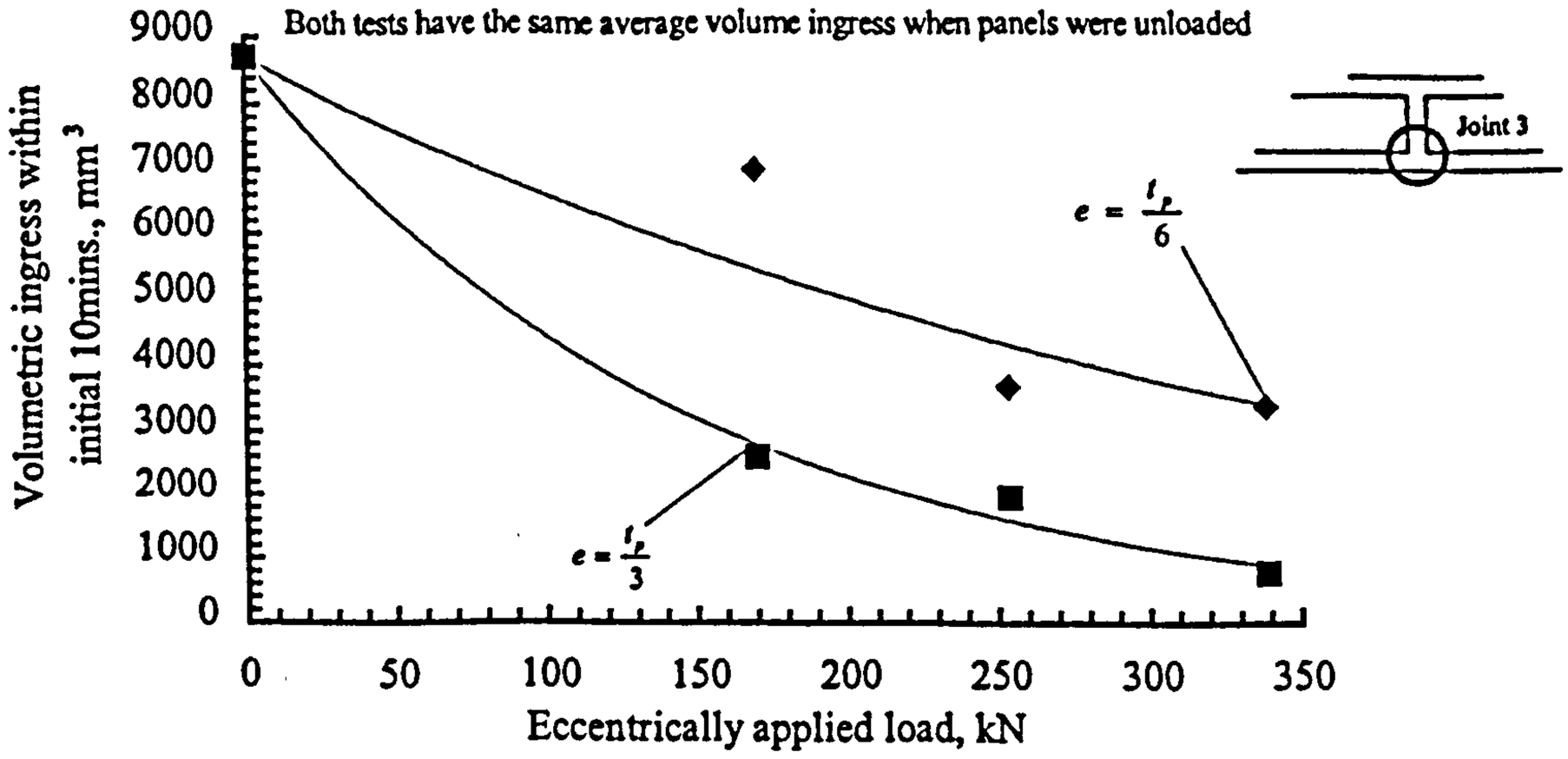

Fig. 7.9 Volume ingress under load at Joint 3 dependent upon eccentricity

As with the relationship exhibited at Joint 1, (Fig. 7.7), panels became increasingly resistant to water ingress as applied load and correspondingly, compressive strains increased. This occurred irrespective of eccentric loading positions.

However, there was a slight difference in water ingress dependent upon eccentric loading position. Panels loaded at eccentricity of $t_p/3$ were found more resistant to water ingress than when loaded at $t_p/6$.

7.4 The Influence of Pre-saturation on the Water Ingress Characteristics of Concentrically Loaded Masonry Panels

When masonry is damp, voids within the brick and mortar and cavities at the brick/mortar interface are filled or partially filled with water. This has the effect of reducing the free space available for additional water ingress.

By measuring water ingress rates for concentrically loaded panels when dry and when saturated, an attempt was made to quantify the effect that pre-saturation has in controlling water ingress.

7.4.1 Panel testing and pre-saturation procedure

Two Type 3 masonry panels were used in this assessment. Type 3 panel (3C) had a cross section of 100x275mm with a concentric ultimate failure load (F_{ult}) of 430kN, equivalent to a failure stress (f_{ult}) of 15.6N/mm^2. For this type of wall, water ingress was monitored at 4.7N/mm^2 ($0.3f_{ult}$), 7.0N/mm^2 ($0.45f_{ult}$) and 9.4N/mm^2 ($0.6f_{ult}$). Panel 3D had a cross section of 100x245mm with an ultimate failure load (F_{ult}) of 117kN, equivalent to a failure stress of 4.8N/mm^2. Water ingress was monitored at 1.4N/mm^2 ($0.3f_{ult}$), 2.1N/mm^2 ($0.45f_{ult}$) and 2.8N/mm^2 ($0.6f_{ult}$).

Permeameter and demec positions for panels 3C and 3D are shown in Fig. 7.10.

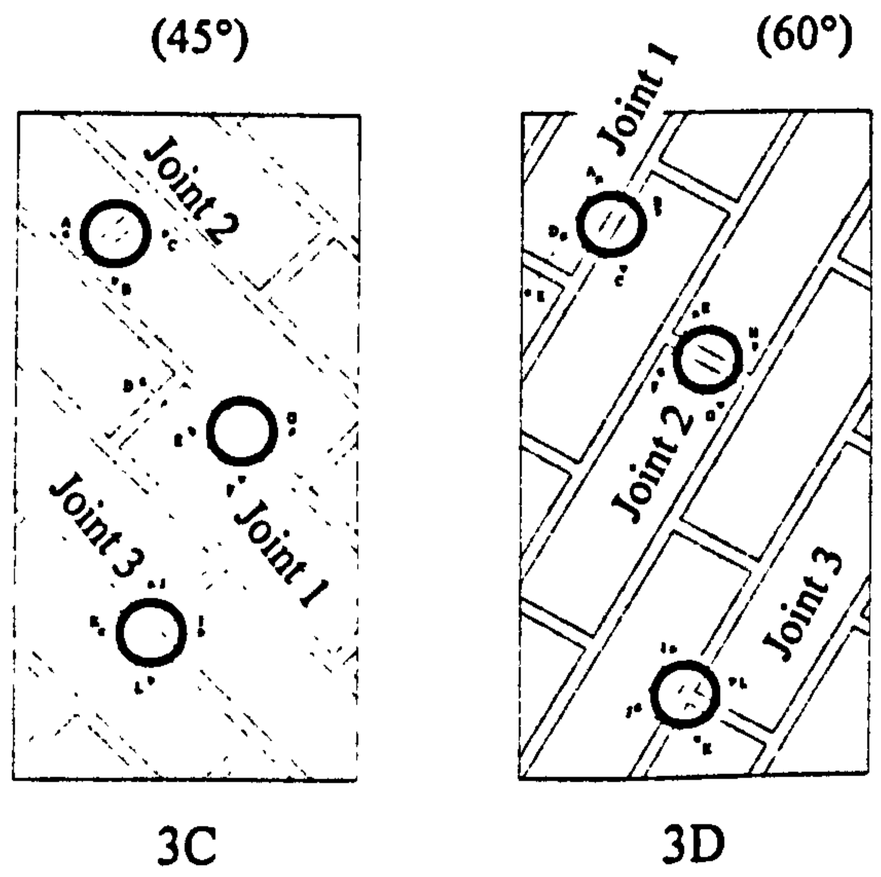

Fig. 7.10 Demec buttons and permeameter position for pre-saturated panels

The bed orientation would have no influence for comparison purposes between water ingress rates when panels were pre-saturated to those when panels were dry.

Pre-saturation involved immersing the test panels in a water tank at a constant temperature of 25°C for 24hrs. Panels were then removed from the tank, fabricated and made ready.

Only an initial head of 1000mm was chosen. This head provided a large enough water reservoir to give good and concise results over a reasonable length of time.

7.4.2 Assessment of pre-saturated panels in resisting water ingress

Table 7.1 shows the improvement in water ingress rates expressed as a percentage, for pre-saturated panels, compared to those when dry, as they were stressed up to $0.6f_{ult}$. This indicated that water ingress rates decreased throughout the test programme irrespective of applied stress level when comparing pre-saturated panels to those when tested dry.

Table 7.1 Average water ingress volumes within initial 10mins of testing for pre-saturated and dry panels when stressed to $0.6f_{ult}$

Applied stress, (N/mm^2)	Average water ingress volumes for panels 3C and 3D								
	Joint 1			Joint 2			Joint 3		
	A (mm^3)	B (mm^3)	%	A (mm^3)	B (mm^3)	%	A (mm^3)	B (mm^3)	%
$0.00f_{ult}$	7300	10000	27	3400	4150	18	14790	17000	13
$0.30f_{ult}$	6440	11500	44	2640	4000	34	14450	16800	14
$0.45f_{ult}$	5985	15750	62	1940	4850	60	10854	20100	46
$0.60f_{ult}$	2880	24000	88	1100	9100	88	14496	30200	52

A - average volume of water ingress for pre-saturated panels within initial 10mins of testing
B - average volume of water ingress for dry panels within initial 10mins of testing (Panels tested when dry and stressed has been discussed in Chapter 6)

$$\% = \frac{(B-A)}{B} \times 100$$

Table 7.1 shows that by pre-saturating a panel, water ingress decreased throughout the stress range of $0.0f_{ult}$ to $0.6f_{ult}$. This was quantified by as much as 88% at Joint 1 when stressed to $0.6f_{ult}$, again by 88% at Joint 2 when stressed to $0.60f_{ult}$ and 52% when stressed to $0.6f_{ult}$ for Joint 3.

Internal water caused by pre-saturation is held in cavities and reservoirs within the masonry panel and can flow relatively easily when a new path caused by stressing is made available. Other water would be held in capillaries within the brick structure. Any effect that caused the widening or the shear of these capillaries caused a loss in suction. This allowed any internal water to flow into the newly developed crack or interstice which then reduced the available space for any external ingressing water.

During experimentation, the panel was observed to act as a 'rigid sponge,' in that during compression the panel pores attempted to 'squeeze' water from the interior to the exterior to accommodate this extra pressure. As water is forced out, it is balanced by the pressurised water from the permeameter attempting to enter. At equilibrium, where external and internal pressures match then there would be no flow at the permeameter position.

However as ingress occurred only over a small effective panel area compared to the whole panel surface, then it is reasonable to assume that the external pressure from the water is greater than the internal pressure from loading. This leads to a pressure differential and causes water to be drawn in at the permeameter positions. The behaviour is influenced by the internal panel water outwith the permeameters' 'circle of influence' having no external pressure being applied. Internal water is therefore free to flow out from the panel face.

7.5 Conclusions

This experimental investigation has shown clearly that both eccentricity of loading and the internal dampness of masonry influence water ingress. The effects of these factors are summarised below:

- As eccentric loads were applied to short, stocky walls which allowed no buckling to occur and hence failure would be by compression, then water ingress rates at Joint 1, 2 and 3 may be considered similar irrespective of eccentric load position.

Only a small differences in ingress rates were recorded between eccentric load positions. Panels loaded at e = $t_p/6$ produced less resistant panel to water ingress than when panels loaded at e = $t_p/3$ for Joint 1 and 3. Joint 2 proved the most resistant to water ingress at both eccentric load positions.

- Irrespective of mortar joint type and applied stress level, pre-saturation of a panel greatly inhibited additional water ingress.

At Joint 1, water ingress volume decreased between 27% (at $0.0f_{ult}$) to 88% (at $0.6f_{ult}$) when pre-saturated panels were compared to corresponding dry panels. Similarly at Joint 2, volume ingress decreased from between 18% to 88% and at Joint 3 by between 13% and 52% over the same stress range.

CHAPTER 8

EMPIRICAL MODELLING OF WATER INGRESS FOR CONCENTRICALLY LOADED MASONRY PANELS

8.1 Introduction

The initial water head, applied stress level and bed orientation were found to be factors in controlling water ingress into masonry panels.

In this chapter, a typical example of the mathematical analysis for water ingress is shown together with comparisons with actual test data for one panel only. Further analytical models for all masonry panels are shown in tabulated form.

8.2 Empirical Modelling of Masonry Panels

Using experimental data, a number of empirical relationships were created that would model the variation in water ingress of concentrically loaded masonry panels under variable initial water heads, applied loads and bed orientations.

Water ingress was identified during testing by the fall in water head in the test reservoir within a given time. This falling head-time relationship was consistently found to follow a best-fit decay curve of the form:

$$y = Ae^{b_0 t} \qquad \text{Eqn. 8.1}$$

y - remaining height of water in test reservoir at time, t, from the commencement of test

A, b_0 - coefficients dependent upon test parameters

These falling head-time relationships were shown throughout Chapter 6 and were classified in terms of mortar joint tested and the bed orientation. Typical examples of these relationships, though not shown here, can be seen in Figs 6.3-6.5 for $\theta=0°$ panels.

The height of water in the reservoir (y) and the related volume of ingress (V_i) can be expressed as a function in terms of a number of experimentally variable parameters.

$$y, V_i = f_1(t) \times f_2(\sigma,\varepsilon) \times f_3(h) \times f_4(\theta) \times f_5(m) \times f_6(\omega) \times f_7(j) \qquad \text{Eqn. 8.2}$$

$f_1(t)$ - time function or duration of test

$f_2(\sigma, \varepsilon)$ - function dependent upon stress and the related strain

$f_3(h)$ - initial head of water in test reservoir

$f_4(\theta)$ - bed orientation of the masonry panel

$f_5(m)$ - material function dependent upon brick and mortar type

$f_6(\omega)$ - function of the construction method at the test position

$f_7(j)$ - function dependent upon joint type and position within test panel (Fig. 8.1)

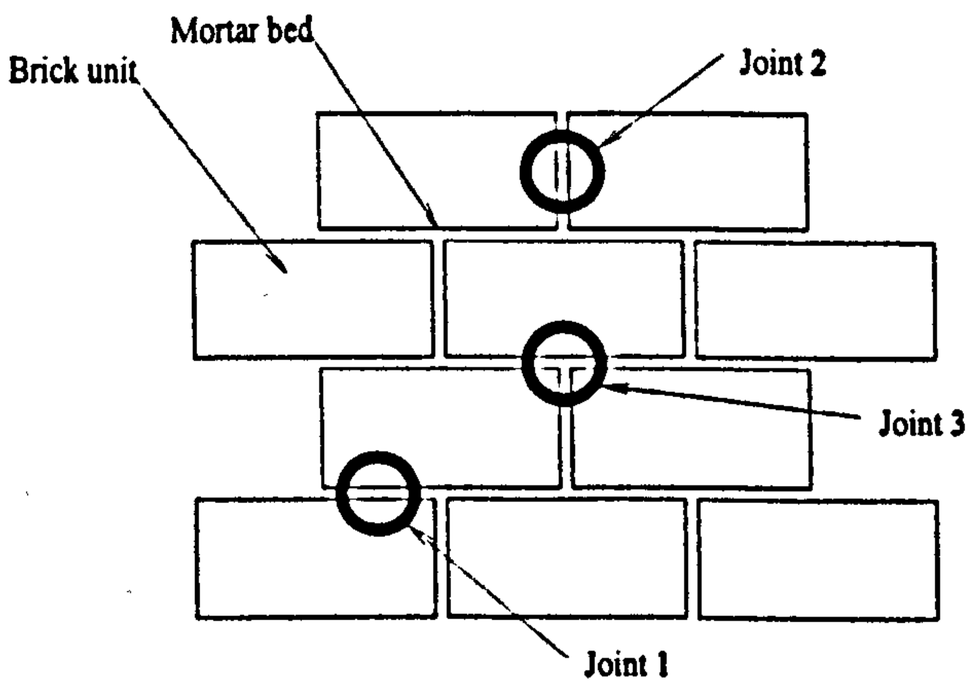

Fig. 8.1 Typical permeameter positions on masonry test panels

These factors are interdependent and have some influence on water ingress rates.

The volume of water ingress (V_i) at a specific time after commencement of testing (t) can be calculated as:

$$V_i = \left(h - y(t)\right).A_r \qquad \text{Eqn. 8.3}$$

h - initial water head of test under consideration

y(t) - level of water head in test reservoir at time, t

A_r - face area of reservoir

Note for this experimental study the reservoir face area was 78.5mm^2 based on a reservoir diameter of 10mm.

8.2.1 Typical example of empirically modelled water ingress

The factors as described in Eqn. 8.2 were incorporated into a general equation that modelled water ingress into a variety of panels in terms of time, initial water head in the reservoir, applied stress level and bed orientation. However, when considering the water ingress into an individual panel then a number of these factors may be discounted.

The bed orientation factor ($f_4(\theta)$) was unique to each masonry panel and was initially discounted. Empirical modelling used average ingress rates from a variety of clay brick panels thereby negating any material factor ($f_5(m)$). Construction ($f_6(\omega)$) was carefully controlled during panel construction and was assumed consistent throughout. .

Due to the unique water ingress behaviour at Joints 1, 2 and 3 then a general equation that would describe ingress irrespective of joint position is not practical. This leads to the $f_7(j)$ factor being discounted from the general equation, and unique equations being generated for each joint position.

(a) Modelled decay curves:

To allow accurate modelling to be undertaken, a full experimental data set describing water ingress into a panel must be available. Panels with bed orientation θ=0° was a typical example. Full data sets were also available for θ=30°, 45° and 60°. It is noted however that a full data set was not available for θ=90° panels due to premature cracking. Therefore this panel type was not considered for modelling.

Table 6.1 (Chapter 6) is shown here for information as Table 8.1. This table shows the average best-fit decay curves based on experimental data for θ=0° panels and dependant upon applied stress, initial head and joint type. The best-fit curves are of the form given in Eqn. 8.1. These decay relationships were generated using Microsoft Excel. The accompanying coefficient of correlation values, R^2, indicate a good agreement between experimental and model data sets, ($R^2 = 0.98$).

Table 8.1 Average decay curves and coefficient of correlation values for panels with bed orientation θ = 0°

Initial head, h, (mm)	Applied stress, (N/mm²)	Joint 1		Joint 2		Joint 3	
		y =	R^2	y =	R^2	y =	R^2
200	0.00 f_{ult}	$139e^{-0.0299t}$	0.99	$173e^{-0.2350t}$	0.98	$180e^{-0.4710t}$	0.98
	0.30 f_{ult}	$149e^{-0.0134t}$	1.0	$159e^{-0.0650t}$	0.96	$200e^{-0.5388t}$	1.0
	0.45 f_{ult}	$151e^{-0.0024t}$	1.0	$164e^{-0.0479t}$	0.96	$188e^{-0.2244t}$	0.99
	0.60 f_{ult}	$151e^{-0.0024t}$	1.0	$165e^{-0.0588t}$	0.97	$188e^{-0.2191t}$	1.0
600	0.00 f_{ult}	$529e^{-0.0171t}$	1.0	$554e^{-0.0223t}$	1.0	$492e^{-0.3568t}$	0.97
	0.30 f_{ult}	$470e^{-0.0049t}$	0.98	$555e^{-0.0235t}$	0.94	$559e^{-0.3151t}$	0.99
	0.45 f_{ult}	$474e^{-0.0041t}$	0.99	$560e^{-0.0220t}$	0.94	$508e^{-0.1393t}$	0.98
	0.60 f_{ult}	$476e^{-0.0034t}$	1.0	$563e^{-0.0204t}$	0.95	$530e^{-0.1041t}$	0.99
1000	0.00 f_{ult}	$851e^{-0.0144t}$	0.99	$850e^{-0.0143t}$	0.99	$753e^{-0.1945t}$	0.85
	0.30 f_{ult}	$847e^{-0.0038t}$	0.95	$848e^{-0.0037t}$	0.97	$767e^{-0.2084t}$	0.90
	0.45 f_{ult}	$863e^{-0.0031t}$	0.98	$864e^{-0.0031t}$	0.98	$872e^{-0.1547t}$	0.99
	0.60 f_{ult}	$859e^{-0.0023t}$	0.98	$860e^{-0.0023t}$	0.97	$869e^{-0.1154t}$	0.98
1500	0.00 f_{ult}	$1358e^{-0.0194t}$	1.0	$1298e^{-0.0114t}$	0.84	$1050e^{-0.1005t}$	0.97
	0.30 f_{ult}	$1351e^{-0.0056t}$	0.98	$1315e^{-0.0045t}$	1.0	$1033e^{-0.1735t}$	0.90
	0.45 f_{ult}	$1349e^{-0.0046t}$	0.98	$1315e^{-0.0135t}$	0.92	$1127e^{-0.0404t}$	0.89
	0.60 f_{ult}	$1361e^{-0.0020t}$	0.97	$1430e^{-0.0162t}$	0.97	$1185e^{-0.0290t}$	0.91

y - Water head in reservoir
t - Time from the commencement of testing
f_{ult} - Average predicted failure stress for panels; for θ=0° panels, f_{ult} =16.4N/mm²

Although the decay curves exhibited in Table 8.1 were unique to θ=0° panels, similar best-fit decay curves based on experimental data were described for θ=30°, 45° and 60° panels. The following procedure for developing empirical models was used for all panel orientations.

(b) Typical joint modelling - Joint 1 only:

Using the best-fit experimental decay relationships as shown in Table 8.1 and the general decay equation, Eqn. 8.1, a linear interpretation in terms of initial head was used to describe the decay coefficient, A.

This decay coefficient was an indication of the height in the reservoir at the start of the test and therefore was highly influenced by the initial head. The linear interpretation was of the form:

$$A = 0.93h - 57 \qquad \text{Eqn. 8.4}$$

Again using Table 8.1 and Eqn. 8.1, a second order polynomial equation was found to correspond with the change in the b_0, which is dependant upon the applied stress. Table 8.2 shows the decay coefficient (b_0) for Joint 1 as a function of the applied stress level and is categorised dependant upon the initial head (h).

Table 8.2 Decay coefficient b_0 as a function of applied stress level for θ=0° panels

Initial head, h (mm)	b_0 (see Eqn. 8.1)	R^2
200	$b_0 = -0.0384\sigma^2 + 0.0700\sigma - 0.0301$	0.98
600	$b_0 = -0.0542\sigma^2 + 0.0548\sigma - 0.0170$	0.99
1000	$b_0 = -0.0458\sigma^2 + 0.0470\sigma - 0.0143$	0.99
1500	$b_0 = -0.0483\sigma^2 + 0.0570\sigma - 0.0192$	0.99

σ - value based on a percentage of the predicted failure stress, f_{ult}

From examining the data in Table 8.2, the coefficient b_0 can be expressed as follows:

$$b_0 = a\sigma^2 + b\sigma + c \qquad \text{Eqn. 8.5}$$

A best-fit second order polynomial was then found to correspond with the change 'a', 'b' and 'c' coefficients dependant upon initial test head (Eqn. 8.5). This is shown in Table 8.3.

Table 8.3 Coefficients a, b and c as a function of initial head

	see Eqn. 8.5	R^2
a	$1.6623x10^{-8}h^2 - 3.3224x10^{-5}h - 3.4433x10^{-2}$	0.85
b	$3.4847x10^{-8}h^2 - 6.9766x10^{-5}h + 8.2959x10^{-2}$	1.0
c	$-2.4534x10^{-8}h^2 + 4.9734x10^{-5}h - 3.8794x10^{-2}$	0.99

Values for the coefficients in Tables 8.2 and 8.3 were taken to four decimal places due to the sensitivity of b_0 to even the small rounding of data. Coefficients of correlation, R^2, exhibited good agreement throughout modelling.

Tables 8.4-8.6 show the modelled data sets for each test panel up to $\theta=60°$. These tables are sub-divided in terms of their joint position using the same technique as described above.

Table 8.4 Empirical modelling coefficients for Joint 1, (Eqn. 8.5)

Panel	a	b	c	A
$\theta = 0°$	$1.6623x10^{-8}h^2 - 3.3224x10^{-5}h - 3.4433x10^{-2}$: $R^2 = 0.85$	$3.4847x10^{-8}h^2 - 6.9766x10^{-5}h + 8.2959x10^{-2}$: $R^2 = 1.0$	$-2.4534x10^{-8}h^2 + 4.9734x10^{-5}h - 3.8794x10^{-2}$: $R^2 = 0.99$	0.93h - 57
$\theta = 30°$	$-7.0687x10^{-8}h^2 + 1.6987x10^{-4}h - 1.0921x10^{-1}$: $R^2 = 0.90$	$2.1608x10^{-8}h^2 - 5.593x10^{-5}h + 3.9297x10^{-2}$: $R^2 = 0.99$	$-3.1944x10^{-9}h^2 + 1.0414x10^{-5}h - 1.1252x10^{-2}$: $R^2 = 0.99$	0.95h - 27
$\theta = 45°$	$-1.5462x10^{-8}h^2 + 3.0572x10^{-5}h - 1.6562x10^{-2}$: $R^2 = 0.76$	$8.5581x10^{-8}h^2 - 1.6934x10^{-4}h + 9.5111x10^{-2}$: $R^2 = 0.83$	$-1.0501x10^{-7}h^2 + 1.9092x10^{-4}h - 1.2802x10^{-1}$: $R^2 = 0.67$	0.89h - 28
$\theta = 60°$	$-9.4739x10^{-7}h^2 + 1.0544x10^{-3}h - 6.0244x10^{-1}$: $R^2 = 0.98$	$3.5128x10^{-7}h^2 - 4.9179x10^{-4}h + 2.7267x10^{-1}$: $R^2 = 0.86$	$-1.5812x10^{-8}h^2 + 2.9685x10^{-5}h - 2.2737x10^{-2}$: $R^2 = 0.90$	0.98h - 17

h - initial head

$b_0 = a\sigma^2 + b\sigma + c$

A - coefficient dependant upon water level in reservoir at start of test - (see Eqn. 8.1)

Table 8.5 Empirical modelling coefficients for Joint 2, (Eqn. 8.5)

Panel	a	b	c	A
$\theta = 0°$	$-2.7233x10^{-7}h^2 + 5.4231x10^{-4}h - 0.2892$: $R^2 = 0.90$	$1.9829x10^{-7}h^2 - 4.4386x10^{-4}h + 0.2652$: $R^2 = 0.90$	$-9.2262x10^{-8}h^2 + 2.2316x10^{-4}h - 0.1396$: $R^2 = 0.99$	0.87h + 5
$\theta = 30°$	$-2.3153x10^{-7}h^2 + 5.8182x10^{-4}h - 3.7756x10^{-1}$: $R^2 = 0.96$	$9.4419x10^{-8}h^2 - 2.2312x10^{-4}h + 1.2989x10^{-1}$: $R^2 = 0.99$	$-2.3272x10^{-8}h^2 + 5.5293x10^{-5}h - 3.7132x10^{-2}$: $R^2 = 0.98$	0.92h - 82
$\theta = 45°$	$2.7525x10^{-8}h^2 - 3.0216x10^{-5}h - 2.7263x10^{-2}$: $R^2 = 0.96$	$-2.4742x10^{-9}h^2 - 1.9862x10^{-5}h + 3.6643x10^{-2}$: $R^2 = 0.86$	$-3.4349x10^{-9}h^2 + 1.6907x10^{-5}h - 2.1589x10^{-2}$: $R^2 = 0.86$	0.97h - 28
$\theta = 60°$	$7.7533x10^{-8}h^2 - 1.4878x10^{-4}h - 1.0179x10^{-2}$: $R^2 = 1.0$	$2.0238x10^{-8}h^2 - 3.4823x10^{-5}h + 3.2412x10^{-2}$: $R^2 = 0.80$	$-9.2346x10^{-9}h^2 + 2.4231x10^{-5}h - 2.0189x10^{-2}$: $R^2 = 0.80$	0.96h - 30

h - initial head

$b_0 = a\sigma^2 + b\sigma + c$

A - coefficient dependant upon water level in reservoir at start of test - (see Eqn. 8.1)

Table 8.6 Empirical modelling coefficients for Joint 3, (Eqn. 8.5)

Panel	a	b	c	A
$\theta = 0°$	$3.4180\times10^{-7}h^2 - 1.4631\times10^{-3}h + 1.4871$: $R^2 = 0.94$	$1.0683\times10^{-8}h^2 + 2.6701\times10^{-4}h - 0.2523$: $R^2 = 0.50$	$-1.6577\times10^{-7}h^2 + 5.3320\times10^{-4}h - 0.5920$: $R^2 = 0.98$	0.69h + 100
$\theta = 30°$	$-1.9006\times10^{-7}h^2 + 3.4710\times10^{-4}h - 1.5770\times10^{-1}$: $R^2 = 0.98$	$1.0289\times10^{-7}h^2 - 1.7340\times10^{-4}h + 7.7072\times10^{-2}$: $R^2 = 1.0$	$-2.127\times10^{-8}h^2 + 3.8151\times10^{-5}h - 2.1208\times10^{-2}$: $R^2 = 0.91$	0.94h - 15
$\theta = 45°$	$2.7520\times10^{-8}h^2 - 3.0216\times10^{-5}h - 2.7263\times10^{-2}$: $R^2 = 0.96$	$-2.4742\times10^{-9}h^2 - 1.9862\times10^{-5}h + 3.6643\times10^{-2}$: $R^2 = 0.86$	$-3.4349\times10^{-9}h^2 + 1.6907\times10^{-5}h - 2.1589\times10^{-2}$: $R^2 = 0.86$	0.93h - 28
$\theta = 60°$	$-2.344\times10^{-7}h^2 + 4.9665\times10^{-4}h - 2.7237\times10^{-1}$: $R^2 = 0.97$	$2.5238\times10^{-7}h^2 - 5.9293\times10^{-4}h + 3.4399\times10^{-1}$: $R^2 = 1.0$	$-7.8459\times10^{-8}h^2 + 1.9113\times10^{-4}h - 1.1836\times10^{-1}$: $R^2 = 1.0$	0.95h - 52

h - initial head

$b_0 = a\sigma^2 + b\sigma + c$

A - coefficient dependant upon water level in reservoir at start of test - (see Eqn. 8.1)

Figures 8.2-8.4 show a typical comparative representation between water ingress rates as measured experimentally and those modelled. This is for $\theta=0°$ panels only. Decay rates as measured by 'A' and 'b_0' (Eqn. 8.1) were calculated using values from Tables 8.4-8.7.

Fig. 8.2 Experimental and theoretical water ingress rates for Joint 1, bed orientation $\theta=0°$

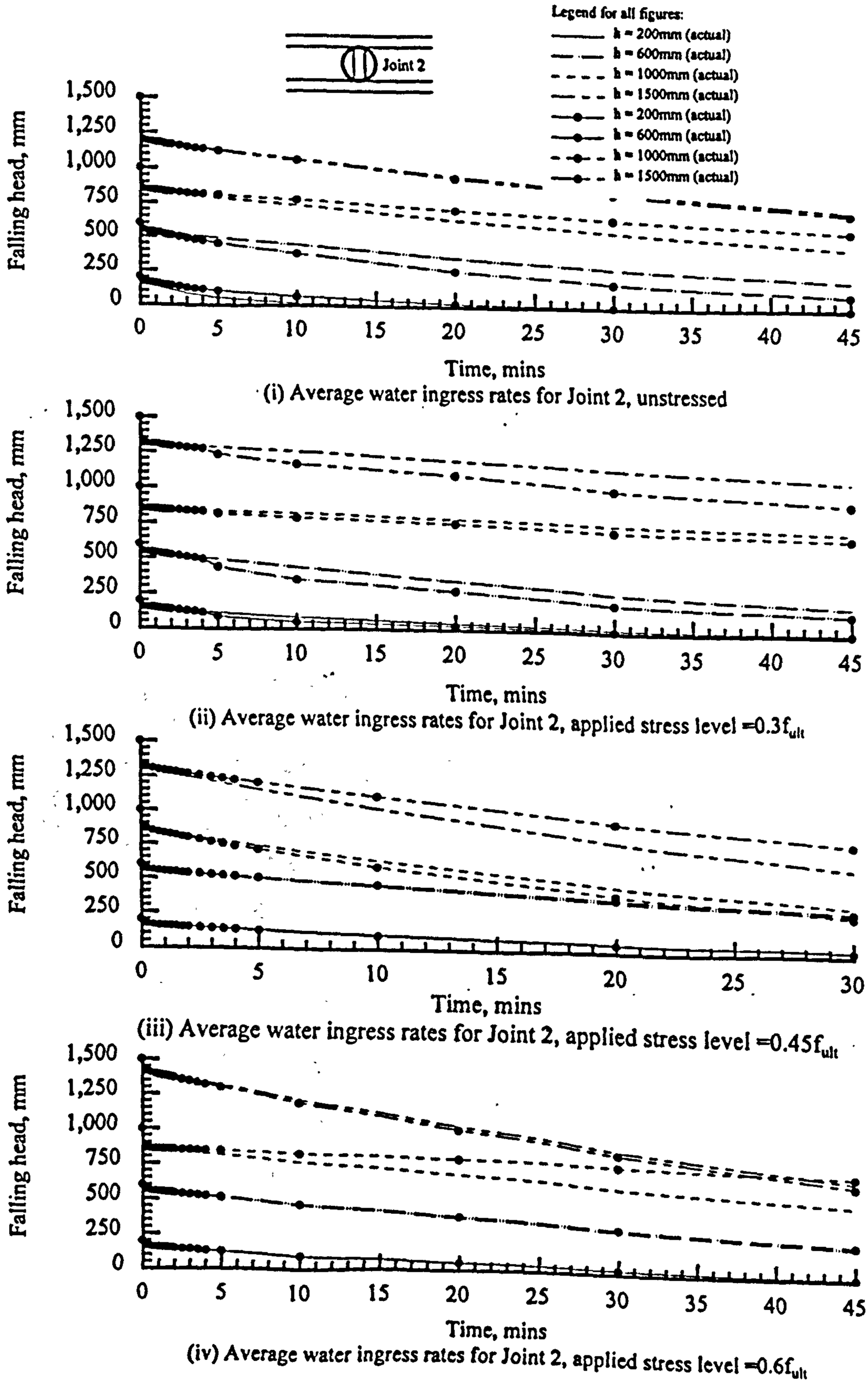

Fig. 8.3 Experimental and theoretical water ingress rates for Joint 2, bed orientation θ=0°

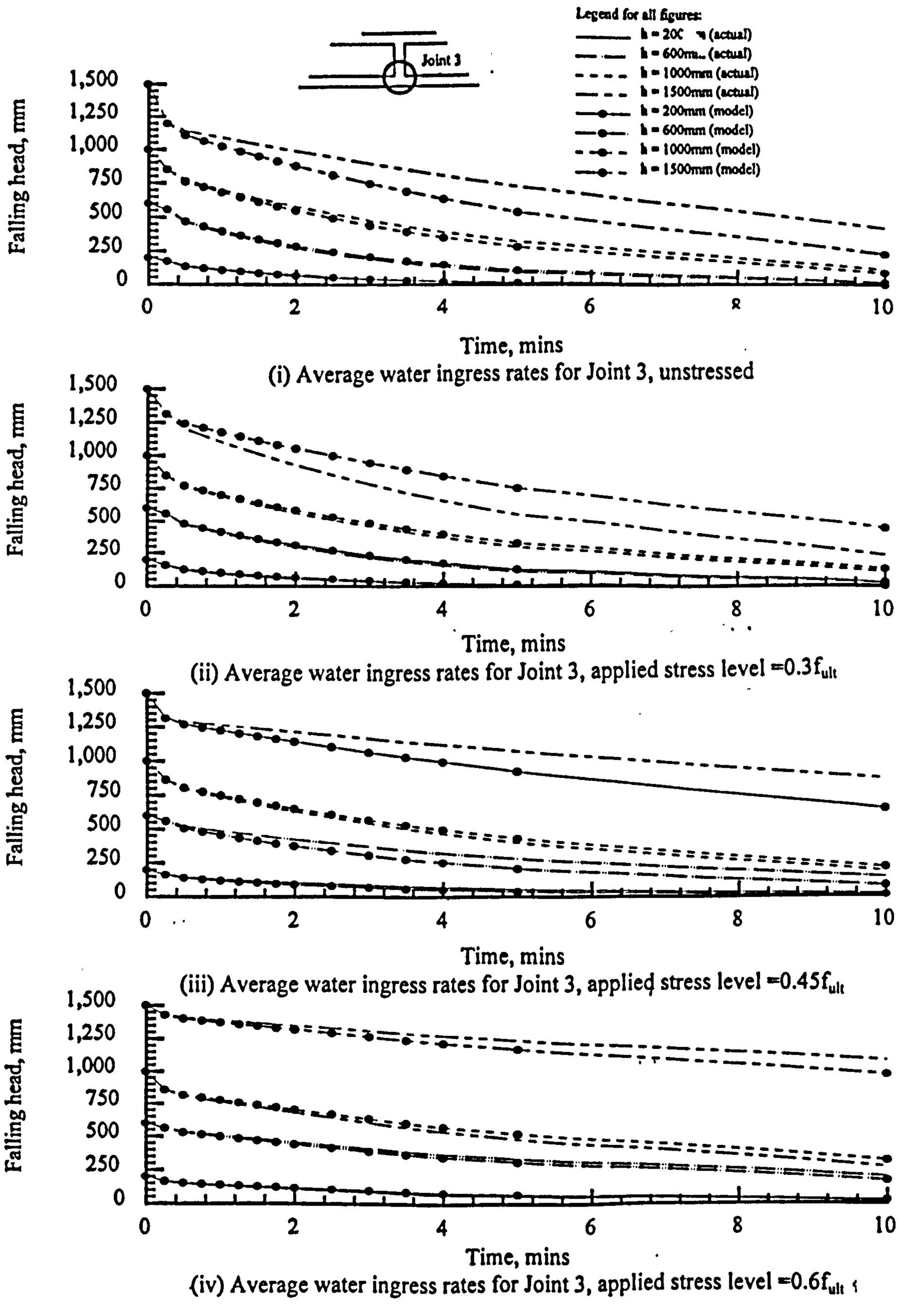

(i) Average water ingress rates for Joint 3, unstressed

(ii) Average water ingress rates for Joint 3, applied stress level =0.3f_{ult}

(iii) Average water ingress rates for Joint 3, applied stress level =0.45f_{ult}

(iv) Average water ingress rates for Joint 3, applied stress level =0.6f_{ult}

Fig. 8.4 Experimental and theoretical water ingress rates for Joint 3, bed orientation θ=0°

The above figures show that empirical modelling of water ingress can be successfully undertaken. This is exhibited by good similarities between experimental and modelled values of ingress rates irrespective of applied stress level, initial head or joint type.

Similar relationships between experimental and modelled water ingress rates were exhibited for all panel types and orientations using the coefficients given in Tables 8.4 - 8.6. To avoid repetition these are not shown.

8.2.2 Empirical modelling incorporating bed orientation

Experimental analysis has shown that the bed orientation of the panels played a significant role in controlling water ingress. By using modelled relationships already described in Tables 8.4-8.6, then a second order best-fit polynomial relationship in terms of bed orientation can be used to describe ingress behaviour at each joint position.

A model of the form similar to that of Eqn. 8.1 (Section 8.2) was then generated (Eqn. 8.6):

$$y = Ae^{b_\theta t} \qquad \text{Eqn. 8.6}$$

b_θ - coefficient as manipulated by the variable bed orientation of the panel

y, A, t - as defined earlier

The coefficient b_θ is of the form:

$$b_\theta = x_\theta \sigma^2 + y_\theta \sigma + z_\theta \qquad \text{Eqn. 8.7}$$

The coefficients in Tables 8.7-8.10 are also influenced by the initial head, h, as exhibited in Eqn. 8.8(a-c):

$$x_\theta = x_{\theta 1} h^2 + x_{\theta 2} h + x_{\theta 3} \qquad \text{Eqn. 8.8(a)}$$

$$y_\theta = y_{\theta 1} h^2 + y_{\theta 2} h + y_{\theta 3} \qquad \text{Eqn. 8.8(b)}$$

$$z_\theta = z_{\theta 1} h^2 + z_{\theta 2} h + z_{\theta 3} \qquad \text{Eqn. 8.8(c)}$$

The coefficients for this general equation (Eqn. 8.6 and 8.7) are exhibited in Tables 8.7-8.10 dependant upon joint type under investigation.

Table 8.7 'A' coefficient for all joints, (Eqn. 8.6)

	A
Joint 1	0.94h - 32
Joint 2	0.93h - 34
Joint 3	0.88h + 2

Table 8.8 'b_θ' coefficient for Joint 1, (Eqn. 8.6)

x_θ	$x_{\theta 1} = -4.6825\times10^{-10}\,\theta^2 + 1.2230\times10^{-8}\,\theta + 1.2769\times10^{-8}$ $x_{\theta 2} = +5.0906\times10^{-7}\,\theta^2 - 1.3983\times10^{-5}\,\theta - 9.7363\times10^{-6}$ $x_{\theta 3} = -2.6622\times10^{-4}\,\theta^2 + 6.9113\times10^{-3}\,\theta - 4.0507\times10^{-2}$
y_θ	$y_{\theta 1} = 1.9592\times10^{-10}\,\theta^2 - 6.8466\times10^{-9}\,\theta + 4.0434\times10^{-8}$ $y_{\theta 2} = -2.6935\times10^{-7}\,\theta^2 + 9.3615\times10^{-6}\,\theta - 7.3279\times10^{-5}$ $y_{\theta 3} = 1.6415\times10^{-4}\,\theta^2 - 6.8361\times10^{-3}\,\theta + 8.4868\times10^{-2}$
z_θ	$z_{\theta 1} = -1.8808\times10^{-11}\,\theta^2 + 1.2732\times10^{-9}\,\theta - 2.4524\times10^{-8}$ $z_{\theta 2} = 3.0824\times10^{-8}\,\theta^2 - 2.1628\times10^{-6}\,\theta + 4.9423\times10^{-5}$ $z_{\theta 3} = -2.1890\times10^{-5}\,\theta^2 + 1.5835\times10^{-3}\,\theta - 3.8832\times10^{-2}$

Table 8.9 'b_θ' coefficient for Joint 2, (Eqn. 8.6)

x_θ	$x_{\theta 1} = 9.3255\times10^{-11}\,\theta^2 + 9.0514\times10^{-10}\,\theta - 2.8237\times10^{-7}$ $x_{\theta 2} = -2.7968\times10^{-7}\,\theta^2 + 3.6426\times10^{-6}\,\theta + 5.6661\times10^{-4}$ $x_{\theta 3} = 1.6286\times10^{-4}\,\theta^2 - 4.0370\times10^{-3}\,\theta - 3.0546\times10^{-1}$
y_θ	$y_{\theta 1} = 3.9158\times10^{-11}\,\theta^2 - 5.5890\times10^{-9}\,\theta + 2.0237\times10^{-7}$ $y_{\theta 2} = -6.0470\times10^{-8}\,\theta^2 + 1.0955\times10^{-5}\,\theta - 4.5150\times10^{-4}$ $y_{\theta 3} = 3.7090\times10^{-5}\,\theta^2 - 6.2981\times10^{-3}\,\theta + 2.6809\times10^{-1}$
z_θ	$z_{\theta 1} = -3.2933\times10^{-11}\,\theta^2 + 3.3886\times10^{-9}\,\theta - 9.2695\times10^{-8}$ $z_{\theta 2} = 7.8326\times10^{-8}\,\theta^2 - 8.0431\times10^{-6}\,\theta + 2.2358\times10^{-4}$ $z_{\theta 3} = -4.6052\times10^{-5}\,\theta^2 + 4.7357\times10^{-3}\,\theta - 1.3934\times10^{-1}$

Table 8.10 'b_θ' coefficient for Joint 3, (Eqn. 8.6)

x_θ	$x_{\theta 1} = 2.5179\times10^{-10}\,\theta^2 - 2.4482\times10^{-8}\,\theta + 3.3837\times10^{-7}$ $x_{\theta 2} = -8.0960\times10^{-7}\,\theta^2 + 7.9888\times10^{-5}\,\theta - 1.4428\times10^{-3}$ $x_{\theta 3} = 6.9693\times10^{-4}\,\theta^2 - 6.9302\times10^{-2}\,\theta - 1.4593\times10^{-1}$
y_θ	$y_{\theta 1} = 4.4541\times10^{-10}\,\theta^2 + 1.2032\times10^{-9}\,\theta + 1.2972\times10^{-7}$ $y_{\theta 2} = -4.7299\times10^{-8}\,\theta^2 - 1.0788\times10^{-5}\,\theta + 2.5641\times10^{-4}$ $y_{\theta 3} = 3.8715\times10^{-5}\,\theta^2 + 6.7343\times10^{-3}\,\theta - 2.3909\times10^{-1}$
z_θ	$z_{\theta 1} = -1.2062\times10^{-10}\,\theta^2 + 8.7954\times10^{-9}\,\theta - 1.6731\times10^{-7}$ $z_{\theta 2} = 3.6678\times10^{-7}\,\theta^2 - 2.7789\times10^{-5}\,\theta + 5.3442\times10^{-4}$ $z_{\theta 3} = -3.3726\times10^{-4}\,\theta^2 + 2.7724\times10^{-2}\,\theta - 5.8591\times10^{-1}$

Figures 8.5-8.7 show the comparison between experimentally measured water ingress rates and those empirically modelled. This is for θ=0° panels only. However, by changing the initial head, stress level and bed orientation then water ingress behaviour can also be modelled for θ=30°, 45° and 60° panels using Tables 8.7-8.10. To avoid repetition, these are not shown.

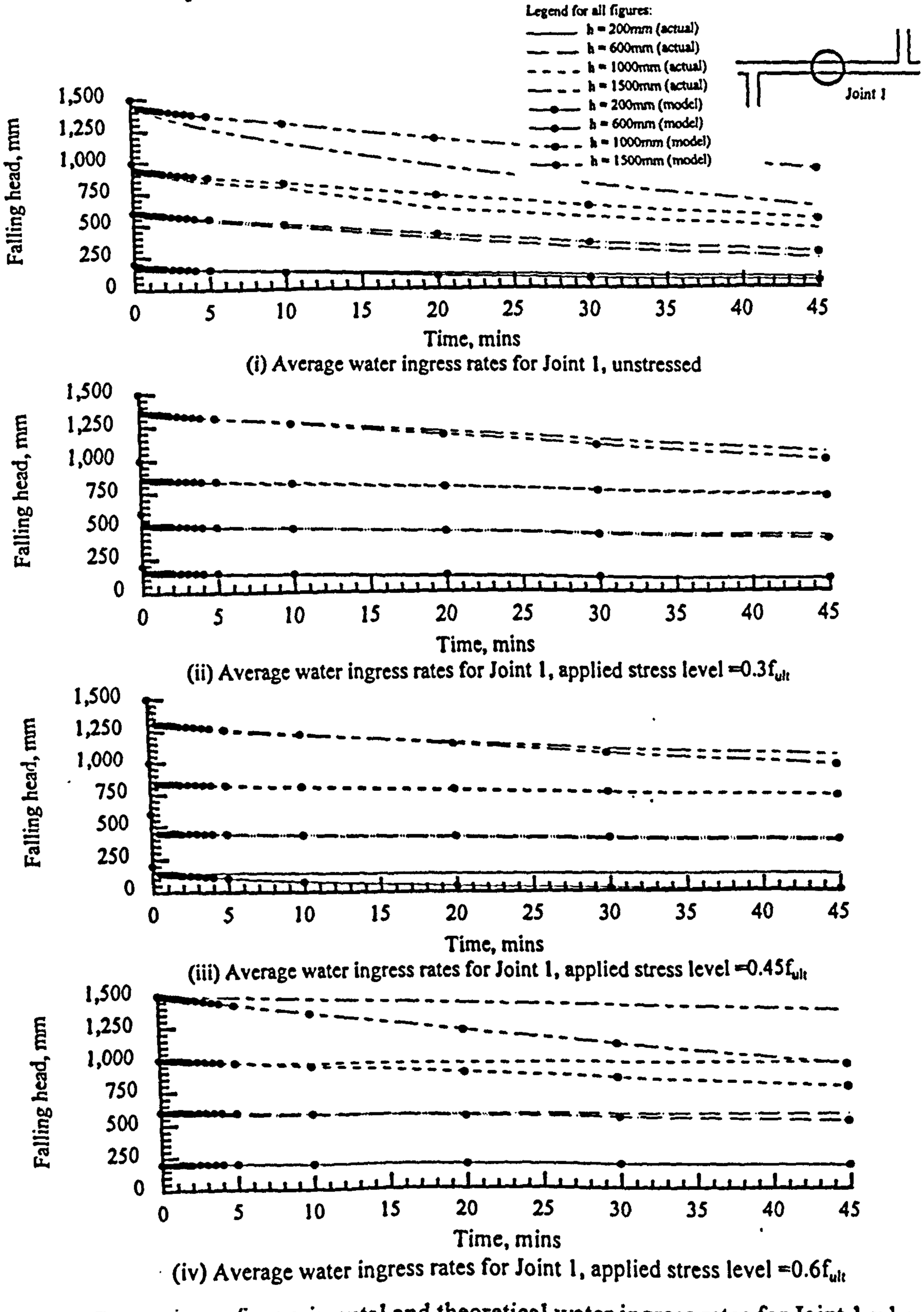

Fig. 8.5 Comparison of experimental and theoretical water ingress rates for Joint 1 when panel orientation was θ=0°, (using Eqns 8.6 and 8.7)

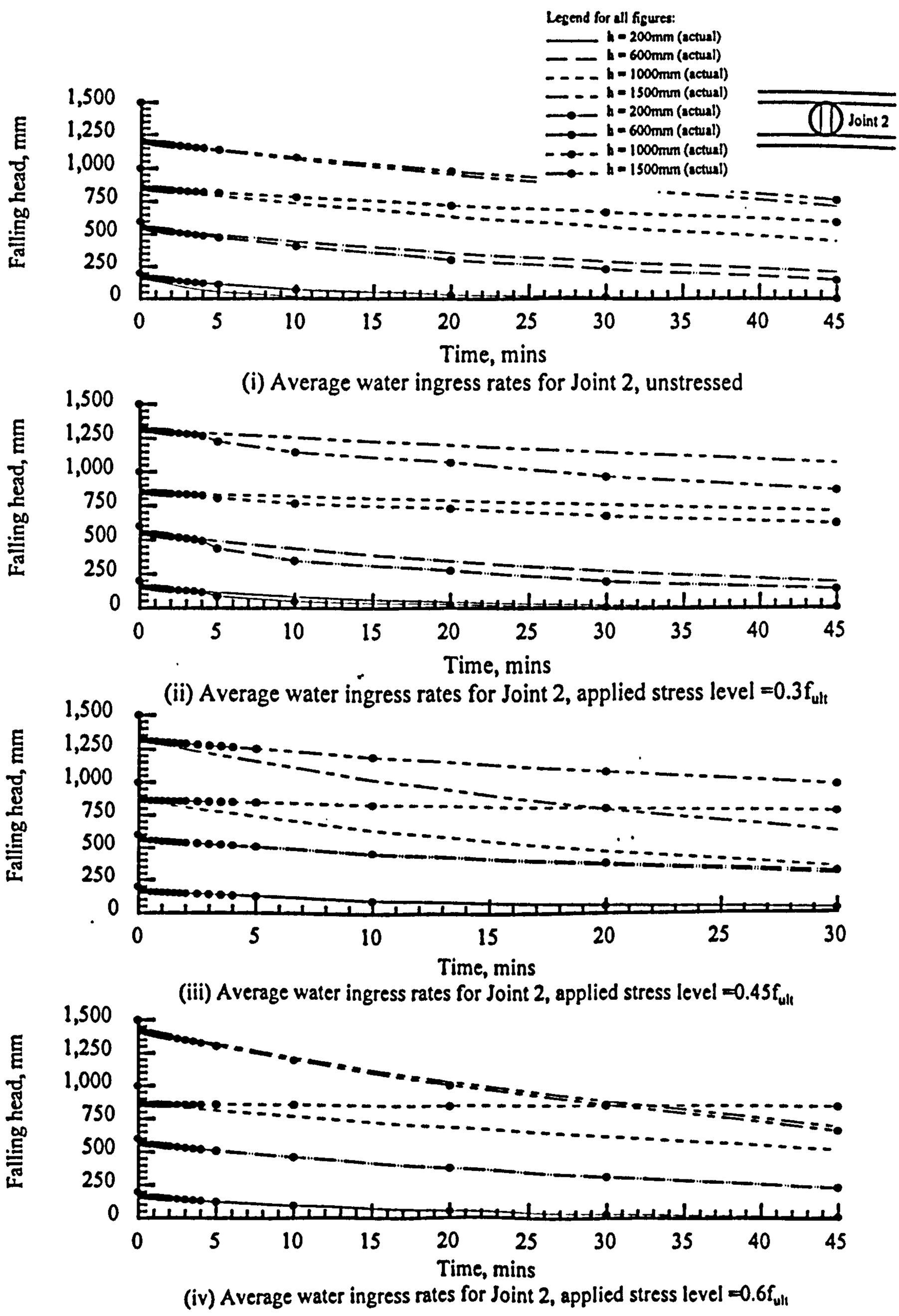

Fig. 8.6 Comparison of experimental and theoretical water ingress rates for Joint 2 when panel orientation was $\theta=0°$, (using Eqns 8.6 and 8.7)

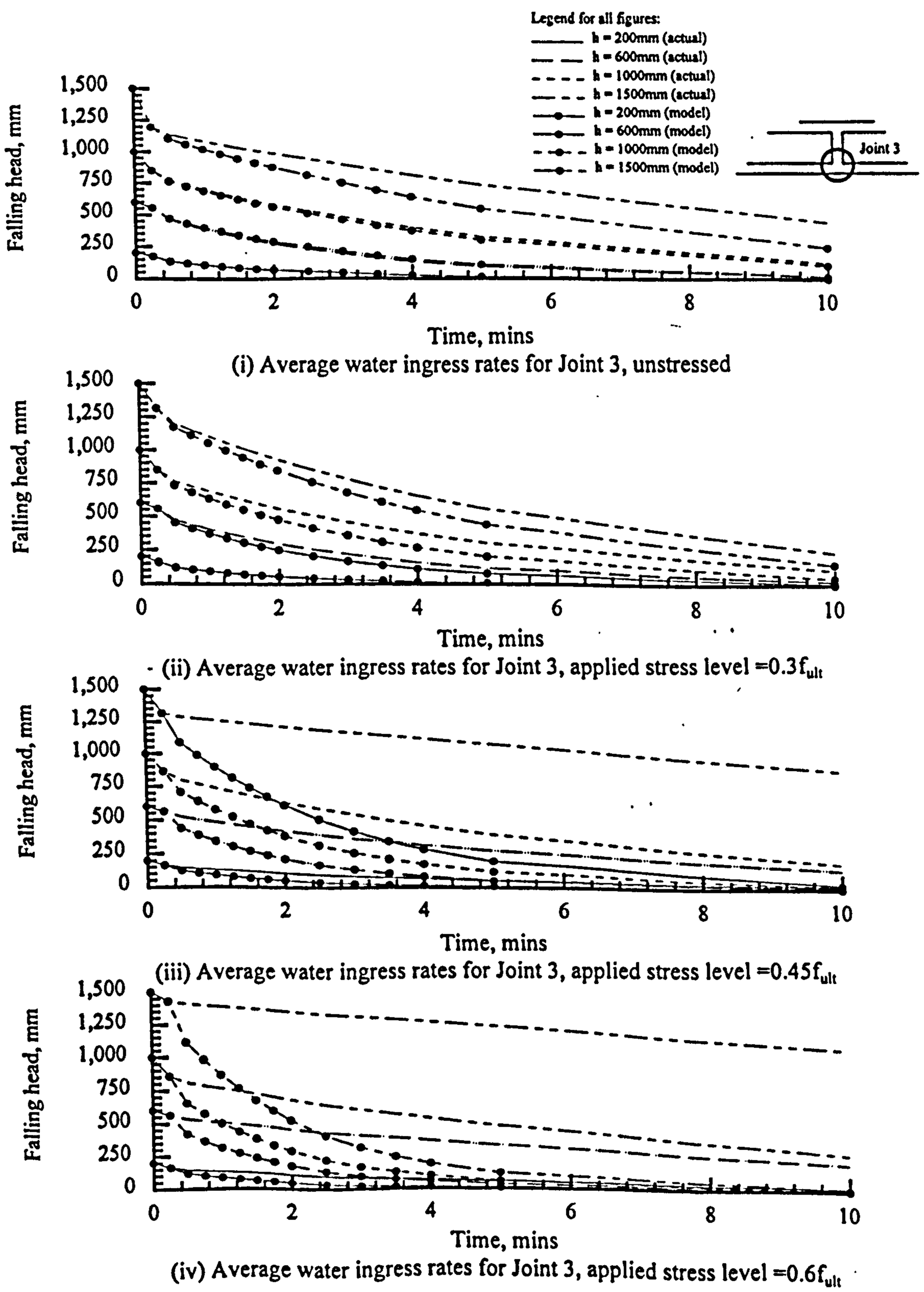

Fig. 8.7 Comparison of experimental and theoretical water ingress rates for Joint 3 when panel orientation was θ=0°, (using Eqns 8.6 and 8.7)

These figures show that empirical modelling of water ingress can be successfully undertaken. These relationships exhibited good agreement between experimental and modelled water ingress rates. This was irrespective of applied stress level, initial head, bed orientation and joint type.

The empirical models were found to compare favourably with experimental data particularly at low load levels. However as the applied stress level increased and influenced greatly the variability of water ingress rates, the model became compromised. This is exhibited most clearly in Fig. 8.6, when applied stress level was $0.45f_{ult}$ and $0.6f_{ult.}$

At Joint 3 (Fig. 8.7), due to the method of construction and the development of stress concentrations and differential strain displacements when panels were loaded only a good correlation was achieved between experimental and modelled water ingress rates at unstressed and low applied stress levels ($\leq 0.3f_{ult}$).

The inclusion of more and more variables results in the water ingress model becoming increasingly complex and compromises the accuracy of empirical models.

8.3 Conclusions

The empirical models for water ingress generated within this chapter exhibited good agreement with experimental data. This showed that mathematical models may be used to generate accurately volumes of water ingressing into a masonry structure from a standing head of water. However, due to the variability in masonry materials and their properties it was recognised that more comprehensive and complex mathematical models considering factors such as brick type, environmental conditions and moisture content would generate increasingly large discrepancies compared to water ingress rates as measured experimentally.

CHAPTER 9

CONCLUSIONS AND RECOMMENDATIONS FOR FUTURE WORK

9.1 Conclusions

From the experimental testing and theoretical analysis carried out in this programme of research a number of conclusions were drawn and these are summarised as follows:

1. The investigation showed that the new permeameter developed during the course of this investigation and used to assess water ingress into masonry is easy to use, cheap to produce and can be used repeatedly without damage. The present study demonstrated that the new permeameters along with the test technique adopted are capable of assessing the volume of water ingress through unstressed and stressed masonry panels.

2. Results from tests on the range of bricks used in this investigation using the new permeameter showed that clay bricks exhibited similar water ingress. These values of water ingress are less than the values determined from tests on calcium silicate bricks.

3. Permeameter tests on mortar showed that water ingress rates are broadly similar for all the different types of mortar used in this investigation. However, for mortar results it was demonstrated that water ingress was 10 times higher than for clay bricks.

4. Changes in bed orientation of the panels exhibited corresponding changes in their concentric ultimate failure load, failure mode and crack development. The results showed that when the mortar bed angle increased, the load carrying capacity of the masonry panels decreased accordingly.

Low bed orientated panels exhibited large vertical cracking through both mortar and brick prior to failure. Shear failure was exhibited for higher bed orientations where the weakest brick/mortar bond was exploited to produce sliding failure along Joint 1. Large tensile cracks at the brick/mortar interface were generated at higher bed orientations before failure was reached.

5. For concentrically loaded panels with bed orientation $\theta=0°$, the main bed (Joint 1) compressed under all levels of applied stress used in the investigation which resulted in the improvement of its resistance to water ingress. Joint 2 exhibited similar improvements up to applied stress levels of $0.45f_{ult}$ as a result of Poisson's ratio effects. However, at applied stress levels of $0.6f_{ult}$, debonding occurred at the brick/mortar interface at Joint 2 which caused an increase in water ingress.

6. At Joint 3, results from unstressed and some of the stressed panels showed that this joint position was less resistant to water ingress than that exhibited at both Joints 1 and 2. The main reason for this was due to the difference in the formation of the mortar joints during the laying of the brick units in the panel. Joints 1 and 2 are formed by compressing the mortar applied to the brick against another previously laid brick. The situation in forming Joint 3 differs fundamentally as there is less mortar in the brick corner after laying and the joint is usually pointed later. This can leave large cavities under the thin mortar skin at the surface with causes large variations in water ingress.

7. Concentrically loaded panels with bed orientation $\theta=90°$ showed severe cracking and debonding at the brick/mortar interface (Joint 1) at a low applied stress level ($0.3f_{ult}$). The panel was broken into a number of distinct columns, which combined and continued to carry more loading though would fail to resist water ingress. This occurred mainly at Joint 1.

Joints 2 and 3 showed an improvement in resistance to water ingress at this level of stress compared to that exhibited at Joint 1. However, due to the distinctive mode of failure of the panel even at these low applied stress levels, the panel was deemed to be structurally unfit to carry applied load or resist water ingress. This result showed the importance of racking shear forces applied to the vertical sides of the panel on its resistance to water ingress.

8. Panels under concentric applied load and orientated at θ=30°, 45° and 60°, relative to the horizontal plane, exhibited mixed compression-tension mode of failure which caused shear slip along Joint 1 together with some cracks and debonding between the brick and mortar interface at Joint 2. The shear mode of failure associated with these types of panel had a fundamental effect on their performance under different levels of applied stress and ultimately their water ingress characteristics. Most of the panels tested with orientations θ=30°, 45° and 60° failed to resist water ingress at an applied stress level approximately equal to $0.45f_{ult}$ though with some this was even lower. The worse water ingress was associated with panels orientated at an angle of θ=60°. The results from these tests proved the importance of monitoring water ingress of walls under load as most load bearing walls in buildings are under combined vertical and horizontal load which may create a shear mode of failure at the mortar joints.

9. The study found that the applied initial water head was not too influential on the water ingress characteristics of unstressed or low stressed panels. This factor was more important when the applied stress level was increased which created micro-cracks caused by compression failure or major cracks caused by shear or splitting failure mainly at the brick/mortar interfaces. Panels under concentric applied load and orientated at θ=30°, 45°, 60° and 90° are typical examples which exhibited this behaviour.

10. Panels constructed using calcium silicate bricks were found to be 2.5-3.8 times more likely to allow water ingress than clay brick counterparts. This was mainly due to differences in the raw materials, method of manufacture and brick/mortar bond.

11. Eccentrically loaded panels exhibited only small differences in water ingress rates despite the variation in the applied eccentric load position. Panels loaded at $e=t_p/6$ produced less resistance to water ingress than panels loaded at $e=t_p/3$.

12. Irrespective of joint type and applied stress level, pre-saturated panels greatly inhibited water ingress compared to correspondingly dry panels.

13. The present study showed that mathematical models may be used to generate accurate volumes of water ingress into masonry panels from a standing head of water. The empirical models for water ingress generated within this study exhibited good agreement with experimental data.

14. Radar testing on brick units highlighted the variation in water contents and successfully indicated its uses in determining areas of dampness and structural decay. This research indicated a clear link between the moisture content within a brick unit and its ability to transmit an electric field.

9.2 Recommendations for Future Work

The investigation of water ingress characteristics of stressed masonry panels was intended to cover and quantify a range of influential parameters. Whilst it was possible to draw direct conclusions of the effects of these parameters, more detailed experimental and analytical work is required to provide accurate ingress modelling.

The objectives of this section is to briefly outline the areas of research which have been shown during this investigation to merit further study.

It is anticipated that the following research would continue through a combined experimental and analytical approach the following:

9.2.1 Experimental research

1. Work should be carried out in two stages; firstly a continuation of the laboratory work; secondly a site investigation programme should be initiated. Laboratory panels and walls built on site differ greatly in terms of quality, workmanship and environmental conditions which should lead to fundamental change in water ingress characteristics. On site tests should be undertaken to verify the suitability of the permeameter apparatus and technique.

2. Laboratory work should examine further the effect of higher applied stresses (up to $0.8f_{ult}$) on water ingress, where higher compressive stresses would induce cracking in all mortar beds irrespective of bed orientation.

3. Tests should be carried out to assess the effects of repeated wetting/drying and freezing/thawing on water ingress of stressed panels to simulate normal environmental conditions.

4. Water ingress assessment should be undertaken on masonry panels with high slenderness ratios that ensure lateral buckling occurs. High lateral buckling would induce high tensile strains and cracking at relatively low load levels. This may compromise the water ingress characteristics of a panel even at low working loads and over a relatively short period of design life. Differing eccentric loading positions should also be considered.

5. Larger panels should be built that can accommodate more permeameters to enable the effect of stressing on the whole of the panel to be assessed with respect to water ingress.

6. To investigate the behaviour of masonry panels to long duration loading and water ingress. This would assess the effect of creep on water ingress.

9.2.2 Numerical modelling

Modelling of small masonry test panels can be successfully undertaken using a finite element mesh, where the panel is effectively discretised into appropriate elements, these elements are assigned properties equivalent to those of either brick or mortar. However for large and more complex structures this type of analysis becomes increasingly time consuming and costly. This has lead to equivalent material properties being developed which homogenises the properties of brick and mortar into an overall masonry property [145-147].

This equivalent material method used in modelling loaded panels assumes that any cracking is negligible in size compared to the size of element in which it is generated, perfect bonds occur on both sides of the crack and the failure mode of the modelled panel is tensile.

This technique has been successfully used to determine failure patterns of masonry which were subsequently confirmed by experimental assessment [147,148]. This method was further used to predict frost damage of masonry and wetting/drying behaviour of structural elements [68,69,149].

Therefore by using the above modelling techniques to develop cracking in the masonry panels together with predicting areas of high stress concentrations, a relationship may be developed to model water ingress into stressed masonry.

REFERENCES

[1] McMillan, F.R. and Lyse, I., 'Some Permeability Studies of Concrete,' Proc. American Concrete Institution, May 1930, pp. 101-142.

[2] Historic Scotland, 'Preparation and use of Lime Mortars,' Technical Advice Notes, Edinburgh, 1995 and Kent, R., Senior Conservation Architect, Historic Scotland, Personal Communication.

[3] Powers, T.C., Copeland, L.E., Hayes, J.C. and Mann, H.M., 'Permeability of Portland Cement Paste,' Proc. American Concrete Institute, Vol. 51, Nov. 1954, pp. 285-298.

[4] Hansen, T.C., 'Physical Structure of Hardened Cement Paste - A Classical Approach,' Materials and Structures, Vol. 49, No. 114, Dec. 1986, pp. 423-436.

[5] Neville, A.M. and Brooks, J.J., 'Concrete Technology - Revised,' Longman Scientific and Technical, Harlow, England, 1993.

[6] Neville, A.M., 'Properties of Concrete,' 2nd Edition, Longman Scientific and Technical, Harlow, England, 1975.

[7] Nyame, B.K., 'Permeability and Pore Structure of Hardened Cement Paste and Mortar,' PhD Thesis, Department of Civil Engineering, University of London, 1979.

[8] Nyame, B.K. and Illston, S.M., 'Relationship between Permeability and Pore Structure of Hardened Cement Paste,' Magazine of Concrete Research, Vol. 33, No. 116, Sept. 1981, pp. 139-146.

[9] Reinhardt, R.W. and Gaber, H.W., 'From Pore Size Distribution to an Equivalent Pore Size of Cement Mortar,' Materials and Structures, Vol. 23, No. 133, Jan. 1990, pp. 3-15.

[10] Feldman, R.F. and Beaudoin, J.J., 'Pretreatment of Hardened Cement Pastes for Mercury Intrusion Measurements,' Cement and Concrete Research, Vol. 21, pp. 297-308.

[11] Day, R.L. and Marsh, B.K., 'Measurement of Porosity in Blended Cement Pastes,' Cement and Concrete Research, Vol. 18, 1988, pp. 63-73.

[12] Powers, T.C., Mann, H.M. and Copeland, L.E., 'Flow of Water in Hardened Portland Cement Paste,' Highways Research Board Specification, Report No. 40, July 1959, pp. 308-323.

[13] Mehta, P.K. and Manmohan, D., 'Pore Size Distribution and Permeability of Hardened Cement Pastes,' The International Congress of Chemistry, Paris, Part 7, 1988, pp. 1 5.

[14] Luping, T. and Nilsson, A., 'A Study of the Quantitative Relationship Between Permeability and Pore Size Distribution of Hardened Cement Paste,' Cement and Concrete Research, Vol. 22, No. 4, July 1992, pp. 541-550.

[15] Muskat, M., 'The Flow of Homogenous Fluids Through a Porous Media,' McGraw-Hill Book Company, New York, 1937.

[16] Scheidegger, A.E., 'Physics of Flow Through Porous Media,' 3rd Edition, University of Toronto Press, 1974.

[17] Hughes, D.C., 'Pore Structure and Permeability of Hardened Cement Paste,' Magazine of Concrete Research, Vol. 37, No. 133, Dec. 1985, pp. 227-233.

[18] Bamforth, P.B., 'The Water Permeability of Concrete and its Relationship with Strength,' Magazine of Concrete Research, Vol. 43, No. 157, Dec. 1991, pp. 233-241.

[19] Klinkenberg, L.J., 'The Permeability of Porous Media to Liquids and Gases,' Drilling and Production Practice, American Petroleum Institute, 1941, pp. 200-214.

[20] Bamforth, P.B., 'The Relationship between Permeability Coefficient for Concrete obtained Using Liquid and Gas,' Magazine of Concrete Research, Vol. 39, No. 138, March 1987, pp. 1-11.

[21] Wiley, G. and Coulson, D.C., 'A Simple Test for Water Permeability,' Journal of the American Concrete Institute, Vol. 34, Sept. 1938, pp. 65-75.

[22] Murata, J., 'Studies on Permeability of Concrete,' Synopsis of Yoshida Prize Paper for 1963, Civil Engineering in Japan, 1964, pp. 39-45.

[23] Ruettgers, A., Vidal, E.N. and Wing, S.P., 'An Investigation of the Permeability of Mass Concrete with particular reference to the Boulder Dam,' Journal of the American Concrete Institute, April 1935, pp. 382-416.

[24] Dhir, R.K., Hewlett, P.C. and Chan, Y.N., 'Near Surface Characteristics of Concrete: Intrinsic Permeability,' Magazine of Concrete Research, Vol. 41, No. 147, June 1989, pp. 87-97.

[25] Dhir, R.K., Arun, G.A. and Munday, J.G.L., 'Effects of In-source Variability of Pulverised Fuel Ash upon the Strength of OPC/PFA Concrete,' Magazine of Concrete Research, Vol. 33, No. 117, Dec. 1981, pp. 199 - 207.

[26] Harrison, W. H., 'Durability Tests on Building Mortars - Effect of Sand Grading,' Magazine of Concrete Research, Vol. 38, No. 135, June 1986, pp. 95-107.

[27] Harrison, W.H. and Barbour, G.K., 'Aspects of Mortar Durability,' Trans. of the British Ceramic Society Journal, Vol. 89, No. 3, May - June 1990, pp. 93-107.

[28] Nyame, B.K., 'Permeability of Normal and Lightweight Mortars,' Magazine of Concrete Research, Vol. 37, No. 130, March 1985, pp. 44-48.

[29] Glanville, W.H., 'The Permeability of Portland Cement Concrete,' Technical Report No. 3, Building Research Station, HMSO, London, 1926.

[30] Dhir, R.K., Hewlett, P.C. and Chan, Y.N., 'Near Surface Characteristics of Concrete: Assessment and Development of In-Situ Methods,' Magazine of Concrete Research, Vol. 39, No. 141, Dec. 1987, pp. 183-196.

[31] Kermani, A., 'Permeability of Stressed Concrete,' International Journal of Research and Development, Building Research and Information, Vol. 19, No. 6, 1991, pp. 360-366.

[32] Tait, C.J., Kermani, A. and Khalaf, F.M., 'Permeability of Concrete: A Practical Approach,' Concrete in the Service of Mankind, International Congress, University of Dundee, Dundee, Scotland, June 1996, pp. 435-441

[33] Ludirdja, D., Berger, R.L. and Young, J.F., 'Simple Methods for Measuring the Water Permeability of Concrete,' ACI Materials Journal, Vol. 86, No. 5, Sept-Oct 1989, pp. 433-439.

[34] Mercer, L.B., 'Permeability of Concrete,' The Commonwealth Engineer, July 1945, pp. 349-357.

[35] Figg, J.W., 'Methods of Measuring Air and Water Permeability of Concrete,' Magazine of Concrete Research, Vol. 25, No. 85, Dec. 1973, pp. 213-219.

[36] Cather, R.W., Figg, J.W., Marsden, A.F. and O'Brien, T.P., 'Improvements to the Figg Method for Determining the Air Permeability of Concrete,' Magazine of Concrete Research, Vol. 36, No. 129, Dec. 1984, pp. 241-245.

[37] Kasai, Y., Matsui, I. and Nagano, M., 'On Site Air Permeability Tests for Concrete,' SPT-108, Malhotra, V.M., Ed., American Concrete Institute, Detroit, 1984, pp. 525-541.

[38] The Concrete Society, 'Permeability of Concrete and its Control,' Report of a Concrete Society Working Party on 'Permeability of site Concrete - A Review of Methods and Experience,' Final Draft, Conference, London, December 1985.

[39] Hansen, A.J., Ottosen, N.S. and Petersen, C.G., 'Gas Permeability of Concrete In-Situ: Theory and Practice,' SPT-108, Malhotra, V.M., Ed., American Concrete Institute, Detroit, 1984, pp. 543-556.

[40] Hudd, R.W., 'Measurement of the In-Situ Concrete Permeability,' PhD Thesis, Dept. of Civil Engineering, Loughborough University of Technology, 1989.

[41] Schonlin, K. and Hilsdorf, H., 'Evaluation of the Effectiveness of Curing of Concrete Structures,' ACI Special Publication No. 100: Concrete Durability, Vol. 1, American Concrete Institute, Detriot 1987, pp. 207-225.

[42] Long, A.E., Montgomery, F.R. and Cleland, D., 'Assessment of Concrete Strengths and Durability On Site,' Section 4 - Investigation Techniques (Concrete), Proc. International Conference on Structural Faults and Repair, Forde, M.C., Ed., Vol. 1, London, July 1987, pp. 61-74.

[43] Long, A.E., Basheer, P.A.M. and Rankin, I., 'In-Situ Testing of Near Surface Concrete - The Foundation for Service Life Prediction,' Insight, Vol. 39, No. 7, July 1997, pp. 482-487.

[44] British Standard Institution, 'Methods of Testing Hardened Concrete for Other than Strength,' London, BS 1881, Part 5, 1980.

[45] Basheer, P.A.M., 'A Brief Review of Methods for Measuring the Permeation Properties of Concrete In-Situ,' Proc. of the Institute of Civil Engineers, Structures and Building, Vol. 99, Issue 1, Feb. 1993, pp. 74-83.

[46] Lindsay, J.D., 'Illinois Develop High Pressure Air Meter for Determination of Hardened Concrete,' Proc. of the Highway Research Board No. 35, 1956, pp. 242-435.

[47] Tyler, I.L. and Erlin, B., 'A Proposed simple Test Method for Determining the Permeability of Concrete,' Journal for the Portland Cement Association and Development Laboratories, Sept. 1961, pp. 2-7.

[48] van der Meulen, G. J.R. and van Dijk, J., 'Permeability - Testing Apparatus for Concrete,' Magazine of Concrete Research, Vol. 21, No. 67, June 1969, pp. 121-123.

[49] Cabrera, J.G. and Lynsdale, C.J., 'A New Gas Permeameter for Measuring the Permeability of Mortar and Concrete,' Magazine of Concrete Research, Vol. 44, No. 144, Sept. 1988, pp. 177-182.

[50] McBurney, J.W., 'The Water Absorption and Penetrability of Brick,' Proc. of the American Society for Testing and Materials, Vol. 29, Part 2, 1929, pp. 711-739.

[51] Palmer, L.A., 'Water Penetration through Brick - Mortar Assemblages,' Journal of the Clay Products Institute, Sept. 1931, pp. 19-31.

[52] Sneck, T., 'The Interaction Between Mortar and Masonry Units as a Basis for Standards for Masonry Mortars,' NBS Special Publication 361, Vol. 1; Performance Concept in Buildings, Proc. Joint RILEM-ASTM-CIB Symposium, Philidelphia, USA, May 1972, pp. 687-692.

[53] Connor, C.C., 'Factors in the Resistance of Brick Masonry Walls to Moisture Penetration,' Proc. American Society for Testing and Materials, Vol. 48, 1948, pp. 1020-1054.

[54] Palmer, L.A. and Parsons, D.A., 'A Study of the Properties of Mortars and Brick and their Relation to Bond,' National Bureau of Standards Research Journal, Research Paper RP683, Vol. 12, 1934, pp. 609-644.

[55] Kampf, L., 'Factors Affecting Bond of Mortar to Brick,' Symposium on Masonry Testing, ASTM STP 320, American Society for Testing and Materials, 1962, pp. 127-142.

[56] Hoskings, J.S. and Hueber, H.V., 'Dimensional Changes Due to Moisture and Brickwork,' Symposium on Masonry Testing, ASTM STP 320, American Society for Testing and Materials, 1962, pp. 107-127.

[57] Jessop, E.L., 'Moisture, Thermal, Elastic and Creep Properties of Masonry: A State of the Art Report,' Proc. of the 2nd Canadian Masonry Symposium, Stutter G.T. and Keller, H., Eds., Carlton University, Canada, 1980, pp. 505-520.

[58] Zsembery, S., 'Developments in the Determination of Moisture Expansion in clay Brick,' Proc. 9th Australian Ceramic Society, Austceram 80, Sydney, Australia, Aug. 1980, pp. 328-338.

[59] British Standards Institution, 'Clay Bricks,' London, BS 3921:1985.

[60] Peake, F. and Ford, R.W., 'A comparison of the Vacuum and Boiling Methods for Measuring the Water Absorption of Bricks,' Trans. British Ceramic Society, Vol. 81, No. 5, Sept-Oct 1982, pp. 160-162.

[61] Hall, C., Hoff, W.D. and Skeldon, M., 'The Sorptivity of Bricks: Dependence on the Limited Water Content,' Journal of Physics D: Applied Physics, Vol. 16, No. 10, Oct. 1983, pp. 1875-1880.

[62] Hall, C., 'Water Sorptivity of Mortars and Concretes: A Review,' Magazine of Concrete Research, Vol. 41, No. 147, June 1989, pp. 51-61.

[63] Hall, C. and Tse, T.K., 'Water Movement in Porous Building Materials - VII. The Sorptivity of Mortars,' Building and Environment, Vol. 21, No. 2, 1986, pp. 113-118.

[64] Butler, A., 'Capillary Absorption by Concrete,' Concrete, July/August 1997, pp. 23-25.

[65] Ritchie, T. and Davidson, J.I., 'Factors affecting Bond Strength and Resistance to Moisture Penetration of Brick Masonry,' Symposium on Masonry Testing, ASTM STP 320, 1962, pp. 16-30.

[66] Dennis, R.H., 'Admixture for Reducing the Water Absorption Rate for Autoclaving Building Materials,' Chemistry and Industry, March 1970, pp. 377-380.

[67] Yorkdale, A.H., 'Initial Rate of absorption and Mortar Bond,' Masonry: Materials, Properties and Performance, ASTM STP 778, Borchelt J.G., Ed., American Society for Testing Materials, 1982, pp. 91-98.

[68] Kralj, B., Middleton, J. and Pande, G.N., 'A Numerical Model for the Prediction of Frost Damage to Brickwork,' Masonry International, Vol. 4, No. 3, 1991, pp. 89 - 93.

[69] Kralj, B., Pande, G.N. and Middleton, J., 'On the Mechanism of Frost Damage to Brick Masonry,' Computers and Structures, Vol. 41, No. 1, 1991, pp. 53 - 66.

[70] Madgwick, E., 'Water Movements in Porous Building Materials,' Proc. International Association for Testing Materials, London Conference, 1937, pp. 366-372.

[71] Stull, R.T. and Johnson, P.V., 'Relation Between Air and Water Permeabilities of Building Brick,' Bulletin of the American Ceramic Society, Vol. 20, No. 12, Dec. 1941, pp. 443-447.

[72] Mills, E.O., 'The Permeability to Air and Water of Some Building Bricks,' Transactions of the British Ceramic Society, Vol. 33, 1933-34, pp. 200-212.

[73] Hansen, W. and Kung, J.H., 'Pore Structure and Frost Durability of Clay Bricks,' Materials and Structures, Vol. 21, No. 126, Nov. 1988, pp. 443-447.

[74] Davidson, J.I., 'Linear Expansion Due to Freezing and Other Properties of Brick,' Proc. of the Second Canadian Symposium, Sutter, G.T. and Keller, H., Eds., Carleton University, 1980, pp. 13-24.

[75] Robinson, G.C., 'The Relationship Between Pore Structure and Permeability of Brick,' American Ceramic Society Bulletin, Vol. 63, No. 2, Feb. 1984, pp. 295-300.

[76] Maage, M., 'Frost resistance and Pore Size Distribution in Bricks,' Materials and Structures, Vol. 17, No. 101, September 1984, pp. 345-350.

[77] Winslow, D.N., Kilgour, C.L. and Crooks, R.W., 'Predicting the Durability of Brick,' Journal of Testing and Evaluation, Vol. 16, No. 6, November, 1988. pp. 527-531.

[78] Barkofsky, P.R. and Driscoll, M.E., 'A Theoretical Model of Water Penetration into Concrete Masonry Units,' Masonry: Design and Construction, Problems and Repair, ASTM STP 1180, J.M. Melander and L.R. Lauersdorf, Eds., American Society for Testing and Materials, 1993, pp. 301-313.

[79] Driscoll, M.E. and Gates, R.E., 'A Comparative Review of Various Test Methods for Evaluating the Water Penetration Resistance of Concrete Masonry Wall Units,' Masonry: Design and Construction, Problems and Repair, ASTM STP 1180, J.M. Melander and L.R. Lauersdorf, Eds., American Society for Testing and Materials, 1993, pp. 228-239.

[80] Gratwick, R.T., 'Dampness in Buildings,' 2nd Edition (Metric), Crosby Lockwood Staples, 1974.

[81] Newman, A.J. and Whiteside, D., 'Water and Air Penetration Through Brick Walls - A Theoretical and Experimental Study,' Trans. of the Journal of the British Ceramics Society, Vol. 80, No. 1, Jan-Feb. 1981, pp. 27-36.

[82] Dearborn, W.D., 'Experiments for Making Brick Masonry Impervious to Water,' Trans. of the American Society of Civil Engineers, Vol. 1, 1872, pp. 203-208.

[83] Thayer, R.D., 'Moisture Control in Masonry Maintenance,' Sewage Works Journal, Vol. 19, No. 5, 1947, pp. 911-914.

[84] The British Clayworker, 'The Cause of Red and Brown Stains of Facing Brick,' Vol. 39, No. 466, pp. 411.

[85] Marusin, S.L., 'Interior Fissures and Microstructure of Clay Brick,' American Ceramic Society Bulletin, Vol. 62, No. 11, Nov. 1983, pp. 1264-1268.

[86] Fishburn, C.C., 'Effects of Wetting and Drying on the Permeability of Masonry Walls,' Building materials and Structures, National Bureau of Standards, BMS 55, Sept. 1940.

[87] Fishburn, C.C. and Peterson, P.H., 'Effects of Heating and Cooling on the Permeability of Masonry Walls,' Building Materials and Structures, National Bureau of Standards, BMS 41, Oct. 1940.

[88] Garden, C.K., 'Rain Penetration and its Control,' Canadian Building Digest, Division of Building Research, National Research Council of Canada, Report CBD40, 1963.

[89] Grimm, C.T., 'Masonry Cracks: Cause, Prevention and Repair,' Masonry International, Vol. 10, No. 3, 1997, pp. 66-76.

[90] Atkinson, R.H. and Noland, J.L., 'A Proposed Failure Theory for Brick Masonry in Compression,' Proc. 3rd Canadian Masonry Symposium, Landworth, J. and Warmurak, J., Eds., Edmonton, Canada, June 1983, pp. 5.1-5.17.

[91] Grimm, C.T., 'A Driving Rain Index for Masonry Walls,' Masonry: Materials, Properties and Performance, ASTM STP 778, Borchelt, J.G., American Society for Testing and Materials, 1982, pp. 237-244.

[92] Eppel, F.J., 'Rain Penetration of Masonry,' International Journal of Masonry Construction, Vol. 2, No. 1, 1981, pp. 20-25.

[93] Anderegg, F.O., 'Construction of Watertight Brick Masonry,' Journal of the American Ceramic Society, Vol. 13, No. 5, 1930, pp. 315-324.

[94] Huizer, A. and Ward, M.A., 'A Single Wyth Concrete Masonry Unit with Good Resistance to Wind Driven Rain,' Masonry: Materials, Properties and Performance, ASTM STP 778, Borchelt, J.G., Ed., American Society for Testing and Materials, 1982, pp. 66-75.

[95] Krogstad, N.V. and Weber, R.A., 'Using Modified ASTM E 1105 to Evaluate the Resistance of Masonry Barrier, Mass and Skin Walls to Rain,' Masonry: Design and Construction, Problems and repair, ASTM STP 1180, Melander, J.M. and Lauersdorf, L.R., Eds., American Society for Testing and Materials, 1993, pp. 265-275.

[96] Department of the Environment Construction, 'Rain Penetration of Brickwork,' March 1977, pp. 26-29.

[97] Fishburn, C.C., Watstein, D. and Parsons, P.E., 'Water Permeability of Masonry Walls,' Building Materials and Structures, National Bureau of Standards, BMS 7, Oct 1938.

[98] Parsons, D.E., 'Brick Laying to Avoid Leaks,' American Builder and Building Age, Vol. 59, 1937, pp. 7-8.

[99] Hendry, A.W., 'Workmanship Factors and Strength of Masonry,' Masonry International, Journal of the British Ceramic Society, Winter, 1988, pp 89-92.

[100] Bright, N.J., Saunders, J.D., and Fudge, C.A., 'Influence of Workmanship on the Aesthetics of Calcium Silicate Brickwork,' Masonry International, Journal of the British Masonry Society, Winter 1989/1990, pp. 73-76.

[101] Hendry, A.W., Sinha, B.P. and Davies, S.R., 'Load Bearing Brickwork Design,' 2nd Edition, Ellis Howard Ltd., Publ., 1987.

[102] Maurenbrecher, A.H.P., 'Axial Compression Tests on Masonry Walls and Prisms,' The Masonry Society, Proc. 3rd North American Conference, Matthys, J.H. and Borchelt, J.G., Eds., University of Texas at Arlington, Texas, June 1985, pp. 19.1-19.14.

[103] Lawrence, S.J. and Cao, H.T., 'An Experimental Study of the Interface Between Brick and Mortar,' Proc. 4th North American Masonry Conference, Lawrence, S.J. and Cao, H.T., Eds., Los Angeles, USA, pp. 48.1-48.14.

[104] Dhansekar, M., Page, A.W. and Kleeman, P.W., 'The Failure of Brick Masonry Under Biaxial Stress,' Proc. Institution of Civil engineers, Vol. 79, June 1985, pp. 295-313.

[105] Drysdale, R.G. and Hamid, A., 'Tension Failure Criteria for Plain Concrete Masonry,' Journal of Structural Engineering, American Society of Civil Engineers, Vol. 110, No. 2, Feb. 1984, pp. 228-244.

[106] Hodgkinson, H.R. and Davies, S.R., The Stress - Strain Relationship of Brickwork when Stressed in Directions other than Normal to the Bed Face,' 6th Inter Brick-Masonry Conference, Rome, May 1982, pp. 290-299.

[107] Ali, S. and Page, A.W., 'Concentrated Loads on Solid Masonry Walls: A Parametric Study and Design Recommendation,' Proc. Institution of Civil Engineers, Part 2, Vol. 85, 1988, pp. 271-289.

[108] Page, A.W., 'An Experimental Investigation of the Biaxial Strength of Brick Masonry,' 6th International Masonry Conference, May 1992, pp. 3-15.

[109] Rivero, C.E. and Phan, D., 'A First Approximation to the Development of a Failure Surface for Masonry Under a Biaxial State of Stress,' Proc. 3rd North American Masonry Conference, University of Texas at Arlington, Texas, June 1985, pp. 67.1-67.14.

[110] Hamid, A.A. and Drysdale, R.G., 'Behaviour of Brick Masonry Under Combined Shear and Compression Loading,' 6th International Masonry Conference, May 1992, pp. 51-64.

[111] Bernadini, A., Modena, C. and Vescori, U., 'Deformation and Failure Models for Hollow Clay Brick Masonry Under Biaxial States of Stress,' Proc. 3rd Canadian Masonry Symposium, Langworth, J. and Warmuruk, J., Eds., Edmonton, Canada, June 1983, pp. 8.1-8.14.

[112] Hamid, A.A. and Drysdale, R.G., 'Concrete Masonry Under Combined Shear and Compression Along the Mortar Joints,' ACI Journal, Sept.-Oct. 1980, pp. 314-320.

[113] Hendry, A.W., 'Structural Masonry,' McMillan Education Ltd., London, 1990.

[114] Khoo, C.L. and Hendry, A.W., 'Strength Tests on Brick and Mortar Under Complex Stresses for the Development of a Failure Criterion for Brickwork in Compression,' Proc. British Ceramic Society, Vol. 21, 1973, pp. 57-66.

[115] Ghazali,, M.Z. and Riddington, J.K., 'Simple Test Method for Masonry Shear Strength,' Proc. Institution of Civil Engineers, Part 2, 1988, pp. 567-574.

[116] Andreaus, U., 'Failure Criterion for Masonry Panels Under In-Plane loading.' Journal of Structural Engineering, American Society of Civil Engineers, Vol. 122, No. 1, January 1996, pp. 37-46.

[117] Birkeland, O., 'Rain Penetration Investigation: A Summary of the Findings of a CIB Working Commission on Rain Penetration,' Norwegian Building Research Institute, Report No. 36, 1963.

[118] Birkeland, O. and Svendsen, S.D., 'Norwegian Test Methods for Rain Penetration Through Masonry Walls,' Symposium on Masonry Testing, ASTM STP 320, American Society for Testing and Materials, 1962, pp. 3-15.

[119] Butterworth, B. and Skeen, J.W., 'Experiments on the Rain Penetration of Brickwork,' Trans. British Ceramic Society, Vol. 61, No. 9, 1962, pp. 487-519.

[120] British Standards Institution, 'BS 4315: Methods of Testing for Resistance to Air and Water Penetration: Part 1 - Windows and Glazing Systems,' London, 1970.

[121] British Standards Institution, 'BS 4315: Methods of Testing for Resistance to air and Water Penetration: Part 2 - Permeable Walling (Construction),' London, 1970.

[122] Thomas, K., 'The Design of Rain Penetration Machine to Comply with British Standard Requirements,' 4th International Brick-Masonry Conference, April 1976, pp. 5-10.

[123] Bloem, D.L., 'Effects of Aggregate on Properties of Masonry Mortar,' Symposium on Masonry Testing, ASTM STP 320, American Society for Testing and Materials, 1962, pp. 67-92.

[124] British Standards Institution, 'Testing Aggregates: Part 103 Methods for Determining Particle Size Distribution: Section 103.1, Sieve Tests,' London, BS 812: Part 103.1: 1983.

[125] British Standards Institution, 'Building Sands from Natural Sources,' London, BS 1200: 1976.

[126] British Standards Institution, 'Sands for Mortar for Plain and Reinforced Brickwork, Blockwork and Masonry,' London, BS 1200: 1976.

[127] British Standards Institution, 'Portland Cement,' London, BS 812: 1989.

[128] British Standards Institution, 'Building Lime,' London, BS 890: 1972.

[129] British Standards Institution, 'Methods for Testing Mortars, Screeds and Plasters,' London, BS 4551: 1980.

[130] Bowler, G.K., Jackson, P.J. and Monk, M.G., 'The Measurement of Mortar Workability,' Masonry International, Vol. 10, No. 1, 1996, pp. 17-23.

[131] Bowler, G.K., Jackson, P.J. and Monk, M.G., 'The Role of Mortar Workability (Cohesivity) in the Rain Penetration of Masonry,' Masonry International, Vol. 10, No. 1, 1996

[132] British Standards Institution, 'Testing Concrete: Part 121 Methods for Determination of Static Modulus of Elasticity in Compression,' London, BS 1881: 1989.

[133] Khalaf, F.M., Hendry, A.W. and Fairbairn, D.R., 'Mechanical Properties of Materials Used in Concrete Blockwork Construction,' Magazine of Concrete Research, Vol. 44, No. 158, March 1992, pp. 1-14.

[134] Khalaf, F.M., Hendry, A.W. and Fairbairn, D.R., 'Elastic Modulii and Strength of Hollow Block Masonry with Reference to the Effect of Lateral Ties,' Magazine of Concrete Research, Vol. 44, No. 160, Sept. 1992, pp. 185-194.

[135] Butterly Bricks Ltd., 'A Complete Guide to Butterly Brick Products,' Brochure Fg2, Jan. 1993.

[136] Hatzinikolas, M., Langworth, J. and Warmuruk, J., 'Failure Modes for Eccentrically Loaded Concrete Block Masonry Walls,' American Concrete Institute Journal, July-August, 1980, pp. 258-263.

[137] Hendry, A.W., 'Structural Brickwork,' Macmillan Press Ltd., London, 1981.

[138] British Standards Institution, 'Structural Masonry: Part 1 Unreinforced Masonry,' London, BS 5628: 1978

[139] Haseltine, B.A. and Moore, J.F.A., 'Handbook to BS 5628: Structural Use of Masonry,' The Brick Development Association.

[140] Bungey, J.H. and Millard, S.G., 'Radar Investigation of Structures,' Proc. Institution of Civil Engineers, Structures and Building, Vol. 99, May 1993, pp. 173 - 186.

[141] Bungey, J.H., 'Radar Testing of Concrete Structures,' Concrete Society Meeting, Roxburgh Hotel, Edinburgh, Dec. 1997.

[142] Bungey, J.H., 'GPR Materials Research,' Proc. Use of Radar to Investigate Site and Structures, Assoc. of Consulting Scientists, Cox, T.G. and Stove, G.C., Eds., London, Feb. 1995, pp. 5.1 - 5.11.

[143] Forde M.C., McCavitt, N., Brinda, L. and Colla, C., 'Identification of Moisture Capillarity in Masonry Using Digital Radar,' Proc. 5th International Conference on Structural Faults and Repair, Vol. 2, pp. 397 - 403.

[144] Bevan, D.J., 'Geotechnical Radar Scanning for: Soil Stratigraphy/Lithography and Geotechnical Analysis and Design Parameters,' Proc. Use of Radar to Investigate Site and Structures, Assoc. of Consulting Scientists, Cox, T.G. and Stove, G.C., Eds., London, Feb. 1995, pp. 2.1 - 2.16.

[145] Middleton, J., Pande, G.N., Liang, J.X. and Kralj, B., 'Some Recent Advances in Computer Methods in Structural Masonry,' Proc. of Computer Methods in Structual Masonry, Conference, Swansea, April 1991, pp. 1-21.

[146] Pande, G.N., Liang, J.X. and Middleton, J., 'Equivalent Elastic Moduli for Brick Masonry,' Computers and Geotechnics, Vol. 8, 1989, pp. 243 - 265.

[147] Lee, J.S., Pande, G.N. and Middleton, J., 'Numerical Modelling of Cracking in Masonry Structures,' Proc. of Computer Methods in Structural Masonry, Conference, April 1993, pp. 1 - 13.

[148] Lee, J.S., Pande, G.N., Middleton, J. and Kralj., B., 'Numerical Modelling of Brick Masonry Panels Subject to Lateral Loading,' Computers and Structures, Vol. 61, No. 4, 1996, pp. 735 - 745.

[149] Garrecht, H., 'Research on Moisture Behaviour and on Moisture Protection Measures with the Support of Numerical Modelling,' Draft Paper, The University of Karlsruhe, Karlsruhe, Germany.